The Catalytic Fast Pyrolysis of Biomass

Joseph Michael Socci

Doctor of Philosophy

ASTON UNIVERSITY

May 2019

Aston University
EBRI (European Bioenergy Research Institute)

The Catalytic Fast Pyrolysis of Biomass

Joseph Michael Socci

Doctor of Philosophy

May 2019

One of the main challenges for the catalytic fast pyrolysis of biomass waste is the development of active and stable catalysts that can deal with the large variety of thermal decomposition intermediates from lignocellulosic biomass waste. The microporous zeolite ZSM-5 is one of the most extensively studied catalysts in this area due to its strong acidity and shape selectivity. However, a major limitation of ZSM-5 is its micropore structure, which limits the diffusion of large molecules produced from the pyrolysis of lignocellulose substrates. For this reason, mesoporous aluminosilicate materials, such as Al-SBA-15 have attracted attention as alternative catalysts. However, these catalysts usually suffer from low acid site loadings and low acid strength compared to zeolites. Therefore, the performance of mesoporous aluminosilicate materials was inferior to ZSM-5 zeolites when previously tested for the catalytic fast pyrolysis of biomass waste.

A range of high acidity Al-SBA-15 catalysts have been synthesised using a novel synthesis method which achieved acidities comparable to ZSM-5. Aluminium incorporation was shown to be positively correlational to acidity. The Al-SBA-15 catalyst with the greatest aluminium to silicon ratio was AlSBA15(5) with a Si:Al= 5 and exhibited a high acidity of 564 μmol g^{-1}. This is one of the highest acidities achieved by an Al-SBA-15 catalyst in the literature currently. AlSBA15(5) was subsequently tested for the catalytic fast pyrolysis of biomass components (model compounds of cellulose, lignin and hemicellulose) and beech wood, compared to industrially relevant solid acid catalysts (ZSM-5, SAPO-34, Al_2O_3, K10 and e-FCC). The findings suggest that all acidic catalysts initially follow a similar reaction pathway, cracking high molecular weight compounds in the pyrolysis vapours into smaller organic molecules. As the ratio of catalyst to biomass was increased, AlSBA15(5) did not increase the yield of valuable compounds and instead favoured the production of coke. In contrast, at increased catalyst to biomass ratios the shape selectivity of ZSM-5 became more significant and increased the yield of valuable aromatic products such as xylene and toluene, while suppressing coke formation. Although the in situ location of the catalyst had a small positive effect on the yield of products in the micro-reactor work, ex situ catalytic fast pyrolysis should be considered for commercial applications due to the independent control of both fast pyrolysis and catalytic temperature and vapour residence times, and the prevention of catalyst deactivation due to AAEMs.

Keywords: Catalytic pyrolysis, Al-SBA-15, mesoporous catalysts, ZSM-5, catalytic upgrading, biofuels.

Acknowledgements

I would like to express my gratitude to my supervisor Professor Tony Bridgwater for agreeing to take over my supervision and for all the guidance, support and advice throughout my PhD.

I would also like to especially thank my colleagues Dr Scott Banks and Dr Stelios Stefanidis for their patience, constant advice and encouragement, which has helped me achieve my goals here at Aston.

I am very thankful to Dr Amin Osatiashtiani and Dr Georgios Kyriakou for their help with the publication.

Thank you to Alireza Saraeian and Professor Brent Shanks for hosting me at the Biorenewables Research Laboratory, Iowa State University, USA and helping me to carry out crucial experiments. Thank you also to SCI for providing funding for the visit.

Thanks also to all the past and present students and staff at the European Bioenergy Research Institute, Aston University who have helped me throughout my PhD.

Thank you to the School of Engineering and Applied Science, Aston University for funding my PhD and providing the facilities at the European Bioenergy Research Institute.

Finally, a big thank you to my family and friends. Firstly, thank you to Mum and Dad for the constant support and advice over the years, I am sure without you both I would not be where I am now. A big thank you to Nan and Grandad for always being there and taking the time to proofread my work. A massive thank you to Sophie for always supporting me and constantly challenging myself to be the best person I can be!

Table of Contents

List of Tables

List of Figures

Abbreviations

E_a	Activation energy
AAEMs	Alkali and Alkaline Earth Metals
ASTM	American Society for Testing and Materials
BJH	Barrett, Joyner and Halenda
BTX	Benzene, Toluene and Xylene
B/L	Bronsted to Lewis ratio
BET	Brunauer-Emmett-Teller
Cn	Carbon chain number
CHNS	Carbon, Hydrogen, Nitrogen and Sulphur
C/B	Catalyst to biomass ratio
CFP	Catalytic fast pyrolysis
CID	Charge injection device
DTG	Derivative thermogravimetric
DRIFTS	Diffuse Reflectance Infrared Fourier Transform Spectroscopy
d.a.f.	Dry ash free
d.b.	Dry basis
EDS	Energy Dispersive Spectroscopy
FCC	Fluid Catalytic Cracking
FT-IR	Fourier Infrared
GC	Gas chromatograph
HHV	Higher Heating Value
H/Ceff	Hydrogen to carbon effective ratio
HDO	Hydrodeoxygenation
HMF	Hydroxymethyl furfural
ICP	Inductively Coupled Plasma
IR	Infrared
IUPAC	International Union of Pure and Applied Chemistry
LDPE	Low density polyethylene
MS	Mass spectrometry
m/z	Mass to charge ratio
Vm	Mesopore volume
MTO	Methanol to olefin
Vμ	Micropore volume
N/A	Not available
OES	Optical Emission Spectroscopy
OMM	Ordered Mesoporous Materials
ppb	Parts per billion
ppm	Parts per million
PAH	Polyaromatic hydrocarbons
Py-GC/MS	Pyrolysis Gas Chromatograph Spectrometry
RSD	Relative Standard Deviation
STEM	Scanning Transmission Electron Microscopy
SAPO	Siliconaluminiumphosphate
TPD	Temperature Programmed Desorption
TEOS	Tetraethyl orthosilicate
TCD	Thermal Conductivity Detector
TGA	Thermogravimetric analysis
Vt	Total pore volume
XRD	X-ray Diffraction
XPS	X-ray Photoelectron Spectroscopy

General Introduction

1. Chapter 1 - General Introduction

Due to the negative environmental impacts of CO_2 production caused by the combustion of fossil-fuels and concerns over energy security, an alternative to fossil-based fuels and chemicals is now essential. Biomass is the only non-gaseous form of renewable carbon and is abundant in many areas around the world. Several biomass conversion processes have been developed for the conversion of biomass waste into renewable fuels, chemicals and electricity. The biomass conversion technologies are generally categorised into two groups, thermo-chemical and bio-chemical. Thermo-chemical biomass conversion technologies include combustion, pyrolysis, gasification and liquefaction. While bio-chemical biomass conversion processes include digestion and fermentation.

The thermo-chemical biomass conversion technology, pyrolysis, has been used for thousands of years for charcoal production. However, in the past forty years, the development of biomass fast pyrolysis at moderate temperatures (500 °C) and very short hot vapour reaction times (up to 2 s) has become of growing interest due to the production of a high yield of liquid (up to 75 wt. %) [1]. Fast pyrolysis rapidly heats biomass in the absence in oxygen, resulting in the thermal deconstruction of the organic polymers into three distinct products: a solid, liquid and gas. A high yield of liquid, termed bio-oil, is formed as the primary product of fast pyrolysis. Non-condensable gases and a solid carbonaceous product, termed biochar, are also formed in smaller proportions (10-20 wt. %) depending on process parameters [2].

Bio-oil has a higher heating value (HHV) of approximately 18 MJ kg^{-1} [3], compared to around 46 MJ kg^{-1} for conventional gasoline. The lower HHV of bio-oil is mainly due to the presence of a high proportion of complex oxygenated compounds and relatively high water content (approximately 25 wt. %) [4]. Preliminary research focussed on using bio-oil for fuel such as in diesel engines. However, initial tests revealed difficulty in achieving autoignition of the bio-oil in the diesel engine tested. Furthermore, acidic and high molecular weight compounds present in the bio-oil are also responsible for several undesirable characteristics such as instability, corrosivity and high viscosity. Testing of bio-oil combined with a small amount of high cetane diesel fuel in an 84-kW tractor engine found rapid corrosion and erosion of the fuel injectors. This was due to the presence of acidic compounds and char fines in the oil. [4] Consequently, bio-oil is not able to be used efficiently as a general transportation fuel in conventional internal combustion engines. There are many characteristics of bio-oil, which relate to the overall quality of the bio-oil (discussed later in the chapter), that require consideration for each prospective application. The overall quality of the bio-oil can be improved through a number of ways; physically, through hot-vapour filtration [5,6], solvent addition [7] and emulsification [8]; or catalytically, through catalytic cracking [9,10], hydrotreating [11,12] and esterification [13,14]. The

physical upgrading of bio-oil is often challenging, and the research is, as such, more limited compared to catalytic upgrading routes.

One of the more promising catalytic upgrading routes of bio-oil is the combined hydrotreatment step via hydrodeoxygenation (HDO) and subsequent cracking by zeolite catalysts [15]. However, the HDO process uses high hydrogen pressure (80-300 bar) at temperatures generally between 250 to 450 °C in order to hydrotreat and deoxygenate the bio-oil (discussed further on) [16–18]. The high hydrogen pressure of HDO presents process challenges and consumes very large quantities of (currently) non-renewable cheap hydrogen. Zeolite cracking, on the other hand, occurs at the more manageable atmospheric pressure. However, zeolite cracking at elevated temperatures (300-600 °C) requires the evaporation of bio-oil which can lead to unwanted degradation [19]. In addition, the direct feeding of bio-oil or HDO oil into existing Fluid Catalytic Cracking (FCC) infrastructure presents several issues such as a significant increase in catalyst coking and fast polymerisation of the feed. This leads to more severe catalyst deactivation compared to conventional crude oil processing [10,16,20].

Catalytic fast pyrolysis, which combines fast pyrolysis with catalysis in an integrated process, has received increased interest due to the capability to catalytically crack and deoxygenate fast pyrolysis vapours at atmospheric pressure without the need to quench the vapours [19]. In catalytic fast pyrolysis, the catalyst could either be directly mixed with the biomass feedstock prior to entering the reactor, or directly mixed with the catalyst within the reactor (in situ) or be exposed to the pyrolysis vapours in a separate catalytic reactor (ex situ). The main advantage of the catalytic fast pyrolysis process is the simplification of the process which avoids the condensation and re-evaporation of the pyrolysis oil. This overcomes the degradation of the bio-oil due to condensation and re-evaporation [21]. In addition, catalytic fast pyrolysis could promote secondary reactions of pyrolysis intermediates towards certain products, thereby considerably improving the conversion and selectivity to desirable components such as deoxygenated aromatics [19]. Consequently, the catalytic pyrolysis of biomass is viewed as one of the most promising routes for the conversion of biomass to a liquid product that can be further upgraded, blended or purified to produce biofuels, commodity chemicals and new bio-based materials such as bioplastics [22,23].

1.1. Context and Background

Biomass waste supplied the vast majority of the world's energy and fuel needs up to the beginning of the 19th century until becoming phased out in industrial societies due to the introduction of fossil-fuels. Carbon forms the basis of all organic materials and hydrocarbon fuels and chemicals, such as naturally occurring polymers (wool, rubber, etc.)[24,25], synthetic polymers (plastics) [26] and energy carriers (fuel oil) [27]. Fixed carbon-containing materials, such as biomass wastes, that renew themselves over

a time span short enough to make them continuously available in sufficient quantities, are needed to maintain carbon-based energy and resources [28].

However, there lies an issue with sustainability of growing biomass for use as fuels and chemicals highlighted by the food vs fuel dilemma [29]. This dilemma highlights the possibility of growing a hunger crisis due to the use of fertile land to supply crops for biofuels such as ethanol, instead of for cultivating crops for food [30]. This debate has heightened the sense of urgency around the development of fuels generated from non-food sources, termed second generation bio-fuels [31]. Nevertheless, as society transitions from fossil-fuel based materials and chemicals to renewable bio-based products, there is a great opportunity to create a sustainable bio-based economy. In a bio-based economy, it is envisaged biofuels, commodity chemicals and new bio-based materials such as bioplastics will be produced with integrated biorefineries in a circular economy [32].

In order for the successful utilisation of biomass and biomass wastes for a new bio-based economy, a sustainable deployment will depend on new innovative conversion methods. Numerous conversion methods have been investigated to transform biomass into more valuable fuels and chemicals including bio-chemical, thermo-chemical and chemical processes. These processes all possess individual advantages and challenges; some are more easily overcome than others which are highlighted below. While bio-chemical processes are generally very selective and produce a number of select products in high yields, at present, only the cellulosic and hemicellulosic portions of lignocellulosic biomass can be processed using existing bio-chemical routes due to the recalcitrant nature of lignin, discussed later [33]. Therefore, bio-chemical processing disregards an attractive source of valuable aromatics and carbon from lignin. Thermo-chemical conversion routes, on the other hand, are more flexible to feedstock variation and complexity, and have been shown to be more energy efficient for conversion to usable liquid fuels compared to fermentation [34,35]. There are four main thermochemical conversion routes, each giving a range of products and employing a variety of equipment configurations:

1. Gasification
2. Pyrolysis
3. Liquefaction
4. Combustion

In all thermochemical conversion routes, the products, proportion of products and product quality (see below) can be influenced by many process factors such as [36]:

- Feed type (more of less ash)

- Catalyst
- Temperature
- Heating rate
- Contact time
- Particle size of feed
- Moisture content (depending on process conditions)
- Reactor geometry
- Feed pre-treatment

Gasification is the partial oxidation of biomass at high-temperature (>700 °C) and is one of the key conversion routes of biomass to a combustible gaseous mixture known as syngas (H_2 and CO). There are several types of gasification reactors, however, the most generally used is the fixed bed gasifier. Fixed bed gasifiers are simple in construction and operate either updraft or downdraft, with low gas velocity and long residence times [37]. Fixed bed gasifiers have been reported to suffer from tar condensation which affects the composition of the produced gas. Moreover, the cleaning of gas mixture becomes important to obtain a fuel gas free from contaminants. Tar has been identified as being a critical challenge to the widespread use of biomass gasification due to problems it causes in downstream applications, particularly due to blockages [38].

Liquefaction or hydrothermal liquefaction is the direct conversion of biomass to liquid by processing in a hot, pressurised aqueous environment for sufficient time to deconstruct the bio-polymeric structure to mainly liquid components. Liquefaction generally takes place between 250 and 380 °C using a pressure between 40 and 220 bar [39]. The process generates a stream of gaseous CO_2, solid residue, bio-crude and an aqueous phase. The aqueous phase can be recirculated through the liquefaction process to reduce water requirement and increase the bio oil yield. The other large steam of water that is produced during liquefaction can be treated anaerobically or via catalytic hydrothermal gasification. Anaerobic digestion of the water cannot be fully treated due to the presence of phenols and furfurals which limits the digestion process. However, liquefaction presents a suitable conversion strategy for the conversion of wet feedstocks such as microalgae.

Of all the thermochemical conversion methods, combustion is the most mature technology available for biomass utilization. The driving force for biomass combustion is the replacement of unsustainable fossil fuels such as coal with sustainable cultivated biomass and the utilization of biomass residues and wastes [40]. However, the large environmental impact of biomass combustion needs to be considered. Biomass furnaces exhibit relatively high emissions of NOx and particulate matter. Therefore, the contribute significantly to particulate matter, ozone and NO_2 in ambient air [41]. These undesirable

emissions can be reduced by using technologies such as staged combustion, including air-staging, fuel staging and advanced staged combustion [42,43]. However, since both pollutants result from fuel constituents (N_2 and ash components in the biomass fuel), there are physical limitations to their reductions.

Of the four thermochemical routes, pyrolysis, and in particular fast pyrolysis, is a promising biomass conversion process due to its ability to convert a diverse range of feedstocks to high yields of liquid with low process complexity. In the biomass fast pyrolysis process, solid biomass is rapidly converted, at moderate temperatures (450-600 °C), in the absence of oxygen, to a liquid product (bio-oil) with reported high yields (between 65-75 wt. %) [44]. However, the use of bio-oil is limited due to adverse properties such as low thermal and chemical stability, corrosivity (due to high acidity), low heating value and high viscosity [45]. The quality of the liquid product of fast pyrolysis can be defined by an assessment of the physical characteristics of the liquid product. The important factors determining the quality of bio-oil including the possible adverse effects were summarised by Bridgwater [1]. The physical characteristics of bio-oil and desirable properties are presented in **Table 1**.

***Table 1**. Factors determining bio-oil quality, produced from reference [1].*

Characteristic	**Bio-oil**	**Possible adverse effect**	**Desirable property**
Acidity	Low pH (~2)	Corrosion of pipework and vessels	Neutral or no pH
Ageing	Continuation of secondary reactions	Increase in viscosity and potential phase separation	No continuation of reactions
Solids	Char particulates from reactor (~0.1 %)	Sedimentation, erosion, corrosion and blockage	No solids
Phase separation	Partial phase separation	Poor mixing	Single phase
Oxygen content	High oxygen content (~35 wt. %)	Poor stability, phase separation and low heating value	Low to nil oxygen content
Viscosity	High viscosity (40-100 mPa s at 40 °C)	High pressure-drop	Low viscosity
Chlorine	Possibly present	Catalyst poisoning in upgrading	No chlorine
Water content	High water content (~25 wt. %)	Low heating value, effect on viscosity and stability.	No water content
Toxicity	Possible present but low	Human and eco-toxicity risk	No toxicity

There are two well-established strategies for upgrading and improving the quality of bio-oil. The first is hydrodeoxygenation (HDO), where the bio-oil is reacted with hydrogen in the presence of a supported metal catalyst (generally Pt, Pd, Rh, Ru, Fe, Ni or Cu) at high or atmospheric pressure [46,47]. As discussed earlier, this removes oxygen from oxygenated compounds, resulting in a less oxygenated and hence more energy dense oil compared to crude bio-oil [48]. However, due to the various adverse physical characteristics of bio-oil (**Table 1**), there are resultant operational challenges during processing. In addition, the economic cost of the hydrodeoxygenation process is high due to the significant hydrogen consumption requirement (around 700 per kg of bio-oil [36]) and high catalyst cost (4500 £/kg)[49]. Furthermore, the sustainability of the hydrotreatment process is questionable due to the current use of inexpensive non-renewable hydrogen [50]. This may be addressed in the future by cost-competitive renewable electricity powered water electrolysis [51] or hydrogen in synthesis gas generated via the gasification of wood [52].

A second bio-oil upgrading strategy is by catalytic cracking using solid-acid catalysts. This process is analogous to the Fluid Catalytic Cracking (FCC) process of crude oil processing and overcomes the need for external hydrogen supply. Nevertheless, the high oxygen content of the bio-oil presents operational challenges leading to very short catalyst lifetime due to coke deactivation and a low H/C ratio liquid product [16]. Much research has been undertaken and is still ongoing by several groups in order to overcome these challenges [53–58], however, the catalytic upgrading of bio-oil is not considered further in this thesis.

Catalytic fast pyrolysis, on the other hand, is an integrated process that incorporates the pyrolysis of the biomass feedstock and the catalytic upgrading into a single step to produce a partially deoxygenated liquid product that is more thermally stable compared to bio-oil. Because the liquid product still contains a relatively high oxygen content (25-35 wt. %) [59], the liquid product is still not of high enough quality to be used as a general transportation fuel. However, the liquid product of catalytic fast pyrolysis is an intermediate product that is either a source of value-added chemical products such as BTX (benzene, toluene and xylene) aromatics, or can be further upgraded to fuel via downstream processes, i.e. hydrodeoxygenation [11] or co-processed with petroleum in refineries [16,60,61]. For the efficient conversion of biomass to value-added fuels and chemicals via catalytic fast pyrolysis it is first necessary to understand the physical nature of the material [19].

1.2. Nature of Lignocellulosic Biomass Waste

Biomass is a complex organic-inorganic solid product formed by natural or anthropogenic processes. Biomass originates from growing land or water-based vegetation produced by photosynthesis or generated via animal and human food digestion [62]. Photosynthesis is the key initial step in the

growth of biomass, whereby solar energy is captured and converts carbon dioxide (CO_2) and water (H_2O) into carbohydrates ($C_nH_mO_y$) and oxygen (O_2). Biomass, either virgin or waste, can be classified into six general categories according to their biological diversity, source and origin [62]:

1) Wood biomass (soft/hard, stems, branches, bark, chips, etc.)
2) Herbaceous and agricultural biomass (grasses, straws, and agricultural and other residues)
3) Aquatic biomass (algae, seaweed, kelp, etc.)
4) Animal and human biomass wastes (bones, chicken litter and manure)
5) Contaminated biomass (municipal solid waste, sewage sludge, waste paper, etc.)
6) Biomass mixtures (combinations of the above)

Of these categories, wood and woody biomass represents an easily accessible, relatively low-cost feedstock as it grows on-land worldwide. Wood biomass is also generally more uniform as the majority of the mass is comprised by the wood of the trunk and branches. This makes it a more suitable feedstock for scientific studies. However, from an economic perspective it may be more desirable to investigate fast growing biomass such as grasses and straws, in addition to contaminated biomass wastes which may add additional value to the process.

The three major components of biomass consist of cellulose (35-50 wt. %), hemicellulose (20-30 wt. %) and lignin (10-25 wt. %) as shown in **Fig. 1**. Due to the significantly wide variance of biomass composition, the fundamental understanding of the decomposition routes of the three main organic components of lignocellulosic waste is important to aid the efficient conversion via catalytic fast pyrolysis to value-added fuels and chemicals [63]. In addition, moisture, Alkali and Alkaline Earth Metals (AAEMs), sulphur (S), phosphorous (P) and nitrogen (N) can also be found in biomass in smaller proportions (0-20 wt. %). Each of these components is present in varying proportions depending on the biomass category, with additional variations between individual categories.

Fig. 1. *Structural components and arrangement of lignocellulosic biomass. Reproduced from reference [64].*

1.2.1. Cellulose

Cellulose is crystalline in nature and is the simplest and most ordered of the three main organic components. An example of the chemical structure of cellulose is depicted in **Fig. 2**. It consists of anhydrous repeating glucose monomers connected through a β-1,4-glycosidic linkage, named cellobiose units [19]. The glucose units are further bound by extensive intramolecular and intermolecular hydrogen bonding. It has been estimated that the chain length of the cellulose molecule ranges from 100 to 14,000 glucose units [65]. Furthermore, cellulose forms the scaffolding of the plant cell walls and is insoluble in water [66]. Cellulose is structurally very similar to amylose (starch), however, the glucose monomers in amylose are connected through a weaker α-1,4-glycosidic linkage, making the degradation of amylose much simpler compared to cellulose.

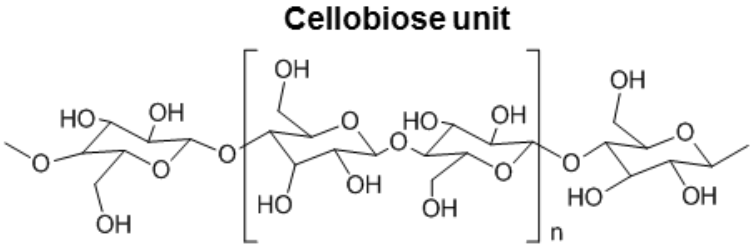

Fig. 2. *Chemical structure of the cellulose polymer chain.*

1.2.2. Hemicellulose

The second major component of biomass is the carbohydrate hemicellulose. Hemicellulose surrounds the cellulose in the plant cell walls. Hemicellulose also contains saccharide monomers connected through β-1,4-glycosidic linkages. However, in contrast to cellulose, hemicellulose contains partial

branches of amorphous polysaccharides as shown in **Fig. 3.** The branched sugars are composed of monosaccharides such as pentoses (xylose and arabinose) and hexoses (glucose, mannose and galactose) [67]. Due to the amorphous nature of hemicellulose and lack of uniformity across different biomasses, xylan is typically used as a model compound in research. Due to the lack of crystallinity and an overall decrease in hydrogen bonding between hemicellulose polymers, the thermal deconstruction of hemicellulose is much simpler compared to cellulose. Furthermore, hemicellulose is soluble in hot water (160-200 °C) and can be converted into its component sugars (listed above) and furfural through acid hydrolysis and through treatment with metal salts and ionic liquids [68,69].

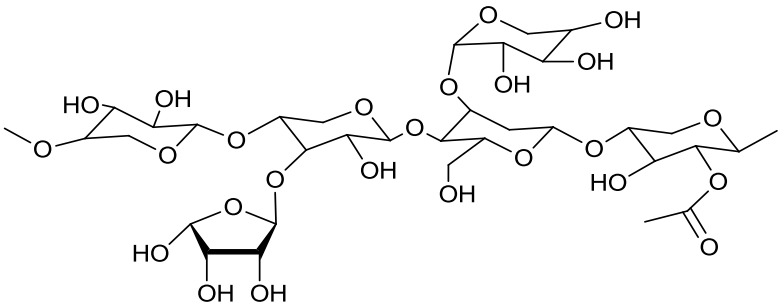

Fig. 3. *Chemical structure of hemicellulose.*

1.2.3. Lignin

The third main component of lignocellulosic biomass is lignin. Lignin is an amorphous, three-dimensional, cross-linked polyphenolic substance with no well-defined structure. Lignin is particularly important to the overall structure of the plant and acts as a binder that agglomerates the fibrous cellulosic components. Furthermore, lignin is less susceptible to enzymatic breakdown caused by bacterial or fungal attacks compared to cellulose and hemicellulose. This prevents the multiplication and movement of attacking bacteria and fungi, and can therefore provide plant cells with a shield [70]. Three general phenylpropane units, *p*-coumaryl, coniferyl and sinapyl, bonded through an irregular array of hydroxy and methoxy bonds, make up the general structure of lignin and are shown in **Fig. 4**. In contrast to cellulose and hemicellulose, which are predominantly bonded through acetal linkages, the organic building blocks of lignin also contain carbon to carbon linkages. Furthermore, the physical and chemical properties of lignin can differ depending on the extraction method used to isolate it [71]. Notably, the highly aromatic nature of lignin presents the potential for the direct preparation of aromatic chemicals such as Benzene, Toluene and Xylenes (BTX) by catalytic fast pyrolysis. This could be achieved through substantial deoxygenation and selective removal of the side chain carbonyl groups, leaving the monocyclic aromatic hydrocarbon products.

Collaborative work carried out by Nowakowski et al. [72] showed that raw lignin cannot be processed using reactor systems designed for the fast pyrolysis of whole biomass materials. This is due to the physical characteristics of purified lignin. When fed into a fluidised bed reactor system, the lignin melts upon contact with the feeding tube. This leads to partial decomposition and char formation resulting in blockages in the feeding system. Therefore, less purified lignin products or combinations with the other biomass waste components, may be more suitable as feedstocks for catalytic fast pyrolysis with minor reactor adjustments.

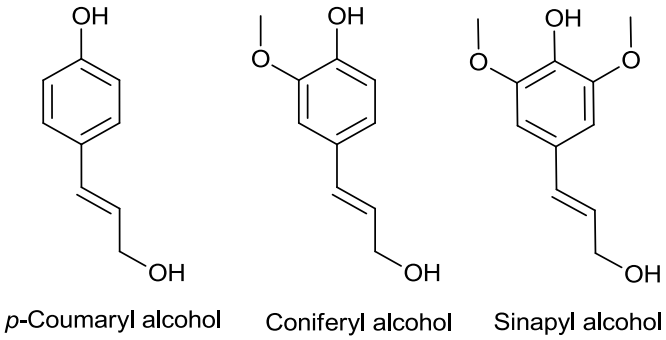

Fig. 4. *Chemical structure of lignin building blocks; p-coumaryl alcohol, coniferyl alcohol and sinapyl alcohol.*

1.2.4. Organic extractives

Organic extractives are another component of biomass waste, though present in much smaller concentrations (< 10 wt. %), and include fats, waxes, proteins, terpenes, essential oils, etc. These are important for the healthy growth of the plant and largely found in the core of the biomass structure such as the branches, bark, leaves, stems and roots. Although the composition and concentration of extractives present in each differs markedly [73] The organic extractives function as energy reserves and provide defence against microbial, fungal and insect attack [65]. In fast pyrolysis, organic extractives generate water (H_2O), carbon monoxide (CO), and carbon dioxide (CO_2) at low temperature and produce phenols and secondary cracking products at high temperature. The existence of organic extractives can also catalyse the formation of less desirable acids such as acetic acid [74]. According to Ranzi et al. [75] the presence of organic extractives blocks the breakdown of levoglucosan causing the formation of acetic acid by interior break of polymer chains [74].

1.2.5. Inorganic compounds

Biomass also contains a mineral content which consists of inorganic materials (ash), such as silica (Si), calcium (Ca), potassium (K), sulphur (S), sodium (Na), magnesium (Mg), phosphorous (P) and chlorine (Cl) [62,76]. Inorganic ions are mainly absorbed from the soil and some are essential during the growth phase. Furthermore, it has been shown that the inorganic concentration in biomass waste shows a

wide diversity as displayed in **Table 2**. The quantity and type of inorganic element present in the biomass varies between species and can also depend on the time of year harvested due to growth processes, growing conditions, plant age, harvest time and technique, transport, storage and processing [77,78]. A study of the inorganic concentration of several typical biomass species was summarised by Vassilev et al. [62]. Major inorganic elements in biomass are generally N, Ca, K. Whereas, minor inorganic elements include Si, P, Al, Mg, Fe, S, Cl and Na [79].

***Table 2**. Ash content and inorganic elements presents in a variety of biomass samples, reproduced from reference [80].*

		Elements (mg kg^{-1})							
	Ash (wt. %)	**Si**	**K**	**Ca**	**Mg**	**P**	**Na**	**Al**	**Fe**
Rice husk	14.1	60,750	5363	1718	538	630	270	166	163
Wheat straw	6.8	20,757	13,063	5627	693	1373	164	429	299
Apple tree residue	3.8	820	3771	9472	872	1325	25	71	58
Apricot tree residue	3.7	990	7254	10,927	1374	1161	41	104	88
Vineyard residue	2.6	1012	5045	7808	1604	1011	37	151	113
Sunflower seed shells	3.3	258	12,926	6392	2812	1323	20	257	233
Alfalfa	7.8	510	25,695	9694	1123	2997	289	83	109

Metal cations, i.e. AAEMs, are known to be particularly detrimental to the quality of bio-oil obtained by fast pyrolysis. Of all the inorganic elements present, K, is known to have the greatest effect on the thermal conversion properties [81]. The precise influence of K on the decomposition of lignocellulosic biomass is not completely understood. However, several studies have observed that the presence of certain metal cations, including K, act as catalysts and promote char and gas formation and substantially reduce the total organic liquid yield [68,81–84].

During biomass fast pyrolysis the inorganic materials i.e., the ash, is mainly sequestered in the char particles and therefore efficient char removal should limit the detrimental effects caused by the metal cations described above. Nevertheless, it has shown that a small concentration of inorganic species may vaporise and escape the cyclone separator [85,86]. Alkali and alkaline earth metals (AAEMs) have the potential to irreversibly deactivate solid acid catalysts used in biomass catalytic fast pyrolysis, discussed in more detail later. Different approaches have been successfully implemented to pre-treat biomass to remove the inorganics including washing with water, surfactants and acids [87–89]. However, the use of a biomass pre-treatment step can increase the cost and complexity of the process, through the disposal of pre-treatment medium and the drying of the feedstock prior to fast pyrolysis [90].

1.3. Principles of Catalysis

Catalysis is vitally important in the chemical industry and is employed for the production of an enormous range of chemical products such as heavy commodity and fine chemicals. Employing catalysts in chemical process reactions increases the efficiency and selectivity of the process, thereby eliminating substantial amounts of by-products and other waste materials [91]. Accordingly, catalysis has played a significant role in reducing pollution in the environment and is considered one of the fundamental pillars of Green Chemistry [92].

1.3.1. Definition of a catalyst

A catalyst is a material that converts reactants into products through a series of rudimentary steps that the catalyst participates in and is regenerated to its original form at the end of each cycle [93]. Catalysts can come in many forms but can be classified into two categories: (**1**) in the same phase as the reactant (homogeneous) or, (**2**) in a different phase to the reactant (heterogeneous). A successful catalyst should have the following attributes [94]:

- It should be highly selective towards the desired product and minimise unwanted by-products.
- It should be active under the required reaction conditions.
- The catalyst should be stable under the required reaction conditions.
- The active sites should be readily accessible (i.e. not blocked by small pore structures) and available to the reactants and products.

Homogeneous catalysts are often highly active for the reaction and selective towards desired products as they exist in the same phase as the reactants (generally liquid phase). However, as the reactant and catalyst are in the same phase, separation and reuse after the reaction is challenging. In addition, reactions requiring elevated temperatures present issues due to evaporation of volatile reactants. Thus, homogeneous catalysts are generally unfavourable for industrial processes [95]. In contrast, heterogeneous catalysts are often more environmentally benign, can be used in multiple reactor configurations and in some cases offer shape selectivity due to their pore structure. As such, it is estimated heterogeneous catalysts are used in 90 % of industrial processes [96].

1.3.2. Principles of heterogeneous catalysts

Heterogeneous catalysts are generally solid materials, while the reactant and product molecules are either in the liquid or gas phase, or both. The catalytic ability of the material involves the active site on the surface. The active site alters the kinetics of the reaction but does not change the thermodynamics. Moreover, the active site provides an alternate pathway for the reaction to take place that lowers the

activation energy (E_a), i.e. the minimum energy required for the reaction to happen. This is summarised in **Fig. 5** below.

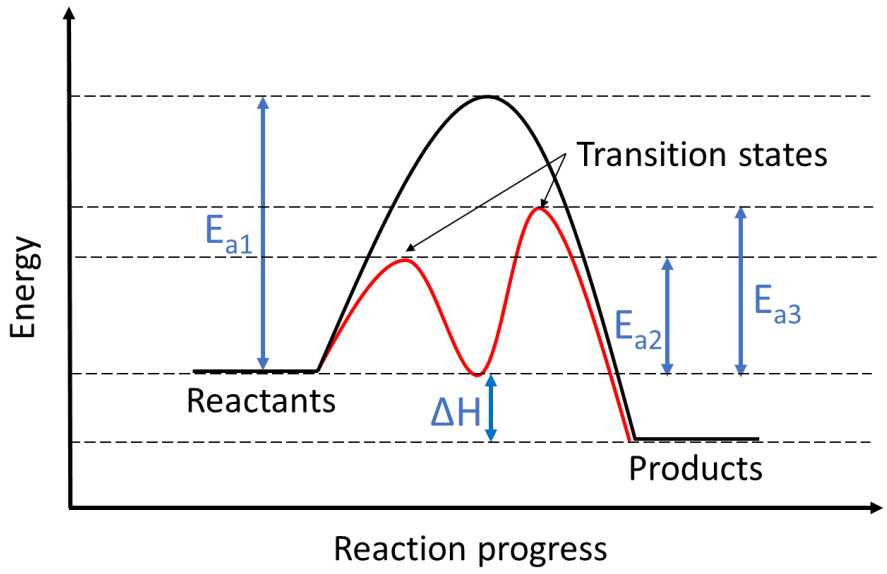

Fig. 5. *Energy profile diagram for an uncatalysed reaction (black line) and the catalytic reaction (red line).*

The catalytic reaction can undergo several transition states (**Fig. 5** above in red) before forming the product or products. The transition states offer reaction routes that are of lower activation energy (E_{a2} and E_{a3}) than without the catalyst (E_{a1}). However, it is often difficult to identify reaction intermediates and derive a mechanism due to challenges in detection. Moreover, the catalyst can lower the activation energy but cannot change the potential energy (ΔH) of the reactants to products [97].

The reactants and products can undergo a series of steps during the overall catalytic reaction on the surface of the heterogeneous catalyst, for example:

- Diffusion of the reactants from the liquid/gas phase to catalyst surface (external mass transfer). Diffusion of the reactants into the catalyst pores to the active site (internal mass transfer).
- Adsorption of the reactants onto active sites.
- Reactions on the active site, involving formation or conversion of various intermediates.
- Desorption of products from active site.
- Diffusion of the products out of the catalyst.

Acid catalysis is the principal area of catalysis used by industries of all sectors of chemical manufacturing [91]. Solid heterogeneous catalysts serve as important materials due to their various advantages over their homogenous counterparts for industrial applications, such as ease of separation

and recycling [97]. They are employed in many indispensable industrial processes such as in petroleum refining from crude oil and in the Haber-Bosch process. The Haber-Bosch process converts atmospheric nitrogen (N_2) and Hydrogen (H_2) to ammonia (NH_3) over an iron-based catalyst. The process was revolutionary for agriculture due to the ability to produce fertilisers [98]. Among the arguably most important catalytic processes is Fluid Catalytic Cracking (FCC), where heavy petroleum fractions are cracked (broken into smaller components). FCC employs an amalgamation of several solid acid catalysts at the heart of the process [99].

1.3.3. Classification of solid acid catalysts

Solid acid catalysts can be classified depending on their physical properties (acid character, surface area and porosity), morphology or other properties. Product selectivity of the reactions can depend on the fine-tuning of these properties. Examples of solid acid catalysts include:

Zeolites

Zeolites are a class of microporous crystalline aluminosilicate materials comprised of interlinked silica (SiO_4) and alumina (AlO_3) units. There are over 200 known zeolite structures, both occurring either naturally or produced synthetically [100]. Among the most interesting and widely studied are: ZSM-5 (framework type MFI), Mordenite (framework type MOR), Zeolite Y (framework type FAU) and Zeolite Beta (framework type BEA) [101]. The physical characteristics of these zeolites are summarised in **Table 3** below. Zeolites possess complex three-dimensional structures with internal micropores and cavities providing high surface areas (>700 m^2/g). The control of the molecular dimensions of the pores can result in pre-activation of the molecules by strong dielectric fields and molecular confinement. The dimensions and geometries of the pore structure can also result in shape selective effects [101].

Table 3. *Physical characteristics of widely studied zeolites.*

Zeolite	Pore size (nm)	Shape of pores	Common SiO_2/Al_2O_3	Approximate surface area ($m^2\ g^{-1}$)
ZSM-5 [102]	0.5 x 0.5	Cylinders and zigzag	30	500
Mordenite [103]	0.65 x 0.7	Cylinders	12	50
Zeolite Y [102]	0.7	Cylinders	12	750
Zeolite Beta [102]	0.7 x 0.6	Cylinders	25	625

The acidic and reactive properties of zeolites arise from the crystallinity and pore cavities of the material. An overall negative charge of the zeolite framework is imparted due to the long-range ordering of tetrahedrally coordinated silicon ions (Si^{4+}) and trivalent aluminium ions (Al^{3+}) [101]. The negative framework charge is balanced by extra-framework positively charged alkali cations such as

Na^+. The Brønsted acid functionality is provided by substitution of the alkali cation with a positively charged proton (H^+), which possesses much higher electron affinity than the alkali cation (Fig. 6A). [104]. In addition, framework oxygen atoms can give rise to weak Lewis acidity.

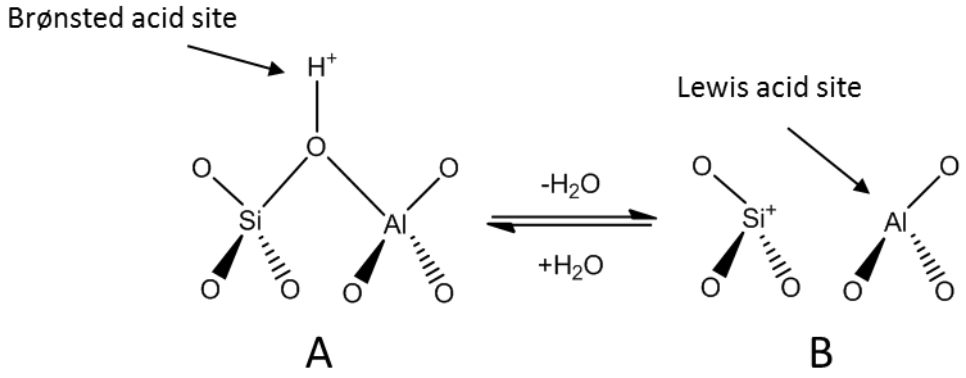

Fig. 6. *Representation of Brønsted acid sites (A) and Lewis acid sites (B) found in zeolite structures.*

Lewis acid sites are generally formed through dihydroxylation of Brønsted acid sites, resulting in a positively charged silicon species and an electron accepting aluminium, as shown in **Fig. 6B** [105]. Lewis acidity can also be generated by extra-framework alumina, i.e. aluminium species coordinated to oxygen on the surface of the zeolite. The number of Brønsted acid sites is controlled by the total number of framework aluminium ions present. Furthermore, the strength of the acid sites is dependent on the density of acid sites. The higher the density of neighbouring Al atoms, the weaker the acid strength [106]. In addition, zeolites are thermally and hydrothermally stable, allowing their use in several industrial processes such as crude oil cracking, isomerisation and fuel synthesis [45,99,107].

Metal oxides

Metal oxides are another important class of catalysts, particularly because they effectively catalyse a wide variety of reactions such as oxidation and acid-base reactions. Metal oxides are formed from a crystalline structure comprised of ionic metallic species (M^{n+}) and oxide (O^{2-}) anions. Furthermore, the surface of the oxide can contain several types of defects and environments (kinks, steps and terraces) [108]. These surface defects generate oxygen vacancies and play a determining role in the catalytic reactivity [109]. The surface defects are often occupied by hydroxyl groups provided by atmospheric water vapour that can operate as Brønsted acids and also provide basicity. Metal oxides also possess Lewis acidity due to the metallic species acting as electron acceptors [110]. The catalytic performance is strongly determined by the preparation method of the metal oxide catalyst including, the choice of

chemical composition, deposition and active phase onto a support, catalyst promotion and oxidative and reductive treatments [111].

Metal oxides are especially useful catalysts for important reaction processes such as olefin formation and oxidation [112,113], the Fischer-Tropsch process [114,115], alkylation [116] and transesterification [111,117]. In addition, metal oxide catalysts play an important role in environmental catalytic reactions such as the oxidation of volatile organic compounds and the reduction of NO_x [118–120]. Some examples of industrial relevant metal oxide catalysts include Al_2O_3, TiO_2, ZnO, ZrO_2, CeO2, CuO V_2O_5, Mn_3O_4 and Mn_2O_3 [121]. Mixed metal oxides are also active as hydrodesulphurisation catalysts such as $CoMoO_4$ and $NiMoO_4$ [94,109]. The physical properties of metal oxide catalysts vary greatly depending on the metal and metal oxide support material. Moreover, each metal oxide may have multiple polymorphs (crystalline phases) or lattice morphologies, each with their own textural (surface area, porosity), as well as thermal, chemical and mechanical stability [109]. For example, Al_2O_3 exists in a number of crystalline phases, three of the most important being γ, θ, κ and α. While only the γ and θ phases have low enough surface energies enabling large surface areas and hence are suitable for catalytic reactions [122]. However, in general, metal oxide catalysts are thermally stable, relatively inexpensive and abundant [111]. These are essential characteristics when considering catalysts for industrial thermal catalytic processes.

Ordered mesoporous materials

For porous solid acid catalysts such as zeolites, the pore size openings and geometries which govern accessibility to internal catalytic active sites are important determinants of the activity and selectivity of the catalyst. However, the small pore openings of zeolites (<1.5 nm) limit the mass transfer of large organic molecules useful in the refining of heavy feeds and in the production of chemicals and fine chemical products [106]. A number of synthesis methods have been developed to construct mesoporous zeolites from scratch via templating approaches, or post-synthesis methods that etch mesopores into previously microporous zeolites through dealumination or desilication [123–126]. Templating approaches to form mesoporous zeolites generally involve the use of expensive surfactant templates and complex preparation procedures [126]. Post-synthesis methods generally result in the significant reduction of zeolite crystallinity and the formation of amorphous aluminosilicate fragments, which can have negative consequences on catalytic performance [127].

Alternatively, synthetic ordered mesoporous materials (OMMs) are a relatively recent class of solid acid catalysts and were developed using an organic polymer template and silica as a substitute for microporous zeolites [128]. The use of an organic polymer template allowed pore sizes to be finely-tuned depending on the chain length of the polymer. The advancement of new synthetic polymers

opened up a variety of achievable pore sizes and new pore architectures [129]. Several ordered mesoporous materials exist; among the most widely researched as promising alternatives to zeolites are: MCM-41, MCM-48, FSM-16, KIT-6 and SBA-15 [130]. Silica OMMs, on their own, exhibit little catalytic activity. Nevertheless, catalytic active sites can be introduced through the addition of metals such as Al, Pt and Pd and also by grafting acidic moieties e.g. sulphonic acid or other reactive functionalities e.g. TiO_2 [131–135].

1.3.4. Application and development of solid acid catalysts

Catalysts can be employed either on their own (carrier free catalysts), supported on a high surface area material or applied as a coating. Importantly, the development of solid acid catalysts requires knowledge, not only of their ability to catalyse the reaction, but also of other parameters which affect the performance and economics of the catalytic process, including [93]:

- Mass transfer
- Heat transfer
- Raw material costs
- Structure of the solid catalyst (phases)
- Chemical and mechanical stability
- Chemical composition of the bulk
- Chemical composition of the surface
- Stability of the active phases
- Production

These parameters can have an impact on the efficiency and hence economics of the catalytic process. Furthermore, multiple chemical reactions take place simultaneously in the catalytic pyrolysis of biomass including cracking, aromatisation, ketonisation, esterification and hydrogenation [136]. In addition to the catalytic activity of the catalyst in the above reactions, the scalability, manufacturing process and robustness of the catalytic material should also be considered when selecting an appropriate catalyst for the catalytic pyrolysis of biomass.

1.4. Catalytic Fast Pyrolysis

As previously discussed, fast pyrolysis is the thermal decomposition of materials at elevated temperatures (450-600 °C) in the absence of oxygen with short hot vapour residence times (typically < 2 s) and the subsequent very rapid cooling of the evolved vapours [65]. The temperature of pyrolysis significantly influences the yield and physical properties of the products. Condensable vapours are typically maximised at temperatures around 500 °C leading to maximum liquid yields of between

approximately 65-75 wt. % [1] At lower temperatures (<400 °C), the breakdown of larger oligomers will be neglected leading to the formation of highly viscous oils. In addition, partially pyrolysed feed will result in an increased char yield. At increased temperatures (>600 °C), gaseous yields will be increased due to the over cracking of larger pyrolysis intermediates into lower molecular weight gaseous molecules [1]. As discussed earlier, the oxygen content of the bio-oil is usually between 35-40 wt. %. In addition to bio-oil, non-condensable gases and a solid char product are formed in lower yields of around 10-20 wt. % each.

Bio-oil produced by fast pyrolysis of biomass waste is a multiple component mixture containing a relatively large amount of water (typically 25 wt. %) and greater than an estimated 400 individual compounds, with the majority of them being oxygenated [137]. The oxygen-containing compounds are mainly responsible for the well documented undesirable properties of bio-oil summarised in **Table 1**. The undesirable properties include: high viscosity, high corrosivity, chemical instability and incompatibility with conventional hydrocarbon fuels [44]. A comparison between the typical physical properties of wood-derived bio-oil and gasoline is displayed in **Table 4**. As shown by the elemental analysis, the oxygen content of bio-oil is much higher than gasoline, while bio-oil is also hydrogen deficient compared. This results in a much lower heating value of bio-oil compared to gasoline and therefore is inefficient in combustion engines. The oxygen content of the bio-oil can be slightly reduced through modification of the pyrolysis reaction parameters. By increasing the temperature of pyrolysis, the oxygen content of the bio-oil is reduced due to cracking of the oxygenated vapours. However, this also reduces the organic liquid yield and increases the formation of gaseous molecules such as CO and CO_2, hence this is less desirable [21].

Table 4. *Typical properties of wood-derived bio-oil and gasoline.*

Physical Property	Bio-oil [1]	Gasoline [138]
Moisture content (%)	25	0
pH	2.5	N/A
Specific gravity	1.20	0.74
Elemental analysis (%)		
C	56	86
H	6	13
O	38	0.6
N	0-0.1	<0.1
Heating value (MJ/kg)	17	45
Viscosity (mpa s)	40-100 (40 °C and 25 % water)	0.39 (20 °C)
Solids (char, %)	0.1	0

Catalytic fast pyrolysis offers an efficient integrated strategy to produce a partially deoxygenated and more stable liquid product compared to bio-oil. As discussed earlier, the liquid product of catalytic fast pyrolysis still contains a relatively high oxygen content (25-35 wt. %) [59]. Therefore, the liquid product is still not of high enough quality to be employed as a general transportation fuel. However, the liquid product of catalytic fast pyrolysis is an intermediate product that can be either a source of value-added chemical products such as BTX (benzene, toluene and xylene) aromatics, or can be further upgraded to fuel via downstream processes, i.e. hydrodeoxygenation [11] or co-processed with petroleum in refineries [16,60,61]. A schematic diagram of the fast and catalytic fast pyrolysis upgrading strategies of lignocellulosic biomass is provided in **Fig. 7** below.

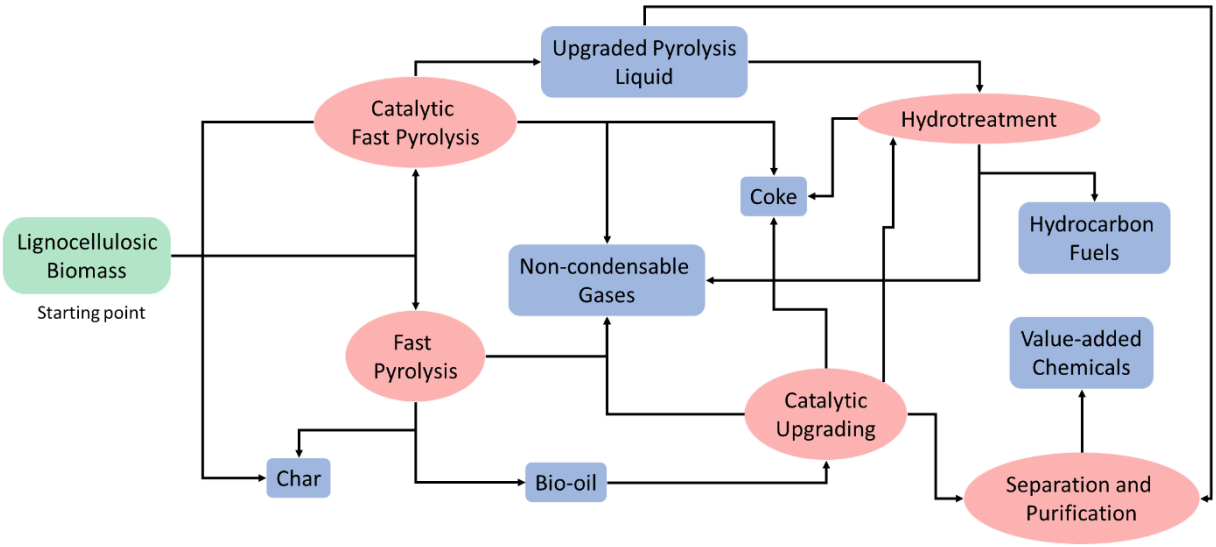

Fig. 7. *Thermochemical upgrading routes of lignocellulosic biomass waste.*

1.4.1. Aims of catalytic fast pyrolysis

The aim of much of the research on catalytic pyrolysis has been focussed on substantial deoxygenation of the liquid product for use as liquid transportation fuels. Due to the drop in the value of crude oil in 2014, fuel prices have subsequently fallen and the price for low sulphur gasoil is now around 650 USD per metric ton (mt) [139]. Therefore, biofuels need to be competitive with crude oil derived products. However, platform and commodity chemicals are generally more valuable. For example, the bulk prices of aromatics such as benzene, toluene and xylene (BTX) are between 600 and 800 USD per metric ton (mt) [140]. Whereas, the price of oxygenated aromatic molecules such as phenol is even greater and is approximately 1200 USD per metric ton (mt) [141]. Therefore, future research of catalytic fast pyrolysis should consider the production of platform and commodity chemicals such as BTX, levulinic acid and four-carbon 1,4- diacids (malic and succinic acid), [142,143] in substantial yields as opposed to low-value applications such as transportation fuels. In addition, there is also now an emergence of biologically derived intermediates from biomass waste that have promising potentials

to produce novel chemical species that enhance the performance properties in their end use. These chemicals can be defined as biological derived chemicals that can efficiently converted to a diversity of chemical products including both novel molecules and drop-in replacements. These “bio-privileged” molecules cannot be effectively accessed from petrochemical sources and, in addition, offer a pathway to a number of existing and novel chemical products. Although these molecules are not labelled as such, a few examples of these “bio-privileged” molecules include 5-hydroxymethylfurfural (HMF), 2,5-difurandicarboxylic acid and muconic acid [144]. HMF, for example, can be readily converted to a number of furanic molecules with novel chemical properties such as 2,5-dimethylfuran. 2,5-dimethyl furan has a high energy density and octane number and could serve as a lubricant additive in gasoline[145] The objective of the catalytic fast pyrolysis process must be carefully considered to determine the selection of an appropriate catalyst in terms of product selectivity and resistance to deactivation, in addition to reactor configurations and processing parameters.

1.4.2. Reactions in catalytic fast pyrolysis of biomass

In order for the rational design of suitable catalysts for use in catalytic fast pyrolysis of biomass waste, an understanding of the underlying reaction mechanisms is essential. However, due to the heterogeneity and complexity of the biomass waste feedstock and the occurrence of simultaneous multiple reactions as explained below, the detailed reaction pathways of biomass catalytic fast pyrolysis are far from being fully understood. Nevertheless, it is known that some general reaction steps take place. According to Corma et al. [9], there are five different classes of reactions: (1) dehydration reactions, producing water (H_2O); (2) cracking of large oxygenated biomass-based molecules into smaller molecules; (3) hydrogen-producing reactions; (4) hydrogen-consuming reactions; and (5) production of larger molecules by carbon-carbon bond formation.

Cracking

Cracking is the most prominent reaction in the pyrolysis and catalytic pyrolysis of biomass. It involves the fragmentation of high molecular weight molecules such as sorbitol and glucose, into lower molecular weight products such as dihydroxyacetone and glyceraldehyde [146]. Traditional catalytic cracking of hydrocarbons chemistry proceeds through several mechanisms such as pyrolytic cracking (cleavage of C-C bonds), hydrogen transfer, isomerisation [147]. The catalytic cracking of oxygenated biomass-based molecules also includes reactions such as retro-aldol condensation, dehydration, decarboxylation and decarbonylation [15], summarised in **Fig. 8** below.

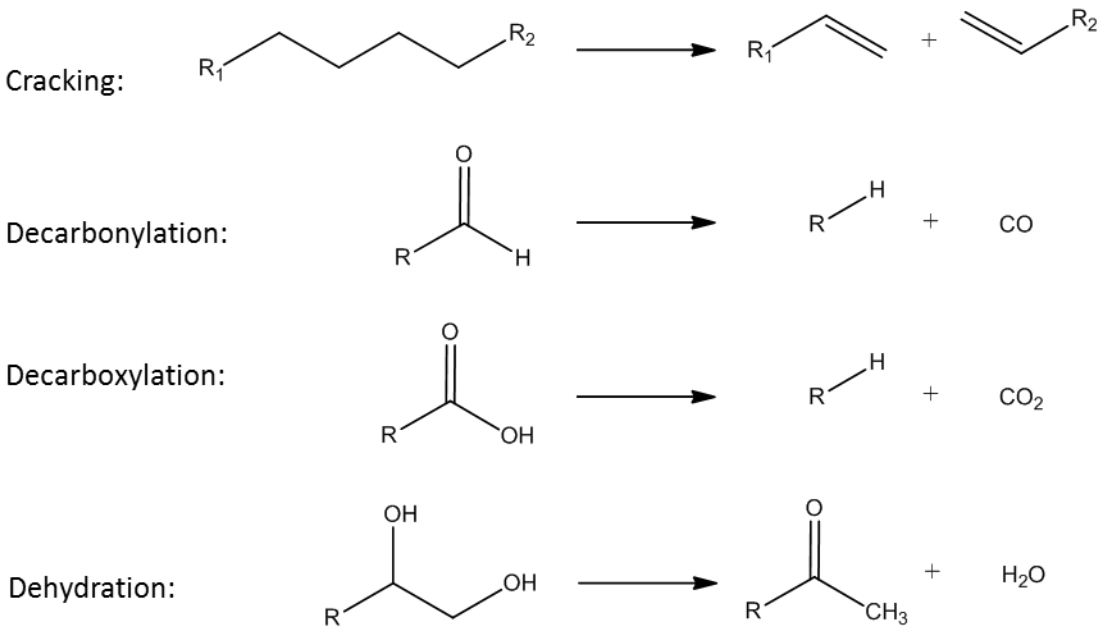

Fig. 8. *Reactions during catalytic cracking routes of biomass-based molecules.*

The majority of these reactions are catalysed by Brønsted acid sites and result in the formation of H_2O, CO_2 and CO as by-products of the reaction, leading to a more deoxygenated organic liquid product. According to Bridgwater [1], zeolite cracking rejects oxygen as CO_2 and the overall reaction can be conceptually summarised by; Reaction 1:

$$C_1H_{1.33} + 0.26\ O_2 \rightarrow 0.65\ CH_{1.2} + 0.34\ CO_2 + 0.27\ H_2O \qquad \text{Reaction 1}$$

It is favourable to remove oxygen in the form of CO_2, rather than CO or H_2O, thus producing a liquid product with a higher H/C_{eff} ratio and thus a greater energy density. The hydrogen to carbon effective (H/C_{eff}) ratio was introduced by Chen et al. [148] and can be used to describe whether a feed can be economically converted into hydrocarbons using zeolite catalysts according to the amount of oxygen, carbon and hydrogen in the feed. The H/C_{eff} ratio is described by **Eq. 1**; shown below:

$$H/C_{eff} = \frac{H-20}{C} \qquad \textbf{Eq. 1}$$

The H/C_{eff} ratio of petroleum-derived feeds is between 1 and 2 [149], whereas biomass waste-derived compounds are generally <1 due to their high oxygen content [9]. Therefore, biomass waste is made of hydrogen deficient molecules and strategies to convert biomass waste-derived feedstocks to hydrocarbons must take H/C_{eff} into account [150].

Aromatisation

The abundance of cracked pyrolysis intermediates in biomass pyrolysis vapour allows the conversion to aromatics in the presence of porous catalysts. To produce aromatic hydrocarbons from biomass

waste-derived oxygenates the oxygen must be first removed and the molecule dehydrated to form an aromatic ring. The oxygen removed from the biomass-derived oxygenate will be rejected as CO, CO_2 and H_2O. Lower molecular weight monocyclic aromatic hydrocarbons can be further aromatised to polyaromatic hydrocarbons (PAHs) with larger molecular weights. The reaction of biomass oxygenates to aromatic hydrocarbons has a maximum stoichiometric yield of 42 wt. % liquid, or a maximum energetic yield of approximately 50 wt. % [36]. Zeolite catalysts, particularly ZSM-5, have been extensively researched due to their high selectivity towards aromatic compounds from both biomass feedstocks and hydrocarbon feedstocks [151]. This will be discussed in more detail later in the thesis.

Ketonisation and esterification

Carboxylic and carbonyl reactive components are present in large quantities in pyrolysis vapours such as acids (acetic, propanoic), alcohols (methanol, ethanol, butanol), furans (furan, furfural), ketones (2-cyclopenten-1-one) aldehydes (hydroxyaetaldehyde) and multifunctional compounds [2]. These oxygenated compounds are responsible for many of the adverse properties of bio-oil, as discussed earlier. Removal of the reactive components through catalytic reactions is a viable option to improve the overall quality of the liquid product of fast pyrolysis and drastically improve the stability and reduce the ageing rate [13]. These reactive components can be ketonised, esterified as shown in **Fig. 9** and reacted by retro-aldol condensation (**Fig. 8**).

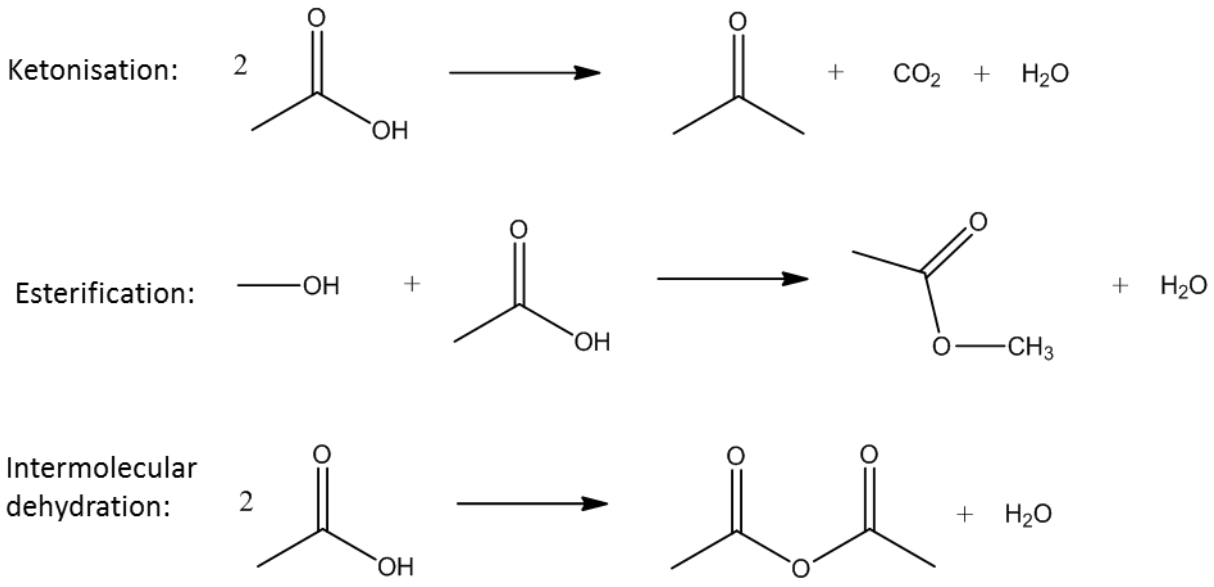

Fig. 9. *Catalytic reaction routes of carboxylic acids and alcohols in the catalytic fast pyrolysis of biomass.*

Ketonisation of two carboxylic acids forms a ketone through C-C bond coupling, where the oxygen is rejected as CO_2 and H_2O as shown in **Fig. 9**. Smaller carboxylic acids are more reactive towards ketonisation reactions compared to longer chain carboxylic acids. Similarly, esterification of reactive

carboxylic acid and alcohols can take place over the acid site of the catalyst to produce an ester and water [14]. In addition, acid anhydrides are often formed due to intermolecular dehydration of two carboxylic reactants, where oxygen is rejected in the form of water [152].

1.4.3. Reactor type and catalyst placement

At the core of the catalytic fast pyrolysis process is the fast pyrolysis reactor. Fluid bed reactors are typically used in fast pyrolysis due to their simple construction and operation, very efficient heat and mass transfer to biomass particles, as well as being well understood [1]. The basic principle behind a fluid bed is a fluid (an inert gas in fast pyrolysis) is passed through a solid granular material (sand or catalyst) at high enough flow rate and superficial velocities in order to suspend the solid and cause it to behave like a fluid when reacted [153]. This is in order to overcome the minimum fluidisation condition of the material.

The rate of pyrolysis is generally controlled by either the internal or external heat transfer of the solid which, in turn, affect the inherent chemical decomposition kinetics [154]. Biomass waste generally has low thermal conductivity due to their relatively high moisture content (8-25 wt. %), low particle density and particle morphology (shape factors) [155]. Therefore, feedstocks should be prepared to lower particle sizes (<3 mm) to ensure sufficient heat and mass transfer rates and hence complete pyrolysis of the biomass particle [156,157]. In addition, thermal degradation reactions are endothermic, therefore very high heat transfer rates to the biomass particle reaction interface are required [158].

The fluidising medium (sand or catalyst) allows good temperature control and very efficient heat transfer to biomass particles. The residence time of the vapours and solids (char) in the reactor is controlled by the flow rate of the fluidising gas. A high fluidisation flow rate is needed to effectively remove char, due to its catalytic effects detrimental on the liquid product quality (discussed in Section 1.2.5). However, a fluidisation flow rate too high will cause the fluidisation medium to be entrained in the vapours and escape the reactor. Therefore, the fluidisation flow rate needs to be carefully controlled to achieve a compromise.

The char is separated from the pyrolysis vapours using one or more cyclones. The by-product char generally has a high calorific value (ca. 30 kJ g^{-1}) [159] due to its high carbon content and can, therefore, be used to provide process heat via combustion or be sold as bio-char briquettes [160] for home burning or as an agricultural soil amendment [161]. Industrially, circulating fluid bed and transported bed reactor systems may be employed, similar to those used in the FCC process, to achieve higher throughput and integrate secondary char combustion and recirculation of the heated sand. Large scale

examples of these reactors have been demonstrated by research institutes such as CEPRI/CERTH, Greece [162], and industrially by Ensyn, Canada [163].

For Catalytic Fast Pyrolysis (CFP), the reactor systems are generally similar to the non-catalytic fast pyrolysis fluid bed reactors described above. The configuration of the integrated catalytic pyrolysis reactor can be divided into two distinct categories based on the location of the catalyst in the process; in situ and ex situ [164].

In situ

During in situ Catalytic Fast Pyrolysis (CFP), the catalyst typically replaces the heat carrier (traditionally sand) and therefore comes into contact with the biomass feed in the pyrolysis reactor (**Fig. 10A**). This enables the immediate diffusion of the generated pyrolysis vapours into the pores of the catalyst. This could potentially enhance decomposition of larger fragments and in turn, reduce the possibility of repolymerisation and char formation. In situ catalytic fast pyrolysis offers an advantage over ex situ CFP in terms of process simplification as the pyrolysis and the catalytic step occur in the same reactor. Hence, in situ CFP should require less capital investment compared to ex situ CFP. Furthermore, the vapour residence time over the catalyst is very short (1-2 s), therefore only the most active species may react, limiting the full potential of the catalyst.

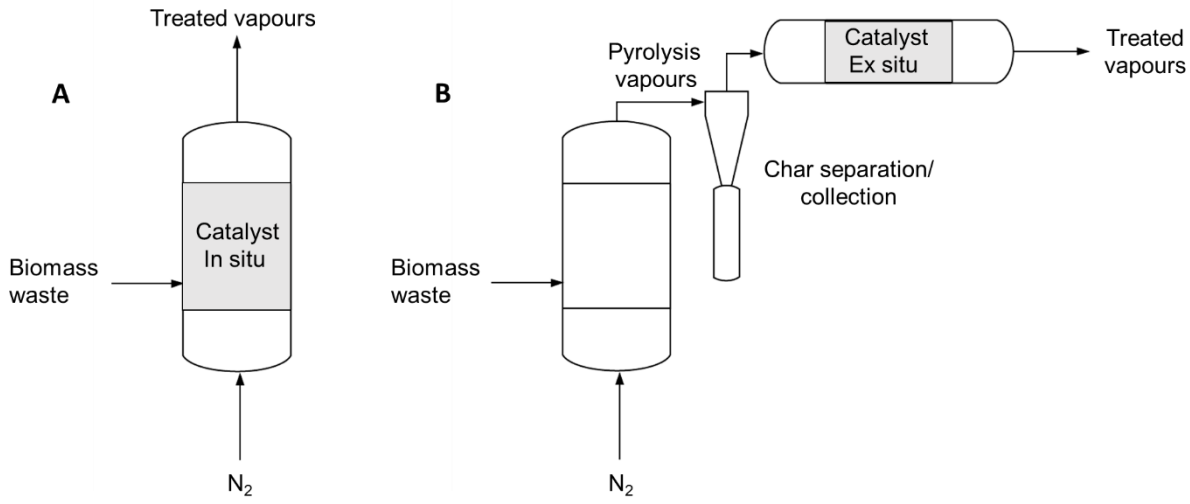

Fig. 10. *Reactor scheme of catalyst fast pyrolysis in the in situ (A) and ex situ (B) configurations.*

A large catalyst to biomass (C/B) weight ratio, generally > 5/1, is necessary to ensure a high degree of upgrading and to sufficiently act as a heat carrier. Moreover, at lower C/B ratios, the catalyst has more time to undergo coking and deactivation [165]. However, several compromises are made due to the necessary simplicity of the process. Firstly, as the catalyst is acting as the heat carrier, the pyrolysis and catalyst upgrading must occur at the same temperature. Therefore, achieving the respective individual

optimal reaction temperatures of pyrolysis and catalytic upgrading is impracticable. There are also additional difficulties of char and catalyst separation due to char/catalyst hydrodynamics and the presence of catalyst fines in the fluid bed.

An additional challenge of in situ CFP is catalyst hydrothermal deactivation of solid acid catalysts due to hot water vapour. The hot water vapour either originates from the moisture in the biomass feedstock or is produced during dehydration reactions in during the catalytic decomposition [166]. In the case of zeolites, the hot water vapour in combination with the high reaction temperatures (approximately 500 °C) can cause dealumination, which results in a reduction in the strength and number of acid sites. In addition, volatilisation of inorganic compounds (i.e. alkali and alkaline earth metals AAEMs) present in biomass, as discussed in Section 1.2.5, can cause catalyst poisoning. This also leads to deactivation due to loss of surface area and acid sites [167,168]. This type of deactivation is much more likely in in situ CFP compared to ex situ CFP due to the close contact between the catalyst and ash in in situ CFP. The inorganics are contained within the char and are separated before entering the catalyst bed in ex situ CFP.

Ex situ

For the ex situ catalyst reactor configuration, the pyrolysis vapours are first produced in the fast pyrolysis reactor and are transported to a secondary catalytic reactor (**Fig. 10B**, above), where the upgrading takes place. With the catalyst in this mode of operation, there is added flexibility to combine optimal pyrolysis reaction temperature and the optimal temperature of catalyst activity. Furthermore, the char can be easily separated from the pyrolysis vapours beforehand, minimising catalyst deactivation due to the volatilisation of alkali earth metals [169]. The ex situ reactor configuration allows the introduction of a secondary input gas (e.g. hydrogen) to the catalytic reactor in order to increase the overall H/C_{eff} of the liquid product. In addition, the ex situ configuration also allows more precise control over the flow of pyrolysis vapours and the residence time over the catalyst. This could be critical in controlling catalytic selectivity and reaction rates.

Although catalyst deactivation due to the accumulation of AAEMs is greatly reduced in ex situ CFP, the deactivation of the catalyst due to coking is the same as for in situ. This could be mitigated by reactor design considerations. For example, by using a Circulating Fluidised Bed (CFB) ex situ catalytic reactor, much like a riser reactor in the FCC process. Therefore, coke formed on the surface of the catalyst could be combusted to supply heat for the overall pyrolysis process. In comparison to in situ CFP, the ex situ catalytic fast pyrolysis requires more reactors and results in longer processing time, therefore substantially increasing operational and asset costs [136].

1.4.4. Analytical pyrolysis reactors (Py-GC/MS)

Fast pyrolysis can be performed using a micro-pyrolysis unit directly coupled to a gas chromatograph (GC) with detectors such as mass spectrometry (MS) and is generally termed Py-GC/MS. This analytical technique allows for the quick screening of various biomass waste species and catalysts at different ratios in order to identify effective catalysts. The temperature (°C), heating rate (°C s^{-1}) and residence time (s) can also be carefully controlled to investigate changes of these parameters on the identifiable products. This helps to identify some of the main catalytic and non-catalytic reactions that occur during catalytic fast pyrolysis and how the physicochemical properties of the catalyst affect the product distribution. Depending on the GC detector available, it is also possible to quantify the volatile compounds based on the calibration of known standards.

Analytical pyrolysis reactors are very useful in determining fundamental catalyst reactivities and selectivities. However, this type of reactor is not fully representative of industrial-scale reactors due to differences in heat transfer, particle attrition and secondary reactions [151]. In addition, determining accurate mass balances, in terms of product yields (solid, liquid and gases) is particularly challenging and in some cases technically impossible.

1.4.5. Challenges

While catalytic fast pyrolysis of biomass has several advantages over non-catalytic fast pyrolysis including a liquid product with improved quality, there are still several challenges that need to be addressed to make the process more economically viable and sustainable. Some of these challenges have been briefly discussed earlier. However, this section aims to summarise and provide more details on several of the main limitations preventing the widespread industrial use of catalytic fast pyrolysis.

Biomass feedstock

One of the advantages of pyrolysis is its ability to process a wide range of feedstocks. However, for a high-quality liquid product, low to moderate lignin and low ash containing biomass feedstocks are preferred in catalytic fast pyrolysis of biomass [170,171]. Woody biomass, besides its vast availability worldwide, generally possesses low ash contents (<2 wt. %) and high cellulose contents (>40 wt. %) [172]. The faster growing components of the tree have such as leaves and bark generally have much higher ash contents and lower cellulose contents [173] . The low ash content and high cellulose content of woody biomass reduce char formation and enhance the formation of pyrolysis vapours, leading to a greater yield of CFP oil yields [174]. Furthermore, ideal feedstocks should have a moisture content below 10 wt. % [1]. Above this value, the liquid product may contain increased water contents, therefore, reducing its heating value due to the added energy requirement to evaporate water.

Moreover, with increased moisture in the feedstock additional energy is needed for pyrolysis to occur or to incorporate a prior drying step into the process. However, a feedstock moisture content too low may result in a higher viscosity of the liquid product as the water dilutes more viscous components of bio-oil [175].

Inorganic compounds

Alkali and alkaline earth metals (AAEMs) (discussed in Section 1.2.5) are known to be detrimental to the composition of the organic liquid product of fast pyrolysis. The AAEMs present have been shown to catalyse cracking reactions of fast pyrolysis vapours, therefore, promoting the formation of char and gas at the expense of liquid [176]. Inorganic compounds, particularly potassium (K), can also poison solid acid catalysts, reducing their acidity and hence their reactive activity [166]. As previously discussed, the inorganic compounds (ash) are generally sequestered in the char. Therefore, the detrimental effects caused by inorganic compounds can be mitigated by the efficient removal of char from the pyrolysis reactor and by using a catalytic ex situ reactor configuration, preventing contact with the catalyst. Moreover, the inorganic content of biomass can be greatly reduced by washing with water, since the majority of alkali metals (ca. 90%) present in biomass waste are in a water-soluble form [89]. In addition, the inorganic content of waste biomass can be almost eliminated by surfactant washing as a pre-treatment step due to the surfactant increasing the cell permeability and thus aiding the removal of inorganics [177]. However, this option is usually uneconomical due to the increased energy, cost and additional processing requirement of drying the biomass prior to pyrolysis.

Coke formation

A significant challenge during the catalytic fast pyrolysis of biomass process is the rapid formation of coke (carbonaceous deposits) on the surface of porous solid acid catalysts, thereby preventing access to the catalyst's pores and leading to a much lower quality liquid yield [178]. Coke formation can generally be described as the result of polymerisation, dehydration, decarboxylation and decarbonylation of mainly anhydrosugars, furans and fragmented oxygenates [179]. Nevertheless, catalyst deactivation due to coke formation is reversible and it has been claimed that the catalyst can be regenerated to near original activity by oxidation at high temperatures [180–183]. This limitation can, therefore, be overcome through adaptive process configurations, such as continuously supplying the catalytic reactor with fresh or regenerated catalyst as in the riser reactor used in the FCC process.

In addition, a high catalyst to biomass (C/B) ratio can be employed to ensure the primary pyrolysis vapours can interact with the surface before they thermally decompose to form catalytic vapours,

gases and more importantly, coke. Therefore, a high catalyst to biomass ratio beneficial to counteract the effects of catalyst deactivation due to coke deposition.

Catalyst design

One of the most important challenges of catalyst fast pyrolysis is the design of efficient and economical catalysts [170]. Efficient catalysts need to be developed to facilitate tailored reaction routes towards desirable products, i.e. through shape selectivity [136], while also minimising coke formation. Oxygen removal from the liquid product should preferably be in the form of CO_2, to maximise oxygen removal, instead of CO and H_2O, which preserves the hydrogen and carbon in the liquid product. Furthermore, the catalyst should be stable under the conditions required for pyrolysis. To achieve all of this, a more in-depth understanding of the underlying mechanism of catalytic conversion of biomass is required [184].

1.5. Literature Review on Catalysts Used in Catalytic Fast Pyrolysis of Biomass

The occurrence of multiple catalytic reactions, many of which happen simultaneously, requires the understanding of how the physicochemical properties of the catalytic material affect the distribution and quality of the products. There have been several recent reviews on catalytic fast pyrolysis by Iliopoulou et al. [184], Zhang et al. [35], Sharma et al. [185] and Venderbosch [61]. A useful, in-depth, review on catalytic fast pyrolysis of lignocellulosic biomass, including catalysts used in CFP, was provided by Liu et al. [136]. This review provided a comprehensive overview of fast pyrolysis chemistry, including the chemistry of the pyrolysis of individual biomass waste components and their decomposition pathways, and a wide-ranging description of catalysts used in catalytic fast pyrolysis in the literature. Therefore, this literature review aims to summarise the main findings of catalyst research in biomass fast pyrolysis.

1.5.1. Catalytic fast pyrolysis using zeolites

Zeolites have been successfully employed in FCC refineries and the methanol to gasoline process. The potential of using zeolites in upgrading biomass via catalytic fast pyrolysis has been extensively investigated over the past 30 years owing to their strong acidic properties and shape selectivity to aromatics [186]. A variety of zeolites and microporous zeolite-type materials have been tested in the catalytic fast pyrolysis such as ZSM-5, Zeolite Y and Beta, Mordenite, FCC, and an assortment of siliconaluminophosphates (SAPOs) [136]. In addition, several metals have been incorporated into zeolites that act as promoters, such as gallium, iron, cobalt and vanadium [187,188].

ZSM-5 zeolites are the most researched for catalytic fast pyrolysis due to their strong acidity, high hydrothermal stability and shape selectivity towards aromatics. Preliminary work by Evans and Milne [189] showed that aromatic products were formed when wood vapour was passed over a ZSM-5 catalyst. Horne and Williams [190] upgraded model biomass pyrolysis compounds over ZSM-5 and concluded the optimum temperature for the upgrading of biomass was shown to be between 500 and 550 °C. Although ZSM-5 produced a high proportion of monocyclic aromatic hydrocarbons, there was also a high yield of less desirable polyaromatic hydrocarbons (PAHs) and coke. The addition of ZSM-5 to the pyrolysis process expectedly reduced the organic liquid yield due to the catalytic deoxygenation reactions which rejected oxygen in the form of CO and CO_2 [191]. Williams and Nugranad [192] showed that for the catalytic deoxygenation of bio-oil using ZSM-5, oxygen was generally rejected as H_2O at lower reaction temperatures (400-550 °C) and largely CO and CO_2 at increased reaction temperatures (500-600 °C).

Carlson et al. [193] achieved a 31.1 carbon % yield (13.5 wt. %) of aromatics with the catalytic pyrolysis of cellulose, but noted the major challenge with catalytic fast pyrolysis is to avoid undesired coke formation. Cook and Conner [194] noted that the crystallographic diameter of the pores for ZSM-5 are approximately 0.55-0.56 nm but when corrected to the Norman radii for Si and O, the pore size of ZSM-5 can be 0.63 nm. Jae et al. [195] investigated the shape selectivity of zeolite catalysts for biomass conversion and found that of the zeolites tested (ZK-5, SAPO-34, Ferrierite, ZSM-23, MCM-22, SSZ-20, ZSM-11, ZSM-5, IM-5, TNU-9, SSZ-55, zeolite Beta, zeolite Y), ZSM-5 displayed by far the greatest conversion to aromatics (35.5 C %) and produced the least amount of coke (30.4 C %). This was attributed to the similar dimensions of the pore openings of ZSM-5 to the kinetic diameter of monocyclic aromatics.

For example, the kinetic diameter of benzene, toluene and p-xylene are all approximately 0.585 nm [196]. Interestingly, PAHs were still produced by smaller pore zeolites such as SAPO-34 which had pores smaller than the kinetic diameter of the majority of PAHs. Therefore, it was suggested that PAHs may have been formed on the surface of the catalyst instead of within the pores. In addition, larger pore zeolites such as Zeolite Beta and Zeolite Y decreased the production of aromatics while coke yields were increased.

Mihalcik, Mullen and Boateng [197] screened acidic zeolites for the catalytic pyrolysis of biomass and its components. They found Zeolite Beta produced the second highest yield of aromatics after ZSM-5, although Zeolite Beta produced a larger amount of coke. This contributed to premature deactivation of the catalyst, whereas Ferrierite and Mordenite lacked reactivity towards the pyrolytic vapours. The large structural framework, coupled with low Si/Al ratio of Zeolite Y, made the catalyst relatively

unstable and increased its susceptibility to deactivation. Upon contact with hot pyrolysis vapours the framework of the Zeolite Y collapsed, therefore no aromatics were produced.

Besides the fine tuning of the Si/Al ratio of the zeolites, doping with metals is another mechanism to improve or introduce additional functionalities to the zeolite catalysts. ZSM-5, in particular, has been impregnated with various metals to increase the production of aromatics. Of the various metals, gallium has been shown to be the most effective at increasing the production of monocyclic aromatics in ZSM-5 [167,198]. Schultz, Mullen and Boateng [199] doped ZSM-5 with Zn, Ga and Ga-Ni and observed a decreased selectivity to PAHs in favour of monocyclic aromatics. However, the incorporation of Zn and Ni caused an overall decrease in aromatic yield, while Ga increased aromatics at high Ga loadings. It is unknown how exactly Ga increases the yield of aromatics, but it is thought to be probably caused by the identity and loading of the metal rather than changes in the physical surface or pore structure. In contrast, Iliopoulou et al. [200] impregnated ZSM-5 with Ni and Co at varying metal loadings and found an overall increase in aromatics and phenolics. However, these results were presented by chromatogram area %. Therefore, the product yields were only semi-quantified thus making comparisons between different studies challenging.

1.5.2. Catalytic fast pyrolysis using metal oxides

Metal oxides have been widely used in heterogeneous catalysis due to their redox capacities, multivalent nature and relative cheapness. These catalysts often have much lower surface areas than zeolites, in the region of 1-200 m^2 g^{-1}. Although, many of them display meso- (2-50 nm) and macroporosity (>50 nm) with a wide distribution of pore sizes achievable. Furthermore, similar to ordered mesoporous materials, the pore sizes of metal oxides can be modified by altering the synthesis parameters [201]. In addition, the lack of the ion exchangeable Brønsted acid site in metal oxides increases their tolerance to deactivation induced by biomass alkali metals. Alumina is used industrially in many processes, such as the Claus process [202], for converting hydrogen sulphide into molecular sulphur and in the dehydration of alcohols to alkenes [203]. Like zeolites, various metal oxides have been screened for their effect on the upgrading of biomass pyrolysis vapours.

Lu et al. [204] screened a variety of nano metal oxides by Py-GC/MS including MgO, CaO, TiO_2, Fe_2O_3, NiO and ZnO. All catalysts displayed different catalytic abilities towards the fast pyrolysis of poplar wood. ZnO appeared to have the least catalytic effect and only slightly altered the pyrolytic products. All catalysts, except NiO and ZnO, reduced the anhydrosugars and linear aldehydes. CaO performed the best as it eliminated acid products and reduced the concentration of phenols, while selectively increased the formation of hydrocarbon products.

Stefanidis et al. [59] also screened a variety of metal oxides such as alumina, MgO, NiO, ZrO_2, TiO_2 and mixed metal oxides including silica-alumina (SiO_2/Al_2O_3) and zirconia/titania (ZrO_2/TiO_2) in a fixed bed reactor for the catalytic fast pyrolysis of biomass. All catalysts reduced the amount of oxygen in the organic liquid fraction, while producing high coke yields in the region of 50 wt. %. Interestingly, the mixed metal oxide zirconia/titania displayed the highest selectivity towards aromatic hydrocarbons. However, this was at the expense of a considerable increase in water, gas and solid yield and a low yield of the organic liquid phase. Similar semi-quantitative (peak area %) results were observed by Lu et al. [205] using a zirconia/titania based catalyst in the catalytic pyrolysis of poplar wood. The results by Kalogiannis et al. [206] also evidenced different bio-oil deoxygenation pathways by either acidic or basic catalysts. Basic catalysts led to a much larger increase in CO_2 yields (3.7 C % increase), while for acidic catalysts CO and water were the dominant by-products.

In a different study, low-cost, naturally occurring, basic MgO catalysts were also investigated by Stefanidis et al. [207] for the upgrading of bio-oil. The MgO catalysts reduced the oxygen content of the resultant oil product and performed equally or arguably better than an industrial ZSM-5 catalyst. The basic sites of the MgO catalyst favoured the reduction of acids and deoxygenation via ketonisation and aldol condensation reactions. On the other hand, the MgO catalysts produced a larger proportion of coke and gases compared to ZSM-5. Nevertheless, oxygen was removed in the more favourable form of CO_2 compared to CO and H_2O for ZSM-5.

1.5.3. Catalytic fast pyrolysis using ordered mesoporous materials

Although zeolites have displayed very positive effects when applied in the catalytic fast pyrolysis of biomass, there are still many drawbacks such as the formation of undesirable PAHs and deactivation by coke deposition. In addition, Jae et al. [195] demonstrated that molecules with a kinetic diameter larger than glucose are unlikely to diffuse into the pores of microporous zeolites. Therefore, ordered mesoporous materials have attracted increased attention with larger pore sizes expected to facilitate the diffusion of bulky pyrolysis intermediates to the catalytic active sites. Many different ordered structures with uniform pore size distributions and high surface areas (2-100 nm) have been created based around a silica structure (SiO_2) [208]. The incorporation or deposition of aluminium on the silica structure results in the formation of acidic sites capable of catalysing a range of reactions in biomass catalytic fast pyrolysis.

Samolada et al. [209] investigated a range of catalytic materials including Al-MCM-41 in the catalytic pyrolysis of biomass using a fixed bed reactor. The use of Al-MCM-41 resulted in slightly lower liquid yields than those obtained with ZSM-5, 80.8 and 85.2 wt.%, respectively. The organic yield was also lower, 16.5 wt. % compared with 20.8 wt. % for ZSM-5, which would suggest increased levels of

deoxygenation by Al-MCM-41. However, the coke yield of Al-MCM-41 was significantly increased by 11 wt.% compared to 3 wt.% with ZSM-5. Analysis of the catalyst using XRD after the experiment showed the destruction of the mesoporous phase of Al-MCM-41, signifying a lack of hydrothermal stability.

Adam et al. [210] tested four samples of Al-MCM-41 each with a Si/Al ratio of 20, with increasing pore sizes, for the catalytic pyrolysis of spruce wood. In all catalytic experiments, levoglucosan was eliminated which signifies an increase in catalytic cracking reactions. Catalysis increased the yield of acetic acid and furfural, became the dominant products. In addition, the larger pore sizes reduced the yield of acetic acid and the number of high molecular weight phenolic products. Antonakou et al. [211] used several types of Al-MCM-41 materials as catalysts in biomass pyrolysis, it was shown that a low Si/Al ratio (increased acidity) had a positive effect on product yields. The addition of Fe and Cu to Al-MCM-41 was also found to have a positive effect on the production of phenols.

Triantafyllidis et al. [212] synthesised mesoporous aluminosilicate materials (MSU-S), assembled from zeolite Beta seeds, as an alternative to organic templated mesoporous materials such as Al-MCM-41. The MSU-S materials displayed increased hydrothermal stability and slightly higher acidity compared to Al-MCM-41 catalysts. The catalytic pyrolysis of beech wood was performed using a fixed-bed reactor. The use of MSU-S materials led to a significantly lower organic phase in the liquid product and higher coke yields than Al-MCM-41. On the other hand, MSU-S increased the yield of monocyclic aromatic hydrocarbons, though at the same time, increased the yield of generally less desirable PAHs.

Jeon et al. [213] studied the catalytic pyrolysis of biomass components (cellulose, hemicellulose and lignin) over SBA-15 based catalysts. SBA-15 is known to have higher hydrothermal and thermal stability than MCM-41 due to its thicker pore walls [214,215]. Al-SBA-15 and Pt/Al-SBA-15 were more successful at producing high-value products than SBA-15 and Pt-SBA-15, due to the additional acidic properties provided by aluminium (Al). With all catalysts, the yield of less desirable acetic acid was increased for the catalytic pyrolysis of cellulose and hemicellulose. Recently, Yaman et al. [216] studied the catalytic upgrading of walnut shell pyrolysis vapours using a bench scale fixed-bed pyrolysis reactor. The authors used a selection of catalysts including ZSM-5, Ni-ZSM-5, Co-ZSM-5, SBA-15, Fe-SBA-15 and Al-SBA-15. In all cases, the heavier compounds were reduced in favour of alkylated phenols and other small oxygenates. Furthermore, the metal impregnated catalysts increased the deoxygenation of the resultant liquid oil compared to non-metal impregnated catalysts.

1.6. Literature review and overall conclusions

According to the literature, zeolites have been extensively studied and show promise in the production of value-added products such as aromatics from the catalytic fast pyrolysis of lignocellulosic biomass. In particular, the doping of ZSM-5 with metals such as gallium (Ga) can increase the production of aromatics while also lowering the yield of less desirable PAHs. Relatively inexpensive metal oxide catalysts are successful for the deoxygenation of the liquid oil product. Zirconia (ZrO_2)/Titania (TiO_2) based catalysts display high selectivities towards producing monocyclic aromatics. In addition, metal oxides remove more of the oxygen in the preferential form of CO_2, therefore retaining more carbon in the product. However, the organic liquid yield is very low due to high gaseous and coke yields. Ordered mesoporous materials such as Al-MCM-41 reduced the yield of large anhydrosugars. It was shown that low Si/Al ratios had a positive effect on the product yields and increased the yield of desirable products such as lower molecular weight oxygenates. Nevertheless, the lack of hydrothermal stability in Al-MCM-41 caused irreversible deactivation. Al-SBA-15 had increased hydrothermal stability compared to Al-MCM-41, however, the acidity of Al-SBA-15 was lower compared to zeolites leading to lower activity of the catalytic reaction.

The catalytic pyrolysis of biomass residues offers a potential technology to convert biomass into a liquid product that is less oxygenated and therefore eliminates several of the undesirable characteristics associated with pyrolysis oil as discussed earlier, see **Table 1**. Although much progress has been made in this field, there are still various challenges that need to be overcome to produce either a liquid product, that can be used as a fuel, or that contains a high yield of valuable chemicals without needing further purification or upgrading. Therefore, the design and selection of an appropriate catalyst that addresses many of the issues are of paramount concern.

The ideal catalyst should have the following features:

- High activity (rate of reaction) – access of pyrolysis reaction intermediates to the catalytically active site.
- High selectivity (percentage conversion of reactant to desired product).
- High stability (the slow decline of activity and selectivity).
- Limit the formation of char and CO, CO_2 and H_2O.
- Be robust enough to resist deactivation both mechanically and through regeneration cycles.

Based on the current literature, zeolites possess many of these desirable properties. Zeolites, especially ZSM-5, have been extensively studied in the catalytic pyrolysis of biomass owing to their current industrial use in the petrochemical refining industry. However, the diffusion of pyrolytic

vapours to the internal pores of the microporous zeolite is restricted and therefore limits their activity. Ordered mesoporous materials such as Al-SBA-15 can overcome these diffusional limitations due to the existence of mesopores. However, the mesoporous aluminosilicates used in previous studies exhibited lower acidity than zeolites. Hence, the deoxygenation of the pyrolysis vapours was limited which resulted in the production of a lower quality liquid product compared to zeolites.

Based on these conclusions, Al-SBA-15 catalysts overcome the diffusional limitations of zeolites due to their mesoporous structure. Although, judging by the limited quantity of previous literature on Al-SBA-15 catalysts used in the catalytic pyrolysis of biomass, these catalysts have not been studied in-depth. It has been shown that low Si/Al ratios are beneficial for catalytic pyrolysis using Al-SBA-15 catalysts. However, the acidity achieved by Al-SBA-15 catalysts is still much lower than zeolites.

1.7. Thesis Aims and Objectives

In view of building on the current literature for the catalytic pyrolysis of biomass waste, while also adding novelty to this area of research, the aims of this thesis are therefore the following:

- To synthesise mesoporous Al-SBA-15 catalysts with high acidity.
- To investigate mesoporous Al-SBA-15 catalysts for the catalytic pyrolysis of biomass.
- To compare the synthesised catalysts to industrially standard catalysts such as ZSM-5.

Experimental methods

2. Chapter 2 - Experimental Methods

2.1. Materials

2.1.1. Chemicals and materials

Pluronic P123 (M_n= 5800, $EO_{20}PO_{70}EO_{20}$), tetraethyl orthosilicate (TEOS, >98 %), Al $(NO_3)_3 \cdot 9H_2O$ (>98 %), hydrochloric acid (37 wt. %) and ammonium hydroxide solution (28-30 % NH_3 basis) were all purchased from Sigma-Aldrich. ZSM-5 (SM-27) with Si/Al = 12 was purchased from Alsi-Penta Zeolithe GmbH. Granular LDPE was kindly supplied by Sabic Europe and was ground to a particle size of <250 µm.

2.1.2. Main lignocellulosic components of biomass waste

The lignocellulosic biomass components cellulose (20 µm), lignin (organosolv) and xylan (birchwood) were all sourced from Sigma Aldrich. Xylan was used as a representative sample of hemicellulose.

2.1.3. Description of commercially available catalysts

The selected commercial catalytic materials sourced from various suppliers and they are listed in **Table 5**. All commercial materials were calcined in air using a ramp rate of 1.5 °C min^{-1} to 550 °C and held for 6 h before use. This was in order to remove surface contaminations and in the case of ZSM-5 convert it to the acidic form.

Table 5*. Description of commercially available catalysts.*

Name	Material	Group	Supplier
SAPO-34	SAPO-34	Siliconaluminophosphate	ACS Materials
K10	Montmorillonite	Clay mineral	Clariant (Sud Chemie)
ZSM-5	ZSM-5 (SM-27)	Zeolite	Alsi-Penta Zeolithe GmbH
Al_2O_3	Aluminium oxide	Aluminium oxide	Alfa Aesar
e-FCC	FCC catalyst	FCC	Confidential

Commercial catalysts applied in the catalytic fast pyrolysis of beech wood

The FCC catalyst used in this study was a commercial equilibrium FCC catalyst and is denoted e-FCC. A ZSM-5 zeolite in the ammonia form was purchased from Alfa Aesar with a Si:Al ratio of 15:1. This ratio was used for a good comparison. The ZSM-5 was converted to the H form by calcination in air at 575 °C for 6 h at a heating rate of 2 °C min^{-1}.

2.1.1. Beech wood characterisation

Beech wood (Fagus Sylvatica) was purchased from J. Rettenmaier & Sohne GmbH + Co. KG, Rosenberg, Germany and was used as biomass feed in this work. The beech wood tested was derived from a single batch, therefore samples are homogeneous allowing for comparison. The beech wood sample was ground using a cutting mill (Retsch Ltd., Germany, Heavy-Duty Cutting Mill, Type SM2000) and sieved to a particle size range of 100-150 µm using a sieve shaker.

2.1.2. Catalyst synthesis

Synthesis of SBA-15

SBA-15 was synthesised following the procedure reported by Zhao and co-workers [217]. Approximately 4 g of Pluronic P123 triblock copolymer was dissolved in 125 ml of 2 M HCl solution and stirred at 35 °C for 4 h. Then, 8.5 ml of TEOS was added to the solution dropwise and left stirring for a further 20 h. The resulting gel was aged at 100 °C for 48 h. The solid product was separated by vacuum filtration, washed with water and dried at 60 °C, then heated to 550 °C at a ramp rate of 1.5 °C min^{-1} and held for 6 h, consistent with literature guidelines.

Incorporation of Aluminium

A series of Al-SBA-15 catalysts was synthesised with Si/Al ratios ranging from 100:1 to 5:1 using a modified two-step "pH adjustment method" developed by Wu and co-workers [218]. The method was modified by using $Al(NO_3)_3 \cdot 9H_2O$ as the aluminium source instead of $Al_2(SO_4)_3 \cdot 18H_2O$; as well as incorporating a longer hydrothermal treatment in the second step (72 h instead of 48 h to increase the pore size) [219]. Approximately 4 g of Pluronic P123 triblock copolymer was dissolved in 125 ml of 2 M HCl solution and stirred at 35 °C for 4 h. 8.5 ml of tetraethyl orthosilicate (TEOS) was added dropwise and left to stir for 3 h. Then, the amount of $Al(NO_3)_3 \cdot 9H_2O$ required to give the specific Si/Al ratio was added to the mixture and left to stir for 20 h. The resulting gel was aged at 100 °C for 48 h before being cooled to room temperature. Afterwards, the pH value of the mixture was increased to 7.5 by the dropwise addition of 4 M NH_4OH with stirring, and the mixture was then subjected to a second hydrothermal treatment at 100 °C for 72 h. The solid product was separated by vacuum filtration, washed with water and dried at 60 °C, before being calcined in air at 550 °C for 6 h at a ramp rate of 1.5 °C min^{-1}. The resulting Al-SBA-15 materials were designated as AlSBA15(X), where X indicates the molar Si/Al ratio in the synthesised catalyst.

2.2. Materials characterisation

2.2.1. Powder X-ray Diffraction

The SBA-15-type catalysts were analysed by powder X-ray diffraction in the low angle region, 2θ = 0.5-5° with a step size of 0.01, on a Bruker D8 Advance diffractometer fitted with an X'celerator and Cu K_α (1.54 Å) radiation source and nickel filter. The powder samples were placed in a spinner to ensure the samples were flat.

X-ray diffraction is a relatively quick analytical technique that allows the identification and study of crystalline solids, i.e. solids that possess an ordered structural arrangement of atoms. The technique is based on the constructive interference between monochromatic X-rays and the sample [93]. The X-ray is typically generated by a beam of high-energy electrons, produced by a heated tungsten filament, striking a rotating target, typically copper. The beam of X-rays is filtered to produce a monochromatic source and subsequently hits the powdered sample, consisting of many small crystals, each randomly orientated [220]. The beam of X-rays interacts with the planes of atoms, some of them are transmitted, part of them are absorbed by the sample and part of them are scattered and diffracted. If the structure contains either short or long-range ordering, constructive or deconstructive interference will occur. When the angle of the incident X-ray photons (theta) are scattered equal to the wavelength, multiplied by an integer (n), constructive interference occurs, and a diffraction peak will be seen (**Fig. 11**). This is described by the Bragg equation (**Eq. 2**) [221]:

$$n\lambda = 2d\ sin\theta \qquad \textbf{Eq. 2}$$

Where, λ = X-ray wavelength, *d* = lattice spacing and θ = diffraction angle.

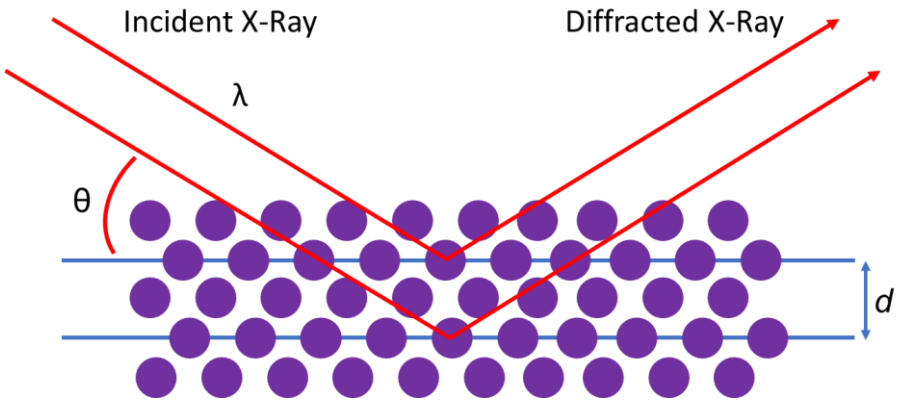

Fig. 11. *Schematic diagram of X-Ray diffraction.*

The diffracted X-rays are detected, processed and counted. By scanning the sample through a range of 2 θ angles, the diffracted x-rays at all possible angles of the lattice should be attained. The identity of the material can be determined by comparison of the intensity and position of the peaks with a reference in a database. The position of the diffraction peaks is inversely proportional to the sample's periodicity [222]. Therefore, crystalline materials display diffraction peaks at high values of 2 θ within 10-80°, described as wide angle. Although strictly amorphous, materials exhibiting long-range order such as porous materials MCM-41 and SBA-15 display peaks in the low angle region, between 0-10° [223,224].

The lattice spacing of hexagonal pore arrangements can be calculated by combining the Bragg equation (**Eq. 2**) with the Miller indices (*h, k, l*) of the lattice planes using **Eq. 3**. For hexagonal shaped structures the reflections with the greatest intensities are (1 0 0), (1 1 0) and (2 0 0) [225]. The thickness of the pore walls can be calculated by simple subtraction of the pore diameter, obtained by gas adsorption, from the lattice spacing [226].

$$a = \frac{\lambda\sqrt{h^2+k^2+l^2}}{2\,sin\,\theta} \qquad \textbf{Eq. 3}$$

Where, a= lattice spacing

2.2.2. Elemental analysis – Inductively Coupled Plasma Optical Emission Spectroscopy (ICP-OES)

The bulk Si and Al contents of the samples were determined by ICP-OES on a Thermo Scientific iCAP 7000 instrument, with a charge injection device (CID) detector, coupled to a CETAC ASX-520 autosampler. Prior to analyses, the solid samples (10 mg) were digested in a mixture of nitric acid (H_2NO_3) (5 ml), sulphuric acid (H_2SO_4) (2 ml) and deionised water (H_2O) (2 ml) using a CEM SP-D discover microwave (300 W). Ammonium fluoride (100 mg) was added to generate hydrofluoric acid in situ before neutralisation with boric acid (1 ml) and HCl (1 ml). The samples were subsequently diluted with deionised water by a factor of 10. Silicon (1000 ppm in nitric acid) and aluminium (1000 ppm in nitric acid) ICP standards were used to create calibration curves. It should be noted, there was difficulty in obtaining replicable Si/Al results. It was hypothesised that in contact with free fluoride ions, silicon would form silicon tetrafluoride during digestion. Silicon tetrafluoride has a boiling point of -86 °C and may volatilise before analyses, which could be the reason for erroneous silicon concentrations in some instances [227].

Inductively Coupled Plasma Optical Emission Spectroscopy (ICP-OES) is a highly sensitive elemental analysis technique capable of detecting elements in the range of parts per billion (ppb). The technique primarily uses a hot plasma “torch”, which is formed using argon gas and a coil that emits radio frequencies. The coil induces an electromagnetic field within the torch which heats the formed plasma to high temperatures (ca. 7000 °C) [228]. Various tubes transmit gases which flow through the plasma torch and are ionised. The sample solution is sprayed through a nebulizer to produce an aerosol. A centrally located gas stream carried the sample aerosol through the plasma where it is desolvated, dissociated, atomised and ionised. The various ionic and atomic species are excited to a higher state. On relaxation to the ground energy level, characteristic radiation is emitted. The energy intensity of the radiation is proportional to the concentration of the element. Each element has a characteristic emission spectrum that is quantified using an optical emission spectrometer. Calculation of the concentration of the element is determined through comparison with a calibration curve [229].

2.2.3. Elemental analysis - X-ray Photoelectron Spectroscopy (XPS)

XPS analysis was carried out on a Kratos Supra employing a monochromated Al Kα X-ray source (hv = 1486.7 eV). The data was processed using CasaXPS version 2.3.14, with binding energies corrected to the C 1s peak at 284.6 eV and surface compositions quantified by application of element and instrument-specific response factors. Spectral fitting was performed using CasaXPS software.

X-ray photon electron spectroscopy is a sensitive technique that measures the elemental composition and electronic state of the elements that exist at the surface of the material. XPS spectra are obtained by irradiating the sample with X-rays emitted by a source such as Al Kα or Mg Kα. The atoms at the surface of the sample are excited and emit a number of electrons [230]. Electron analysers detect the kinetic energy and the number of electrons escaping from the surface. Using the intensity of the emitted photoelectrons from the surface of the material and the binding energy (calculated from the kinetic energy measured), an XPS spectrum is produced. The spectrum can be used to quantitatively and qualitatively (the oxidation state of the element) estimate the elemental composition at the surface of the sample [93,231].

2.2.4. Nitrogen physisorption analysis

Nitrogen physisorption analyses were carried out using a Quantachrome Nova 4000 porosimeter and analysed with NovaWin software. Before analysis, approximately 50 mg of the sample was degassed under vacuum at 120 °C for mesoporous samples and at 250 °C for microporous samples, for a duration of 10 h to remove any physisorbed species. The sample cell was then accurately weighed before the sample is cooled to -196 °C using liquid nitrogen.

The surface area of the materials was calculated using the Brunauer-Emmet-Teller (BET) model [232] and the de Boer "t-plot" method [233] was applied to calculate the micropore volume. The total pore volume was calculated using the amount of gas adsorbed at a relative pressure of 0.98 in the desorption branch using the Barrett, Joyner and Halenda (BJH) method [234]. The volume of the mesopores was calculated using the equation $V_m = V_T - V_\mu$, where, V_m is the mesopore volume, V_T is the total pore volume and V_μ is the micropore volume. The BJH method was also applied to the adsorption branch to calculate average pore size.

Gas physisorption (physical adsorption) is widely used to characterise textural properties of solid materials. The method involves the exposure of the sample to an inert gas, in this case, nitrogen, below its critical point to enable the physisorption of the adsorbate onto the surface of the material [235]. The amount of nitrogen adsorbed is dependent on the equilibrium pressure and temperature. Therefore, the adsorption isotherm is the relationship between the amount of gas adsorbed and the equilibrium pressure or relative pressure at a constant temperature [93]. Adsorption isotherms are dependent on the nature of the adsorbent. The isotherms can be interpreted by comparison to physisorption isotherms and associated hysteresis loops defined by IUPAC shown in **Fig. 12** [236].

Fig. 12. *IUPAC classified adsorption isotherms and hysteresis loops* [237].

Type I isotherms are characteristic of microporous materials such as zeolites and carbons. The Type II isotherm is observed for non-porous or macroporous materials, and point B corresponds to the point of monolayer coverage. Type III is more extreme where there is no obvious monolayer coverage and the adsorbate is clustered around favourable sites. Type IV isotherms display the appearance of a hysteresis loop (H1 and H2) and are characteristic of mesoporous materials. The H1 hysteresis loop can be attributed to a narrow range of uniform mesopores usually of cylindrical dimensions. The H2 hysteresis loop is indicative of a complex pore network and, importantly, can often give a misleading picture of the pore size. Therefore, it is recommended that pore size distribution should be calculated on the adsorption branch. A Type V isotherm is similar to Type III in the initial adsorption curve, however at a higher relative pressure (P/P_0) nanopore filling becomes apparent. Type V isotherms are relatively uncommon and are given by some activated carbons. Finally, Type VI isotherms are characteristic of layer-by-layer adsorption on highly uniform non-porous surfaces such as graphite [235].

Textural properties of the materials can be derived from the implementation of various mathematical models to the isotherm data. The Brunauer-Emmet-Teller (BET) calculation is widely used to measure the surface area of the material and is given in **Eq. 4**[238].

$$\frac{V}{V_m} = C\left(\frac{P}{P_o}\right)/[1 + (C-1)\left(\frac{P}{P_o}\right)][1 - \left(\frac{P}{P_0}\right)] \qquad \textbf{Eq. 4}$$

Where, V is volume adsorbed, V_m is the volume of the monolayer, C refers to the multilayer adsorption parameter, P is the pressure and P_0 is the saturation pressure.

Pore size and pore size distributions were calculated by a method developed by Barret-Joyner-Halenda (BJH) which is based on the Kelvin model of pore filling [234]. It describes the condensation of gases within a pore as the relative pressure is increased. However, it is only accurately applied to mesopore and small macropores. To determine the external surface area and micropore volume the DeBoer t-plot method can be employed.

2.2.5. Thermogravimetric Temperature Programmed Desorption of adsorbed n-propylamine (TG-TPD)

The number of acid sites was determined by n-propylamine adsorption followed by temperature programmed desorption using Thermogravimetric Analysis coupled to a Mass Spectrometer (TGA-MS).

Prior to analyses, propylamine was added dropwise to the samples until fully saturated. Excess physisorbed propylamine was removed from the samples by vacuum drying at 35 °C overnight. Doped samples (5-10 mg) were weighed accurately using a microbalance and added to an alumina crucible (70 µl). Temperature programmed desorption was performed on a Mettler Toledo TGA/DSC 2 StarSystem between 40 and 800 °C at a ramp rate of 10 °C min^{-1} under a He flow of 20 ml min^{-1}. Reactively formed propene and ammonia were detected using a Pfeiffer Vacuum ThermoStar MS at m/z = 41 and 17 respectively. The number of acid sites was calculated using the thermogravimetric data for the mass loss in the temperature range of propene and ammonia detection.

The number of acid sites on the surface of the material can be determined using the temperature programmed desorption of n-propylamine [239]. Propylamine reacts with acid sites on the surface to form propyl ammonium ions. These decompose to ammonia and propene over a well-defined temperature range similar to the Hofmann elimination reaction. Thermal energy is applied using a TGA which monitors mass changes under applied heat. An inert carrier gas, in this case, nitrogen, transfers the reactively formed propene from the sample to the mass spectrometer where it is detected. By measuring the precise decrease in sample mass as the temperature is increased, the total number of acid sites can be determined [240].

2.2.6. Diffuse Reflectance Infrared Fourier Transform Spectroscopy (DRIFTS)

The Brønsted/Lewis acid character of the catalysts was studied by means of Diffuse Reflectance Infrared Fourier Transform Spectroscopy (DRIFTS) using pyridine as a probe molecule. Ex situ pyridine adsorption was performed by the saturation of diluted samples (10 wt. % in KBr). Excess physisorbed pyridine was removed under vacuum at 35 °C prior to spectral acquisition on a Thermo Scientific Nicolet iS50 FT-IR spectrometer with a mercury cadmium telluride (MCT-A) photo detector at -196 °C, cooled by liquid nitrogen. Analyses were performed under vacuum in an environmental cell at 110 °C, to remove physisorbed water/moisture. Omnic software was used for the collection and plotting of the spectra as a function of wavenumber.

Infrared (IR) spectroscopy is a non-destructive technique that studies the vibrational transitions of a molecule or material associated with changes in dipole moment during exposure to infrared radiation [93]. DRIFTS combined with a probe molecule, such as pyridine, distinguishes between Brønsted and Lewis acid sites and can provide their concentration. Upon interaction with a Brønsted acid, pyridine is protonated and absorbs at a specific wavelength around 1540-1545 cm^{-1}. Upon interaction with a Lewis acid site, pyridine will form a coordinatively bonded complex with a specific IR absorption band at approximately 1449-1452 cm^{-1}. A band at approximately 1490 cm^{-1} is also common for absorption by both species [241]. Moreover, Brønsted to Lewis ratios (B/L) can be derived through the integration

of the peak areas associated with each band. Diffuse reflectance can be used for materials in the form of powders or pellets which strongly scatters IR radiation. Samples are generally diluted using an alkyl halide such as KBr, which does not absorb in the IR region. This is to prevent over absorption by the sample in the mid-IR region.

2.2.7. Scanning Transmission Electron Microscopy (STEM)

High-resolution Scanning Transmission Electron Microscopy (STEM)images were taken using a FEI Philips TECNAI F20 at 200 kV equipped with an Oxford instruments ISIS Energy Dispersive Spectroscopy (EDS) detector, located at The Centre for Electron Microscopy, University of Birmingham. The sample was diluted in ethanol and then deposited by drop casting onto a carbon coated mesh copper grid and then dried under ambient conditions. Images were analysed using ImageJ software.

The Scanning Transmission Electron Microscopy (STEM) method is an important tool for the imaging of nanostructures with the sensitivity of a single atom. The technique involves the rastering (moving side to side/top to bottom) of a high-energy electron beam over a sample. The high-energy electron beam is focussed through an objective lens onto the sample where the electrons that either transmit through the sample are scattered or are diffracted. The transmitted electrons are focussed through a series of magnetic fields where they produce an image which is then projected onto a fluorescent screen at the bottom of the microscope. In bright-field imaging, the area where the electrons are diffracted loses its image intensity and hence areas are darker, known as “diffraction contrast”. Diffraction of electrons can occur due to different orientations of the crystals. In addition, areas of darkness in bright-field TEM imaging can occur due to “amplitude contrast”. This is caused by differences in thickness across the sample as the electron beam interacts with greater amounts of material [242]. Electron dispersive spectroscopy (EDS), detects X-rays that are produced as the electron beam passes through the sample. The X-rays produced have emission spectrums characteristic to individual elements, allowing the distribution of elements in the sample to be mapped.

2.2.8. Scanning electron microscopy (SEM)

Scanning electron microscopy (SEM) was performed using a JEOL 7800F Prime FEG SEM fitted with a BSE and SE detector. This was employed to characterise the crystal size and morphology of the three catalysts. Images were recorded at a probe current of 3 mA and an accelerating voltage from 1 to 15 kV.

Scanning electron microscopy uses a focused beam of electrons to scan the surface of a sample produced by an electron and focused by multiple condenser lenses. The electrons interact with the

atoms in the sample which produces signals due to the emission of secondary electrons, backscattered electrons, characteristic X-rays, Auger electrons and photons of various energies. The beam of electrons scans in a raster pattern and the signals produced are combined with the detected signals to produce an image [243].

2.3. Characterisation of lignocellulosic biomass feedstock

Ash content

The ash content of the beech wood sample was determined according to the ASTM E1755-01 method [244]. Prior to analyses, the feedstock was dried at 60 °C for 24 h as per ASTM standards. Approximately 0.5 to 1.0 g of dried beech wood sample was placed in dry pre-weighed crucibles. Crucibles were covered with lids and placed in a furnace and heated to 250 °C at 10 °C min^{-1} and held for 30 min. The temperature was then increased to 575 °C for 3 h. After this, the samples were removed and cooled in a desiccator. Each crucible was weighed to the nearest 0.1 mg. Samples were subjected to further heating at 575 °C for 1 h intervals until the measured weights were within 0.3 mg.

CHNS

Elemental analysis was performed on the beech wood feedstock to derive the quantity of carbon, hydrogen, nitrogen and sulphur (CHNS) on a wt. % dry ash-free basis (d.a.f). The elemental analysis was determined using a ThermoScientific Flash 2000 CHNS-O analyser. The oxygen (O) content was estimated as the percentage difference after consideration of the ASTM ash content. Duplicate measurements were taken, and the average value was calculated.

CHNS analysis uses flash combustion in a quartz reactor tube heated at ca. 1000 °C. During the combustion process, the carbon in the sample is converted to CO_2, while hydrogen is converted to H_2O, nitrogen compounds to N_2 or NO_2 and sulphur to SO_2. Any other products formed during the combustion process are removed via absorbents. The resultant gases are passed over a high purity copper catalyst to remove trace oxygen and to convert the products to their elemental gaseous forms. The gases are then separated by GC and quantified using a thermal conductivity detector (TCD).

Thermogravimetric analysis (TGA)

The proximate analysis of the beech wood feed was determined by thermogravimetric analysis using a Perkin-Elmer Pyris 1 TGA. Approximately 10 mg of beech wood sample was heated from 50 °C to 900 °C at 10 °C min^{-1} under a nitrogen flow rate of 20 ml min^{-1} to provide a sample of char and ash. The ash content was determined by heating the sample to 575 °C at 10 °C min under an oxygen flow rate of 20

ml min^{-1} to combust the solid carbon. The ash content was calculated by weight difference. Duplicate measurements were taken, and the average value was calculated.

The proximate analysis quantifies the moisture, volatile matter, fixed carbon and ash of a sample. The moisture content of the sample only includes physisorbed water and is released up to the boiling point of water. The volatile content of the sample consists of the gases and vapours released during heating. Ash is comprised of inorganic compounds after combustion of the feedstock.

Bomb calorimetry

The higher heating value (*HHV*) of the beech wood feedstock was measured experimentally using an IKA C 1 static jacket oxygen bomb calorimeter. Approximately 0.6 g of beech wood was placed in a crucible inside an inner sealed vessel. The sealed vessel was pressurised with 40 bar of O_2.

Bomb calorimetry is used to determine the enthalpy of combustion of a sample, a schematic diagram of a bomb calorimeter is presented in **Fig. 13.** The process of bomb calorimetry combusts a known quantity of sample in a pressurised "bomb" in an environment of oxygen. The heat produced by the ignition of the sample heats a known quantity of water surrounding the vessel. The temperature change of the water is accurately measured using a temperature sensor. The calorific value of the sample can then be calculated from the temperature change of the water surrounding the vessel.

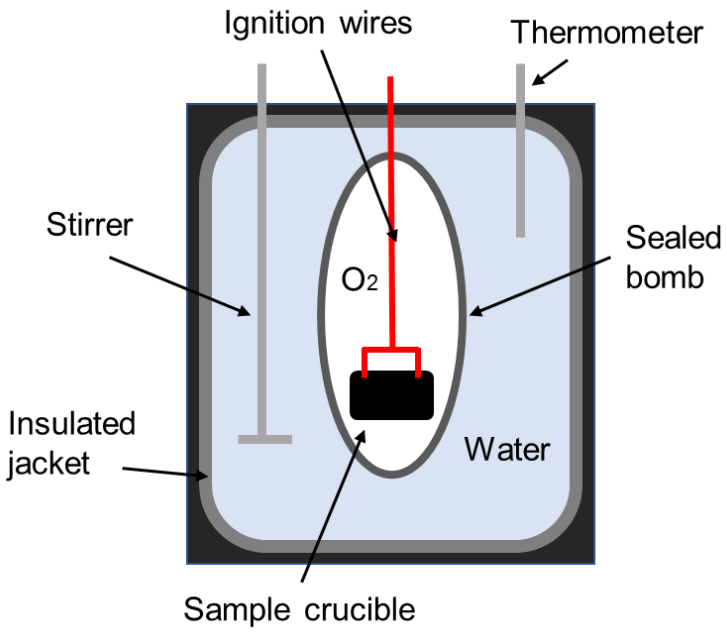

Fig. 13. *Schematic diagram of a bomb calorimeter*

2.4. Catalytic reactor systems and procedures

2.4.1. Catalytic pyrolysis of LDPE using Thermogravimetric Analysis (TGA)

Both thermal and catalytic cracking of LDPE was investigated using a Perkin-Elmer Pyris 1 thermogravimetric analyser (TGA) equipped with a 20 position autosampler. The polymer and powdered catalyst were ground and thoroughly mixed in a weight ratio of 3:1 using a mortar and pestle to ensure the samples were fully mixed. Approximately 5 mg of the sample mixture was then loaded into ceramic crucibles for analysis. The sample was heated from 50 to 600 °C at 10 °C min^{-1}, under an inert nitrogen atmosphere with a flow rate of 20 ml min^{-1}. These conditions were chosen in order to compare with literature references [245]. Upon heating by the TGA, the LDPE melted and cracked over the active sites of the catalyst. Each experiment was performed in triplicate and an average of the measured values was calculated. The temperature marking the maximum degradation rate (T_{max}) of the sample was determined using the derivative thermogravimetric (DTG) plots.

2.4.2. Catalytic pyrolysis of LDPE by Py-GC/MS

The catalytic pyrolysis of low density (LDPE) was investigated by Py-GC/MS on a CDS analytics (Chemical Data Systems, Oxford, PA) 5200 series pyrolyser close-coupled to a PerkinElmer Clarus 680 gas chromatograph (GC) and Clarus 600S mass spectrometer. A schematic representation of the reactor setup is presented in **Fig. 14.** For each experiment, the polymer and powdered catalyst were ground and thoroughly mixed with a weight ratio of 3:1 plastic to catalyst. A relatively high ratio of catalyst to plastic was used to ensure full conversion (catalytic pyrolysis) of the plastic in order to compare between catalysts. A small amount of LDPE (approximately 0.7 mg) was placed inside a 25 mm quartz tube between two threads of quartz wool, for catalytic runs a small mass of catalyst/LDPE mixture (approximately 1 mg) was used.

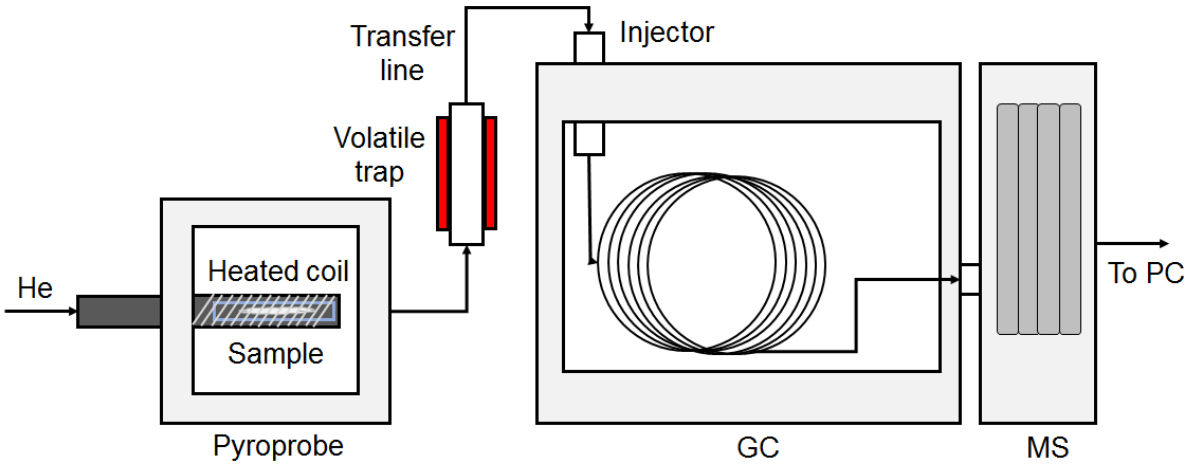

Fig. 14. *Scheme of the pyro-probe reactor and GC/MS setup.*

The samples were heated by a platinum coil probe to 700 °C at 10 °C/ms with a hold time of 10 s, the pyrolysis interface was maintained at 290 °C. Volatilised compounds were immediately trapped on a Tenax ®-TA adsorbent trap at 45 °C to avoid secondary/recombination reactions. The Tenax ®-TA adsorbent trap was then heated to 295 °C and the pyrolysis products were transferred onto the GC column via a heated transfer line kept at 310 °C. A PerkinElmer Elite-1701 column (cross-bond: 14 % cyanopropylphenyl and 85% dimethyl polysiloxane; 30 m, 0.25 mm i.d., 0.25 mm df) was used to separate the products using Helium as a carrier gas. The GC injection port was kept at 275 °C and a 1:125 split ratio was used. The GC oven was heated at 5 °C min^{-1} from 45 °C to 280 °C. Proposed peak assignments (m/z = 45-300) were made from mass spectra detection using the NIST 2011 MS library. Thermal and catalytic Py-GC/MS experiments were performed in at least duplicate, which confirmed the reproducibility of the reported procedure.

2.4.1. Thermogravimetric analysis (TGA) and differential scanning calorimetry (DSC) of the main lignocellulosic biomass components

The pyrolysis of the three main lignocellulosic biomass components (cellulose, lignin and hemicellulose) was carried out using a Metler Toledo TGA/DSC 2 StarSystem between 40 and 900 °C under a N_2 flow of 40 ml min^{-1} to provide an inert atmosphere using a ramp rate of 10 °C min^{-1}. A blank was taken prior to analyses which was subtracted from the results to correct for the Archimedes effect (Archimedes' principle of buoyancy) of the nitrogen gas as the temperature increases [246].

2.4.1. Catalytic pyrolysis of the main lignocellulosic biomass components using Py-GC/MS

The catalytic and thermal pyrolysis of lignocellulosic biomass components (cellulose, lignin and hemicellulose) was carried out on a CDS analytical (Chemical Data Systems, Oxford, PA) Pyroprobe 5200 series pyrolyser close-coupled to a PerkinElmer Clarus 680 gas chromatograph (GC) and Clarus 600S mass spectrometer (MS), see Section 2.4.2 above.

Firstly, the individual components cellulose, lignin and hemicellulose were pyrolysed at 550 °C to identify the products from the non-catalytic pyrolysis for comparison. This temperature was chosen to best simulate fast pyrolysis to maximise the production of volatiles (liquid yield) [36]. A heating rate of 20 °C ms^{-1} was also used to ensure the instantaneous pyrolysis of the sample. This was the maximum temperature ramp rate of the system and was chosen to best mimic the conditions in large-scale fast pyrolysis reactors. The temperature was held at the final temperature for 30 s to ensure the complete pyrolysis of the sample.

For the catalytic experiments, the catalyst and individual biomass component (either cellulose, lignin or hemicellulose) were individually weighed accurately to 3 decimal places on a Sartorius ME36s balance. The quartz tubes were plugged with a quartz wool packing, a low amount (1 mg) of powdered catalyst was added as a bottom layer in case of any back-flowing gases. 2 mg of biomass waste component (either cellulose, lignin or hemicellulose) was added, and 2 mg of powdered catalyst was weighed and added to the tube to give a catalyst to biomass ratio of 1:1 on a mass basis. This ratio was chosen due to the low bulk density of many of the catalysts compared to biomass. Due to the low bulk density of the catalyst, the same mass of the catalyst occupies a much larger volume of the quartz tube compared to the biomass. Therefore, larger catalyst to biomass (C/B) ratios are difficult to achieve without the risk of catalyst particles escaping into the system. This should be avoided due to the possibility of blockages in the pyroprobe system. Quartz wool was packed at the end of the quartz tube to prevent any solids from escaping into the pyrolysis system. During pyrolysis, the vapours flow from the open end of the quartz tube into the pyrolysis interface carried by the helium stream and into the GC-MS.

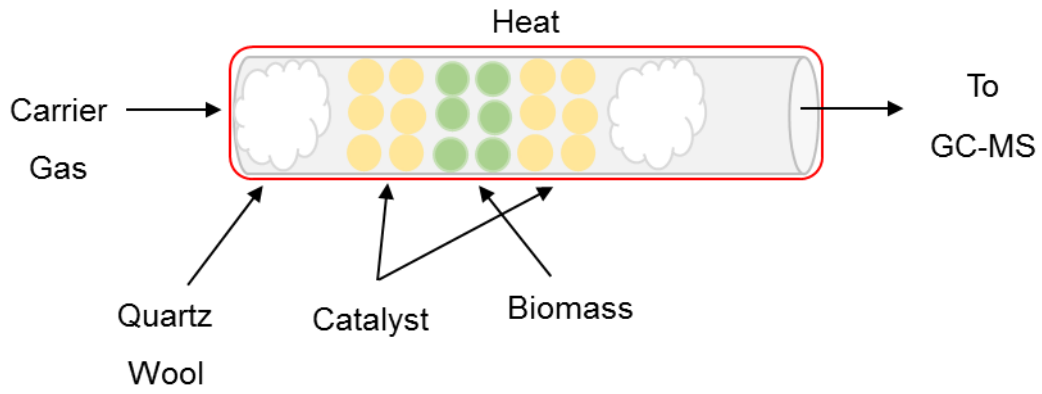

Fig. 15. *The arrangement of catalyst and biomass component in quartz tube for pyrolysis.*

In all experiments, the samples were placed inside the pyroprobe reactor and heated to 550 °C at 20 °C ms^{-1} with a hold time of 30 s. These conditions were chosen to best simulate fast pyrolysis conditions in a fluid bed reactor. The long hold time of 30 s ensures the maximum quantity of volatiles are produced. Volatilised compounds were separated and identified using a PerkinElmer 1701 column, see Section 2.4.2 for further details.

2.4.1. Micropyrolysis gas chromatography – MS/FID/TCD

All experiments were carried out using a Frontier Labs single-shot tandem micropyrolysis system (Rx-3050tr, **Fig. 16**). The system contained two quartz pyrolysis tube reactors (4.7 mm ID, 114 mm length), each independently temperature controlled. The interfaces of the two reactors were each set at 350 °C

to prevent premature condensation of pyrolysis products. During the experiment, helium was used as a carrier gas to transport the volatile products through the reactor system to the GC for separation and identification.

Fig. 16. *Schematic diagram of frontier labs tandem micro-pyrolysis reactor-GC-MS/FID/TCD. Reproduced from reference (*[247]*)*

In situ catalytic pyrolysis of beech wood

For the in situ catalytic fast pyrolysis experiments, the biomass sample (approx. 0.3 µg) was first weighed into a deactivated stainless-steel sample cup. Then, the required amount of catalyst was added to the sample cup to achieve the stated C/B ratio (either 1, 5 or 10). Finally, a small amount of quartz wool was added to prevent any escape of solid particles. The sample cups were purged with helium for approximately 5 min and then dropped into the pyrolysis reactor. For the in situ experiments, only the first micro-reactor was used; the second micro-reactor was maintained at 500 °C to prevent vapour condensation. Vapours were transferred directly to the GC injector using a carrier gas flow of He set to 120 ml min^{-1}.

Ex situ catalytic pyrolysis of beech wood

For the ex situ catalytic fast pyrolysis experiments, the biomass sample (approx. 0.3 µg) was again first weighed into a deactivated stainless-steel sample cup, to be introduced to the reactor when ready. The second microreactor (**Fig. 16**) situated ex situ to the main pyrolysis reactor contained a quartz tube. 1.5 mg of catalyst, to achieve a C/B ratio of 5:1, was mixed thoroughly with approximately 30 mg of acid washed glass beads (45-90 µm). The mixture of catalyst and glass beads was loaded into the ex situ quartz tube packed with quartz wool at either end to prevent any from escaping. The addition of the glass beads is necessary to prevent channelling or flow bypass and to maintain similar bed lengths

across different catalyst densities. Pyrolysis of the beech wood feedstock was performed at 500 °C. The vapours were passed over the catalyst packed bed in the second reactor, maintained at 500 °C, using a carrier gas flow of He set to 120 ml min^{-1}.

Deactivation of catalysts in ex situ catalytic pyrolysis of beech wood

The resistance to deactivation of each catalyst was investigated in the ex situ configuration. This was achieved via subjecting each catalyst to five shots of beech wood pyrolytic vapour intermittently. The products formed after each shot of pyrolysis vapours were analysed by GC-MS/FID/TCD, to provide information on the activity of the catalyst.

Product analysis and quantification

The pyrolysis products were analysed by an Agilent gas chromatograph (Agilent 7890B) equipped with two Agilent medium polarity 1701 columns (Agilent VF1701 ms, 60 m x 250 µm x 0.25 µm) to separate the condensable compounds. The injector was maintained at 270 °C with a split ratio of 42:1 and a carrier gas flow of He set to 120 ml min^{-1}. The GC oven was programmed to start at 35 °C for 7.5 min and then the temperature was ramped to reach 300 °C at a rate of 10 °C min^{-1}. Products were identified using a coupled mass spectrometer (Agilent 5977A) and quantified using an FID. Light gases and hydrocarbons were separated using a GasPro column (Agilent GS-GasPro) and quantified using a TCD.

A set of calibration curves were produced using standard solutions comprised of 33 biomass pyrolysis compounds (see Appendix C, **Table A 2**), representing a range of the most abundant pyrolysis products. All standards were purchased from Sigma-Aldrich. Instead of sample cups, a syringe was used for the introduction of liquid and gas standards into the micro-reactor through a septum. The calibration curves produced linear correlations with coefficient of determination (R^2) values exceeding 0.99.

The product yields from fast pyrolysis experiments are presented on a carbon basis, which was defined in **Eq. 5** as:

$$Yield\ (C\ \%) = \frac{carbon\ mass\ of\ product}{carbon\ mass\ in\ reactant\ feed}\ x\ 100\% \qquad \textbf{\textit{Eq. 5}}$$

This provides the moles of carbon in the feed converted to products. Carbon percent basis was chosen to standardise product reporting to allow for easier comparison across studies [248]. Reporting on a carbon basis allows the tracking of carbon in the feedstock to the products, in order to obtain information of catalytic deoxygenation efficacy. In addition, yields presented on a carbon basis will not

be affected by the presence of hydrocarbons of varying degrees of unsaturation (alkanes *vs.* alkenes, or, cycloalkanes *vs.* aromatics)

For the calculation of the yield of char/coke a known amount of beech wood (ca. 0.5 mg) and catalyst, corresponding to the desired C/B ratio, was added into the pyrolysis cups and pyrolysed at 500 °C. The mass of the samples was recorded before and after pyrolysis using a microbalance. The mass difference was considered to be volatile components, while the remaining mass minus the catalyst mass was assumed to be all carbon and was reported as char/coke. All calculations were on a biomass dry ash free basis.

Mesoporous Catalyst Synthesis and Testing

3. Chapter 3 - Mesoporous Catalyst Synthesis and Testing

3.1. Introduction

Porous materials have been intensively studied for their use as catalysts and catalysis supports. They are divided into three classes based on their pore sizes as defined by IUPAC: microporous materials (<2 nm), mesoporous materials (2-50 nm) and macroporous materials (>50 nm) [249]. The most widely known and used porous materials are zeolites and possess a well-ordered pore structure with a narrow range of pore size distributions due to their crystallinity. Zeolites typically have pore sizes in the range of between 0.5 and 2 nm and are hence classified as being microporous [250]. Furthermore, zeolites have raised strong interest in the area of heterogeneous catalysis owing to their strong acidity. This enables the substitution of harmful liquid acids with zeolites in many chemical processes, in order to reduce the generation of harmful wastes [129]. However, as discussed in the General Introduction, zeolites present severe limitations when using large reactant molecules due to their small pore sizes. The diffusion of large molecules to the internal pore network of zeolites is hindered by the small diameter of the micropores. Several attempts to overcome the diffusional limitations of zeolites such as increasing the zeolite pore sizes [251], decreasing zeolite crystal size [252] and the creation of hierarchical zeolites [125], are currently under investigation by other research groups.

The quest to overcome the diffusional limitations presented by zeolites led to the recognised invention of ordered mesoporous materials (OMMs) from silica by Mobil Oil Corporation scientists in 1992 [253]. Interestingly, a similar discovery was made over 20 years previously by scientists synthesising low bulk-density silica [254], however the significance was not recognised at the time. The new material named MCM-41, which stands for Mobil Composition of Matter No. 41, possessed a highly ordered hexagonal array of pores with a very narrow pore size distribution. The material was synthesised using an ionic surfactant as a template. Interactions between the positively charged surfactant and the negatively charged silica species led to the ordering of a silica structure around the template. Subsequent calcination removes the template resulting in an ordered mesoporous silica structure (**Fig. 17**). Depending on the silica source or type of surfactant (including chain length) many other mesoporous materials, with varying pore sizes and structures, can be synthesised following similar pathways [129]. The pore size of OMMs can be tailored from 1.5 nm and up to 60 nm with the addition of auxiliary pore expanding agents [255,256].

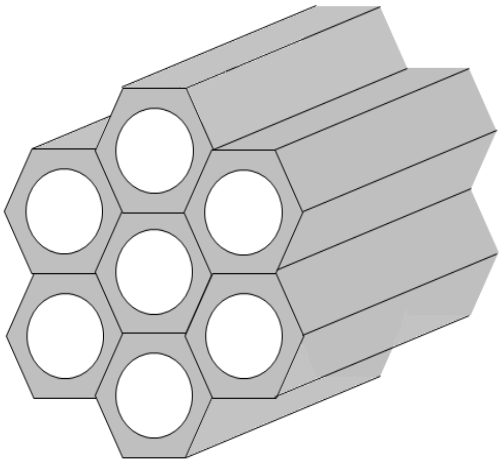

Fig. 17. *Hexagonal mesoporous structure of MCM-41 and SBA-15.*

OMMs offer great opportunities in the catalysis of larger molecules beyond the micropore domain typical of zeolites. The performance of OMMs as catalysts is strongly dependent on their pore size and pore volume which allow the quick diffusion of reactants and products. However, their application in many different catalytic processes requires high thermal and hydrothermal stability to be able to cope with the stresses and pressures of thermal catalytic reactions. The stability of OMMs is highly dependent on their wall thickness and pore sizes, with thicker pore walls being the most stable [257]. SBA-15 (Santa Barbara Amorphous, #15) invented by Zhao and co-workers in 1999 [217], is structurally very similar to MCM-41 but possess thicker pore walls as a consequence of improved framework crosslinking and larger pore sizes (2-12 nm compared to 2-5 nm for MCM-41). The substantial increase in wall thickness of SBA-15 (2-8 nm) compared to MCM-41 (1-1.5 nm) leads to greatly increased hydrothermal stability and structural integrity of the former [258].

In their pure form, both MCM-41 and SBA-15 are not typically used as catalysts. The incorporation of active sites into the silica framework or the deposition of active species on the surface enables enhanced catalytic functionalities. As discussed, zeolites are particularly successful as catalysts due to their strong Brønsted acid properties. The presence of aluminium in the structure of zeolites invokes a negative charge in its framework. The negative charge is balanced by metal cations or hydroxyl protons, the latter producing a Brønsted acid site [105]. Generally, there is an inverse relation between Si/Al ratio and the number of Brønsted acid sites, i.e. the more aluminium incorporated the more acid sites generated. Several attempts to incorporate aluminium into the framework of SBA-15 have been made to obtain similar acidic properties to zeolites. However, high levels of aluminium incorporation into Al-SBA-15 has proved difficult to accomplish. This is due to the difference in hydrolysis rates of Al and Si at the low pH required for SBA-15 synthesis [259].

According to the literature, the quality of aluminium incorporation for the generation of Brønsted acid sites is highly dependent on the synthesis procedure. The direct synthesis is the direct mixing of silicon and aluminium precursors in the synthesis solution. Whereas, post-synthesis procedures are the addition or grafting of aluminium on the SBA-15 after the initial synthesis. The pH adjustment method is similar to direct synthesis; however, the pH is increased from <2 to 7 before a second hydrothermal treatment in order to increase the hydrolysis of aluminium into the silica framework. The direct synthesis of Al-SBA-15 results in Al species that are not retained in the silica framework and often end up as extra-framework aluminium. Likewise, post-synthesis techniques require additional preparation steps and further calcination also leading to a high amount of extra-framework aluminium [260]. On the other hand, the pH adjustment method is a simple, but effective, technique for the incorporation of high amounts of aluminium (Si/Al ≤ 25) into the SBA-15 structure, with high Brønsted acidity similar to those found in zeolites. Furthermore, the structural/textural properties of Al-SBA-15 are also heavily dependent on synthesis parameters such as ageing temperature and time: generally higher temperatures and longer hydrothermal treatment steps lead to larger mesopore diameters and higher surface areas [261]. An overview of various reported methods for the incorporation of aluminium into the structure of SBA-15 is given in **Table 6**.

***Table 6**. Comparison of Al-SBA-15 synthesis and acidity evaluation referenced in literature. References are presented in chronological order.*

Method	Lowest Si/Al	Acidity (μmol g^{-1})	Brief evaluation	Ref.
Direct synthesis	8.5	N/A	Acidity not evaluated.	[262]
Direct synthesis	10	N/A	Samples with highest Al incorporation displayed superior cracking ability.	[261]
Post-synthesis	4.8	N/A	Py-IR confirms existence of Brønsted acid sites and confirmed by cumene cracking reaction, though not quantified.	[263]
Direct synthesis/two step	22	N/A	Py-IR shows increase in Brønsted and Lewis acidity with a decrease in Si/Al, not quantified.	[259]
Direct synthesis	10	N/A	Cracking of waste fatty acid mixture shows conversion is inversely proportional to Si/Al.	[264]
pH adjustment	2.4	N/A	Acid sites not measured.	[218]
Nanostairs technique	5	N/A	NH_3 TPD confirms the existence of medium strength acid sites, weaker than most zeolites.	[265]
Post-synthesis	7.2	430	Acidity quantified by Py-IR, highest Brønsted acidity achieved at Si/Al = 9.8 (81.2 μmol g^{-1}).	[266]
Post-synthesis	10	160	Acid sites evaluated by probe molecules and NMR. Acid site strength is dependent on the probe molecule.	[267]
Direct synthesis	10	N/A	Catalytic activity inversely proportional to Si/Al.	[268]
pH adjustment	31	110	Acid properties measured by NH_3 TPD, shows acidity is 0.11 mequiv.NH_3 g^{-1} (Si/Al = 30).	[269]
Post-synthesis	0.8	N/A	Acid sites evaluated by Py-IR and NH3, NH_3 TPD determined acid sites are mainly of medium strength. Acid sites not quantified.	[270]
pH adjustment	30	N/A	NH_3 confirms presence of medium strength acid sites.	[271]
Direct synthesis	11.4	402	Acidity evaluated by NH_3, linear relationship between acidity and cumene cracking. Highest total acidity achieved at Si/Al = 11 (402 μmol g^{-1}).	[272]
Direct synthesis	10	N/A	Acidity not evaluated.	[273]
Direct synthesis	4.1	N/A	Acidity not evaluated.	[274]
Direct and post-synthesis	8	491	Acidity evaluated by both Py-IR and NH_3 TPD, highest acidity achieved at Si/Al = 8 (470 and 491 μmol g^{-1}, Py-IR and NH_3 TPD respectively).	[275]
Direct synthesis	10	N/A	Acidity not evaluated.	[276]
pH adjustment and post-synthesis	13.2	417	Acidity quantified and evaluated by Py-IR and NH_3 TPD, highest Brønsted acidity achieved with post-synthesis method. Si/Al = 15 (128 and 622 μmol g^{-1}, Py-IR and NH_3 TPD respectively).	[260]
Post synthesis	20	N/A	NH3 TPD shows acidic quantity is 2400 μmol g^{-1} with Si/Al = 20.	[277]
Direct synthesis	20	440	Acidity quantified by NH3 TPD. Highest total acidity was seen at Si/Al = 20 (440 μmol g^{-1}) decreasing Si/Al decreased quantity of Brønsted sites.	[278]
pH adjustment	5	N/A	Acidity evaluated by NH_3 TPD, results show a positive correlation between Al content and NH_3 peak area.	[279]
Direct synthesis	5	N/A	Acidity not evaluated.	[280]
Direct synthesis	14	4	Acidity evaluated by activity of n-heptane conversion. Highest Brønsted acidity at Si/Al = 14 (3.6 μmol g^{-1}).	[281]
pH adjustment	5.2	471	Acidity quantified and evaluated by Py-IR, no difference in Brønsted/Lewis ratios with Al incorporation.	[219]
Direct synthesis		N/A	Acidity evaluated by Py-IR, confirms the existence of Brønsted acid sites.	[282]
Direct synthesis	34	2960	Acidity quantified and evaluated by NH_3 TPD, highest total acidity at Si/Al = 34 (2960 μmol g^{-1}).	[283]
pH adjustment	3.4	438	Acidity evaluated by NH_3 TPD, highest total acidity at Si/Al = 3.4 (438 μmol g^{-1}).	[284]
Direct synthesis	13	58	Acidity evaluated by Py-IR, highest Brønsted acidity achieved at Si/Al = 13 (58 μmol g^{-1}).	[285]

As discussed in the general introduction chapter (Section 1.2), biomass is a complex polymeric material containing a multitude of different molecules with a range of elements and functional groups. Due to these complexities, it is challenging to correlate differences in structural and acidic properties of the catalyst and their effects on the products obtained in the catalytic pyrolysis of biomass.

Plastics, on the other hand, are generally much simpler in terms of their structure and the vast majority are formed of hydrocarbon chains in repeatable units. Polyolefin plastics, in particular Low-Density Polythylene (LDPE) in **Fig. 18**, account for the majority of plastics consumed and find use in many applications such as packaging and insulation [286]. The analysis of the catalytic cracking of LDPE by thermogravimetric analysis (TGA) and Py-GC/MS provides a good comparison of both the activity and selectivity of a catalyst. This can help establish the relationship between structural properties and the catalytic reactivity. The catalytic cracking of polyolefins proceeds through a carbocationic mechanism, forming carbonium ions upon reaction with a Brønsted or Lewis acid site [287]. Following the formation of a carbonium ion (CH_5^+), several acid-catalysed reactions may occur on the acid sites such as isomerisation, oligomerisation, cyclisation, aromatisation and cracking [286]. These reactions are all analogous to the ones which take place in the catalytic pyrolysis of biomass.

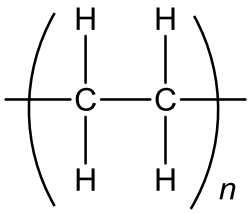

Fig. 18. *The repeatable monomer of low density polyethylene (LDPE).*

Many solid acid catalysts have been employed successfully for the catalytic cracking of LDPE such as zeolites (ZSM-5 [124,245,252], HY [288], Zeolite Beta [245]) and OMMs (Al-MCM-41 [245,289] and Al-SBA-15 [245,289,290]). Zeolites possess active acid sites both on the exterior of the zeolite crystal surface and internally within the pore network. However, the majority of the surface area is located within the pore network. It has been reported in the literature [195,291] that for some potentially useful chemical reactions, the steric requirements of the reactants or products are beyond the pore size limits of the zeolite structures. Therefore, the activity of the zeolite catalysts is limited due to diffusional constraints, as larger reactants are unable to access the majority of the catalytic active sites located within the pores. In contrast to zeolites, the aluminosilicate OMMs investigated, including Al-SBA-15, was able to process bulky molecules and have potential catalytic capabilities, however, they are currently limited by their low acid strength. The Al-SBA-15 used in these studies were synthesised using either direct synthesis or post-synthesis grafting at medium Si/Al ratios, which were unable to

yield large quantities of aluminium in the tetrahedral environment, leading to low acidity materials compared to zeolites [245,289,290].

In this chapter, Al-SBA-15 was synthesised over a range of Si/Al ratios (100-5:1) using the pH adjustment method, in order to produce Al-SBA-15 with a high quantity of acid sites and high strength, that are comparable to zeolites. The physicochemical properties of the synthesised catalysts were characterised to confirm their structural and acidic properties. The Al-SBA-15 catalysts were applied in the catalytic cracking of LDPE, a simpler polymer than biomass but where analogous reactions should take place. The activities and selectivities of the Al-SBA-15's in this reaction were compared to ZSM-5 in order to assess the viability of future catalytic biomass pyrolysis experiments.

3.2. Results and Discussion

3.2.1. Characterisation results

Elemental analysis data of the Al-SBA-15 catalysts are given in **Table 7**. The experimentally determined Al content (given as Si/Al ratio) is close to the planned composition. This highlights the advantage of using the pH-adjustment method, which offers a high-level control of the incorporation of aluminium from the initial synthesis gel to the final solid, in agreement with prior work [218,219,284].

***Table 7**. Physicochemical properties of the studied catalysts.*

Sample	Bulk Si/Al (at.)[a]	Surface Si/Al (at.)[b]	Lattice spacing *d* (nm)	Surface area ($m^2 g^{-1}$)[c]	Vol. micr. ($cm^3 g^{-1}$)[d]	Vol. meso. ($cm^3 g^{-1}$)	Vol. total ($cm^3 g^{-1}$)[e]	Avg. pore size (nm)	Acid sites (µmol g^{-1})[f]	B (µmol g^{-1})[g]	L (µmol g^{-1})[g]	B/L
AlSBA15(5)	5	5	9.7	414	0.00	1.0	1.0	6.8	564	347	217	1.6
AlSBA15(15)	17	12	10.2	412	0.00	0.8	0.8	6.0	409	194	215	0.9
AlSBA15(35)	27	15	10.3	432	0.02	1.3	1.4	7.4	232	103	129	0.8
AlSBA15(100)	75	30	10.1	485	0.03	1.3	1.3	9.5	124	29	95	0.3
SBA-15	-	-	9.8	857	0.06	1.2	1.3	6.0	17	2	15	0.1
ZSM-5	12*	0.2	-	304	0.11	0.0	0.2	0.9	672	380	292	1.3

Determined by [a] ICP-OES, [b] XPS, [c] BET, [d] t-plot, [e] BJH, [f] TG-TPD of n-propylamine, [g] pyridine-FT-IR *commercial specification

XPS analysis of the catalysts shows a deviation of the Si/Al ratios at the surface as compared to the bulk of the materials derived from ICP-OES data (**Table 7**). The surface and bulk Si/Al ratio of the aluminium rich catalysts (nominal Si/Al = 5 and 15) are quite similar, suggesting that aluminium is uniformly dispersed within the SBA-15 structure. However, at higher Si/Al ratios (nominal Si/Al > 35), larger quantities of aluminium were found at the surface of the material, indicating that the aluminium is not homogeneously distributed throughout the material as was also noted in a previous study on the synthesis of ZSM-5 [292]. The increase in aluminium at the surface could possibly be due to extra-framework aluminium, leading to the generation of Lewis acid sites as opposed to Brønsted acid sites. Although an excess of Al in the synthesis procedure has not been investigated in this study, it can be assumed further incorporation of Al will lead to the formation of predominantly extra-framework Al.

Analysis of the Si 2p region in **Fig. 19A** shows a perturbation of the peaks to lower binding energies with increasing aluminium incorporation, attributed to the generation of Si-O-Al species, in agreement with previous work [135]. The emergence of a peak at high aluminium levels is also evident at a binding energy of around 74 eV (**Fig. 19B**). This shifts slightly to higher binding energies, due to the formation of Si-O-Al species [293].

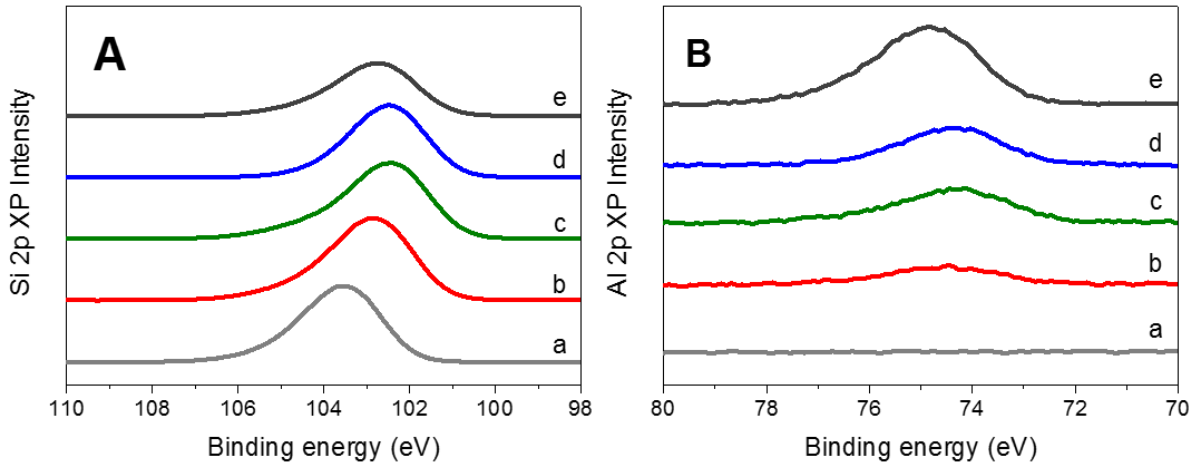

Fig. 19. *High resolution XP spectra of (A) Si 2p and (B) Al 2p for Al-SBA-15 catalysts: (a) SBA-15, (b) AlSBA15(100), (c) AlSBA15(35), (d) AlSBA15(15) and (e) AlSBA15(5).*

Fig. 20 shows the low-angle XRD patterns of the Al-SBA-15 catalysts and pure SBA-15, as a reference. The diffraction pattern in the low angle region displays an intense peak associated with the (100) plane and two less intense peaks associated with the (110) and (200) planes of the lattice. The diffraction patterns are all consistent with well-ordered 2D hexagonal structures typically displayed by SBA-15 mesoporous silica. This is also graphically evident in **Fig. 20** inset, where the (100) reflection only slightly scatters. A slight shift of the peak towards lower angles is evident in the (100) plane (B to D, **Fig. 20** inset), due to an increase in lattice spacing (d) in **Table 7**. However, at the highest aluminium

loading, i.e. AlSBA15(5), the lattice spacing is reduced close to the value of the Al-free SBA-15. The evidence of three distinct reflections in the low-angle XRD patterns in the series confirms that the short and long-range order of the hexagonal structure is unaffected with the incorporation of aluminium.

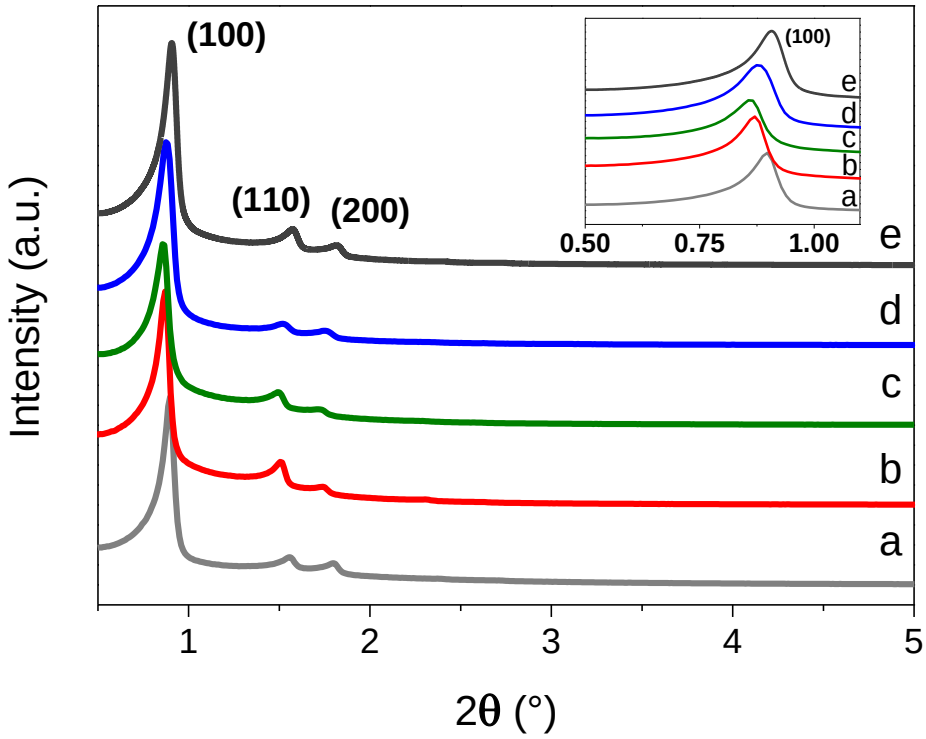

Fig. 20. *Low angle XRD patterns of Al-SBA-15 catalysts: (a) SBA-15, (b) AlSBA15(100), (c) AlSBA15(35), (d) AlSBA15(15) and (e) AlSBA15(5) (inset: amplification of 2ϑ in the region between 0.5 and 1.1°).*

The textural properties of the synthesised materials were analysed by N_2 physisorption (**Fig. 21**). All SBA-15 type catalysts exhibit type IV isotherms with H1 hysteresis, which are characteristic of mesoporous solids possessing cylindrical pore geometry and a high degree of pore size uniformity as defined by IUPAC [294]. It appears that in the isotherms of the Al-SBA-15 catalysts with increasing aluminium content (b to e), the hysteresis loops are shifted to lower relative pressures. This is indicative of a decrease in pore size, with the exception of AlSBA15(5) which displayed a similar pore size to the Al-free counterpart. At high Si/Al ratios (such as AlSBA15(35)), irregular hysteresis loops are evident, indicative of broad pore size distributions and large cylindrical pores. This is in agreement with the measurements obtained by XRD and indicate that structural ordering decreases at high Si/Al. Previous work by Ungureanu et al. [219], noted an increase in structural ordering with a decrease in Si/Al. Their explanation for this observation was due to the addition of highly charged aluminium nitrate in the synthesis solution. This resulted in increased ionic strength in the synthesis solution and hence a higher degree of ordering of the hexagonal structure of the SBA-15.

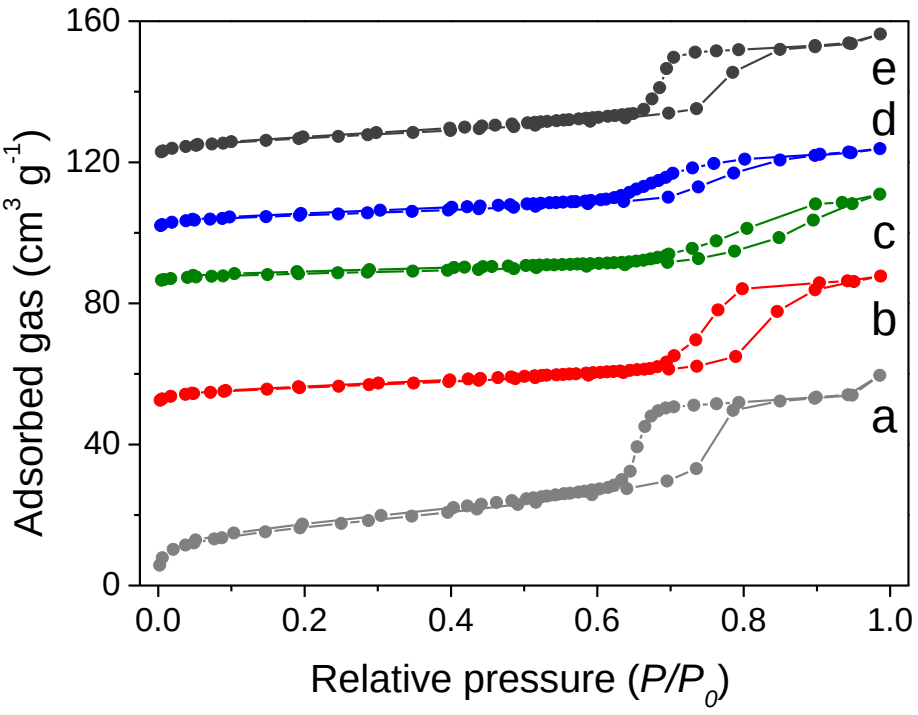

Fig. 21. *N_2 physisorption isotherms of the Al-SBA-15 catalysts: (a) SBA-15, (b) AlSBA15(100), (c) AlSBA15(35), (d) AlSBA15(15) and (e) AlSBA15(5) (isotherms were offset for clarity).*

The structural properties derived from the physisorption isotherms are summarised in **Table 7**. It is clear from the BET results that increasing the incorporation of aluminium dramatically decreases the surface area in the aluminium-rich catalysts compared with the Al-free SBA-15. This is due to the disappearance of the micropore volume in the series, i.e. the micropores disappear with the increasing Al content; the Al-free material has a micropore volume of 0.06 cm^3 g^{-1} in comparison to 0.00 cm^3 g^{-1} for the AlSBA15(5) material. Hence, the introduction of Al species into the SBA-15 structure inhibits the formation of micropores in the synthesis. As such, micropore volume is below the detection limit for the AlSBA15(15) and AlSBA15(5) materials, therefore leading to a purely mesoporous material at higher Al concentrations.

Decreasing the Al content of the materials causes a mild decrease in the volume of mesopores and total pore volume. On the other hand, the average pore size of all the SBA-15 materials is in the region of 6-9 nm. These values are consistent with reported values in the literature for SBA-15 using similar preparation procedures [295–297]. It is worth noting that the pore diameter of the Al-rich materials appears to be larger than the Al-free SBA-15. The increase in pore diameter is associated with the longer hydrothermal treatment experienced by the Al-rich materials, which were treated for an additional 72 h in comparison to Al-free SBA-15 [214]. **Fig. 22** shows the BJH pore size distributions of the Al-SBA-15 catalysts. SBA-15 exhibits the typical narrow pore size distribution centred at 6.0 nm.

Incorporating Al up to a Si/Al ratio of 35 broadens the pore size distribution and shifts its centre to larger pore diameters. Further increase of the Al content (AlSBA15(5)) narrows the pore size distribution and centres at a lower diameter of 6.8 nm. The bimodal pore size distribution of AlSBA15(15) and AlSBA15(35) is further evidence of the lack of structural ordering at high Si/Al ratios, also observed by Ungureanu et al. [219].

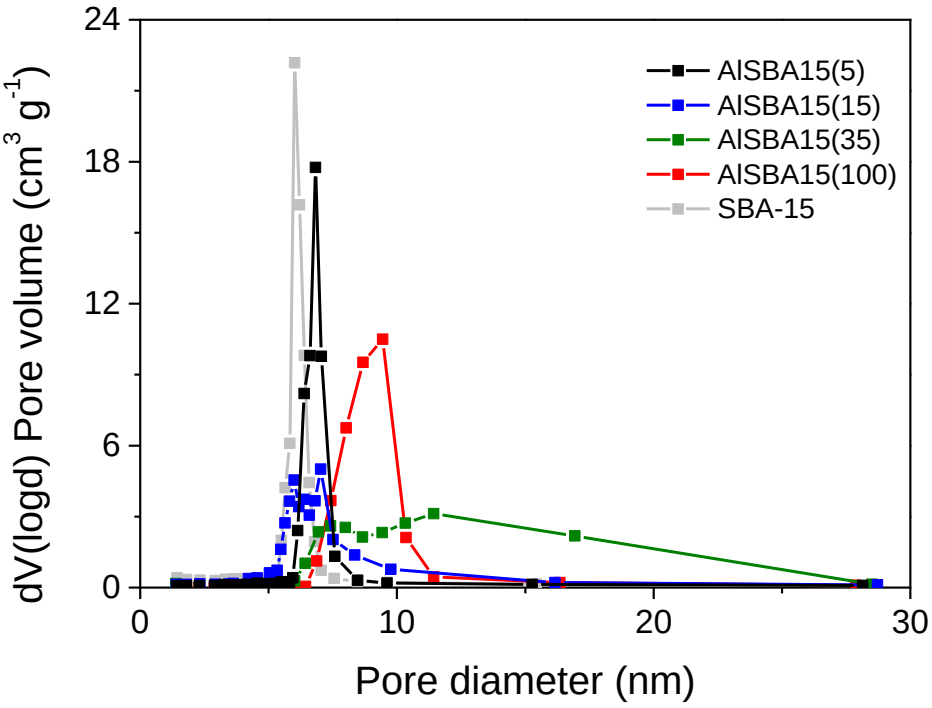

Fig. 22. *Corresponding BJH pore size distribution derived from N_2 porosimetry isotherms.*

N_2 physisorption analysis of the ZSM-5 confirms the microporous nature of crystalline zeolite, with a micropore volume of 0.11 $cm^3 g^{-1}$ and an average pore diameter of 0.9 nm. This is approximately an order of magnitude smaller compared to the Al-SBA-15 materials.

To further elucidate the preservation of the ordered porous structure of the Al-rich SBA-15 material, STEM was performed on both SBA-15 and AlSBA15(5) for comparison between no aluminium incorporation and high levels of aluminium incorporation. **Fig. 23** (A and B) show well-ordered channels within both the representative particle structures; therefore, it can be assumed the ordering is preserved after incorporation of aluminium. It could be envisaged the reactant molecules could enter at either end of the pore channels and travel the internal length of the mesopore whilst being exposed to the reactive acid sites. In addition to STEM, EDS analysis was also carried out on the highest Al/Si ratio catalyst, AlSBA15(5), to map the distribution of Al across the catalyst particle. **Fig. 24** shows EDS maps of the main elements (Si, O, and Al), which confirmed the high dispersion of Al, Si and O atoms.

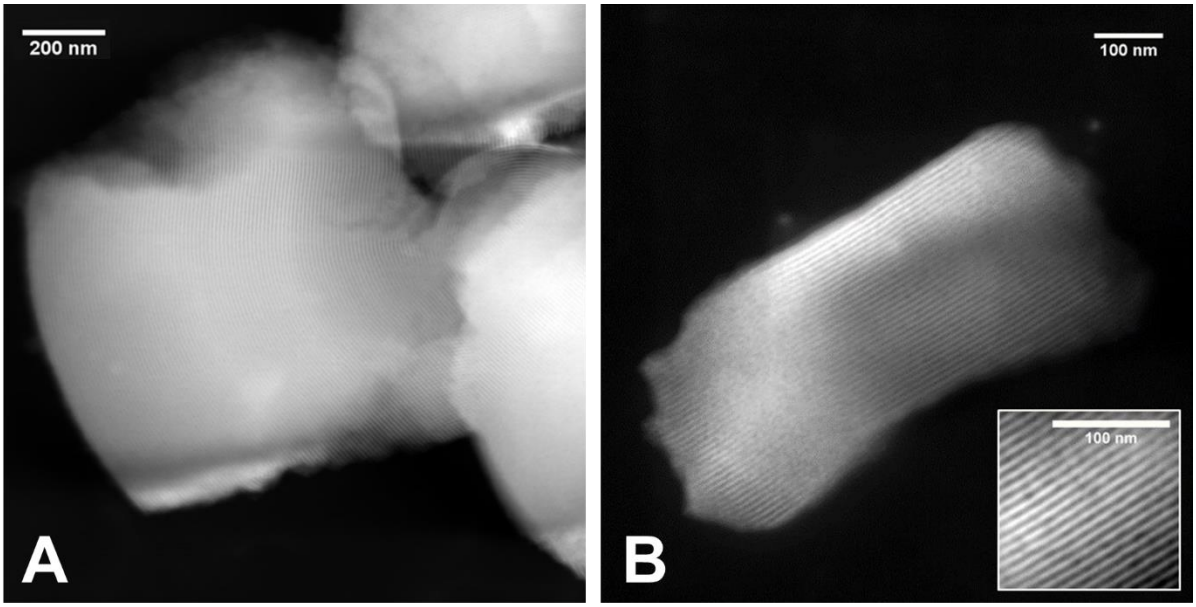

Fig. 23. *High-resolution STEM image of (A) SBA-15 and (B) AlSBA15(5). (B Inset) increased magnification.*

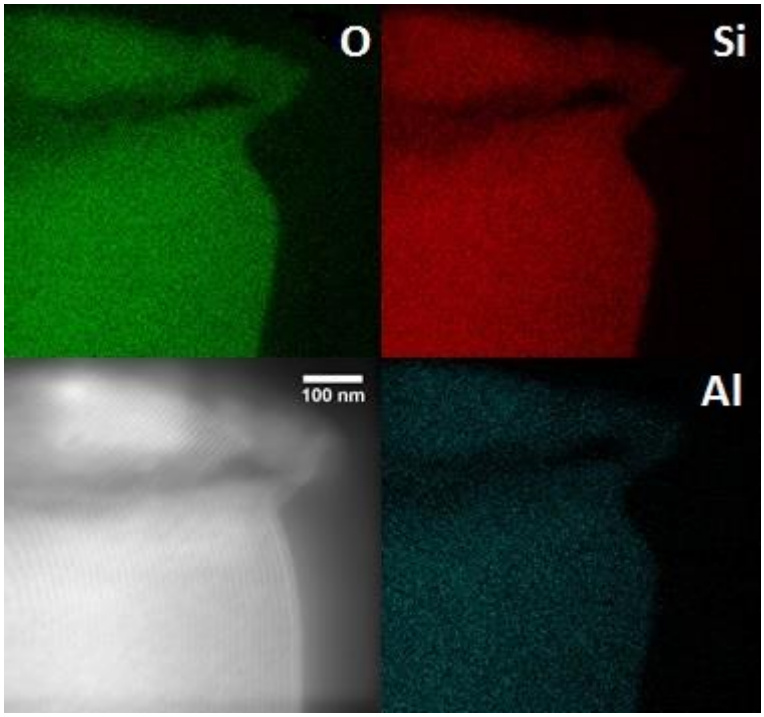

Fig. 24. *Energy Dispersive X-Ray Spectroscopy (EDS) analysis of the highest Al/Si catalyst, AlSBA15(5).*

The acidic properties of all materials were investigated via thermogravimetric temperature programmed desorption of n-propylamine. Propylamine is a weak base that reacts with accessible acid sites to form propene and ammonia under thermal conditions. The desorption temperature of reactively-formed propene is inversely proportional to the strength of the acid site. **Fig. 25A** shows that increasing the Al content of the material barely changes the propene desorption temperature of

435 °C, suggesting that all the Al-SBA-15 materials possess acid sites of similar strength. In contrast to the Al-SBA-15s, ZSM-5 exhibits two types of acid sites; strong acid sites (major peak centred at 407 °C) and weak acid sites (small peak centred at 473 °C). The acid site loadings were calculated and are presented in **Table 7**. The results show that the acid site loading closely mirrors the aluminium content of the catalysts. The aluminium species withdraw electrons from the framework hydroxyl groups, therefore increasing the dissociation capability of the proton [298]. A small number of acid sites were identified in SBA-15 which could be attributed to surface silanol groups. AlSBA15(5), with the highest aluminium incorporation, displays the highest total acidity. The total acidity appears to be nonlinearly proportional to bulk aluminium incorporation where it reaches a plateau, evident in **Fig. 25 B**. The reason for a plateau is unknown, however, as more aluminium is incorporated into the catalysts' structures, the number and density of acid sites in closer proximity are increased. This may lead to oversaturation of acid sites on the surface and causes the strength of all adjacent acid sites to be reduced due to proton crowding [299].

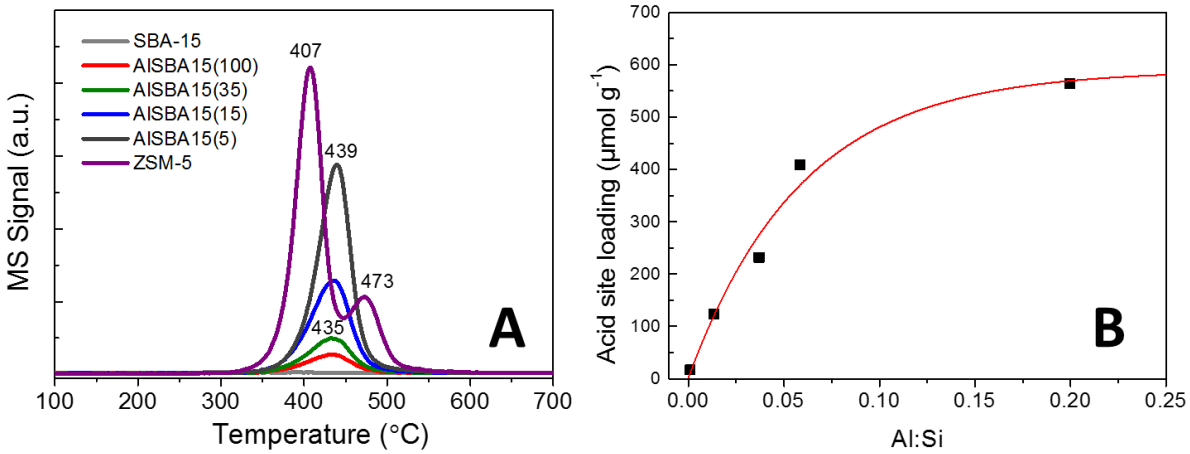

Fig. 25. *(A) Thermogravimetric temperature programmed desorption of reactively formed propene from n-propylamine decomposition over Al-SBA-15 and ZSM-5 catalysts. (B) Relationship between the acid site loading and incorporation of Al into SBA-15.*

The adsorption of pyridine was studied using FTIR spectroscopy to assess the nature of the acid sites of the materials. The DRIFT spectra of the Al-SBA-15 catalysts and ZSM-5 zeolite, following chemisorption of pyridine, are shown in **Fig. 26.** Absorption features at 1445 and 1595 cm^{-1} are assigned to pyridine interacting by electron donation to Lewis acid sites, due to partially coordinated Al atoms in the extra-framework aluminium and silanol groups. This band is present in all samples and decreases in intensity with an increase in aluminium along the series of Al-SBA-15. An absorption band at 1545 cm^{-1} is more visible in AlSBA15(15), AlSBA15(5) and ZSM-5, which is commonly assigned to pyridinium ions (PyH^+) coordinated to a Brønsted acid site. The absorption band at 1490 cm^{-1} is assigned to pyridine adsorbed over Brønsted and Lewis sites [300]. The ratio of Brønsted to Lewis

acidity present in the materials was calculated by integration of the 1445 and 1545 cm^{-1} absorption bands and are presented in **Table 7**, along with the individual contributions. It is apparent that the Brønsted/Lewis ratio is positively correlated with the incorporation of aluminium, though a very small quantity of Brønsted and Lewis sites are present in the Al-free SBA-15. It is worth noting that 27Al NMR combined with acid site analysis on similar materials suggests that the Brønsted acid sites are generated by framework Al. Extra-framework Al typically led to Lewis acid sites [219].

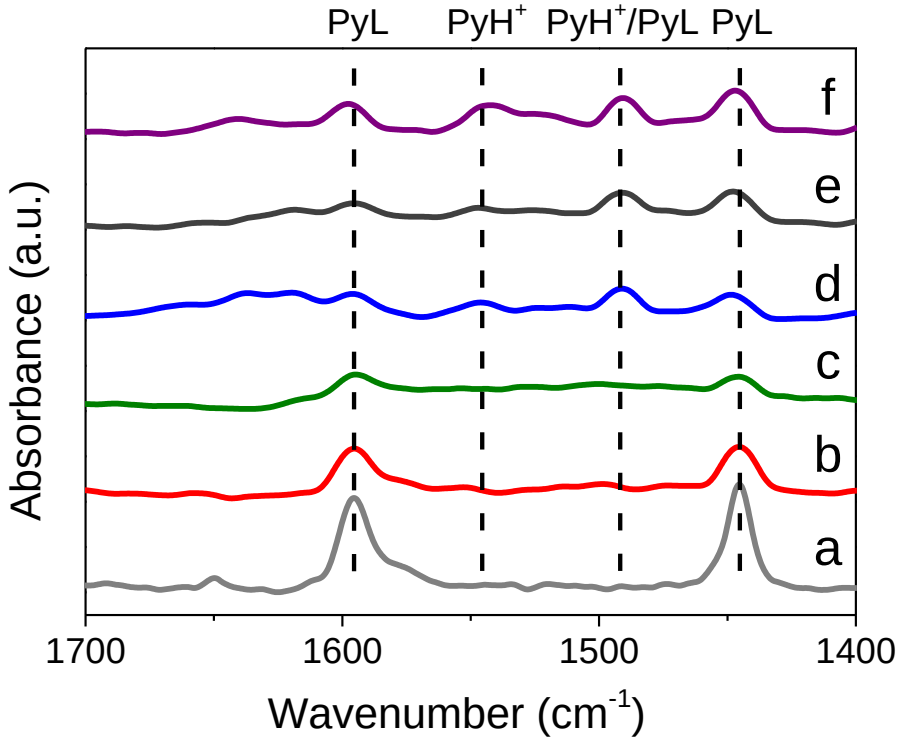

Fig. 26. *DRIFT spectra of chemisorbed pyridine over Al-SBA-15 and ZSM-5 catalysts: (a) SBA-15, (b) AlSBA15(100), (c) AlSBA15(35), (d) AlSBA15(15), (e) AlSBA15(5) and (f) ZSM-5.*

TPD of ammonia is widely used for the characterisation of acid sites. However, due to the high basicity of ammonia, weak sites that may not contribute to the acidity of the catalyst are capable of being titrated. This can lead to an overestimation of the number of acid sites by this method. In addition, the small molecular size of ammonia enables the accessibility of all pores of the solid which may be impenetrable by larger molecules commonly found in cracking reactions [101]. In contrast, propylamine, used in this study, gives a more realistic insight as it only titrates strong and medium strength acid sites. Furthermore, due to its larger size, it is only able to access pore sizes in the range required for catalytic cracking reactions.

In summary, the quantity of Brønsted acid sites generated in the Al-SBA-15 materials synthesised in this work is comparable with previously reported values where the “pH adjustment” method was

employed. These observations highlight that the “pH adjustment” method allows precise control over the incorporation of Al into the silica framework. Therefore, materials derived from this method afford acidic properties comparable to zeolites. It is worth noting, that the “pH adjustment” method is highly reproducible offering consistent results across studies [219,259,301].

3.2.2. Catalyst Testing

Thermogravimetric analysis

Thermogravimetric analysis was carried out to compare the activity of Al-SBA-15 catalysts with different Si/Al ratio on cracking of LDPE. Additionally, the protonic form of ZSM-5 (Alsi-Penta SM-27) with a nominal Si/Al of 12 was employed as a reference material. The results of the thermal and catalytic degradation of LDPE derived from thermogravimetric analysis are plotted in **Fig. 27.**

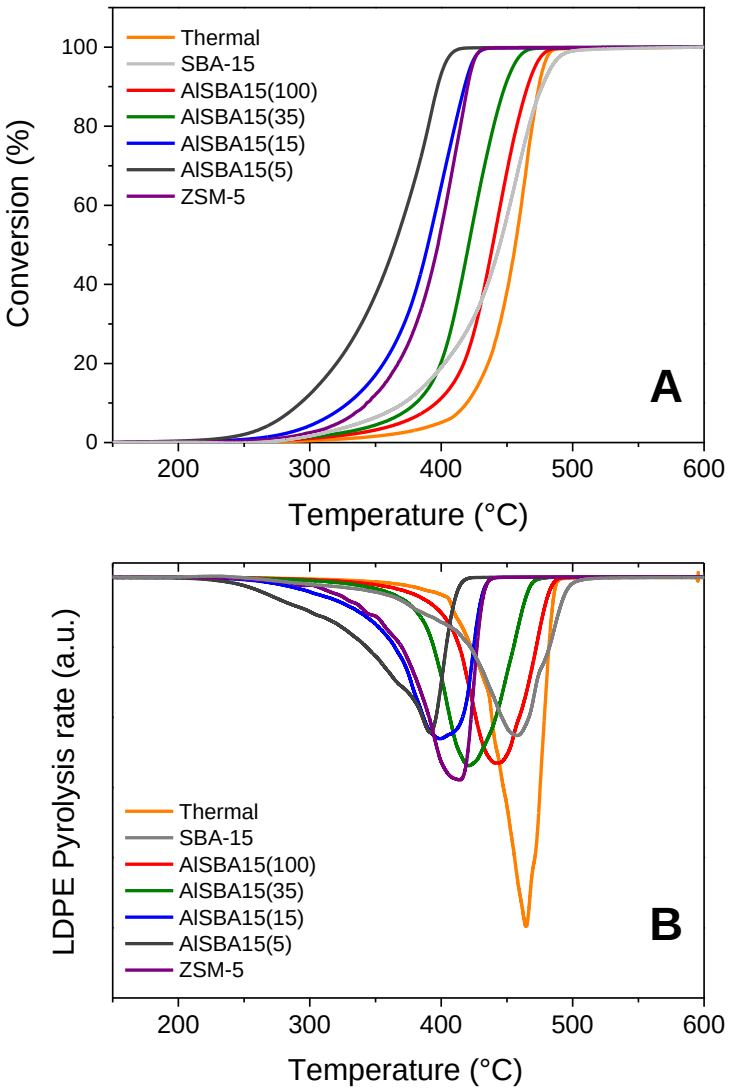

Fig. 27. *(A) Conversion plot for the thermal and catalytic degradation of LDPE measured by thermogravimetric analysis. (B) Derivative thermogravimetric analysis plot of the thermal and catalytic degradation of LDPE.*

Thermal degradation of pure LDPE polymer commenced around 400 °C, reaching a maximum reaction rate at 464 °C. In the presence of solid acid catalysts, the temperature of maximum degradation rate is shifted much lower due to the catalytic cracking over Brønsted acid sites [252]. The presence of pure SBA-15 causes a decrease of 7 °C to the temperature of maximum degradation rate suggesting that even with a low quantity of acid sites a noticeable catalytic effect is observed. Furthermore, **Fig. 27** shows that LDPE degradation temperature decreases continuously with increasing Al loading of the catalyst. This can be attributed to the increasing Brønsted/Lewis acid site ratio. The lowest temperature of LDPE degradation was achieved with the AlSBA15(5), with a maximum reaction rate at around 390 °C. **Fig. 28** shows the temperature at which point the LDPE was degraded (temperature of conversions) at 5, 50 and 80 %, in relation to the Brønsted/Lewis ratio of the Al-SBA-15 catalysts. There

is a clear linear correlation between the lower temperatures of LDPE degradation and increasing Brønsted acidity. There is a greater deviation of T5 values than at higher conversion temperatures (T50 and T80) as can be seen by the error bars in **Fig. 28**. In addition, it is evident more error occurs at lower Brønsted/Lewis ratios. This could be explained by thermal lag caused by inefficient heat transfer of the high surface area materials, as the surface area is inversely proportional to the Brønsted/Lewis ratios in the Al-SBA-15 materials(**Table 7**).

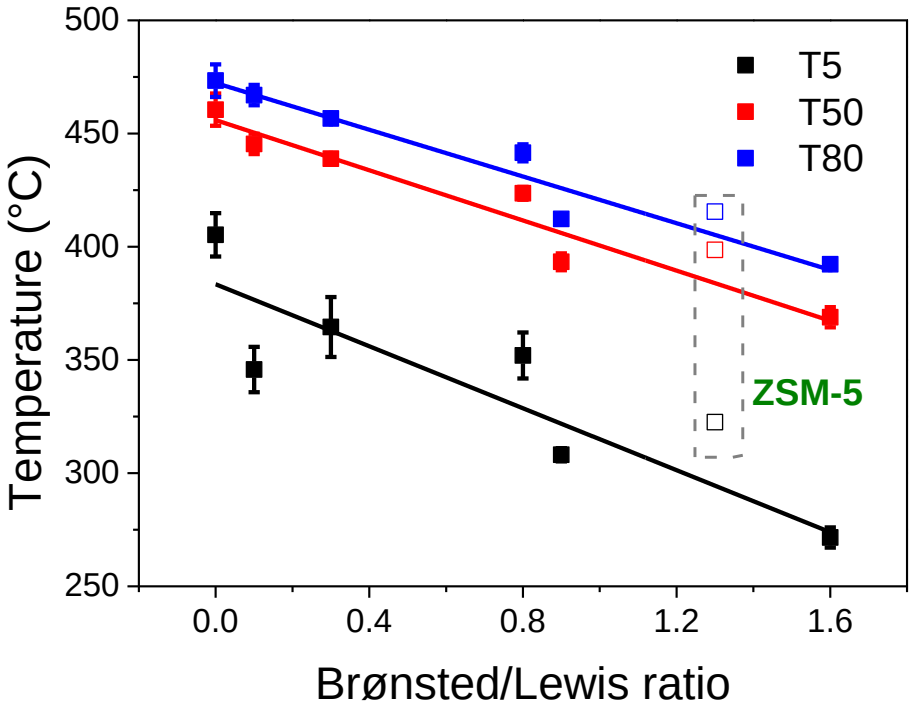

Fig. 28. *Temperatures at conversions of 5, 50 and 80 % of LDPE pyrolysis in relation to Brønsted to Lewis ratio of Al-SBA-15 catalysts and ZSM-5 (hollow squares).*

Since the Brønsted/Lewis ratio for the Al-SBA-15 catalysts increases with the incorporation of aluminium, a similar correlation can be seen for the number of acid sites. Nevertheless, it is difficult to distinguish the individual contribution of the two types of acid sites. However, based on the acidity analysis, it can be observed that the two Al-rich catalysts (AlSBA15(5) and AlSBA15(15)) possess very similar quantities of Lewis acid sites (**Table 7**) and similar acid strength (**Fig. 25** A). Despite these similarities, the activity of AlSBA15(5) is considerably greater than that of AlSBA15(15) (**Fig. 27** and **Table 8**). Hence, the greater activity of AlSBA15(5) can be attributed to the higher Brønsted acid site loading. This hypothesis is supported by the literature, based on theoretical modelling performed by Li et al. [302], it was shown that Lewis acid catalysed cracking has a higher energy barrier compared to Brønsted acid cracking. Therefore, it can be concluded that both types of acid sites may contribute to the catalytic cracking of LDPE, however, the contribution of Brønsted acid sites are more significant.

***Table 8**. Average temperature of conversions at 5, 50 and 80 % conversion for the thermal and catalytic degradation of LDPE.*

Sample		Average T_{Conv} (°C)		RSD (%)
LDPE	T5	405.3	±	2.4
	T50	460.6	±	1.5
	T80	473.4	±	1.5
SBA-15	T5	345.8	±	2.9
	T50	445.4	±	1.0
	T80	467.0	±	1.0
Al-SBA-15(100)	T5	364.5	±	3.6
	T50	438.9	±	0.1
	T80	456.6	±	0.5
Al-SBA-15(35)	T5	352.0	±	2.9
	T50	423.6	±	0.7
	T80	441.5	±	0.9
Al-SBA-15(15)	T5	308.1	±	0.9
	T50	393.3	±	1.0
	T80	412.3	±	0.5
Al-SBA-15(5)	T5	271.6	±	1.9
	T50	368.9	±	1.2
	T80	392.2	±	0.4
ZSM-5	T5	322.5	±	0.1
	T50	398.6	±	0.4
	T80	415.5	±	0.3

An assessment of catalytic activity can be determined by a simple measurement of the temperature at which maximum cracking is observed (see **Fig. 27** B), using thermogravimetric analysis. The catalyst lowers the activation energy of the cracking reaction; therefore, catalysts with higher activity perform maximum cracking at lower temperatures. As expected, ZSM-5 was highly active for the cracking reaction due to its high acid site loading (672 $\mu mol\ g^{-1}$) and high Brønsted/Lewis ratio. However, ZSM-5 performed the degradation at a slightly higher temperature than the AlSBA15(15) catalyst, with a comparative Si/Al ratio, much higher than the AlSBA15(5) catalyst. This comparatively lower activity can be associated with the microporous nature of the ZSM-5 structure, which restricts the diffusion of sterically challenging molecules, such as high molecular weight polyolefins, into its internal acid sites. This highlights the importance of evaluating a combination of increased Brønsted acidity and acid site accessibility for cracking sterically challenging molecules.

Previous investigations by Aguado et al. [245] into the catalytic degradation of LDPE, by a variety of catalysts, reported a maximum degradation temperature of 396 °C using nanometer crystal-sized ZSM-5. A more recent investigation by Ding et al. [124], on the synthesis of mesoporous ZSM-5, reported a maximum degradation temperature of 348 °C, much lower than that of conventional ZSM-5. In this work, the lowest temperature of LDPE degradation was achieved with the AlSBA15(5), with a maximum degradation rate at around 390 °C. Therefore, it is clear the accessibility of the reactant molecules has a profound effect on the catalytic activity of the cracking of polyolefins. However, from a commercial

perspective, the selectivity of the catalyst may be of more value, allowing the conversion to be tailored towards more desirable products such as monoaromatic hydrocarbons for use as platform chemicals, or to a desired carbon range as high octane fuels.

Py-GC/MS analysis

Pyrolysis gas chromatography/mass spectroscopy (Py-GC/MS) was employed to investigate the product distribution of the catalysts, i.e. the proportion of desired products compared to total products. The product distribution is highly dependent on pyrolysis temperature, heating rate and also on the occurrence of secondary reactions. With the introduction of a volatile trap (**Fig. 14**), secondary reactions are minimised due to the short residence time of the generated vapours. While this work was only able to consider volatile products with molecular weights below 300 g mol^{-1}, Py-GC/MS presents a simple analytical technique for the qualitative assessment of catalyst selectivity in LDPE catalytic pyrolysis. It is well known that the catalytic cracking of hydrocarbons is initiated through either the generation of a carbonium ion or a carbenium ion by a Brønsted or Lewis acid site, respectively, as shown in **Fig. 29** [252].

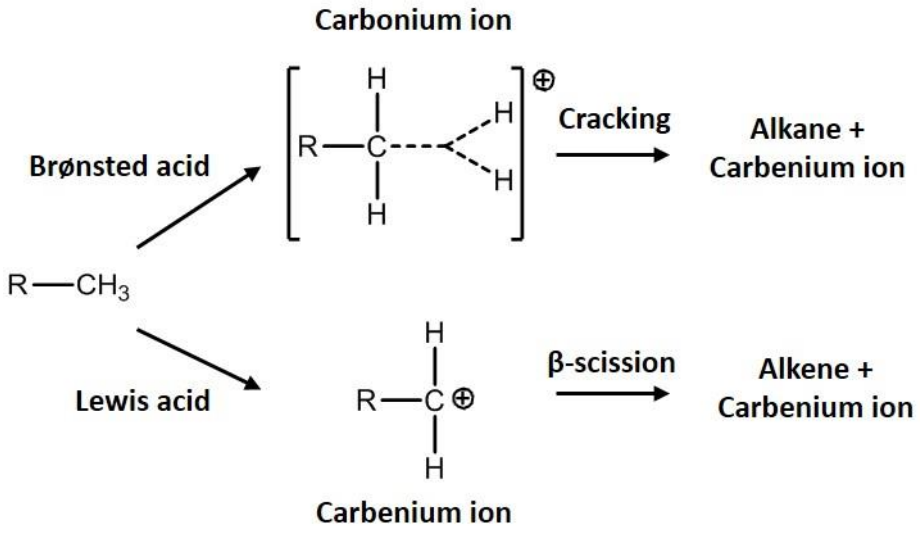

Fig. 29. Mechanism of acid catalysed cracking of hydrocarbons [252].

The Py-GC/MS chromatograms for the non-catalytic and catalytic experiments are shown in Appendix A, **Fig. A 1**. The peaks were identified using mass spectrometry and were grouped by the carbon chain length of the molecule. **Fig. 30** shows the product distribution arranged by the carbon number (C_n) of products obtained, corresponding to the peak area % in the chromatogram, for the thermal and catalytic pyrolysis of LDPE studied by Py-GC/MS. The product distribution of thermal LDPE pyrolysis

yields a wide range of products, spread between 4-20 C_n, mainly forming C_7 products such as heptane and 1-heptene, with ca. 14 % selectivity. These can chemicals can find use as industrial solvents or fuel lubricants. In the catalytic pyrolysis of LDPE, SBA-15 showed the least activity, with a selectivity similar to thermal pyrolysis, consistent with the thermogravimetric data. Comparing the product distribution of LDPE cracking over SBA-15 with simple thermal cracking reveals that the selectivity to small compounds with $1 < C_n < 10$ slightly increased while lowering the selectivity of $C_n > 10$ products.

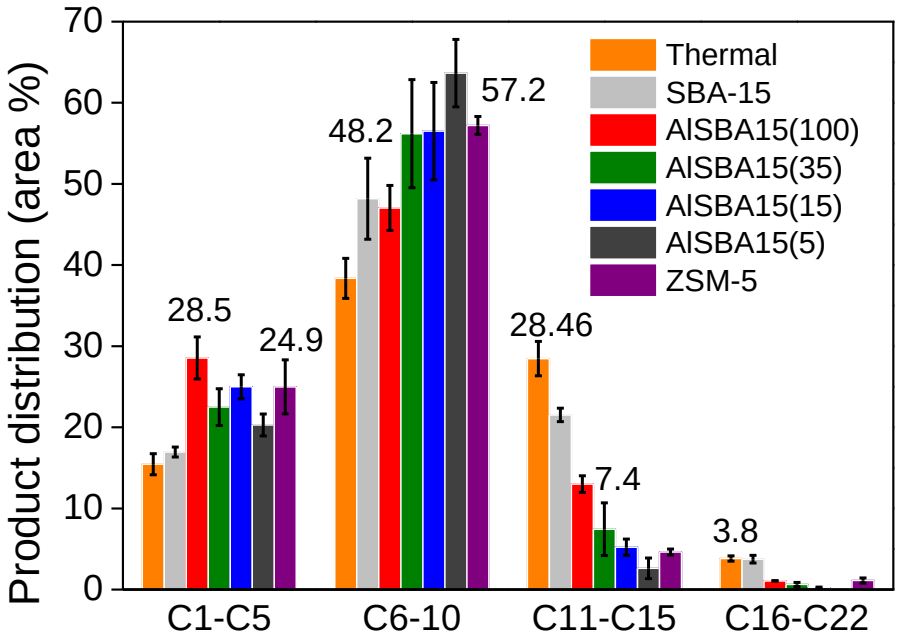

Fig. 30. *The relative abundance of products of the thermal and catalytic cracking of LDPE analysed at 700 °C with a rate of 10 °C/ms and a hold time of 10 s by Py-GC/MS, grouped by number of carbon atoms.*

Critically, the product distribution from the catalytic cracking of LDPE appears to depend strongly on the Al content of the SBA-15 materials. In other words, by tuning the Al content of SBA-15 the selectivity of the LPDE catalytic cracking can be altered, directing the reaction towards a different range of products. The results in **Fig. 30** show that with an increased aluminium content of the Al-SBA-15 catalysts, a higher degree of cracking is achieved. More specifically, increasing the Al content of the materials lead to a significant reduction in the selectivity of $C_n > 10$ products in favour of forming $C_n < 10$ compounds in the range of gasoline (C_6-C_{12}), as shown in **Fig. 30**. This trend can be attributed to the increase in acidity of the catalysts with the addition of higher quantities of aluminium, therefore enhancing the efficiency of cracking of the polymer backbone chain.

ZSM-5 also resulted in a high level of cracking, reducing the number of products with $C_{11\text{-}22}$, and increasing the number of lower C_n products, particularly between $C_{7\text{-}8}$. Interestingly, ZSM-5 produced

more products in the region of C_{16-22} than even the AlSBA15(100) catalyst, with the lowest incorporation of Al of the series. Again, this could be due to the microporous nature of the material and thus the diffusional hindrances of the long-chained polymers in comparison to the mesoporous SBA-15 type materials.

To investigate the differences in selectivity further, the relative abundance of aromatic products was calculated and is presented in **Fig. 31** A. For the thermal, uncatalysed, pyrolysis of LDPE at 700 °C, the relative abundance of aromatic products by peak area % was low at approximately 4 %. Using SBA-15 as a catalyst, the peak area of aromatic products more than doubled, suggesting that either the slight acidity or shape of the catalyst was favourable in the production of aromatics. With the incorporation of Al into SBA-15, the peak area of aromatic products is significantly increased, reaching a peak at AlSBA15(35). It should be noted that there was a high degree of error in the area of aromatic products for AlSBA15(35). At greater Al incorporations (Si/Al= > 35), the peak area of aromatic products is gradually reduced. The aromatic selectivity is plotted against the total acidity of the Al-SBA-15 catalyst in **Fig. 31** B. It is evident that the acidity has a positive effect on the production of aromatics in the catalytic pyrolysis of LDPE. However, there is a maxima of this trend, after such, the selectivity to aromatic products is reduced. This can be explained by increased cracking at high acidity, as the LDPE pyrolysis intermediates are cracked to lower molecular weight hydrocarbons.

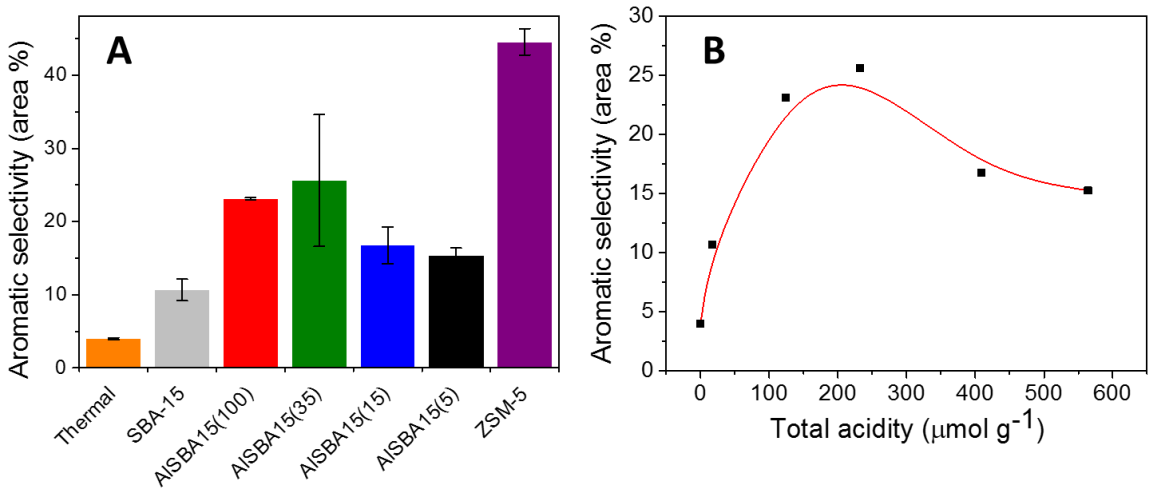

Fig. 31. *(A) The relative abundance of aromatic products of the thermal and catalytic cracking of LDPE analysed at 700 °C with a rate of 10 °C/ms and a hold time of 10 s by Py-GC/MS. (B) the relative abundance of aromatic products compared to total acidity of the catalyst.*

In comparison, ZSM-5 was highly selective towards the production of aromatic products, producing ca. 45 % of the total peak area of aromatics, although the true quantity is not known due to the limitations of the experimental set-up. Nevertheless, t the high aromatic peak area is not surprising, as ZSM-5 is well known to be highly selective towards the production of aromatics due to its shape-selective ability

from its complementary pore size and structure, as referenced in the literature review in the general introduction chapter, Chapter 1 [150,286]. These results suggest that the larger pores of the Al-SBA-15 catalysts are too large to selectively produce aromatic products. The absence of a geometric restriction in the Al-SBA-15 catalysts allows cracking to continue, resulting in lower molecular weight products compared to ZSM-5.

3.3. Conclusion

To conclude this chapter, a series of high acidity mesoporous Al-SBA-15 catalysts were synthesised and characterised by XRD, XPS, ICP-OES, propylamine-TPD, pyridine-FTIR and STEM. The results of the characterisation confirmed the long-range structural ordering was unaffected as aluminium was incorporated into SBA-15 at increasing Al/Si ratios. However, the increasing proportion of aluminium was inversely proportional to the resulting surface area in the Al-SBA-15 catalysts. Nevertheless, the incorporation of aluminium into the SBA-15 framework was highly successful in the creation of acid sites. Lewis acid sites were mainly formed at low aluminium loadings, whereas Brønsted acid sites were increasingly formed as the aluminium loading was increased. Interestingly, the N_2 physisorption data and derived pore size distribution calculations showed that the uniformity of the Al-SBA-15 catalysts increased at high aluminium loadings.

The Al-SBA-15 catalysts were applied in the catalytic pyrolysis of LDPE, to provide a preliminary assessment of their catalytic activity and selectivity of a simple polymer, compared to biomass waste. The zeolite ZSM-5 was used as an industrial reference catalyst in these experiments. It was shown by TGA that the activity of the Al-SBA-15 for the catalytic pyrolysis of LDPE was strongly correlated to the aluminium incorporation, and hence, the acidity of the catalyst. The Al-SBA-15 catalysts significantly decreased the temperature at which the LDPE was catalytically cracked compared to the thermal cracking. Furthermore, AlSBA15(5), with the highest Al/Si ratio, but similar total acidity to ZSM-5, catalytically cracked LDPE at a lower temperature than ZSM-5. Therefore, it can be concluded that the increase pore sizes of the Al-SBA-15 catalysts have a positive effect on the cracking of large polymers, and the diffusion is otherwise limited in ZSM-5 due to its smaller pore sizes.

The products of the catalytic fast pyrolysis of LDPE at 700 °C using the series of Al-SBA-15 catalysts and ZSM-5 were identified using Py-GC/MS. The product distribution depended strongly on the Al content of the SBA-15 materials. Therefore, by tuning the Al content of SBA-15 materials the selectivity of the LPDE catalytic cracking can be altered, directing the reaction towards a different range of products. It was shown that ZSM-5 was highly selective towards the production of aromatic products, producing ca. 45 % of the total peak area of aromatics. On the other hand, the aromatic production of Al-SBA-15 from LDPE was much lower and was correlated to aluminium incorporation of the catalysts.

These results have real industrial relevance towards a possibly economic attractive route from undesirable waste plastics to value-added chemicals such as aromatics and liquid hydrocarbon fuels through catalytic fast pyrolysis. This chapter has highlighted how tuneable mesoporous high acidity catalysts such as Al-SBA-15 are highly selective towards organic hydrocarbons in the gasoline range.

Catalytic Fast Pyrolysis of the Main Lignocellulosic Biomass Components

4. Chapter 4 - Catalytic Fast Pyrolysis of the Main Lignocellulosic Biomass Components

4.1. Introduction

Biomass is an extremely complex organic-inorganic solid product, with several definitions and encompasses a wide range of materials derived from natural sources. IUPAC defines biomass as a "*material produced by the growth of microorganisms, plants and animals*" [303]. A more comprehensive definition was provided by Vassilev et al. [62] and describes biomass as a material "*generated by natural processes, originating from land or water-based vegetation, including technogenic products derived from processes of the said natural components*." In addition, biomass was defined by the EU commission Renewable Energy Directive, 2009 [304], as being: "the biodegradable fraction of products, waste and residues from biological origin from agriculture (including vegetal and animal substances), forestry and related industries including fisheries and aquaculture, as well as the biodegradable fraction of industrial and municipal waste."

In the previous chapter, the catalytic ability of synthesised mesoporous Al-SBA-15 catalysts was investigated for the catalytic pyrolysis of a simple synthetic organic polymer, low density polyethylene (LDPE). However, one of the main objectives of this thesis is to use the synthesised mesoporous catalysts for the catalytic fast pyrolysis of biomass. In order to develop an understanding of the effect of the catalyst on the products of catalytic pyrolysis of biomass, it is first necessary to gain an insight into the fundamental reactions of the pyrolysis of each biomass component. In addition, it is important to consider the intermediate pyrolysis products and how these products interact with the catalyst. As discussed in the General Introduction chapter, Section 1.2, biomass is composed of mainly three main organic component polymers: cellulose, lignin and hemicellulose, including other extractives and inorganic elements. The cellulose, hemicellulose and lignin composition of various biomass waste feedstocks are presented in **Table 9**. As shown in the table, the proportion of each main biomass component varies greatly depending on the biomass waste.

Table 9. *The proportions of cellulose, hemicellulose and lignin of various feedstocks.*

Feedstock	Cellulose (%)	Hemicellulose (%)	Lignin (%)
Wood	35–50	20–30	25–30
Wheat straw	33–40	20–25	15–20
Switch grass	30–50	10–40	5–20
Sugarcane bagasse	19–24	32–48	23–32
Miscanthus	24	44	17
Corn stover	28	35	16–21
Hazelnut shell	28.8	30.4	42.9
Olive husk	24	23.6	48.4
Corncob	50.5	31	15
Tea waste	30.2	19.9	40
Walnut shell	25.6	22.7	52.3
Almond shell	50.7	28.9	20.4
Sunflower shell	48.4	34.6	17
Nut shell	25–30	25–30	30–40
Paper	85–99	0	0–15
Rice straw	32.1	24	18
Stored refuse	60	20	20
Leaves	15–20	80–85	0
Cotton seed hairs	80–95	5–20	0

Kinetic modelling of the pyrolysis of biomass components carried out by Orfão, Antunes and Figueriredo [305], evidenced that the pyrolytic behaviour of biomass materials can be predicted by the proportion of the three main components it contained. Therefore, knowledge of the pyrolysis characteristics of the three main components is the basis and essentially important for a better understanding of biomass thermal chemical and catalytic conversion. It would also be possible to predict the yield and potential composition of any feedstock based on the known proportion of the biomass components. For this to be possible, without the need for enormous computing power, the pyrolysis behaviour of each individual component must be independent of each other. If there are synergistic effects between components, then the prediction of the behaviour of the feedstock would be much more complex [306]. In this respect, the first section of this chapter has been devoted to a brief literature survey of the fundamental pyrolysis reactions of the three individual components.

4.2. Literature survey of the decomposition products of biomass components

Several groups in the literature have studied the pyrolysis of individual lignocellulosic biomass components. Raveendran, Ganesh and Khilar [307] investigated the individual component characteristic of biomass pyrolysis using thermogravimetric analysis (TGA) and a packed-bed pyrolyser. The researchers inferred that there is no detectable interaction among the components during pyrolysis. It was also suggested biomass pyrolysis can be divided into four individual stages: **1**) moisture

evolution; **2**) hemicellulose decomposition; **3**) cellulose decomposition and **4**) lignin decomposition. In contrast, a negligible interaction between the three biomass components when studied using TGA was observed by Yang et al. [308]. More recent research conducted by Wang et al. [309], evidenced strong interactions between cellulose and hemicellulose during pyrolysis using TG-FTIR and GC-MS analysis of the pyrolysis products. Hence, the authors argued that pyrolysis characteristics of biomass cannot be solely predicted through knowledge of the proportion of the main components in the feedstock.

Cellulose is the main component of lignocellulosic biomass and is predominantly located in the cell wall [310]. Details of the chemical structure of cellulose are provided in General Introduction, Section 1.2.1. Cellulose consists of anhydrous repeating glucose monomers bound through beta-1,4 glycosidic bonds. Although the thermal decomposition of cellulose has received extensive attention, the precise reaction pathway is still debated. It has been proposed by many researchers that on exposure to thermal energy cellulose is activated to form "active cellulose" [311]. This is a transition state where reducing ends of cellulose are formed at relatively low temperatures (260 °C). The formation of reducing ends catalyses the thermal decomposition of cellulose to volatiles [312].

The depolymerisation of cellulose begins between 100-150 °C. Investigations by Lin et al. [311] suggested that cellulose is initially decomposed to form oligosaccharides with lower molecular weight units, until the complete chain decomposes. The primary decomposition product of cellulose pyrolysis is levoglucosan (1,6-anhydro-β-D-glucopyranose, LGA) and is formed in high yields. Reported yields of levoglucosan in the literature derived from cellulose pyrolysis are inconsistent and are dependent on several parameters such as reactor configuration, operating conditions and selected feedstock [313]. The highest yield of levoglucosan from cellulose pyrolysis in the literature was reported by Dobele et al. [314] using a CDS pyroprobe reactor and is 79.3 carbon %. According to Lin et al. [311], levoglucosan is subsequently hydrated or isomerised to form other anhydro-monosaccharides such as 1,4:3,6-dianhydro-β-D-glucopyranose (DGP), levoglucosenone (LGO) and 1,6-anhydro-β-D-glucofuranose (AGF) which are shown in **Fig. 32**. The monosaccharides are decomposed to form furanoses and a variety of fragmentation species such as glycolaldehyde and glyceraldehyde, through dehydration, decarbonylation, decarboxylation and retro/aldol condensation reactions.

Fig. 32. *Cellulose decomposition pathway proposed by Lin et al.* [311].

Paine et al. [315] used isotopic labelling with ^{13}C to investigate the production of furans from the flash pyrolysis of D-glucose. They concluded that there are multiple competing mechanisms of furan formation from D-glucose, the most dominant was the cyclic Grob fragmentation reaction. It was hypothesised that methyl furans were formed by mechanisms that involve hydrogenation. Therefore, the formation of various furans in pyrolysis is likely to be very complex. Furthermore, CO, CO_2 and H_2O

are often formed as the by-products of these reactions. Several competing pathways exist to convert the pyrolysis intermediates to char or light gases.

The second core biomass component, hemicellulose, is a complex polysaccharide which has no well-defined structure. Xylan is the most abundant type of hemicellulose (10-30 wt.%) and generally exists in woody biomass [316]. Due to the lack of crystallinity of hemicellulose, its thermal deconstruction is much simpler compared to cellulose. Patwardhan, Brown and Shanks [317] classified the products of hemicellulose pyrolysis into three categories: **1**) low molecular weight compounds such as CO, CO_2, formic acid, acetaldehyde and acetic acid; **2**) furan or pyran ring derivatives such as 2-methyl furan, 2-furaldehyde and dianhydro xyloses; and **3**) anhydrosugars such as anhhydro xylopyranose. The primary pyrolysis products of hemicellulose are shown in **Fig. 33.** The char yield from hemicellulose pyrolysis (10.7 wt.%) has been reported to be higher than for cellulose (5 wt.%), however, there are inconsistencies in char yields reported in the literature. Yang et al. [318] reported char yields from hemicellulose to be 22 wt. %, whereas Shafizadeh et al. [319] reported char yields of approximately 31 wt. %. Though these inconsistencies may be caused by differences in heating rates and differences in the purity and form of hemicellulose model compound.

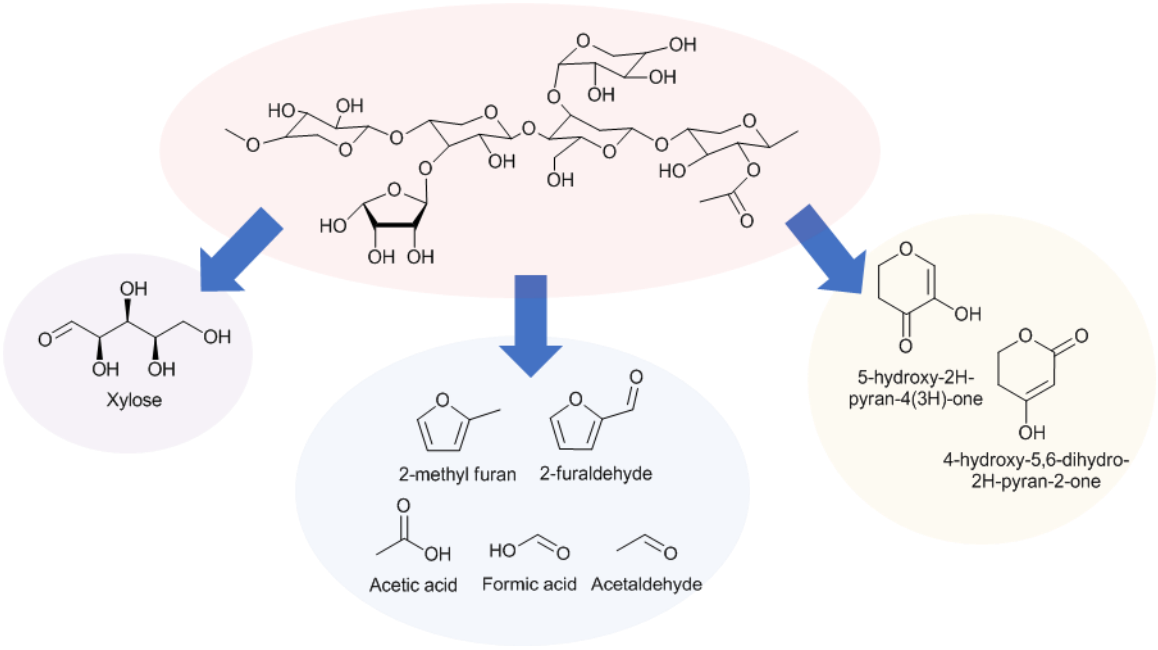

Fig. 33. *Primary pyrolysis products of hemicellulose.*

Lignin is the third main component of biomass waste and like hemicellulose, lignin is amorphous and as such it has no well-defined structure. Lignin generally constitutes three main phenylpropane units; *p*-coumaryl, coniferyl alcohol and sinapyl alcohol, bonded through an array of hydroxy and methoxy bonds. An example of a possible structure of lignin is shown in **Fig. 34.** The bonding and polymerisation of these building blocks create units of *p*-hydroxy-phenyl (**H**), guaiacyl (4-hydroxy-3-methoxyphenyl)

(**G**) and syringyl (3,5-dimethoxy-4-hydroxyphenyl) (**S**) [71]. The proportion of different linkages between the phenylpropane units varies between wood and biomass type [320]. Lignin serves as a plant's defence to microbial and chemical attacks and there is the most recalcitrant to decomposition. Hence, there is a frequently used statement concerning lignin in the scientific community: "You can make anything you want out of lignin – except money" [321]. Nevertheless, the thermal decomposition of lignin is relatively effective and was studied and reviewed in detail by Kawamoto [322].

Fig. 34. *Possible lignin structure with p-hydroxyphenyl (H), guiacyl (G) and syringyl (S) units highlighted. Structure reproduced from reference* [323].

The thermal decomposition of lignin commences around 200 °C with dehydration, followed by the breakdown of the β-O-4 linkages [136]. During the primary pyrolysis stage (200-400 °C), aromatic products are released and are predominantly composed of substituted guaiacols (2-methoxyphenols) from G-lignin, and substituted syringols (2,6-dimethoxyphenols) from S-lignin. In addition, various

saturated and unsaturated alkyl side chain groups are also produced. After 400 °C, secondary pyrolysis reactions take place and produce catechols (2-hydroxyphenols), pyrogallols, xylenols, *o*-cresols (2-methoxyphenols) and other phenolics. At higher temperatures, the number of cracking reactions is increased resulting in an increase in the yield of monomers. Phenols and *o*-cresols are relatively stable at increased temperatures, hence they will be observed along with PAHs in the products during high-temperature pyrolysis experiments [322]. As can be seen by the types of chemicals obtained from the pyrolysis of lignin in **Fig. 35**, there is an abundance of aromatic-based products. This presents the potential for direct catalytic conversion to valuable aromatic compounds.

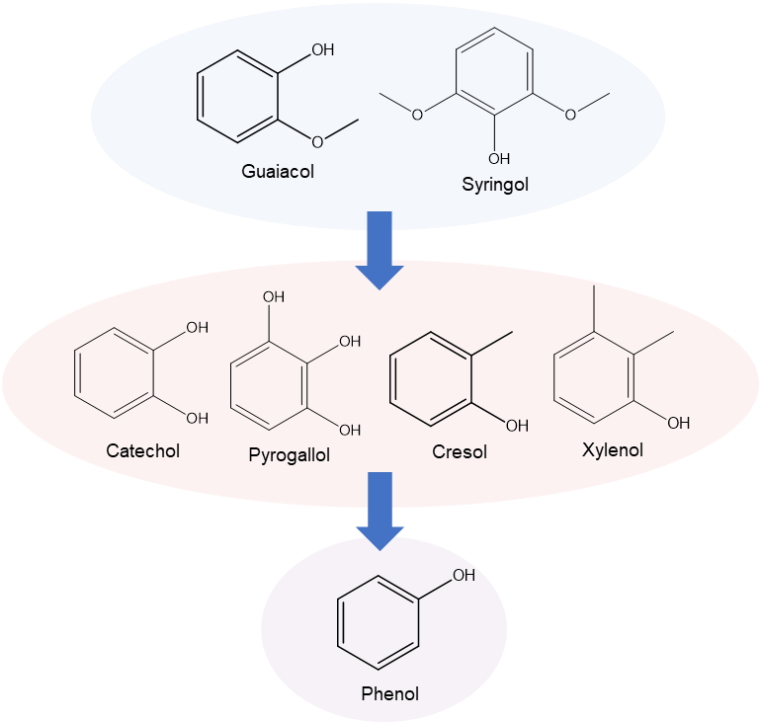

Fig. 35. *Main products obtained from primary and secondary pyrolysis reactions of lignin.*

A literature review on the catalysts used for the catalytic pyrolysis of biomass was presented in the General Introduction, Section 1.5, and therefore will not be covered here. However, to reiterate the main conclusions, zeolites have been extensively used in catalytic fast pyrolysis of biomass and show promise in the production of high-value products such as aromatics. However, the small pore openings prohibit the diffusion of the larger pyrolysis intermediates to the active site for reactions to occur. It has been shown in the previous chapter that Al-SBA-15 type mesoporous catalysts significantly reduced the temperature of LDPE pyrolysis compared to ZSM-5 due to the increased pore size. It was also shown that the activity of Al-SBA-15 catalysts used for LDPE pyrolysis was strongly correlated to the acidity of the catalyst. Based on these findings catalytic pyrolysis will now be carried out on biomass components to increase the complexity of the feedstock to try and observe any differences between these and industrially relevant solid acid catalysts.

4.3. Chapter aims

The aim of this chapter is to gain a comprehensive insight into the effect of the properties of solid acid catalysts on the products obtained from each individual biomass component, cellulose, lignin and hemicellulose. This chapter aims to test a range of solid acid catalysts that each possess sufficiently different physicochemical properties. The properties of which will be compared to a high acidity Al-SBA-15 catalyst synthesised in the previous chapter. Preliminary investigations will be carried out on each of the three biomass components, cellulose, lignin and hemicellulose, using a TGA-DSC. This will provide an understanding of the volatile-releasing behaviours of each of the components. Subsequently, analytical pyrolysis (Py-GC/MS) using a pyroprobe reactor, will be employed to give the products of the uncatalysed pyrolysis of each biomass components. This will be used for comparison of the products obtained in the catalytic pyrolysis experiments. The products identified for the catalytic pyrolysis of each of the biomass components will hopefully highlight and uncover interactions between the properties of the catalyst and the products obtained during the experiment. It should be noted that the very small scale pyroprobe reactor has significant differences to larger scale reactors that would be used for lignin catalytic fast pyrolysis on an industrial scale. Although analytical micro-sized pyrolysis reactors attempt to simulate pyrolysis on the industrial scale, there may be differences in heating rate, vapour residence time and vapour quenching at the industrial scale in fluid bed reactors. This may lead to the occurrence of separate reactions, and hence slightly different product distributions of micro-pyrolysis units compared to the industrial scale. However, the pyroprobe is an effective tool for studying the chemistry of the catalytic pyrolysis reaction. Furthermore, information on the products will suggest whether the mesoporous Al-SBA-15 catalyst is superior to microporous zeolite ZSM-5 or other industrially relevant solid acid catalysts.

4.4. Catalyst selection

A selection of industrially relevant solid acid catalysts with different structural and acidic properties were chosen for comparison to the highest acidity Al-SBA-15 catalyst, synthesised in the previous chapter (Section 3, and employed for the catalytic pyrolysis of each biomass component.

Some of the earliest cracking catalysts employed industrially were acid-activated clays such as bentonite and kaolinite. The natural aluminosilicate clays are activated by treatment with a mineral acid at 90° C in order to leach quantities of aluminium, magnesium and iron cations from the clay structure. This leads to surface area and pore diameter increase and creates a three-dimensional structure [324]. Although there are many modified clay catalysts applied in organic syntheses, among the most common is the montmorillonite K10 synthetic clay [325]. The chemical formula of K10 is $Al_2Si_4(OH)_2nH_2O$. In addition, K10 is safe to handle, environmentally benign and is relatively

inexpensive. As such, K10 is used to catalyse several reactions such as the Biginelli reaction, Dials-Alder reaction, Fischer indole cyclisation, Friedel-Crafts acylation and alkylation, and many more, all under mild conditions while producing high yields and selectivities of the desired chemicals in each reaction [325].

The Methanol-to Olefin (MtO) process has proven to be one of the most successful non-petrochemical routes for the production of light olefins from abundant non-oil resources such as natural gas and biomass [326]. The silicoaluminophosphate (SAPO) zeolite SAPO-34, is one of the best industrial catalysts for the methanol to olefin (MtO) conversion reactions due to its CHA framework structure, which contains an eight-ring pore opening, and moderate acidity. Silicoaluminophosphates were the result of a breakthrough in zeolite synthesis after a number of researchers recognised that aluminium and phosphate framework structures were known in nature [101]. The CHA cages of SAPO-34 are 0.75 by 0.82 nm in diameter and are accessible through six eight-rings each 0.45 by 0.41 nm [327]. For the MTO reaction, the SAPO-34 can induce a high selectivity (>90 %), in the temperature range of 350-500 °C, of ethylene and propylene with complete conversion of methanol [328]. Although SAPO-44 also has the CHA framework topology, SAPO-44 differs in its catalytic ability compared to SAPO-34 [329].

Aluminium oxide has been extensively used in catalysis for many years due to its unique properties and finds itself employed in the dehydration of alcohols, in the Claus process and hydrocracking reactions. It is also used as a support for metal and oxide catalysts used in hydrogenation and reforming [330]. Aluminium oxide exists in many metastable polymorph structures as well as the thermally stable amorphous alumina (α-Al_2O_3). Of all the polymorph structures, the γ-Al_2O_3 is extremely important as a catalyst and catalyst support due to its high surface area structural defects, giving way to cationic vacancies [331]. The distorted arrangement of O^{2-} anions and Al^{3+} cations intersects provide the existence of both acidic and basic sites at the surface.

Therefore, the industrially relevant catalysts that have been chosen to compare to the synthesised Al-SBA-15 catalyst and previously used ZSM-5 catalyst are:

- K10
- SAPO-34
- γ-Al_2O_3

4.5. Results and Discussion

4.5.1. Thermogravimetric analysis of the three main components

The pyrolysis characteristics of the three components are presented in **Fig. 36**. It is clear from the three curves that there are significant differences in the pyrolysis behaviour of each component. The mass loss prior to 150 °C is assumed to be mainly adsorbed water vapour and light volatile compounds. Of the three components, hemicellulose (xylan) displayed the largest mass loss prior to 150 °C, with little mass loss before this temperature by either of the other two components (cellulose and lignin). Hemicellulose (xylan) decomposed the most readily, with the maximum mass loss occurring between 250 and 315 °C. After, this the mass only slightly decreased, with approximately 20 wt. % of the mass left at 900 °C, as a solid residue.

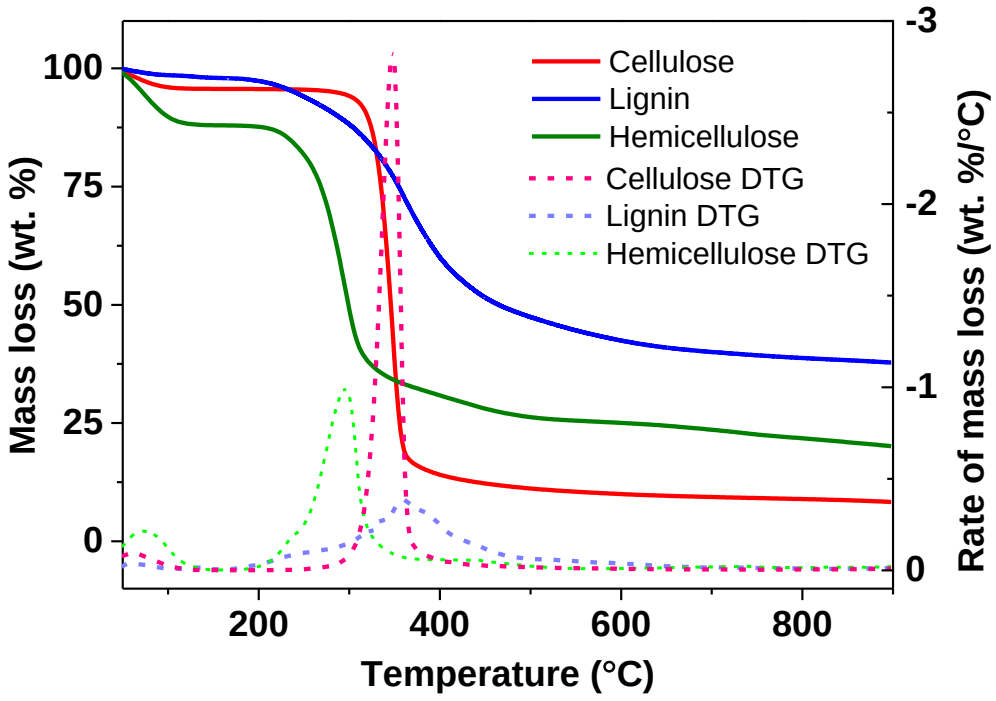

Fig. 36. *Thermal degradation of biomass components, cellulose, lignin and xylan using TGA analysis at 10 °C min^{-1}.*

Cellulose pyrolysis took place at a higher temperature, between 300 and 380 °C. The mass loss of cellulose was more extreme as expressed by the sharp peak in the derivative curve (dashed line) in **Fig. 36.** The temperature range of degradation of the main components of biomass (cellulose, hemicellulose and lignin) are well-within the range that can be found in the literature, presented in **Table 10**. All temperature measurements disclosed in the literature are in agreement that hemicellulose degradation is first to commence thermal degradation (around 180- 200 °C) and occurs

over the narrowest temperature range of the three main components. Cellulose is second to commence degradation at approximately 280 to 300 °C and takes place over a temperature range of around 80-100 °C. The commencement of the thermal degradation of lignin varied depending on the literature reference. The most common initial degradation temperature of lignin was at around 145 °C, while the final degradation temperature was around 600 °C. The reason for the large variance may be due to differences in lignin purification procedures and hence, different lignin structures. Nevertheless, it can be assumed that the thermal decomposition of lignin takes place over a large temperature range compared to cellulose and hemicellulose.

***Table 10**. Comparison of the decomposition temperature range of cellulose, hemicellulose and lignin from the literature.*

Author	Year	Heating rate (°C min^{-1})	Temperature range of decomposition (°C)			Ref
			Cellulose	Hemicellulose	Lignin	
Koufopanosi et al.	1989	20	300-400	230-310	300-600	[332]
Rao et al.	1998	20	300-400			[333]
J. Orfão et al.	1999	5	280-380	180-330	130-630	[305]
Yang et al.	2007	10	315-400	220-315	25-900	[318]
Stefanidis et al.	2014	10	280-360	200-320	140-600	[306]
This study	2019	10	300-380	200-315	170-600	

The composition of the biomass components was calculated from the thermogravimetric data to quantify the moisture content, volatile matter and solid residue on a weight percentage basis. The data is presented in

Table 11. Approximately 90 wt. % of cellulose's mass was converted to volatile products. Furthermore, cellulose had the smallest mass of solid residue remaining (7.65 wt. %), of the three components after the thermal treatment up to 900 °C. In contrast, the thermal decomposition of lignin was much more gradual. The main decomposition was gradual and spread over nearly 350 °C, which initially started at approximately 170 °C and ended at approximately 600 °C. A large proportion of lignin (ca. 38 wt. %) was nonvolatilisable and remained as solid residue after the thermal treatment. Although all three main components are primarily composed of carbon (C), oxygen (O) and hydrogen (H) as shown in

Table 11 below, the variance in the chemical structures (i.e. the type of sugar building blocks; pentoses and hexoses; or aromatics) of the three components inevitably accounts for the different behaviours observed [318].

***Table 11**. Proximate and ultimate analysis of biomass components by thermogravimetric analysis.*

	Cellulose	Hemicellulose (xylan)	Lignin
Supplier	Sigma-aldrich	Sigma-aldrich	Sigma-aldrich
Extraction method	Acid hydrolysis	Alkaline	Organosolv
Moisture (wt. %)	2.39	8.54	1.13
Volatile matter (wt. %)	89.95	76.27	61.56
Fixed carbon (wt. %	7.65	15.19	37.31
C (wt. %) [306]	42.27	42.07	63.41
H (wt. %) [306]	6.40	5.82	5.89
O (wt. %) [306]	51.33	45.75	28.42
Ash (w.t %) [306]	0.00	6.36	2.28

In addition to the thermal mass loss, further information can be provided using differential scanning calorimetry (DSC) to measure the energy consumption properties of each component. The results of each experiment are plotted in **Fig. 37**. In all cases, there is an endothermal reaction below 200 °C. This can be ascribed to the loss of moisture and light volatile products such as phenols and cyclic ketones [334] when the sample was heated. The largest endothermal peak in this range was produced by hemicellulose which is in agreement with the largest mass loss measured by TGA.

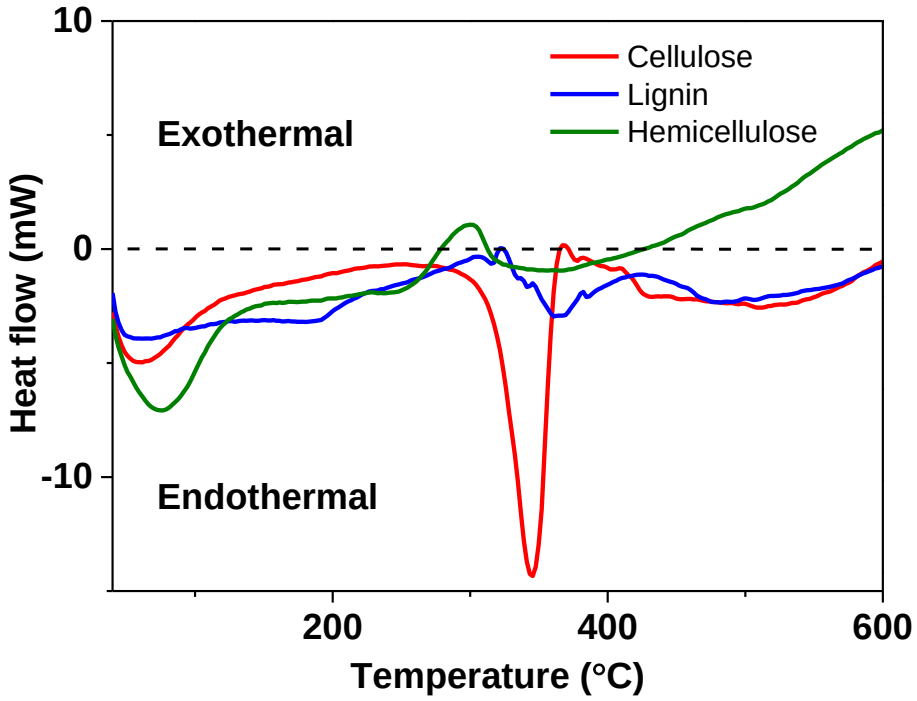

***Fig. 37.** Heat flow curves of cellulose, lignin and xylan thermal degradation from DSC at 10 °C min^{-1}.*

As the temperature is increased there is a large endothermic peak produced by cellulose at approximately 350 °C. Ball et al. [335] examined the decomposition of cellulose and evidenced that char formation is an exothermal process, while volatilisation requires high activation energy and is an endothermal process. Therefore, it can be concluded that the large endothermal peak produced by cellulose corresponds to the endothermic volatilisation during the pyrolysis. In addition, the gradual exothermal peak by hemicellulose could possibly be due to the charring processes and is responsible for the solid residue after the experiment.

The heat flow curve for lignin undergoes many changes and is quite varied. This is in stark contrast to the TGA curve for lignin which gradually declines and is smooth. This suggests that although the mass loss steadily increased with increasing temperature (TGA), many chemical reactions occur within the structure of lignin that does not necessarily involve the loss of mass. After 400 °C, the heat flow of both cellulose and lignin stay negative. This indicates the endothermal properties of the reactions which could be the result of bond breakages, as would be expected with pyrolysis.

In conclusion, the TGA-DSC of all three main components of lignocellulosic biomass (cellulose, lignin and hemicellulose), clearly evidenced how differences in structural compositions of each component have a profound effect on the reactions and energy required for the decomposition of the biopolymer. Hemicellulose was the easiest of the three to decompose and resulted in a significant amount of solid residue after thermal treatment by TGA. This may be due to a variety of reasons, namely the lack of crystallinity and the presence of side-chains that are easy to break away from the main pentose backbone of hemicellulose. It has also been noted that xylan, used as a representative sample of hemicellulose, contains a relatively high ash content (ca. 6 wt. %) [306]. The high ash content of xylan may catalyse its early breakdown and lead to the formation of gases, water and char. Lignin also produced a very significant proportion of solid residue, with almost half of its initial mass ending up as a solid product. In contrast, the decomposition of cellulose required a notable amount of thermal energy and happened over a short temperature range. There was relatively little solid residue remaining with cellulose as the majority of the starting mass was volatilised to decomposition products, namely levoglucosan.

4.5.2. Characterisation of catalysts

Nitrogen physisorption analysis

The difference in structural textural properties of each of the catalytic materials was investigated using N_2 physisorption analysis. The corresponding N_2 physisorption isotherms are displayed in **Fig. 38** below. Both SAPO-34 (blue) and ZSM-5 (purple) display type I isotherms which are characteristic of

microporous materials (see Section 2.2.4). As shown in the two isotherms, SAPO-34 had a slightly higher adsorption volume of nitrogen compared to ZSM-5 which suggests a higher surface area. K10 and Al_2O_3, on the other hand, both display type II type isotherms which correspond to non-porous or macroporous materials. The isotherms of both materials display the occurrence of a hysteresis loop. The H3 hysteresis loop displayed by K10 is typically produced by the adsorption of polar phases by montmorillonite clays [336]. On the contrary, AlSBA15(5) displays a type IV isotherm with a H2 hysteresis loop, indicative of mesoporous materials with uniform cylindrical pores. At higher relative pressure, AlSBA15(5) adsorbs a significantly higher volume of adsorbate gas, therefore displaying increased total pore volume.

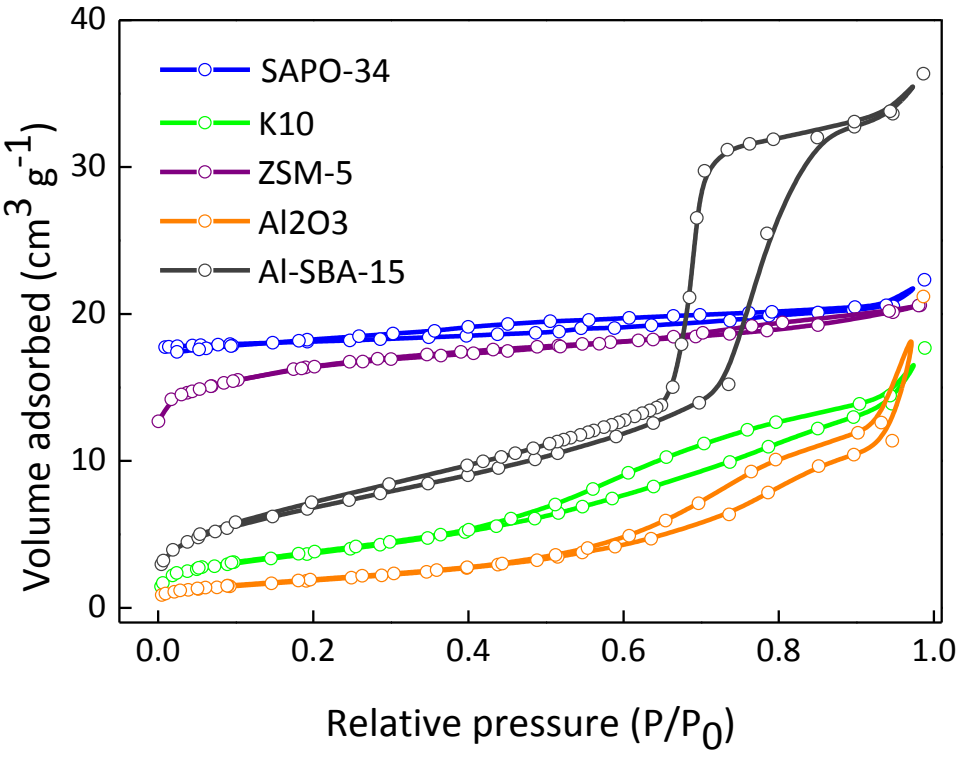

Fig. 38. *N_2 physisorption isotherms of select catalysts.*

The approximate surface area, pore volume and average pore size of each material were calculated, and the results are summarised in **Table 12**. SAPO-34 displays the highest surface area along with the smallest pore volume and microporous average pore size openings. This suggests SAPO-34 is composed of many micropores with relatively narrow openings that are small in internal volume. Likewise, ZSM-5 has comparatively similar sized pore openings with a small internal pore volume. However, the surface area of ZSM-5 is roughly half of SAPO-34. Although they possess similar pore size properties, the large difference in surface areas of SAPO-34 and ZSM-5 (ca. 300 $m^2\ g^{-1}$) may be due to differences in crystallite sizes or a higher density of pores in the case of SAPO-34.

***Table 12**. Physicochemical properties of the studied catalysts.*

Catalyst	Main elements[a]	Surface area ($m^2\ g^{-1}$)[b]	Pore volume ($cm^3\ g^{-1}$)[c]	Average pore size (nm)	Acid sites ($\mu mol\ g^{-1}$)[d]	B/L[e]
SAPO-34	Si, Al, P	599	0.1	1.5	121	N.A.
K10	Si, Al, Fe, Mg, K	266	0.5	4.4	254	0.1
ZSM-5	Si, Al	304	0.2	0.9	672	1.3
Al_2O_3	Al	111	0.4	6.6	N.A.	N.A.
AlSBA15(5)	Si, Al	414	1.0	6.8	564	1.6

[a]Excluding O and H, determined by [b] BET, [c] BJH, [d] TG-TPD of n-propylamine, [e] pyridine-FTIR

K10 and Al_2O_3 have similar pore volumes which are approximately 0.5 $cm^3\ g^{-1}$ and are in the middle in terms of volume compared to the other catalysts tested here. However, Al_2O_3 has a larger average pore size than K10, at the expense of a comparatively lower surface area. AlSBA15(5) has the largest average pore size and pore volume, with a moderately large total surface area. With the exception of Al_2O_3, which is purely aluminium and oxygen, all other materials are composed of a combination of aluminium and silicon oxides in different arrangements and ratios, including other elements in smaller quantities. However, it is evident using N_2 physisorption analysis that there is a diverse range of achievable structural and textural properties.

Thermogravimetric Temperature Programmed Desorption of adsorbed n-propylamine (TG-TPD)

The acidic properties of all materials were investigated via n-propylamine chemisorption followed by TGA-MS analysis. As described in the experimental methods chapter, Chapter 2 Section 2.2.5 in more detail, n-propylamine is a weak base that reacts with accessible acid sites to form propene and ammonia under thermal conditions. The thermal desorption of propene was measured by mass spectrometry and is shown in **Fig. 39**. The quantity of propene corresponds to the number of acid sites present in the material. The acid site loadings of all materials were calculated, and the results are presented in **Table 12**. ZSM-5 had the highest acidity at 672 $\mu mol\ g^{-1}$ followed by AlSBA15(5) at 564 $\mu mol\ g^{-1}$. K10 had a medium acidity with 254 $\mu mol\ g^{-1}$ but SAPO-34 had a much lower acidity, approximately half of K10 at 121 $\mu mol\ g^{-1}$. Al_2O_3 had the lowest acidity of all the catalysts and was below detectable limits via this method.

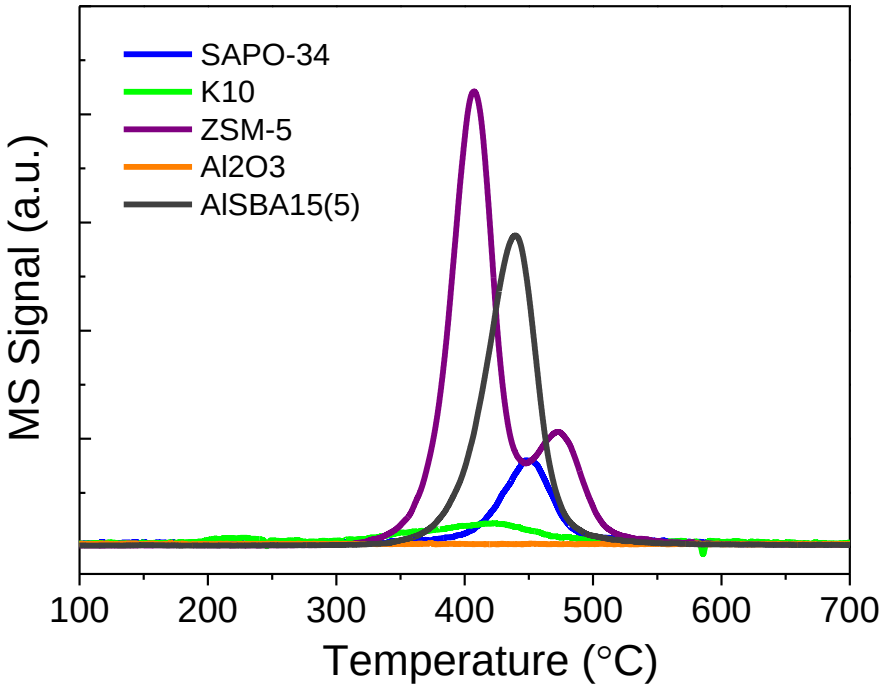

Fig. 39. *Temperature programmed desorption (TPD) of propyl amine over acid sites of select catalysts*

Pyridine-FTIR analysis

The nature of the acidic sites of the select catalysts were investigated using pyridine-FTIR spectroscopy. The resultant DRIFT spectra of the select catalysts following chemisorption of pyridine, after subtraction of IR absorbance of the fresh material, are shown in **Fig. 40**. The peaks at around 1445 cm^{-1} and 1595 cm^{-1} are characteristic of pyridine interaction with a Lewis acid site through electron donation. This band is clearly evident in K10, ZSM-5 and AlSBA15(5). A small peak can be differentiated in SAPO-34, however, there is no obvious peak in Al_2O_3. An absorption peak at 1545 cm^{-1} is clearly visible in ZSM-5 and slightly visible in AlSBA15(5) and K10. This is commonly assigned to pyridinium ions (PyH^+) coordinated to a Brønsted acid site. The absorption band at 1490 cm^{-1} is assigned to pyridine adsorbed over Brønsted and Lewis sites [300]. The ratio of Brønsted to Lewis acidity present in the materials was calculated by integration of the 1445 cm^{-1} and 1545 cm^{-1} absorption bands and are presented in **Table 12**.

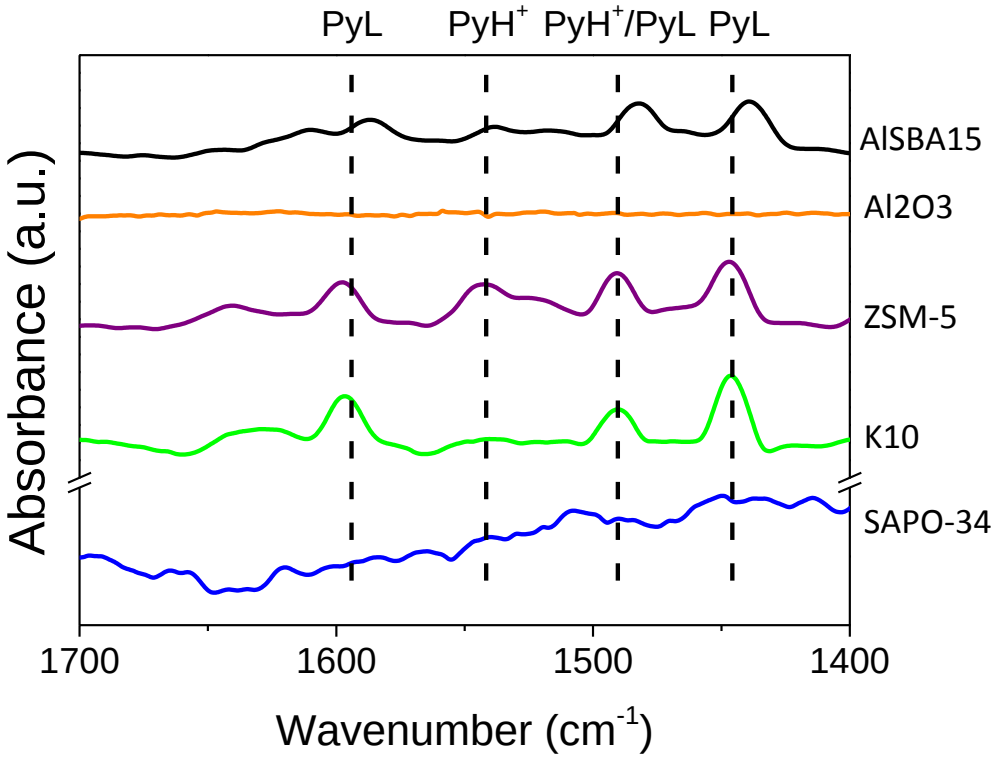

Fig. 40. *DRIFT spectra of chemisorbed pyridine after subtraction of background infrared absorption of select catalysts.*

Although the DRIFT spectra of SAPO-34 and Al_2O_3 do not show obvious peaks in the characteristic region of chemisorbed pyridine (1400-1700 cm^{-1}), this should not rule out the existence of Brønsted or Lewis acid sites on these materials. Firstly, in the case of SAPO-34, Brønsted acidity was evidenced by the reaction of n-propylamine over reactive sites by propylamine TPD previously. Medium strength Brønsted acid sites of SAPO-34 were also confirmed by Liang et al. [337], using a combination of TPD of ammonia and FTIR of chemisorbed pyridine, in the literature. As discussed, the acidic and structural properties of Al_2O_3 are very dependent on the specific phase of alumina. The gamma (γ) phase used in this study is the most catalytically active due to the highest concentration of surface hydroxyl groups per square metre [330]. It is well known that CO molecules form complexes with surface Lewis and Brønsted acid sites of Al_2O_3. However, in this study the adsorption of both weak bases, propylamine and pyridine was undetected. The reason for this is unknown, however, this may have been due inadequate removal of moisture during the experiment which also absorbs across these wavelengths [241].

4.5.3. Non-catalytic pyrolysis of biomass components using Py-GC/MS

The catalytic selectivity of the select catalysts for the catalytic pyrolysis of biomass components was carried out using analytical scale pyrolysis-GC/MS. In order to simplify comparisons between the

selectivity of each catalyst, the products identified were categorised into eleven groups based on the chemical functionality. A full list of all the products identified by GC-MS can be found in Appendix B – Pyroprobe identified products by mass spectrometry using NIST database, including a breakdown of the groups to which the products were assigned. The eleven product groups are comprised as follows:

- Aliphatic hydrocarbons
- Acids
- Alcohols
- Aldehydes
- Ketones
- Esters/Ethers
- Aromatics (monocyclic aromatic hydrocarbons)
- Polycyclic aromatic hydrocarbons (PAHs)
- Furans
- Phenolics
- Anhydrosugars

It should be noted that due to the complexity of the products, multiple functionalities were often present in single molecules. Therefore, overlaps between the eleven groups sometimes occurred. In these cases, the compounds were sorted into the groups regarding their 'best fit'.

Defining catalytic success, in terms of product selectivity, is often challenging due to the wide variety of chemical functionalities achievable. In general, for use as a fuel/fuel additive or for use as platform chemicals, aromatics (monocyclic aromatics) and hydrocarbon products are usually preferred. However, greater value may be attainable in select oxygenated compounds such as furans, phenolics and ketones, among others. The presence of acidic compounds in bio-oil is often responsible for increased corrosivity and instability, therefore reducing the number of acid products is desirable. Furthermore, the presence of larger molecular weight compounds such as anhydrosugars and phenolic derivatives of lignin would rather be avoided due to the increased viscosity of the resultant liquid product [338]. It should also be recognised that certain PAHs are toxic and have been identified as being carcinogens, therefore the production of PAHs would also be rather avoided [339].

To distinguish the effect of each of the catalyst, the non-catalytic fast pyrolysis of each of the components (cellulose, lignin and hemicellulose) was carried out and analysed before the catalytic studies.

Non-catalytic fast pyrolysis of cellulose at 550 °C

The fast pyrolysis of cellulose at 550 °C produced a multitude of peaks separated by gas chromatography (GC) and detected by mass spectrometry (MS). The corresponding chromatogram is provided in **Fig. 41**. It should be noted, due to the poor thermal conductivity of cellulose, the actual heating rate of the cellulose may be less than the stated 20 °C ms^{-1}. However, due to the low mass of the sample used, the heating rate can be considered uniform and fast, consistent with other studies [340–342]. The fast pyrolysis of cellulose at 550 °C produced many compounds with low retention times (<15 min). This corresponds to the production of low molecular weight compounds. There are several well-resolved large peaks with high relative abundances. Most notably, there is a large broad peak at 52 to 55 min which represents the highest molecular weight compound produced by cellulose.

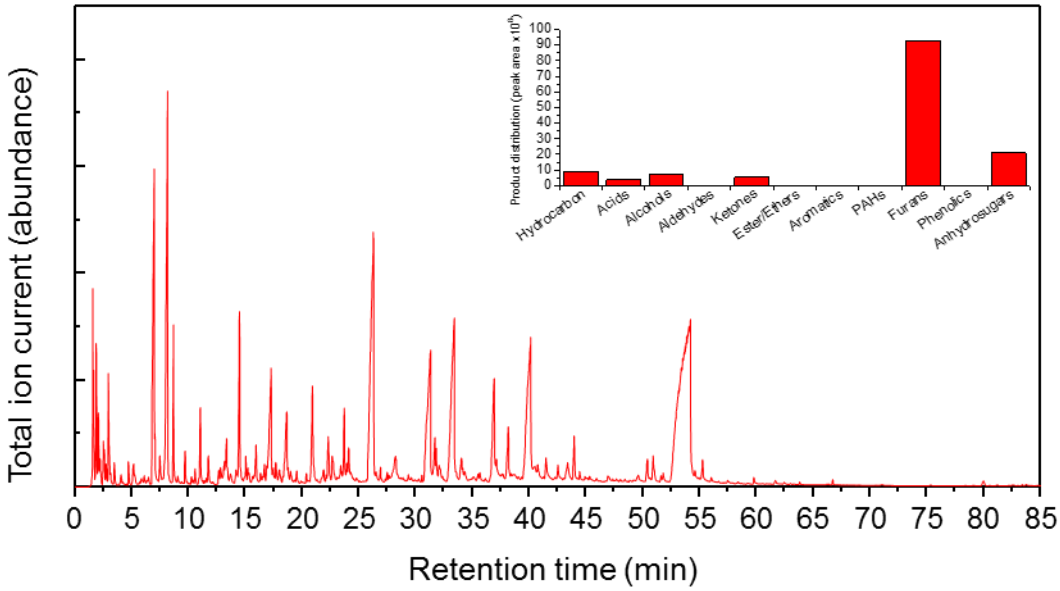

Fig. 41. *GC chromatogram with MS detector of cellulose pyrolysis at 550 °C using a CDS pyroprobe reactor. Product distribution in the inset.*

After integration of the individual peak areas and subsequent identification of the peaks by reference of the mass spectrum on the NIST library using the GC software, the compounds were categorised into groups. The results are presented in **Table 13** and can also be seen in the inset in **Fig. 41** in graphical form. Due to the limitations of the analytical system (full separation by the column and limits to mass spectrum referencing database), a high proportion of peaks remained unidentified. Caution was taken when identifying peaks using the NIST database and mass spectra software. When peaks displayed a relatively low match score in the mass spectra software (< 65 %), these peaks were labelled unidentified. In some cases, “common sense” was exercised when choosing between two closely

related prospective identifications. It is important to recognise that with all the identified peaks there is a degree of uncertainty attached.

***Table 13**. Table of data for the catalytic and non-catalytic pyrolysis of lignocellulosic biomass components using the pyroprobe reactor. Quantitative data is presented as peak area.*

	Cellulose						Lignin						Hemicellulose					
	Non-catalytic	SAPO-34	ZSM-5	K10	Al2O3	AlSBA15	Non-catalytic	SAPO-34	ZSM-5	K10	Al2O3	AlSBA15	Non-catalytic	SAPO-34	ZSM-5	K10	Al2O3	AlSBA15
Peak area (x10^8)																		
Hydrocarbons	9.3	8.0	23.6	7.9	2.0	0.0	0.2	0.0	0.0	0.0	0.0	0.0	7.8	0.0	0.0	0.0	1.0	4.1
Acids	3.7	3.2	0.8	3.1	0.0	0.0	0.0	0.0	0.0	0.0	0.0	0.0	0.0	0.3	0.0	0.0	0.5	0.0
Alcohols	7.5	0.0	0.6	0.4	0.0	0.0	0.5	0.1	0.0	0.0	0.3	0.0	0.0	1.0	0.8	0.0	1.7	0.0
Aldehyde	0.0	0.0	0.0	0.8	0.0	0.0	0.1	0.2	0.0	0.0	0.3	0.0	0.0	0.2	0.0	2.4	5.0	8.4
Ketones	5.6	3.4	3.7	5.6	10.1	2.7	0.2	0.1	0.0	0.0	0.1	0.0	53.3	1.9	0.0	5.0	4.9	1.2
Esters/Ethers	0.0	3.7	6.6	0.0	9.2	0.0	1.0	0.0	0.0	0.0	0.1	0.0	0.0	0.0	0.0	0.0	0.0	0.0
Aromatics	0.0	0.0	49.9	3.1	2.6	1.5	1.0	0.7	12.6	0.2	0.6	0.1	11.4	0.3	56.4	10.8	7.3	6.3
PAHs	0.0	0.0	25.0	0.3	0.0	0.0	0.0	0.0	3.0	0.0	0.0	0.0	0.0	0.2	13.7	2.9	0.7	0.6
Furans	92.8	32.2	40.6	40.8	75.2	49.6	0.3	2.6	0.1	0.3	1.4	0.1	16.5	0.8	0.0	1.1	1.5	2.2
Phenolics	0.0	3.6	0.0	0.9	6.1	6.1	35.7	33.3	32.4	6.8	19.5	6.0	9.6	2.7	0.0	0.0	0.0	0.0
Anhydrosugars	21.0	6.6	9.6	6.8	10.0	12.2	0.0	0.0	0.0	0.0	0.0	0.0	5.0	0.1	0.0	0.0	0.0	0.0

As shown in **Fig. 41** and **Table 13**, the non-catalytic pyrolysis of cellulose at 550 °C resulted in a high proportion of anhydrosugars, namely levoglucosan and other derivatives such as levoglucosenone and 1,4:3,6-Dianhydro-α-d-glucopyranose. It should be noted that the levoglucosan yield in these experiments was significantly lower than in similar experiments by other research groups. This may be due to the high boiling point of levoglucosan (385 °C) [343], which is greater than the highest achievable temperature of the transfer line to the GC, and thus prior condensation may have occurred. Kawamoto et al. [344] showed that anhydrosugars can be produced by the primary pyrolysis of cellulose or through the secondary pyrolysis of levoglucosan. However, the precise pathway of cellulose degradation and the formation of anhydrosugars and their derivatives is still unknown. Evidence from studies suggests that levoglucosan is a highly thermally stable intermediate [345] and therefore levoglucosenone is produced concurrently with levoglucosan [310].

Furans produced the highest peak area of the product groups and contributed to over 40 % of the total peak area. As discussed in the literature review earlier in this chapter (Section 4.2) on cellulose pyrolysis, according to Lin et al. [311], the monosaccharides derived from the anhydrosugars are decomposed to form furanoses. Of the many furan products, furfural, 2(5H)-Furanone and furan produced the largest peak areas. Furan 2-methyl, 5-hydroxymethylfurfural (5-HMF) and Furan 2,5-dimethyl all produced smaller peak areas. The formation pathways of furfural and 5-HMF have not been definitively confirmed. Shen and Gu [346] suggested two chemical pathways for the formation of 5-HMF and furfural, one through direct ring-opening and rearrangement of cellulose unit molecules, and the other through the decomposition of levoglucosan. It was generally assumed that furfural was the product of 5-HMF decomposition, however, Lu et al. [310] verified this was not the case and determined furfural was formed concurrently to 5-HMF. A speculative formation pathway for the formation of 5-HMF and furfural is presented in **Fig. 42**.

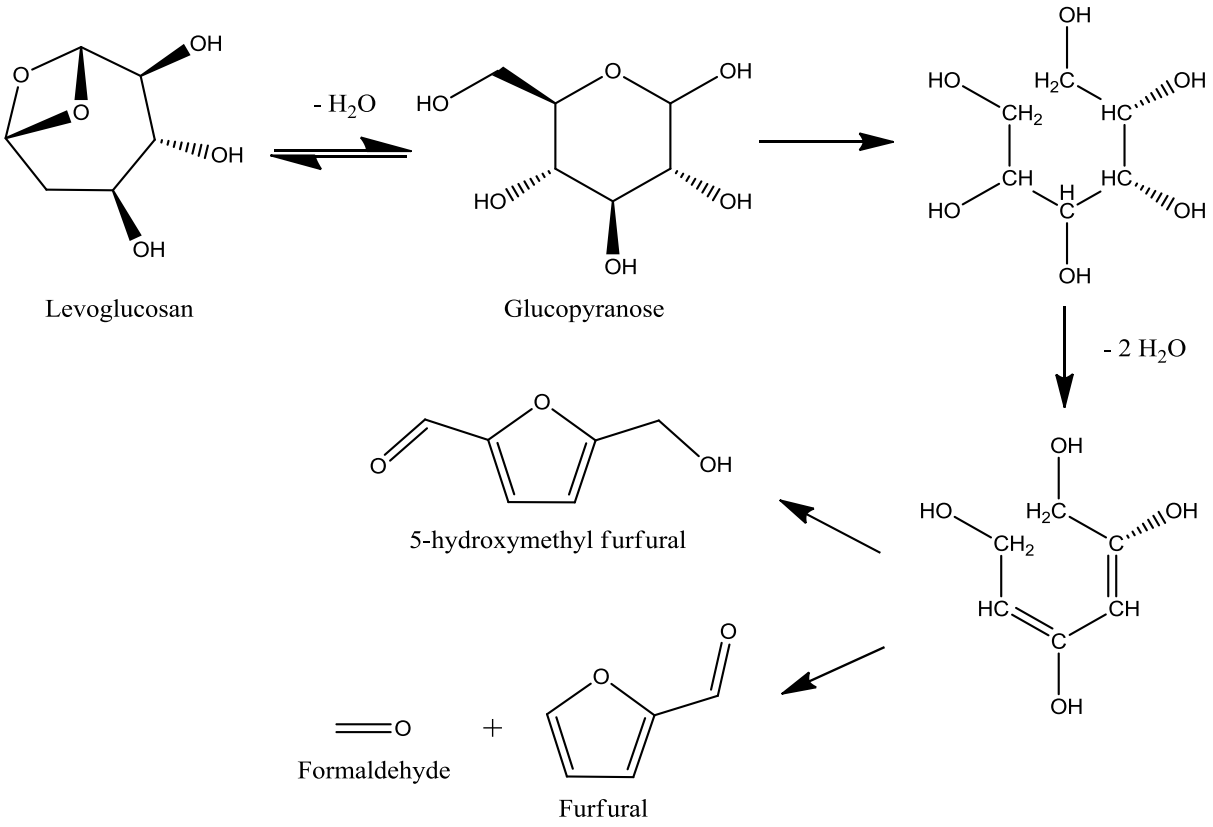

***Fig. 42**. Proposed formation pathway of furfural and 5-hydroxymethyl furfural (5-HMF) from levoglucosan.*

In addition to furan products, a plethora of lower molecular weight molecules produced a number of smaller peak areas. Cyclic and aliphatic ketones were also identified such as cyclohexene 1,2-diol and butadiene-1-ol, as well as acids such as propanoic and formic acid. Wang et al. [347] evidenced the formation of these acid products during the fast pyrolysis of 5-HMF, while the fast pyrolysis of furfural produced no acid products. Other researchers have reported small yields of phenolic products which were identified as being formed by secondary reactions between short chained alkenes in the gas phase [334,348]. However, no phenolic products were identified in the fast pyrolysis of cellulose in this work. This supports the use of a trap when conducting Py-GC/MS experiments, which reduces the likelihood of secondary recombination reactions.

Lignin

The fast pyrolysis of lignin at 550 °C produced a significantly different MS chromatogram compared to cellulose. As can be seen by the chromatogram in **Fig. 43**, the fast pyrolysis of lignin at 550 °C resulted in fewer peaks corresponding to low molecular weight compounds (retention time <15 min), compared to cellulose. In contrast, the majority of peaks were formed after 20 min, with a comparably high abundance and broad peak size. Therefore, this suggests that many pyrolysis products from lignin are

of higher molecular weight (> MW) in comparison to cellulose. Furthermore, due to the increased peak sizes, it is evident each compound was produced in higher relative proportions.

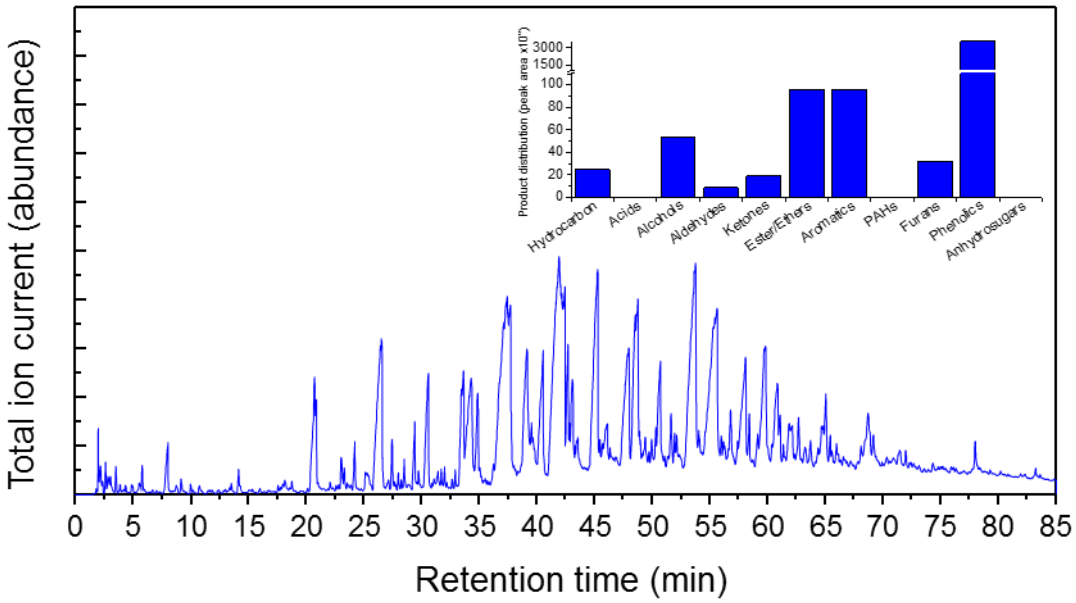

***Fig. 43**. GC chromatogram with MS detector of lignin pyrolysis at 550 °C using a CDS pyroprobe reactor. Product distribution in the inset.*

The mass spectra generated for each peak was matched in the NIST library using the MS software. The peak area of the identified peaks was measured and was categorised to provide the product distribution which can be seen in the inset of **Fig. 43**. Unsurprisingly, greater than 90 % of the peaks identified were phenolic products. The largest peak areas of the phenolics were assigned to syringol (phenol 2,6-dimethoxy) and guaiacol (2-methoxyphenol), together they are the characteristic products of the thermal decomposition of lignin as discussed earlier in this chapter, i.e. review paper by Kawamoto [322] on lignin decomposition pathways (see literature survey in Section 4.2). A number of large phenolic products were also identified as having high peak areas such as vanillin, desapidinol, eugenol, and creosol. A few smaller peaks were assigned to aromatic products such as toluene and p-xylene, presumably formed by full deoxygenation and fragmentation of the larger phenolic products. Due to the complexity of the products and the limitations of this method, just over 36 area % of the peaks were unidentified.

Hemicellulose (xylan)

The GC chromatogram produced by the fast pyrolysis of hemicellulose (xylan) at 550 °C is shown in **Fig. 44**. The chromatogram shows many peaks towards the lower retention times, suggesting a large number of low molecular weight compounds are produced. A large peak is apparent at 52- 55 min,

similar to cellulose. There are no significant peaks that appear after the large peak suggesting that this is the largest molecule formed. In addition, compared to lignin, which had a multitude of large peaks between 35 and 70 min, hemicellulose had much fewer peaks after 35 min retention time. This suggests fewer high molecular weight compounds and much more low molecular weight compounds were being formed.

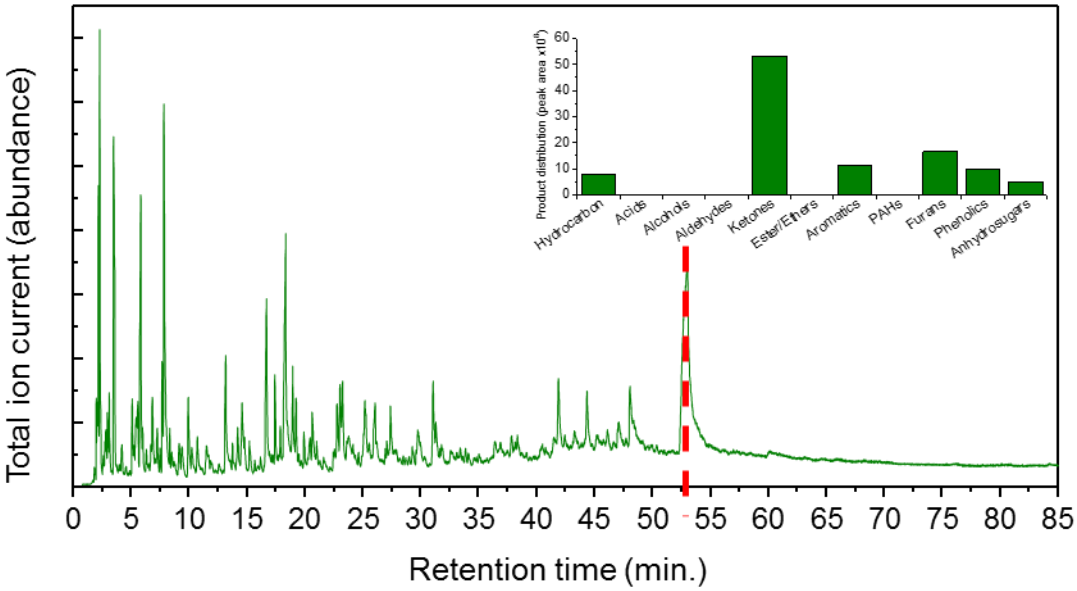

***Fig. 44**. GC chromatogram with MS detector of hemicellulose pyrolysis at 550 °C using a CDS pyroprobe reactor. Product distribution in the inset.*

By far the most abundant category of peaks identified for the pyrolysis of hemicellulose at 550 °C were ketone type products. These are made up of a range of ketones of varying molecular weights such as 6-methyloxan-3-one with a large molecular weight and linear ketones such as pentadiones, hexadiones, butanones and pentanones. There was a small number of peaks attributed to monocyclic aromatic products, presumably formed from the substituted phenolics branches of the pentose backbone that constitutes hemicellulose. Furan products such as furfural and dimethylfuran were also observed. For hemicellulose, approximately 50 % of the peak area was unable to be identified. This leaves a large degree of uncertainty with the products of the fast pyrolysis of hemicellulose. Furthermore, in published papers in the literature authors have noted that acids such as acetic acid, formic acid and propanoic acid comprise some of the most abundant products in the fast pyrolysis of hemicellulose [349].

4.5.4. Catalytic fast pyrolysis of cellulose, lignin and hemicellulose using Py-GC/MS

Following on from the non-catalytic fast pyrolysis of the biomass components, the catalytic fast pyrolysis was performed individually with each component using a selection of commercially available solid acid catalysts, and a synthesised Al-SBA-15 catalyst (AlSBA15(5)). The catalytic pyrolysis was performed on a CDS analytical 5200 pyrolyser. The volatile products were separated and evaluated using gas chromatography coupled to a mass spectrometer for peak area integration and identification. The evaluated results from the catalytic pyrolysis of each component can be compared to the non-catalytic results in order to compare reaction pathways. The results should also provide evidence on the effectiveness of using the synthesised mesoporous AlSBA15(5) catalyst for the catalytic pyrolysis of biomass compared to current commercially available materials.

Catalytic fast pyrolysis of cellulose at 550 °C

The results of the catalytic fast pyrolysis of cellulose with a selection of commercial solid acid catalysts and a synthesised Al-SBA-15 (AlSBA15(5)) mesoporous catalyst is presented in **Fig. 45**. The ratio of catalyst and cellulose were kept constant in all cases using a ratio of 1:1 catalyst to biomass. As can be seen from the bar chart in **Fig. 45**, the cumulative peak area appears reduced by the use of solid acid catalysts for the catalytic pyrolysis of cellulose. This is consistent with previous catalytic pyrolysis experiments where a reduction of an organic liquid yield can be observed [59,174]. It appears that in all cases the peak area of anhydrosugars was reduced. The reduction of the overall peak area was observed more by K10 and SAPO-34. Similarly to the non-catalytic pyrolysis of cellulose, the major product group in nearly all cases of catalytic pyrolysis of cellulose with a selection of solid acid catalysts was furan products. The only exception to this trend was ZSM-5, which produced aromatic products with the most abundant peak areas.

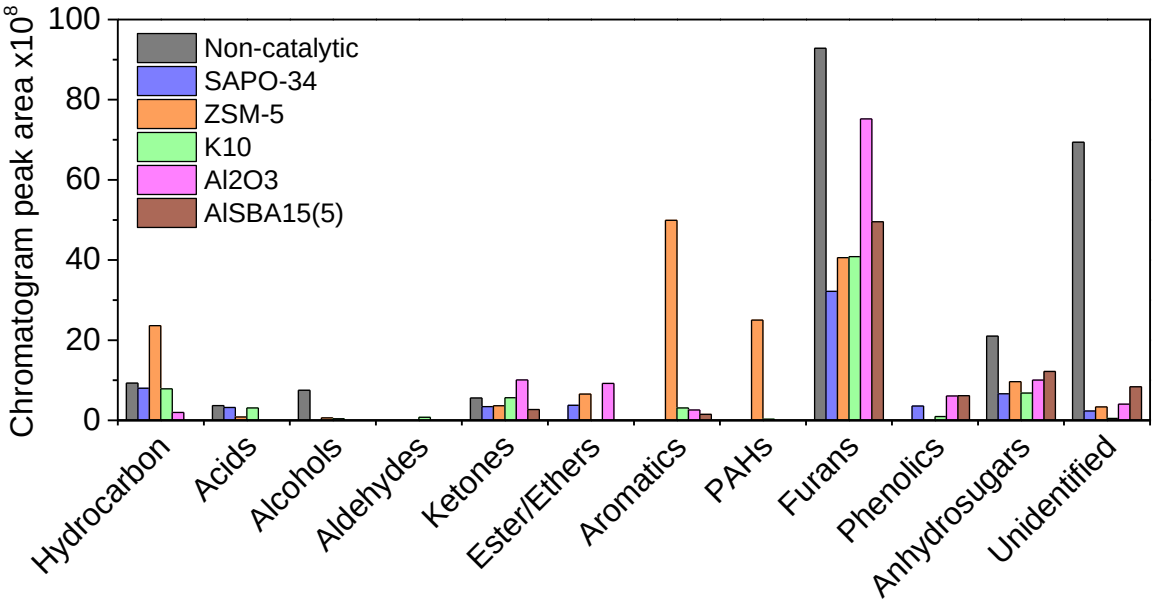

***Fig. 45**. Product distribution from the non-catalytic and catalytic pyrolysis of cellulose at 550 °C over a range of catalysts.*

A more detailed analysis of the type of furan products identified by each of the catalysts shows a difference in selectivity between the solid acid catalysts employed. A chart showing the selectivity of furans for the catalytic fast pyrolysis of cellulose is provided in **Fig. 46**. As discussed, the selectivity of non-catalytic fast pyrolysis of cellulose at 550 °C produces furfural, 2(5H)-furanone and furan as the most abundant peaks. In the catalytic experiments, there is a noticeable reduction in the peak area of "others" furans. This suggests that with the addition of a catalyst, the selectivity is increased to the identified furan products. Of all the catalysts, AlSBA15(5) produced the most similar selectivity to the non-catalytic pyrolysis of cellulose, as the most abundant furan products identified were furfural, 2(5H)-furanone and 5-HMF. The low acidity Al_2O_3 catalyst produced the highest peak area of furan products of all catalysts, mainly furfural and furan 2-methyl. K10, the montmorillonite clay-based material, also produced a high proportion of furan 2-methyl and 3-furaldehyde. SAPO-34 and ZSM-5 both produced a low peak area of furan products. There appears to be no obvious correlation between catalyst acidity and furan selectivity in these experiments. Both ZSM-5 and AlSBA15(5) had the highest acidities (**Table 12**) but produced significantly different furan selectivities. Whereas, SAPO-34 and ZSM-5 had different acidities but the most similar pore properties of the selection of catalysts. Moreover, SAPO-34 and ZSM-5 produced the most comparable furan selectivities of all the materials. Therefore, this similarity in furan selectivity may stem from the pore properties of both catalysts and may rely less on the catalyst acidity.

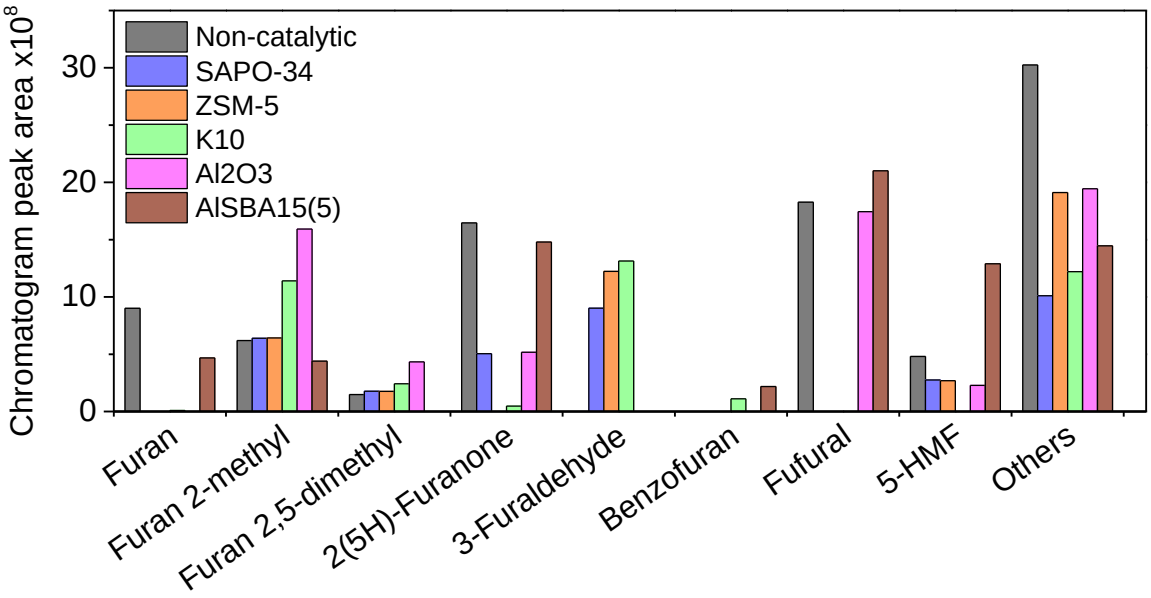

***Fig. 46**. Selectivity of furans from the non-catalytic and catalytic pyrolysis of cellulose at 550 °C over a range of catalysts.*

The peak area of anhydrosugars, such as levoglucosan, was reduced by all catalysts in the catalytic experiments. Whereas, the peak area of esters and ethers were generally slightly increased. This suggests the larger sugars are being further converted through cracking reactions to lower molecular weight molecules. Interestingly, ZSM-5 was remarkably selective towards aromatic products. This suggests that while the intermediate products of cellulose pyrolysis are most likely furans and small oxygenates, as evidenced by the non-catalytic pyrolysis of cellulose results, ZSM-5 is still highly successful at deoxygenation and aromatisation to produce monocyclic aromatic products. These are completely deoxygenated, therefore, it is assumed that there would be a high proportion of CO and CO_2 being formed, although, it was not possible to measure these by this system. Furthermore, ZSM-5 also produced a high peak area percentage of polycyclic aromatic hydrocarbon products. Although AlSBA15(5) had a larger mean pore size and pore volume than all of the other solid acid catalysts, including ZSM-5, there was no significant difference in products obtained with the significant increase in pore size. For the catalytic pyrolysis of cellulose, by far the greatest selectivity was by ZSM-5 to aromatic products.

Catalytic fast pyrolysis of lignin

A comparison of the results for the non-catalytic and catalytic pyrolysis of lignin at 550 °C is presented in **Fig. 47**. Similarly to the non-catalytic pyrolysis of lignin, all solid acid catalysts produced phenolic products as the major product group. SAPO-34 displayed the highest peak area of phenolic products. K10 and AlSBA15(5) produced the lowest peak area of phenolics. However, the peak area of other

groups did not notably increase with the addition of these catalysts. ZSM-5 was again selective towards monocyclic and polyaromatic hydrocarbons, though much less compared with cellulose. This suggests the refractory nature of lignin. It is known the C-O bond is challenging for ZSM-5 to dissociate from phenolics and therefore may be the reason for the low selectivity towards hydrocarbons [306].

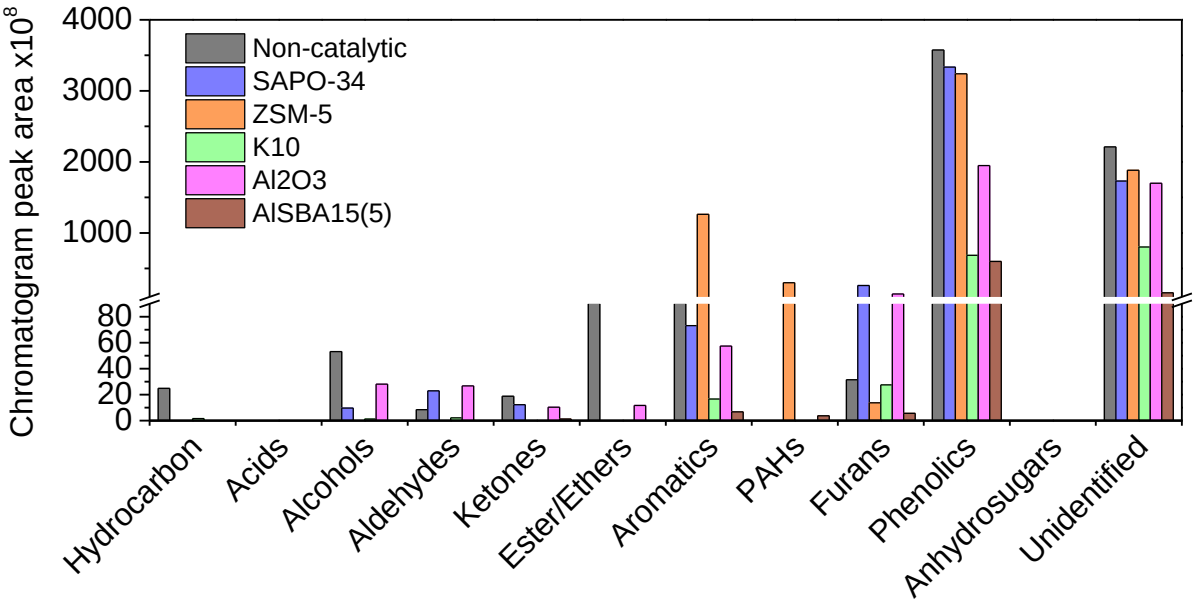

***Fig. 47**. Product distribution from the non-catalytic and catalytic pyrolysis of lignin at 550 °C over a range of catalysts.*

In order to investigate the catalytic selectivity of phenolic products in more detail, a breakdown of the phenolic product selectivity in the non-catalytic and catalytic pyrolysis of lignin at 550 °C is provided in **Fig. 48**. The group with the largest peak area was “others” products for all solid acid catalysts. This suggests that not one specific phenolic product was catalytically selectively produced and a range of phenolics were obtained. In a reaction scheme proposed by Ma et al. [350], lignin depolymerisation intermediates are stabilised by adsorption in low acidity porous materials. Whereas in high acidity materials the phenolic intermediates were converted over strong acid sites to aromatics. In this work, only ZSM-5 was selective for aromatic hydrocarbons through dehydration and decarboxylation reactions. The comparably high acidity AlSBA15(5) produced almost no aromatics, suggesting that high acidity alone is not responsible for the production of aromatics in the catalytic fast pyrolysis of lignin.

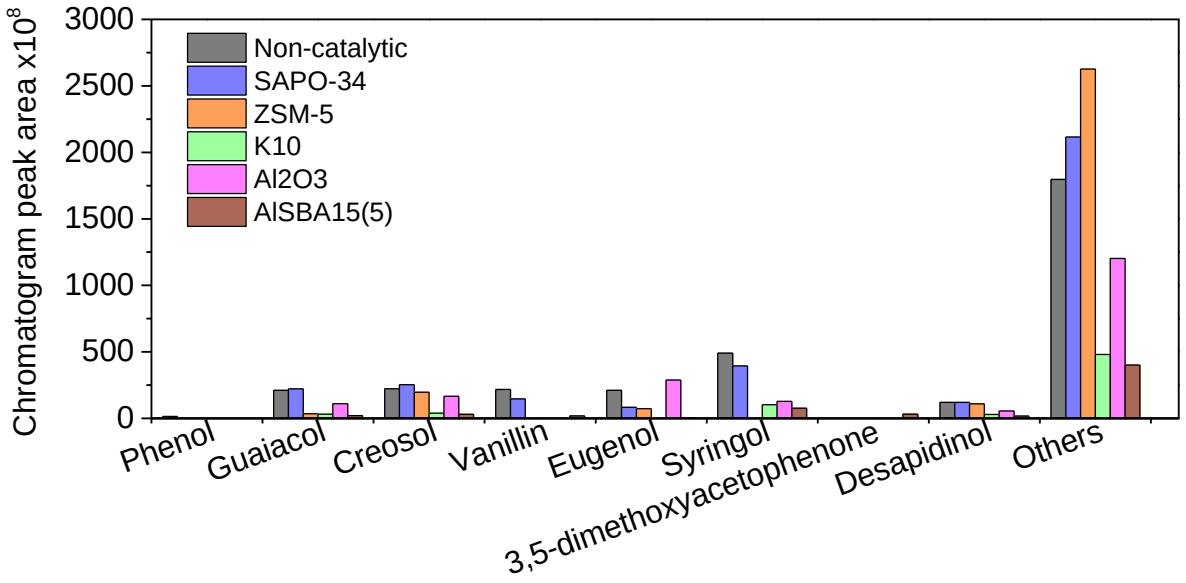

***Fig. 48**. Distribution of phenolics from the non-catalytic and catalytic pyrolysis of lignin at 550 °C over a range of catalysts.*

In a similar experiment by Mullen and Boateng [351], the researchers suggested that the guaiacol and syringol primary pyrolysis products are converted by acid sites to simple phenolics. However, the simple phenolics are likely to be tightly bound to the acidic active sites. This conclusion was supported by an observed increase in char and coke production, which were not measured in this work. A decrease in total phenolic products was observed in this work using all solid acid catalysts, consequently a complimentary increase in production of other pyrolysis products such as light gases and char/coke should be expected. However, due to constraints of the experimental set-up, the coke/char yields and yields of light gases such as CO, CO_2 and low molecular hydrocarbons were not measured. It should be recognised that due to the production of potential sources of catalyst deactivation and coke intermediates, feedstocks containing high proportions of lignin should be avoided for catalytic fast pyrolysis.

Catalytic fast pyrolysis of hemicellulose (xylan)

The majority of products observed in the non-catalytic pyrolysis of hemicellulose were ketones. The results of the catalytic pyrolysis of hemicellulose at 550 °C by a selection of solid acid catalysts are presented in **Fig. 49**. The catalytic pyrolysis of hemicellulose produced a variety of product groups, however with much lower overall peak area. All solid acid catalysts reduced the peak area of ketones. ZSM-5 produced nearly exclusively aromatic products, including monocyclic aromatic hydrocarbons and PAHs. Horne and Williams [190] demonstrated the conversion of cyclic ketones to simple aromatic products when passed over ZSM-5. Monocyclic aromatic hydrocarbons were also produced in the non-catalytic pyrolysis; however, these were all reduced by all catalysts. The catalytic pyrolysis of

hemicellulose, again as in the case of lignin, produced no clear trend in terms of the acidity, porosity and the surface area of the catalysts.

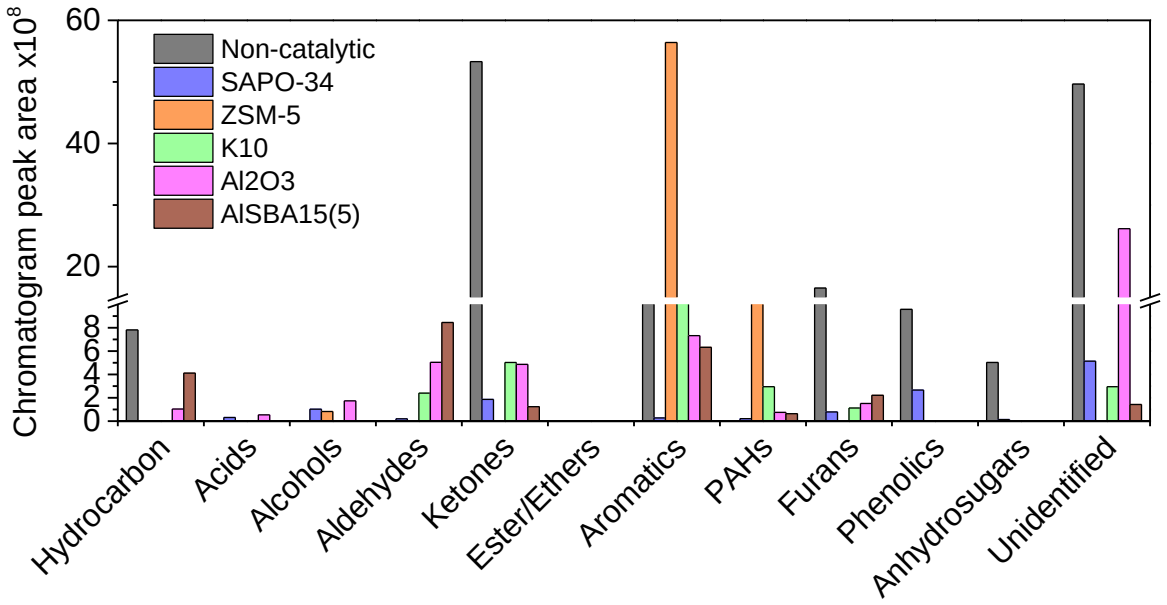

Fig. 49. *Product distribution from the non-catalytic and catalytic pyrolysis of hemicellulose at 550 °C over a range of catalysts.*

4.5.5. Overall comparison

A comparative graphical illustration of the product distribution of the non-catalytic and catalytic fast pyrolysis of the three biomass components with a selection of solid acid catalysts is shown in **Fig. 50**. As shown in **Fig. 50**, there are significant differences in the compounds achievable with the use of both starting biomass component feedstock and associated catalyst. It is clearly evident due to the higher relative chromatogram peak areas that of the three main biomass components, cellulose, produced a larger quantity and more varied range of products. The use of solid acid catalysts leads to the breakdown of larger pyrolysis intermediates such as anhydrosugars in favour of the production of lower molecular weight oxygenated compounds. Furans were the main products obtained by all catalysts except ZSM-5, which produced a range of deoxygenated aromatic hydrocarbons. Although Al_2O_3 has only slight acidity compared to the more acidic Al-SBA-15 and ZSM-5, it resulted in the conversion of the fast pyrolysis vapours to ketones and esters.

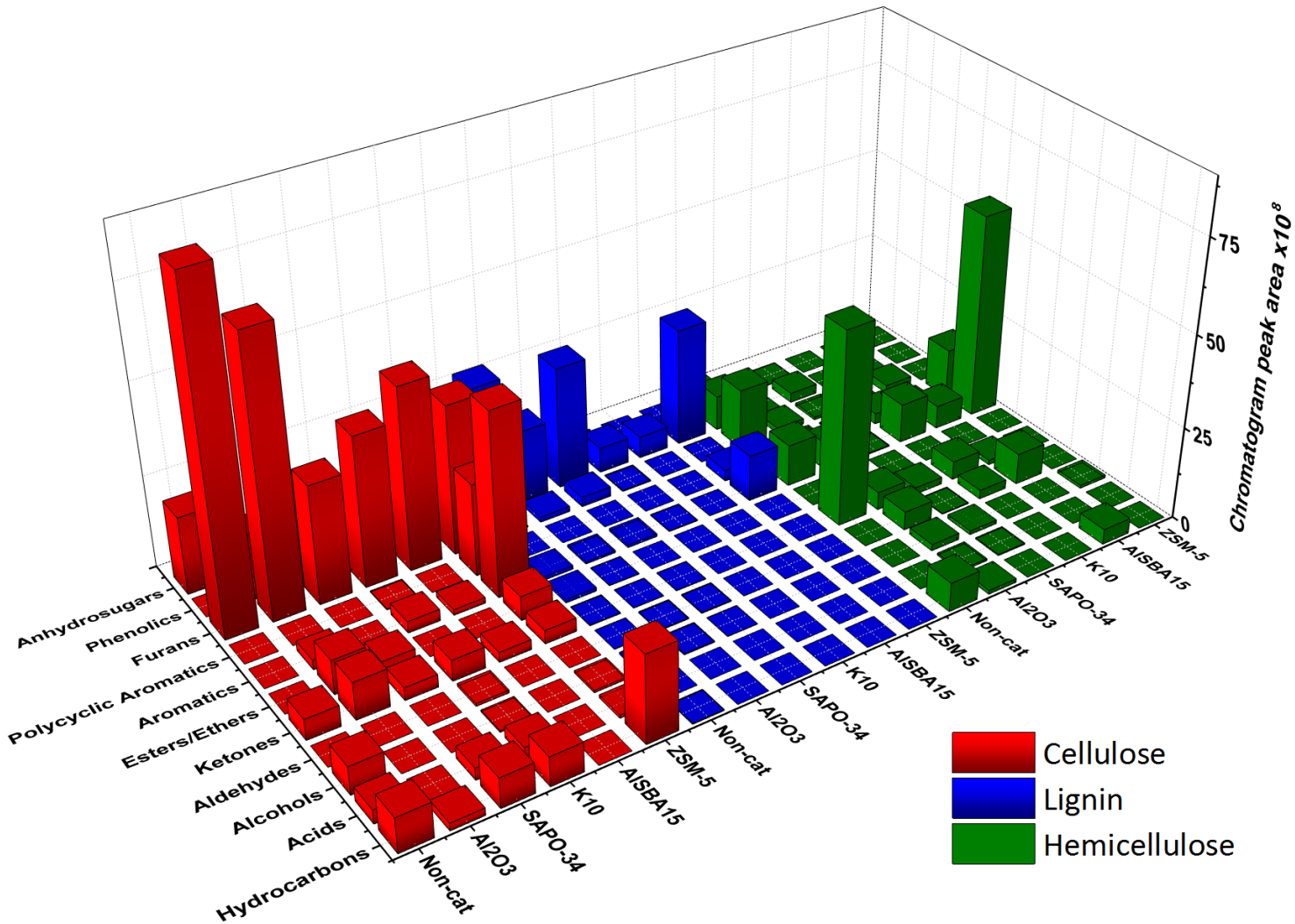

***Fig. 50**. Distribution of products from the catalytic pyrolysis of cellulose, lignin and hemicellulose at 550 °C, sorted in order of increasing acidity from left to right (x axis).*

In stark contrast, lignin was highly recalcitrant to catalytic conversion and produced a range of phenolic products similar to the non-catalytic experiment. Only the ZSM-5 catalyst was able to deoxygenate the pyrolysis vapours to form monocyclic aromatic products. The yield of phenolics was not increased by any catalyst. However, one of the limitations with this analytical pyrolysis method was the inability to detect large lignin oligomers that are present in the lignin fast pyrolysis vapours. There may have been a catalytic effect causing the partial breakdown of these large molecular weight lignin oligomers, however, they were still too large for detection. Future experiments may consider increasing the catalyst to biomass (C/B) ratio which should increase the catalytic degradation of the lignin in order to produce a measurable difference in the formed products.

For the results of the catalytic fast pyrolysis of each biomass component type (cellulose, hemicellulose and lignin), the catalysts are sorted in increasing acidity as determined by acidity analysis earlier in the chapter, Section 4.5.2. There appears to be little correlation between the product groups and the acidity of the catalyst obtained. However, as there are a broad range of molecules achievable in the catalytic fast pyrolysis of each component, this does not necessarily mean there is no effect. More detailed analysis of each product may provide further details on the pyrolysis mechanism and the nature of the catalytic reaction.

As can be observed by the product distribution in **Fig. 50**, the product distribution of the catalytic pyrolysis of three biomass components do not alter significantly, with the exception of ZSM-5 which was highly selective towards aromatic hydrocarbons. The catalytic experiments were undertaken using a catalyst to biomass waste ratio of 1:1 (C/B), therefore, to achieve higher catalytic conversion a higher proportion of catalyst should be employed in subsequent experiments. As previously aforementioned, if the ratio of catalyst to lignin was increased, a further breakdown of phenolics into lower molecular weight oxygenates and monocyclic aromatics may occur. Nevertheless, the catalytic pyrolysis of cellulose and hemicellulose using solid acid catalysts evidenced minor differences in selectivities of each material.

Due to the low activity of all catalysts, except for ZSM-5, it is hard to draw meaningful conclusions of the results. However, it was evidenced that although ZSM-5 and AlSBA15(5) had similar acidities, only ZSM-5 produced a significant yield of aromatic products. Therefore, it can be concluded, though, ZSM-5 is highly selective towards the production of mono-aromatic hydrocarbons such as benzene, toluene and xylene and their isomers. It should be noted that the commercial catalysts selected have proven catalytic ability in other thermal catalytic processes such as the methanol to olefin process and as catalyst supports in the refining of petrochemicals. Furthermore, in the initial catalytic testing with AlSBA15(5) in the previous chapter, AlSBA15(5) produced aromatic products using a simpler

hydrocarbon feedstock, LDPE (see Section 3.2.2). This demonstrates the challenging nature of catalysing the complex reactions involved in the catalytic pyrolysis of biomass.

4.5.6. Conclusion

Using the CDS analytics pyroprobe for the comparison of catalysts in the catalytic pyrolysis of biomass components is a valuable tool for the early assessment of catalytic activity and selectivity. There are identifiable differences between the production of certain categories of molecules by each of the different biomass components, cellulose, lignin and hemicellulose. As shown in the non-catalytic pyrolysis of biomass components, cellulose, produced a variety of molecules and but mainly focussed produced furans and larger anhydrosugar compounds. In contrast, lignin was highly selective for the production of phenolic compounds due to the pyrolytic decomposition of the aromatic polymer. Hemicellulose pyrolysis resulted in the production of mainly ketones and other smaller oxygenated compounds.

An important consideration of this work is that the results of the pyroprobe experiments are presented in chromatogram peak area. This assumes that the peak area of the identified products are directly proportional to the concentration of the molecule. However, it is known that each product will have an individual response factor under the given instrumental conditions which will vary between analytes. Consequently, full calibration is required to determine the actual concentration of the products. Furthermore, the proportion of the non-condensable gases such as CO, CO_2 and methane, in addition to the char and coke yields, were not quantified due to the limitations of the experimental set-up. The main limitations being the detectors (FID and MS) available on the gas chromatograph equipment connected to the pyroprobe reactor being unable to detect the non-condensable, gaseous, molecules. To overcome this a larger range of detection methods are needed such as thermal conductivity detection (TCD), in order to measure incombustible light gases. In addition, it may be possible to employ HPLC in order to detect the larger oligomers and large molecular weight sugars that are produced during pyrolysis that are not volatisable and hence cannot be detected by gas chromatography. In order to completely discern differences in the catalytic formation of products and elucidate complex pyrolysis pathways between each catalytic materials, more precise and accurate analytical detection and identification methods are required.

4.6. Overall Conclusion

This chapter has highlighted the differences in the primary make up of biomass and how the individual constituents; cellulose, lignin and hemicellulose lead to the generation of different organic product groups. Measurements from thermogravimetric analysis and differential scanning calorimetry showed

differences in the breakdown and volatilisability of the individual components. Lignin was evidently the most difficult of the three to thermally decompose and took place over a large temperature range (170-600 °C). Although lignin displayed steady mass loss over time using TGA, heat flow data derived from DSC showed the structure of lignin undergoes many chemical changes as thermal energy is applied which do not necessarily involve the release of volatiles. In contrast, hemicellulose thermally degraded over a much narrower temperature range (200-315 °C).. However, hemicellulose resulted in low volatile content and high char production which may be due to the relatively high ash content (ca. 6 wt. %) compared to cellulose and lignin. The pyrolysis of cellulose resulted in the highest volatile compounds and lowest char yield. Furthermore, the pyrolysis of cellulose was achievable at moderate temperatures (300-380 °C). Therefore, of the three biomass components, cellulose represents the most promising for the catalytic thermochemical conversion to more desirable volatile products such as pentose sugars and their derivatives.

Analytical pyrolysis was subsequently employed to separate and identify volatile products from the non-catalytic and catalytic pyrolysis of each component. All screened catalysts had an effect on the distribution of products obtained from the catalytic pyrolysis of each component. However, lignin being the hardest to the catalyse, displayed the least catalytic conversion compared to cellulose and hemicellulose. It was shown that a wide range of organic products are obtainable by the selection of an appropriate catalyst and biomass component combination. However, the low catalyst to biomass ratio employed limited the activity of the catalysts due to the complexity of each of the components. Of all the catalysts, ZSM-5 displayed significant selectivity to aromatics in the catalytic pyrolysis of all three components. Although AlSBA15(5) possessed larger pore sizes and similar acidity compared to ZSM-5, the conversion to aromatics was much less pronounced, 49.9 % compared to 1.5 % for cellulose (see **Table 13**). In order to fully compare the effectiveness of each catalyst, quantification of the desired product and associated by-products such as CO, CO_2 and char is required.

Catalytic Fast Pyrolysis of Biomass - Microscale Investigation

5. Chapter 5 - Catalytic Fast Pyrolysis of Biomass – Microscale Investigation

5.1. Introduction

Following on from the previous chapter where a selection of solid acid catalysts, including a synthesised high acidity mesoporous Al-SBA-15 catalyst, were compared for the catalytic fast pyrolysis of biomass components (cellulose, lignin and hemicellulose), this chapter advances further and focusses on the catalytic pyrolysis of raw biomass residue. Although the catalytic fast pyrolysis of biomass components offers an adequate preliminary assessment for the catalytic activity and selectivity of catalysts, there exist inevitable differences in the pyrolysis of raw biomass and the refined biomass components for several reasons:

- Method of biomass fractionation.
- Variation of physical properties of biomass (moisture content, particle size, diameter, density etc.).
- Inorganic interactions

Firstly, the biomass pre-treatment method of fractionation into its components may have a profound effect on its chemical structure and reactivity, leading to differences when undergoing pyrolysis [352]. For the catalytic pyrolysis of raw biomass, the biomass needs to be dried, milled and then sieved to manageable particle sizes. The increased moisture content of the biomass will lead to the generation of steam in the reactor which may have negative consequences [166] depending on the hydrothermal stability of the catalyst. In the most serious case, it could lead to total loss of surface area of the catalyst and is irreversible; the catalyst cannot be restored to its original activity and needs to be replaced with fresh, active catalyst. This can significantly increase operating costs of the process. Whereas the particle size and geometry of the biomass feed may lead to differences in heat transfer, volatilisation and char formation [353]. Raw biomass also contains many other inorganic constituent minerals and elements with various reactivities such as relatively inert SiO_2 and catalytically active alkali earth metals, such as K, as discussed in the General Introduction (see section 1.2.5) [68]. The presence of inorganic ash may favour the production of water, gas and char at the expense of an organic liquid yield. Furthermore, the presence of alkali earth metals may lead to irreversible catalyst deactivation due to poisoning.

Generally, woody biomass feedstocks tend to be lower in ash and be easier to process in terms of handling and feeding. Beech wood is composed of approximately 48 wt. % cellulose, 26 wt. % lignin and less than 0. 5 wt. % of ash [354]. Therefore, beech wood was selected as a representative biomass feedstock for this study due to its low ash content and wide availability compared to more

economically attractive, more heterogeneous waste feedstocks such as fast growing energy crops. The low ash content is particularly important when studying the effect of the catalyst in order to differentiate the catalytic effect of the material from the catalytic effect of the inorganics present in the feedstock. In addition, beech wood is plentifully available in the northern hemisphere [355]. Thus, beech wood is widely used and one of the most studied lignocellulosic feedstocks for the valorisation of biomass wastes [353,354,356].

One of the main conclusions of the previous chapter was the inability to quantify the products of the catalytic fast pyrolysis of the biomass components, in order to fully compare the effects of the catalysts (see section 4.6). Therefore, to quantify the products in order to better compare between catalysts, in this chapter a Frontier Laboratories (RX-3050 TR) tandem microreactor system was employed. The system was close-coupled to a gas chromatograph (GC) equipped with three separate detectors, a mass spectrometer (MS), a flame ionisation detector (FID) and a thermal conductivity detector (TCD). A schematic diagram of the system set-up is provided in **Fig. 16**. The GC also had an autosampler which enabled the fast processing of a larger number of liquid reference samples used for standard quantification. Furthermore, the presence of the TCD allowed the quantification of non-condensable gases such as CO and CO_2. The system was located at the Biorenewables Research Laboratory at Iowa State University, USA.

Another advantage the frontier laboratories system offers over the CDS analytics pyroprobe, is the existence of two independently thermally controlled micro-reactors. The first microreactor is generally used for fast pyrolysis and the vaporisation of the sample materials. It is possible to physically mix the biomass feedstock and the catalyst prior to pyrolysis in the first microreactor, thus simulating in situ catalytic fast pyrolysis. The second micro-reactor housed a quartz tube capable of operating as an ex situ catalytic fixed bed reactor. Single-shot introduction of the biomass feed into the first microreactor also makes it possible to study the sequential pyrolysis and on-line deactivation of the catalyst.

The effect of catalyst placement has been investigated by several groups but not researched in great detail [357,358]. For in situ catalytic fast pyrolysis, the biomass feed is intimately mixed in the pyrolysis reactor, enabling immediate contact between the catalyst and the pyrolysis vapours. Therefore, the catalyst will have an effect on the vapours at an earlier stage when compared to ex situ catalysis. This quick interaction may enhance the decomposition of larger pyrolysis intermediates and in turn, reduce the possibility of re-combination of primary pyrolysis intermediates [136].

For ex situ catalytic fast pyrolysis, the initial pyrolysis and catalytic upgrading can operate under independent conditions such as reaction temperature and residence time for each step. Furthermore, the char formed by fast pyrolysis can be readily separated before the vapours are transferred to the

catalytic reactor. This is an important consideration as the inorganics present in the ash can, as discussed, deactivate the catalyst and/or have a significant effect on the chemistry of the pyrolysis reactions by possibly introducing basic sites on the surface [166,359]. The gradual loss of activity and eventual deactivation of the catalyst by AAEMs requires the removal of deactivated catalyst and replacement with fresh active catalyst, hence leading to increased process expenditure.

From an engineering perspective, in situ catalytic fast pyrolysis is simpler compared to ex situ catalytic fast pyrolysis as it occurs in a single reactor. Whereas ex situ catalytic fast pyrolysis is inherently more complex, however, it allows a greater degree of control over the residence time and temperature. The added complexity of the ex situ process requires more reactors and thus may lead to higher capital and operational expenditure.

Due to the more advanced analytical capabilities of this system and the versatility of the reactor configuration this chapter aims to address two questions: **1**) does the high acidity mesoporous Al-SBA-15 perform better than a commercially available, similar acidity ZSM-5 catalyst? **2**) how does catalyst placement affect the yield of favoured products. In the previous chapter, ZSM-5 was shown to display a larger peak area percentage conversion to aromatic products compared to any other catalyst, including AlSBA15(5). Therefore, by quantifying the concentration of aromatics produced a full comparison between ZSM-5 and the mesoporous AlSBA15(5) catalyst can be made. For full scale up to bench and pilot scale reactors, both ZSM-5 and AlSBA15(5) would have to be pelletised in order to be fluidisable and operate in a fluidised bed reactor. In order to do this, a binder must be used to bind the catalyst particles together which likely result in a reduction in acidity. In this chapter, the two catalysts (ZSM-5 and AlSBA15(5)) were also compared to a commercially used Fluid Catalytic Cracking (FCC) equilibrium catalyst to benchmark against a relevant catalyst currently used industrially.

5.2. Results and Discussion

5.2.1. Materials characterisations

Biomass characterisation results

The results of the ultimate and proximate analyses, as well as the higher heating value are given in **Table 14**. Beech wood was used as a representative hard wood feedstock. The results in **Table 14** show that the beech wood had a high oxygen content (50 wt. %) and relatively low ash content (< 1 wt. %), both of which are typical values for wood biomass feedstocks.

***Table 14**. Elemental and compositional analysis of beech wood.*

	Beech wood
Ultimate analysis (wt. %$^{(d.a.f)}$)	
C	44.08
H	6.31
N	0.19
S	0.00
O*	49.42
Proximate analysis (wt. %$^{(d.b)}$)	
Moisture	4.69
Volatile matter	87.57
Fixed carbon	7.95
ASTM ash content	0.81
Higher heating value (MJ kg^{-1})	19.45

*by difference

5.2.2. Catalyst characterisation results

The XRD patterns of the catalysts, shown in **Fig. 51** below, exhibited the crystalline nature of the e-FCC and ZSM-5 materials. In addition, the diffraction pattern of the e-FCC catalyst is consistent with the planes of the overlaid zeolite Y diffraction pattern (type FAU) [360], which confirms the high level of incorporation of zeolite Y in the e-FCC material. The XRD taken in the low-angle region of the Al-SBA-15 material shows one intense peak attributed to the (1 0 0) plane and two lower intensity peaks attributed to the (1 1 0) and (2 0 0) planes, characteristic of well-ordered two-dimensional hexagonal structures [219].

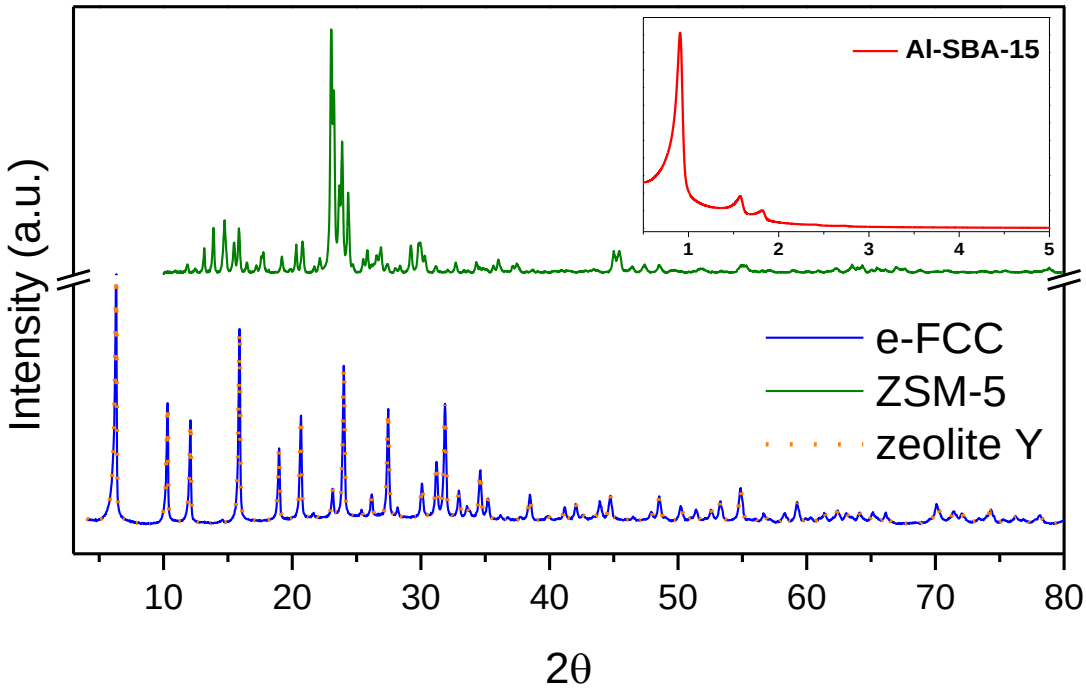

***Fig. 51**. X-ray diffraction patterns of e-FCC, AlSBA15(5) and ZSM-5 (AlSBA15(5), in inset, was measured in the low angle region).*

The SEM images of each catalyst were taken at different magnifications to determine particle morphology and are presented in **Fig. 52**. The image of the e-FCC catalyst displays the particles of spherical morphology with an approximate diameter of between 10-100 µm, which is consistent with industry standards [99]. The image of the AlSBA15(5) catalyst shows the characteristic pellet/rod-shaped morphology of the parent SBA-15 silica framework with an approximate length of 2 µm. It can be assumed that the entrance to the particle is at either end of the pellet particle and hence the reactant molecules will diffuse into the pores and travel and react with the acid sites located inside. It may be possible for acid sites to be located on the external surface area of the particles, leading to cracking on the exterior. SEM images of the ZSM-5 particles indicate that they are agglomerates of small ZSM-5 crystallites (< 10 µm). This suggests that there may be voids in between individual crystals for large molecular weight pyrolysis intermediates to enter and react with the acid sites located on the exterior of the ZSM-5 crystallites.

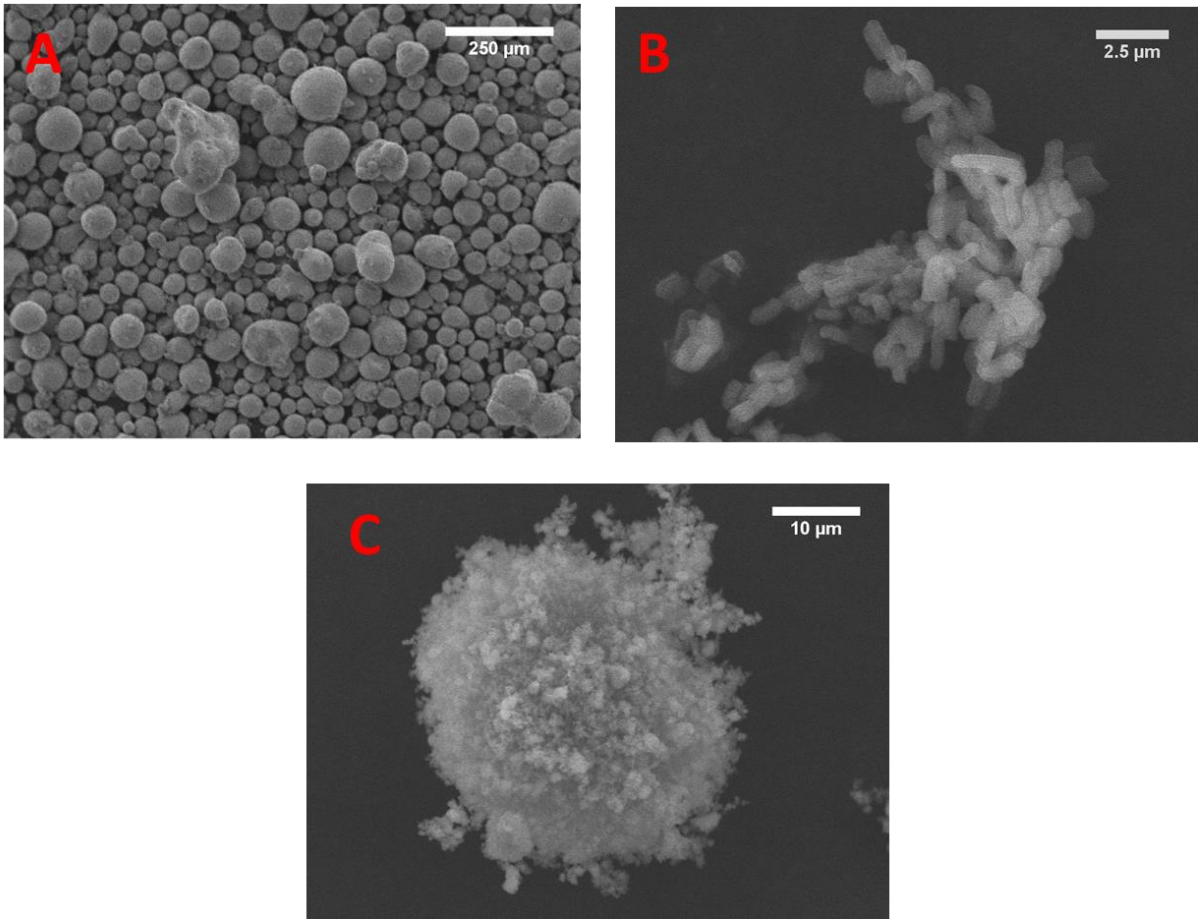

***Fig. 52**. SEM images of catalyst materials. A) e-FCC B) AlSBA15(5) C) ZSM-5.*

The nitrogen physisorption isotherms are presented in **Fig. 53**. The isotherm of e-FCC was characterised as a type IV isotherm, indicative of mesoporous solids and is associated with capillary condensation taking place in the mesopores [361]. The corresponding hysteresis loop was classified as being H4 type. H4 hysteresis loops are associated with particles with internal voids of irregular shape and broad size distribution. This was attributed partly to interparticle mesoporosity and partly to the mesoporosity of the non-zeolitic catalyst phase [237,293].

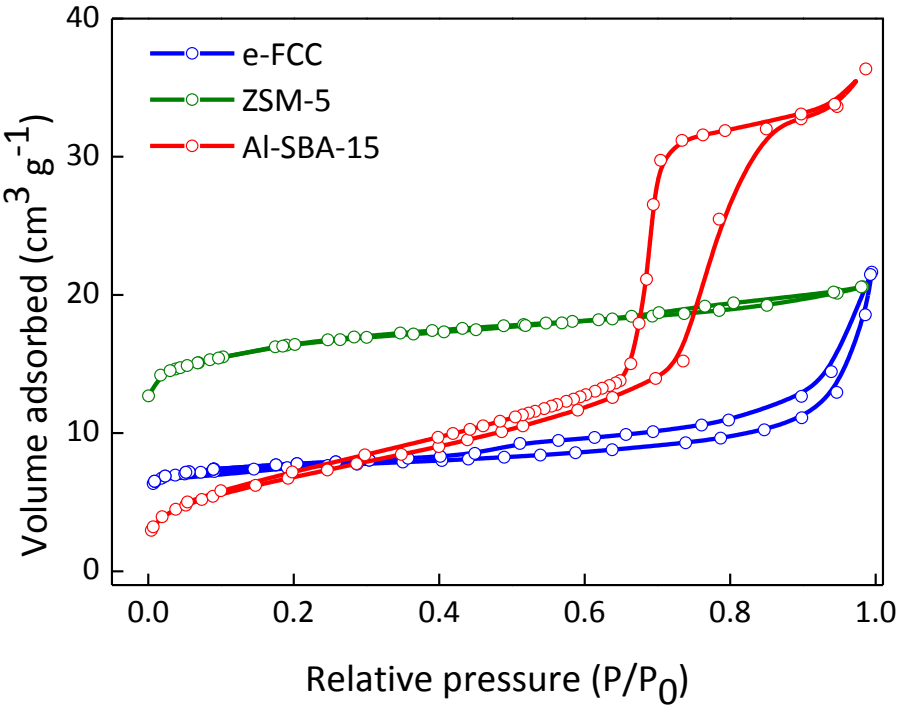

Fig. 53. Nitrogen physisorption isotherms of the three catalysts.

The ZSM-5 catalyst exhibited a Type I isotherm, as expected from a purely microporous material. On the other hand, Al-SBA-15 exhibited a Type IV isotherm with an H1 hysteresis loop, which indicated that it was a mesoporous material possessing a cylindrical pore geometry and a high degree of pore size uniformity as defined by IUPAC [294].

The BET surface areas of the catalysts, shown in **Table 15**, clearly show a significant difference (roughly 300 $m^2\ g^{-1}$) between the e-FCC catalyst and both the ZSM-5 zeolite and the AlSBA15(5) material. The e-FCC catalyst, in addition to containing an FAU zeolite phase, contains alumina, amorphous silica and clay as a binder as well as many proprietary additives. This results in macroporous voids in the particle matrix and hence a lower overall surface area. The BET surface area measurement for ZSM-5 is typical and is in the range of manufacturer stated values [362].

The AlSBA15(5) catalyst had a much lower surface area compared to typical Al-free SBA-15 materials, which generally have surface areas of approximately 800 $m^2\ g^{-1}$ [363], as discussed earlier in this thesis (see section 3.2.1). This reduction in surface area was ascribed to the incorporation of aluminium into the silica structure and the subsequent loss of microporosity, leading to a substantially mesoporous structure as evidenced by the type H1 hysteresis loop in the raw isotherm above [364]. Nevertheless, the general cylindrical pore geometries associated with SBA-15 remained unaffected by the

incorporation of aluminium. It is noteworthy that the AlSBA15(5) and the ZSM-5 catalyst had very similar surface areas.

***Table 15**. Physicochemical properties of e-FCC, AlSBA15(5) and ZSM-5.*

Catalyst	Surface area ($m^2\ g^{-1}$)	Micropore surface area ($m^2\ g^{-1}$)	Vol. micropore ($cm^3\ g^{-1}$)	Vol. total ($cm^3\ g^{-1}$)	Average pore size (nm)	Acid sites ($\mu mol\ g^{-1}$)
e-FCC	167	133	0.06	0.2	1.5	45
AlSBA15(5)	414	0	0.00	1.0	6.8	564
ZSM-5	420	353	0.16	0.2	1.2	539

To summarise the comparison of the porous properties of the catalysts (**Table 15**), ZSM-5 was a microporous material with relatively high micropore volume and micropore surface area, while AlSBA15(5) was a purely mesoporous material with a significantly higher total pore volume. Similarly, the e-FCC catalyst also exhibited mesoporosity, however, it also contained a relatively high micropore surface area, which contributed nearly to all of its total surface area. This microporosity was attributed to the zeolite Y phase of the material as also confirmed by XRD above.

The average pore diameter of the three catalysts was calculated using the BJH method, applied to the adsorption branch of the isotherms (**Fig. 53**). A plot of the pore size distributions is presented in **Fig. 54** and were expectedly different between the catalysts. AlSBA15(5) exhibited the largest average pore diameter at 6.8 nm, with a narrow pore size distribution. On the other hand, both the e-FCC and the ZSM-5 displayed a wide pore size distribution, spanning a range of different pore sizes.

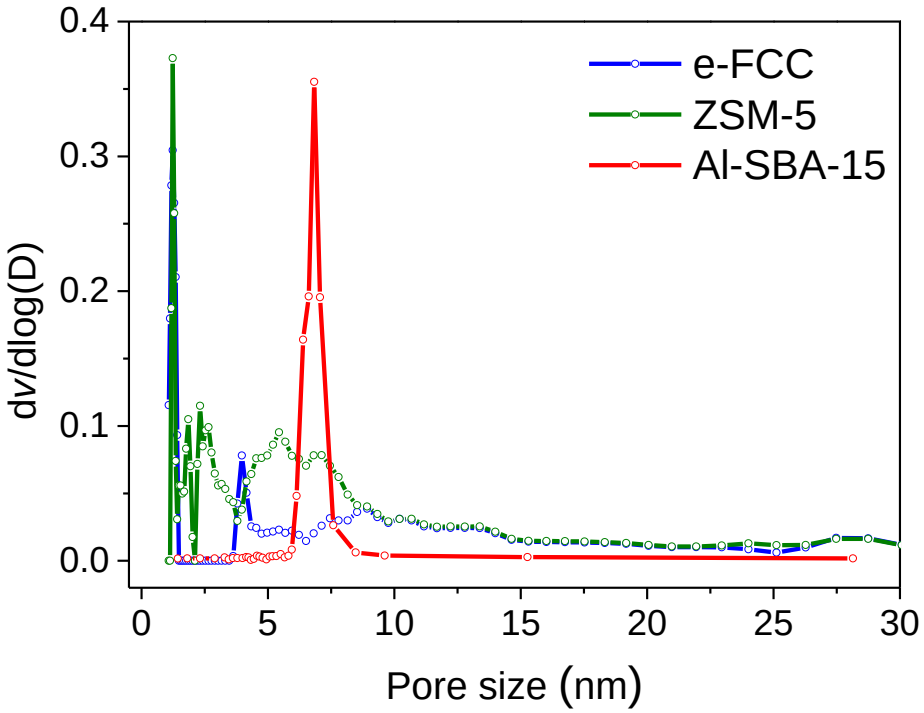

Fig. 54. *Pore size distribution plots for e-FCC, AlSBA15(5) and ZSM-5.*

ZSM-5 and FAU zeolite (the zeolite type present in e-FCC) are known to have pore sizes of ca. 0.5 nm and ca. 0.7 nm, respectively [250]. The wide pore size distribution would be expected in the case of e-FCC due to the presence of non-zeolite phases in the catalyst particle. However, for a crystalline material with a well-defined pore network such as ZSM-5, a narrow pore size distribution would be expected. This wider than expected pore size distribution in the case of ZSM-5 could be explained by intercrystalline voidage between the particles. It should be noted that the characterisation of micro and mesoporous materials by gas adsorption is not as straight forward as is probably assumed. Phenomena like the tensile strength effect, adsorbate phase transitions and monolayer formation can lead to erroneous results. In addition, the conventional models typically applied to adsorption isotherms such as BJH, HK and SF, can only partially deal with adsorption in more sophisticated materials such as in the case of e-FCC [365].

The acidic properties of the catalysts were measured and quantified using TG-TPD of n-propylamine and are also presented in **Table 15**. The ZSM-5 and AlSBA15(5) catalysts both displayed high and comparable acidity of 539 and 564 µmol g^{-1}, respectively. This indicated that the synthesis procedure employed for AlSBA15(5) (see Section 2.1.2) was effective for the incorporation of a substantial quantity of Al atoms in the tetrahedral environment in the SBA-15 structure. As discussed earlier in the thesis, the high acidity in both ZSM-5 and Al-SBA-15 was caused by framework aluminium and is

responsible for catalysing a host of reactions such as cracking, deoxygenation and aromatization, which are prominent in catalytic pyrolysis [213,366]. In contrast, e-FCC exhibited the lowest number of acid sites at 45 µmol g^{-1}, which is expected due to its low surface area. The zeolite Y (FAU type) present in e-FCC is responsible for much of the acidity. Being an equilibrium catalyst (partially deactivated) it would be expected the constant cycles of hydrothermal and high-temperature oxidation stresses that the e-FCC catalyst was exposed to during the FCC process would also lower the acidity [367].

Although acid strength cannot be directly quantified using propylamine-TPD, the acid strength of the three catalysts can be assessed by comparing the temperature of peak propene desorption (**Fig. 55**). The greater the temperature of maximum propene desorption the weaker the acid strength due to the requirement of increased thermal energy to drive the reaction rate. The propene TPD profiles (**Fig. 55**) revealed two distinct peaks for ZSM-5 (T= 419 and 487 °C), indicative of two types of acid sites with different strengths. The type of site with the greatest acid strength, T= 419 °C, was around four times larger than the type of site with weaker strength, T= 487 °C. In contrast, both e-FCC and AlSBA15(5) had only one distinguishable peak at 430 °C and 441 °C, respectively. Therefore, together with the quantitative data, the AlSBA15(5) can be considered to display similar acidic properties to those found in zeolites.

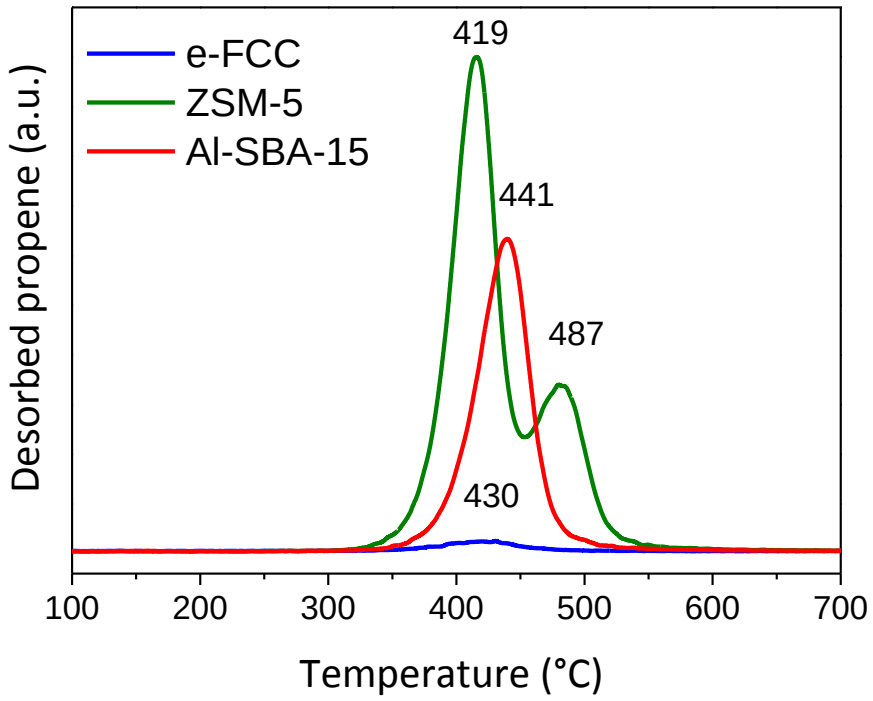

***Fig. 55**. TPD profiles of reactively formed propene from propylamine decomposition over the e-FCC, ZSM-5 and AlSBA15(5) catalysts.*

5.2.3. Micro-reactor experimental results

Non-catalytic fast pyrolysis of beech wood

The non-catalytic fast pyrolysis of beech wood at 500 °C decomposed the woody-biomass sample into a wide range of products. It must be noted that the product distribution in non-catalytic fast pyrolysis of beech wood yielded a very complex mixture of volatiles with over 300 individual products identified [15]. Quantification of the most common 30 volatile compounds and non-condensable gases (listed in Appendix C, **Table A 2** and **Table A 3)** are consistent with previously reported data [368] and provided a baseline for comparison with catalytic pyrolysis results. The quantification results are presented in **Table 16**, where the condensable products were grouped into acids, alcohols, aldehydes, esters/ethers, monocyclic aromatic hydrocarbons, polyaromatic hydrocarbons, furans, phenolics and anhydrosugars for easier comprehension. A more detailed breakdown of the quantified condensable products is provided in Appendix C, **Table A 4**. All product yields are displayed in carbon %, this is described in more detail in Chapter 2, Section 2.4.1.

Table 16. *Product distribution from the non-catalytic and in-situ catalytic fast pyrolysis of beech wood, at different catalyst to biomass ratios (C/B) at 500 °C (Carbon yields, C %).*

	No catalyst	e-FCC			AlSBA15(5)			ZSM-5		
C/B		1:1	5:1	10:1	1:1	5:1	10:1	1:1	5:1	10:1
Yield (C %)										
Acids	7.0 ±0.2	7.6 ±0.2	7.6 ±0.2	7.1 ±0.0	6.3 ±0.3	2.3 ±0.0	0.7 ±0.0	5.7 ±0.3	0.9 ±0.0	0.4 ±0.1
Alcohols	2.3 ±0.0	2.7 ±0.3	3.6 ±0.1	3.4 ±0.4	4.1 ±0.1	3.0 ±0.1	4.1 ±0.3	0.0 ±0.0	0.0 ±0.0	0.0 ±0.0
Aldehydes	7.3 ±0.2	6.9 ±0.4	3.5 ±1.9	1.6 ±0.0	1.5 ±0.1	0.0 ±0.0	0.0 ±0.0	1.2 ±0.0	0.0 ±0.0	0.0 ±0.0
Ester/Ethers	4.2 ±0.1	2.2 ±0.0	2.1 ±0.0	1.7 ±0.2	2.3 ±0.1	2.2 ±0.2	2.0 ±0.2	1.4 ±0.1	0.0 ±0.0	0.0 ±0.0
Aromatics[a]	0.0 ±0.0	0.00 ±0.0	0.04 ±0.01	0.05 ±0.01	0.0 ±0.0	0.5 ±0.0	0.7 ±0.1	2.0 ±0.1	13.9 ±0.5	15.7 ±0.5
PAHs	0.0 ±0.0	0.0 ±0.0	0.0 ±0.0	0.0 ±0.0	0.0 ±0.0	0.3 ±0.0	0.4 ±0.0	1.5 ±0.1	5.2 ±0.2	5.8 ±0.0
Furans	0.8 ±0.0	1.8 ±0.1	2.6 ±0.2	3.2 ±0.0	2.6 ±0.1	2.8 ±0.0	1.9 ±0.0	2.7 ±0.2	0.3 ±0.0	0.0 ±0.0
Phenolics	2.4 ±0.1	2.6 ±0.1	2.4 ±0.1	1.8 ±0.1	1.4 ±0.1	0.1 ±0.0	0.0 ±0.0	2.9 ±0.5	0.5 ±0.0	0.1 ±0.0
Anhydrosugars	7.6 ±0.8	4.0 ±0.9	0.8 ±0.3	0.0 ±0.0	1.0 ±0.1	0.0 ±0.0	0.0 ±0.0	2.5 ±0.4	0.0 ±0.0	0.0 ±0.0
Total Gas	6.3 ±0.5	7.9 ±0.2	9.0 ±0.6	11.1 ±0.4	10.5 ±0.2	13.2 ±0.2	15.5 ±0.5	15.3 ±0.2	22.8 ±0.6	25.1 ±1.5
CO	3.1 ±0.3	4.1 ±0.0	5.2 ±0.5	6.8 ±0.3	6.6 ±0.2	8.9 ±0.2	9.5 ±0.1	9.7 ±0.1	14.2 ±0.2	15.6 ±0.8
CO_2	3.1 ±0.2	3.8 ±0.2	3.8 ±0.1	4.3 ±0.0	3.8 ±0.0	4.2 ±0.0	4.6 ±0.1	4.1 ±0.3	5.1 ±0.0	5.4 ±0.1
Ethene	0.0 ±0.0	0.0 ±0.0	0.0 ±0.0	0.0 ±0.0	0.0 ±0.0	0.0 ±0.0	0.8 ±0.5	0.8 ±0.0	2.3 ±0.4	2.6 ±0.5
Propene	0.0 ±0.0	0.0 ±0.0	0.0 ±0.0	0.0 ±0.0	0.0 ±0.0	0.0 ±0.0	0.6 ±0.2	0.6 ±0.0	1.2 ±0.0	1.5 ±0.1
Char/Coke	19.8 ±1.6	29.5 ±2.0	28.0 ±3.7	27.3 ±0.3	46.1 ±2.7	47.5 ±6.2	40.3 ±5.1	32.5 ±8.4	33.7 ±7.2	35.6 ±2.9
Total	57.6	65.2	59.6	57.3	75.7	71.9	65.6	67.7	77.3	82.7

[a]Monocyclic aromatic hydrocarbons

The three main product groups obtained from the non-catalytic fast pyrolysis of beech wood, on a C % basis, were acids (7%), aldehydes (7.3%) and anhydrosugars (7.6%). Acids were primarily composed of acetic acid; aldehydes were mainly composed of succindialdehyde and glycolaldehyde, in equal proportions. Anhydrosugars were mostly composed of levoglucosan, the primary decomposition product of cellulose. Lower MW compounds, including alcohols, esters, ethers and furans, were produced in smaller quantities. A wide range of phenolic products were observed in relatively low concentrations and were primarily alkoxy-phenols, i.e. guaiacyl- and syringyl-type compounds that were derived from the decomposition of lignin.

The total gas yield for the non-catalytic run was 6.3 C %, with carbon ending up as both CO and CO_2 in relatively equal proportions. The char/coke yields obtained by the non-catalytic pyrolysis of beech wood were consistent with the proximate analysis results obtained by thermogravimetric analysis (see **Table 14**) and demonstrated that 8.7 % on a weight percentage basis was char. On a carbon percentage yield, this was 19.8 % of the carbon in the feedstock, as shown in **Table 16**. The total carbon yield from non-catalytic pyrolysis of beech wood was ca. 57.6 C %, which is relatively low. This was attributed to the fact that a significant portion of the products from the pyrolysis of lignocellulosic biomass are non-GC-detectable and could not be quantified [137].

In situ catalytic pyrolysis of beech wood

The in situ (biomass and catalyst were mixed) catalytic fast pyrolysis of beech wood with ZSM-5, AlSBA15(5) and e-FCC was investigated at 500 °C and at three different C/B ratios; 1, 5 and 10:1. Due to the complexity of the product stream, key pyrolysis compounds were selected in order to assess the effect of each catalyst on the conversion of the biomass pyrolysis vapours shown in **Fig. 56**. These were selected on the basis of their relative abundance and their contribution to the overall quality of the liquid product of CFP. The yields of the selected compounds are presented in greater detail **Table A 4** in Appendix C. The ZSM-5 and AlSBA15(5) catalysts had similar acidity and surface areas (see **Table 15**), enabling a close comparison between their catalytic activity. On the other hand, the e-FCC had significantly lower acidity and surface area, as explained earlier. This enabled a comparison of the products from CFP using two highly acidic catalysts (ZSM-5 and AlSBA15(5)) and a typical industrial catalyst with significantly lower acidity and surface area (e-FCC).

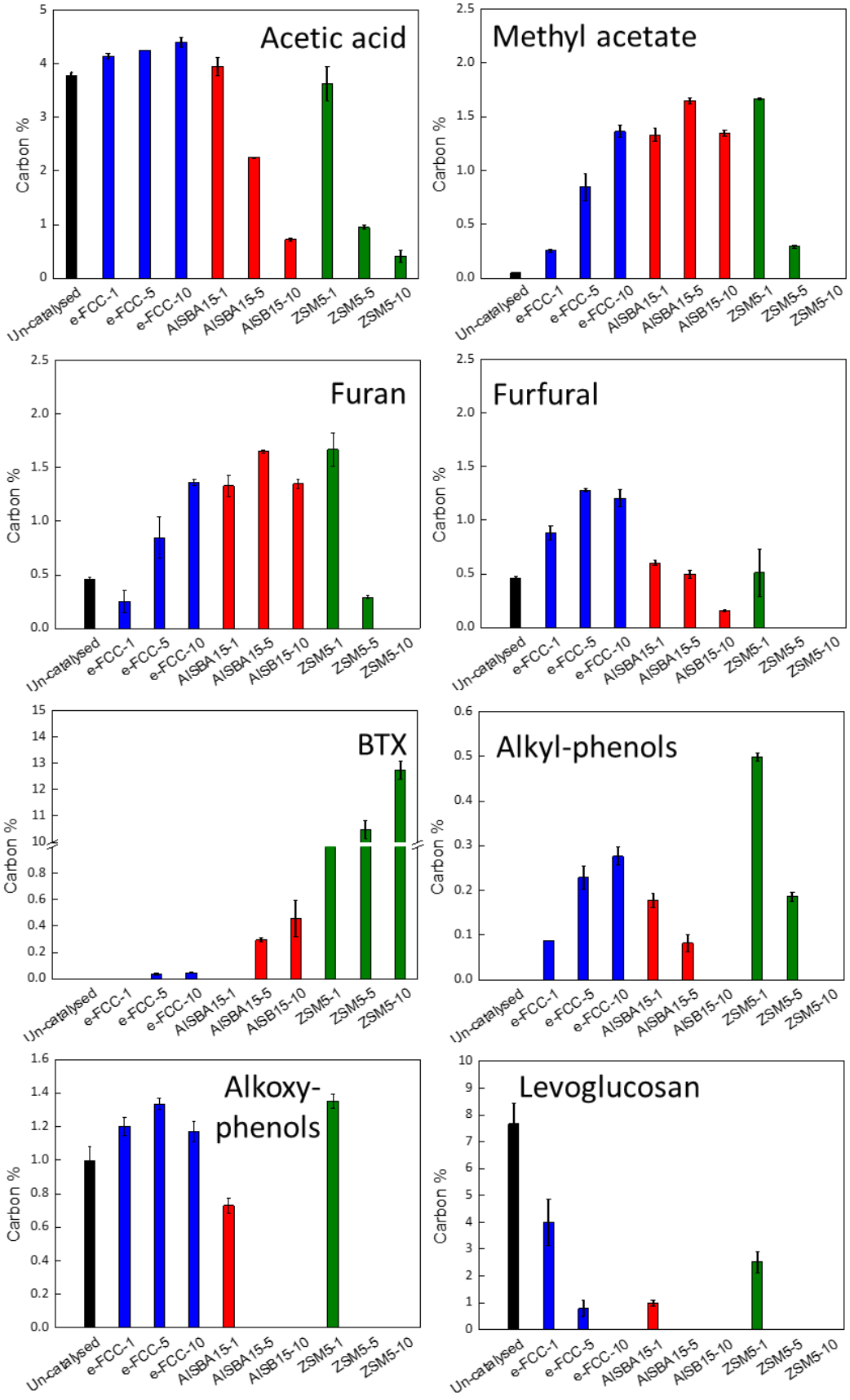

***Fig. 56**. Comparison of yields of key products from the non-catalytic and catalytic fast pyrolysis of beech wood. The number following each catalyst's name indicates the C/B ratio.*

Effect on the formation of non-condensable gases

One of the most notable observations was that all catalysts significantly increased the yields of gaseous products in the order of ZSM-5 > AlSBA15(5)> e-FCC, as can be seen in **Fig. 57**. The main gaseous products in all experiments were CO and CO_2. Notably, the CO:CO_2 ratio increased in all catalytic experiments, suggesting that the acidic catalysts primarily catalysed decarbonylation reactions, consistent with CFP studies at larger scales [54,59]. With the introduction of ZSM-5 at a C/B ratio of 1:1, total gas production was increased by approximately threefold in comparison to the non-catalytic pyrolysis. In particular, the production of alkenes, which is characteristic of extensive cracking reactions, was apparent from a low C/B ratio (1:1) in the case of ZSM-5. e-FCC did not form alkene gases, even at a higher C/B ratio (10:1).

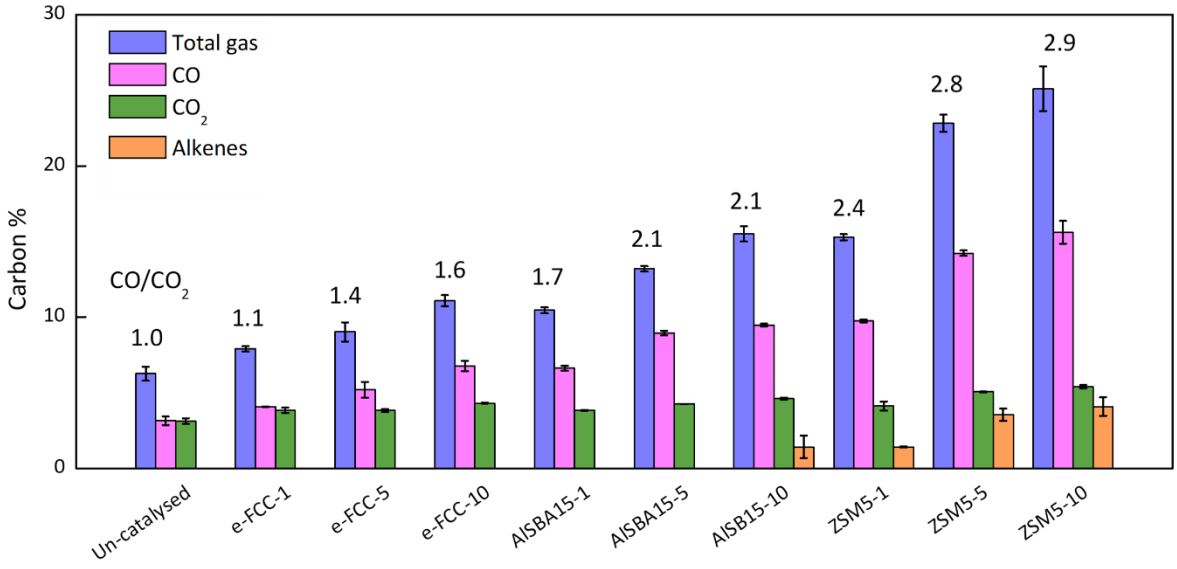

***Fig. 57**. The yield on a carbon % basis of the original feed of non-condensable gaseous products in the non-catalytic and catalytic pyrolysis of beech wood at 500 °C.*

In comparison, in the case of the AlSBA15(5) catalyst, alkenes were not detected until a C/B ratio of 10:1 was used. Moreover, the total gas yield with the AlSBA15(5) catalyst was markedly lower than for ZSM-5, despite the similar number of acid sites and surface area of both catalysts. This suggested that the number of acid sites was not the only factor the cracking and deoxygenation of the pyrolysis vapours; pore structure, acid site density (number of acid sites per unit of pore volume) and acid strength (see **Fig. 55**) possibly also played a significant role. Nonetheless, as previously stated, alkenes were not detected using e-FCC suggesting that the low acidity and surface area was still too low to produce the hydrocarbon gases.

Effect on the formation of anhydrosugars

All catalysts decreased the yield of levoglucosan, even at low C/B ratios. e-FCC decreased the yield of levoglucosan to approximately 4 C % from around 8 C %, while ZSM-5 decreased the yield to around 2.5 C %. AlSBA15(5) was the most effective catalyst for the degradation of levoglucosan and reduced the yield to approximately 1 C %. Levoglucosan is the primary decomposition product of cellulose and is a thermally stable intermediate. Cracking experiments by other researchers at temperatures as high as 600 °C have displayed no subsequent degradation intermediates [345]. Therefore, in this work, the decomposition of levoglucosan was solely attributed to catalytic reactions and not to thermal cracking.

The kinetic diameter of levoglucosan is 0.67 nm [195], whereas the well-defined pore geometries of FAU (e-FCC) and MFI (ZSM-5) are ca. 0.7 nm [369] and ca. 0.5 x 0.5 nm [370], respectively. The N_2 physisorption measurements of the AlSBA15(5) catalyst showed that the catalyst exhibited a hexagonal cylindrical pore arrangement with a much larger mean pore diameter of approximately 7 nm (**Table 15**). Therefore, the diffusion of levoglucosan was most likely limited in ZSM-5, hindering its conversion on the majority of acid sites of the internal zeolite structure. Instead, the catalytic degradation of levoglucosan took place on the acid sites located on the external surface of the ZSM-5. A combination of the acidity of the catalyst and the accessibility of the acid sites were key factors in the amount of levoglucosan conversion, as AlSBA15(5) with a fairly similar number of acid sites to ZSM-5 displayed higher conversion of levoglucosan at lower C/B ratios. In comparison, e-FCC, with a lower quantity of acid sites present, was significantly less effective for the conversion of levoglucosan.

In the proposed mechanism of acid catalysed decomposition of levoglucosan by Lin et al. [311] (discussed in more detail in the previous chapter, see section 4.2), levoglucosan is first decomposed through dehydration to other anhydro-monosaccharides such as levoglucosenone. These are then decomposed to form furanoses and a variety of fragmentation species such as glycolaldehyde and glyceraldehyde, through dehydration, decarbonylation, decarboxylation and retro/aldol condensation reactions.

Effect on the formation of furans

The production of furan compounds was increased by all three catalysts in comparison to the non-catalytic fast pyrolysis of beech wood (**Table 16** and **Fig. 56**). This was attributed to the breakdown of levoglucosan, as described above, as well as to the cyclisation of hemicellulose intermediates [349]. The highest yield of furans was achieved with the e-FCC catalyst at a C/B ratio of 10:1 (**Table 16**) and increased with the increasing C/B ratio. Similarly, high initial yields were evident in both ZSM-5 and AlSBA15(5), confirming acid catalysed degradation of levoglucosan and hemicellulose for the

formation of furan compound. However, at increased C/B ratios of ZSM-5 and AlSBA15(5) the yield of furans was reduced. This suggested that furans were intermediate catalytic products and were evidently further converted to other compounds when more acid sites became available.

The data on the yields of individual furan type products, provided in Appendix C (**Table A 4**), shows there was variability across the three C/B ratios and across the three catalysts. This may provide mechanistic information on their formation and conversion. For example, as evident in **Fig. 56**, the yield of furfural initially increased, using the e-FCC catalyst, from 0.9 C % to 1.3 C % at C/B ratio of 1:1 and 5:1, respectively. At a C/B ratio of 10:1 of e-FCC, the yield of furfural is decreased in favour of the formation of furan. This suggests that furfural is probably decarbonylated to furan as the number of available acid sites increases.

A mechanism for the decarbonylation of furfural to furan was proposed by Charoenwiangnuea et al. [371] and is represented mechanistically in **Fig. 58**. A previous experimental investigation by Fanchiang and Lin [372] and a successive theoretical investigation over ZSM-5 by Charoenwiangnuea et al. [371], both proposed that furan is subsequently converted to intermediates such as cyclohexene and 3,4-dimethylbenzaldehyde and then to higher aromatics in the pores of ZSM-5. This is supported in this work with high initial yields of furan using ZSM-5 at 1:1 C/B ratio (2.7 C %) and then a reduction of furan (0.3 C %) in favour of aromatics at higher C/B ratios (5 and 10:1). The conversion of furan at high C/B ratio was also observed using AlSBA15(5). However, due to the low yield of aromatics by this catalyst, it was unlikely that furan was converted to aromatics by AlSBA15(5).

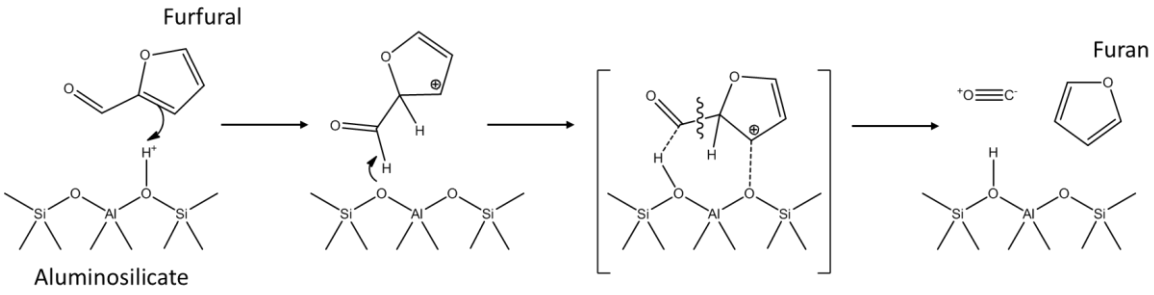

***Fig. 58**. Proposed mechanism by Charoenwiangnuea et al. [23] for the acid catalysed conversion of furfural to furan and carbon monoxide.*

Effect on the formation of acids

The high yield of acidic products in fast pyrolysis liquid, in particular, acetic acid, is well-known and is responsible for its detrimental effects such as low stability and corrosiveness [21]. In this study, there was a high yield of acid products for the uncatalysed pyrolysis of beech wood. The yield of acidic products was increased slightly with the introduction of the e-FCC catalyst. This was attributed to the

acid-catalysed cracking of biomass oligomers facilitated by e-FCC. In contrast, a significant reduction in the yield of acidic products was evidenced by both the AlSBA15(5) and ZSM-5 catalysts.

It was suggested by Corma et al.[9] that acetic acid is first converted to acetone and subsequently dehydrated to iso-butene. It is then further converted to aromatics, alkenes and coke in acidic catalysts, which is in agreement with our observations in the case of the ZSM-5 catalyst (see **Table 16** and **Fig. 56**). However, the conversion of acetic acid in of AlSBA15(5) did not result in any significant yields of other compounds except non-condensable gases and coke. This was despite the fact that the AlSBA15(5) catalyst had very similar total surface area and acidity to the ZSM-5 catalyst (see **Table 15**). This suggested that the higher acidity and the microporous shape-selective structure of the ZSM-5 were more important factors for the formation of desirable aromatic hydrocarbons (**Fig. 59**, acetic acid and toluene). The absence of these key properties resulted in the conversion of the highly reactive biomass-derived compounds to coke and non-condensable gases, as was observed in the case of the AlSBA15(5) catalyst.

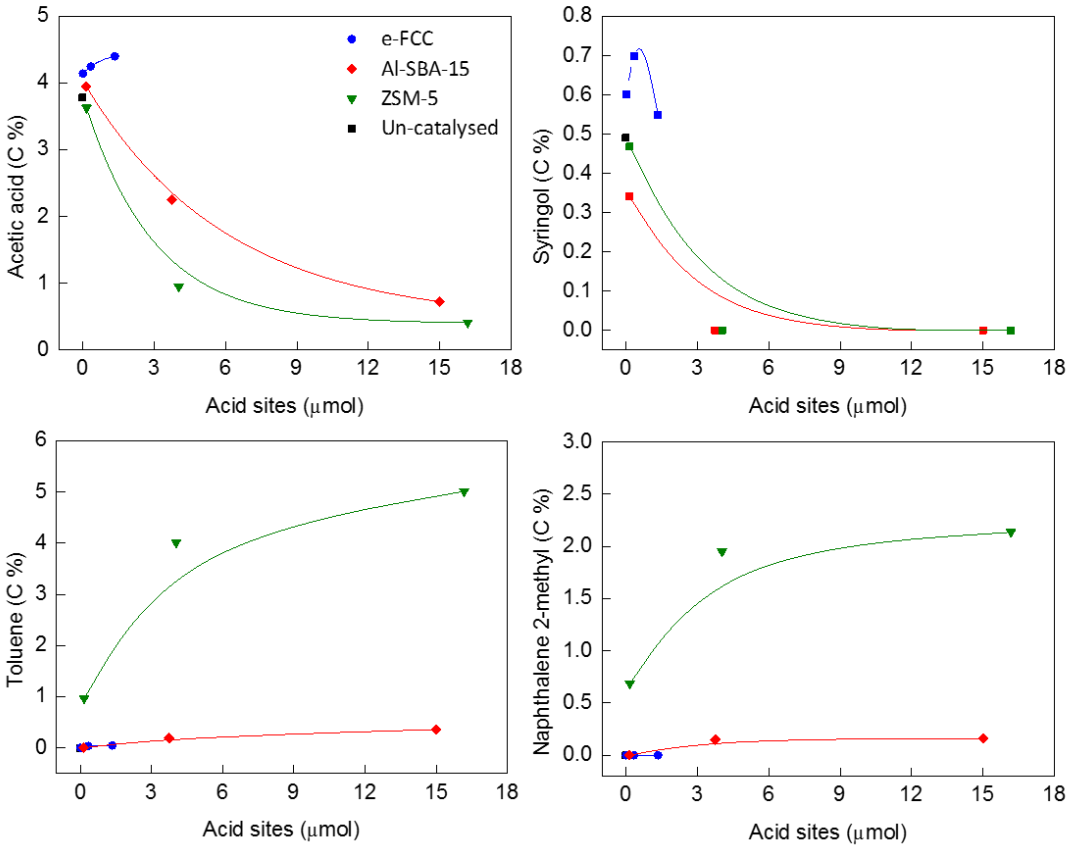

***Fig. 59**. Relationship between acetic acid, syringol, toluene and naphthalene 2-methyl and number of acid sites in each experiment.*

Effect on the formation of phenolic compounds

Fig. 56 shows that the yield of alkoxy-phenols was slightly reduced, while the formation of alkylated phenols was observed using Al-SBA-15 and ZSM-5 catalysts compared to the non-catalytic pyrolysis. This effect was more pronounced in the case of the AlSBA15(5) catalyst. Considering the similar acidity and surface area, this was attributed to the lack of diffusional limitations compared to the ZSM-5 catalyst. Increased C/B ratio of these catalysts resulted in the complete elimination of alkoxy-phenols but also the reduction and eventual elimination of alkyl-phenols as well, which was advantageous in terms of oxygen rejection. On the other hand, in the case of the e-FCC catalyst, a notable increase of alkoxy-phenols was observed, accompanied by an increase in the yields of alkyl-phenols, which further increased with increasing C/B ratio. Based on these observations it can be concluded that the acid catalysts facilitated the decomposition of lignin-derived oligomers into alkoxy-phenolic products (**Fig. 59**, syringol), which further reacted on the acid sites to form deoxygenated alkyl-phenols, i.e. increased oxygen rejection. Higher acid site availability by the introduction of more catalyst in the reactor (higher C/B ratios) resulted in the conversion of the alkyl-phenols to other products, such as aromatic hydrocarbons, non-condensable gases and coke.

Work by To and Resasco [373], on the conversion of low MW phenolic compounds over ZSM-5 and zeolite Y (FAU type), evidenced the conversion of phenolics to aromatics via the formation of a reactive phenolic pool. Furthermore, in their work, ZSM-5 showed better performance in terms of production of aromatics and increased resistance to deactivation than zeolite Y. However, it was observed that below 600 °C, a considerable proportion of the reactant phenolics and products became trapped inside the pores of the zeolites resulting in coke formation. This was due to the high adsorption capacity of the zeolites which led to increased coke yields due to entrapment within the pores. Increasing the temperature of their experiments resulted in the cracking of the adsorbed phenolics and the formation of aromatic hydrocarbons. Consequently, the yield of coke was also reduced.

The results in this thesis appear to be in disagreement with other studies where the catalytic fast pyrolysis of biomass with mesoporous aluminosilicates was investigated. In other studies increased yields of phenolic compounds were observed [212,374]. However, other studies have used mesoporous aluminosilicates with much lower acidity compared to the acidity of AlSBA15(5) used in this study, so a direct comparison of high acidity zeolites is unreasonable. As previously discussed, an increase in phenolics was observed using the low acidity e-FCC catalyst, of similar acidity to mesoporous aluminosilicates used in other studies. It is therefore likely that higher acidity results in the elimination of phenols.

Effect on the formation of aromatics

As expected, the ZSM-5 catalyst was particularly effective for the formation of monocyclic aromatic hydrocarbons. At the lowest C/B ratio (1:1), the monocyclic aromatic hydrocarbons yield was ca. 2 C % yield and was significantly increased to nearly 14 C % at a 5:1 ratio. Interestingly, at 10:1 ratio there was only a relatively slight increase in aromatics and was not proportional to the increased C/B ratio. This suggests that there is an optimum ZSM-5 C/B ratio for the formation of aromatic hydrocarbons.

As discussed earlier, despite the similar acidity and surface area of AlSBA15(5) to ZSM-5, the AlSBA15(5) produced a lower quantity of aromatics in comparison to ZSM-5. It was hypothesised the combination of large pore volume and a high number of acid sites facilitated the repolymerization of the highly reactive biomass-derived products to large, high molecular weight products and eventually to coke [190]. e-FCC produced a very small quantity of aromatics (< 0.05 C %), even when high C/B ratios were employed. The low yield was attributed to the low acidity and low surface area of the catalyst.

Effect on the formation of PAHs

An almost linear trend is evident between the formation of monocyclic aromatic hydrocarbons, namely benzene, toluene and xylenes, and PAHs in ZSM-5. This suggests an inefficient diffusion of the monocyclic aromatics out of the pore network of the ZSM-5, allowing further aromatisation reactions to take place. However, the ZSM-5 catalyst exhibited superior performance compared to AlSBA15(5) in terms of limiting excessive aromatisation reactions for the formation of bulky PAH products. Even though the overall yield of aromatics produced by AlSBA15(5) was much lower, the ratio of PAHs to monocyclic aromatics was substantially greater in the case of AlSBA15(5) (0.64) compared to ZSM-5 (0.37). This again can be attributed to the larger pore size of AlSBA15(5) compared to ZSM-5.

The larger pore size of AlSBA15(5) resulted in enhanced product and reactant diffusion, however, due to the large available pore space, it also readily allowed the formation of higher MW PAHs. This was further supported by the fact that lower MW PAHs, such as naphthalene and naphthalene 2-methyl, were formed in ZSM-5 in higher proportions due to the restricted pore space (**Fig. 59**, naphthalene 2-methyl). In contrast, AlSBA15(5) produced a larger proportion of higher MW PAHs, such as anthracenes. These contributed to 52 % of overall PAHs compared to 7 % in ZSM-5. It is therefore evident that both ZSM-5 and AlSBA15(5) catalysed aromatization reactions. Though the production of undesirable high molecular weight PAHs and coke (discussed later) was increased by AlSBA15(5) due to the absence of micropores which restricted excessive aromatisation. It should be noted that the production of PAHs should be minimised due to concerns over their toxicity [339].

Effect on the formation of coke

The coking and subsequent deactivation of the catalyst is one of the major factors that impact the economic feasibility of many biomass catalytic upgrading procedures, including catalytic fast pyrolysis [375]. The effect of coking can be managed in CFP using circulating fluidised bed reactor designs, whereby coke burning for the regeneration of the catalyst also provides the process with heat. However, the main problem with coking is the carbon loss from the liquid product resulting in an unfavourable high O/C ratio and lower liquid product yield. Therefore, the minimisation of coke yields while maintaining high levels of catalytic activity is essential for future catalyst design.

Coke is mainly formed on the active acid sites and is produced by several mechanisms such as condensation and hydrogen transfer [376]. Moreover, so-called coke-precursors, often oxygenated hydrocarbons such as phenolics and the polymerisation of larger aromatic products, are notorious for favouring the production of coke [377,378]. In the catalytic fast pyrolysis experiments, it can be expected that char yields remain relatively constant. Therefore, any significant increase in the char/coke yields can be attributed to catalytically formed coke on the surface of the catalyst. The results show that there was a significant increase in the char/coke yields in the catalytic experiments compared to the non-catalytic experiment (char yield 19.8 C %, **Table 16**).

In the catalytic experiments, ZSM-5 produced coke yields in the range of ca. 32 to 36 C %. The coke yields increased slightly with increasing C/B but overall remained relatively stable. AlSBA15(5) produced considerably higher yields of coke in the range of ca. 40 C % and 48 C %. The mesoporous nature of the AlSBA15(5) proved to be favourable for coke formation, compared to ZSM-5, by providing more space for coke precursors to form and polymerise. On the other hand, the microporous pore geometries of ZSM-5 restricted the formation of undesirable coke by preventing the repolymerisation of oxygenates and other compounds. e-FCC exhibited the lowest char/coke yield among all three catalysts (27-30 C %), which was attributed to its low overall activity. The char/coke yields produced by e-FCC remained relatively stable with increased C/B ratios and displayed lower standard deviation between experiments.

The standard deviation of the char/coke yields was notably high due to the accuracy of the char/coke yield experimental method. Although there was significant variance between the char/coke yield results, there were no other products observed by GC-MS. Therefore, it is reasonable to assume that any increase in mass was due to catalytically formed coke.

5.2.4. Ex situ catalytic pyrolysis of beech wood

The ex situ catalytic fast pyrolysis of beech wood was performed using the same Frontier Labs microreactor for comparison with the in situ experiments. In these experiments, the beech wood pyrolysis vapour was passed over the catalyst bed which was maintained at 500 °C. Based on the results from the in situ experiments, it was decided the C/B ratio to be used was 5:1, to provide optimal conversion to condensable liquid products without further cracking to low molecular weight compounds and non-condensable gases. The resultant chromatograms were integrated and quantified for comparison with the in situ catalytic pyrolysis of beech wood at C/B = 5:1.

5.2.5. Comparison with in situ catalytic fast pyrolysis

e-FCC

A comparison of the FID gas chromatogram traces for both the ex situ and in situ catalytic pyrolysis of beech wood is presented in **Fig. 60**. The two GC traces are very similar to each other suggesting that there is little difference between the two reactor configurations. Although many of the peaks occur at similar retention times, after closer inspection it is apparent that there are subtle differences in peak height and area. The increase in peak area and height appears to happen for the majority of ex situ peaks.

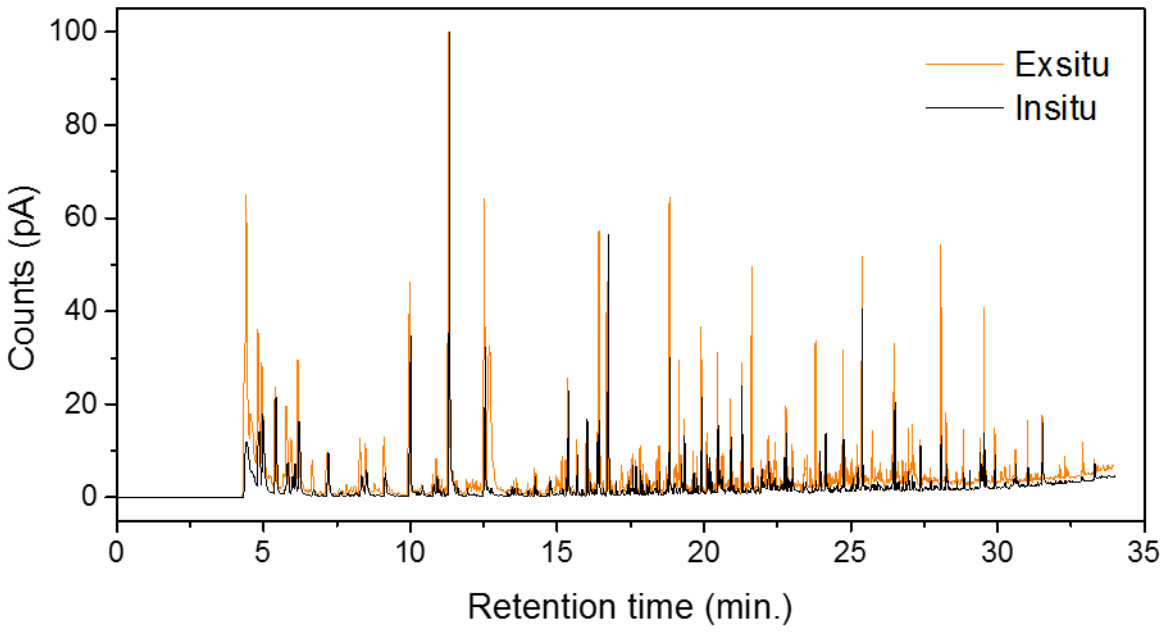

***Fig. 60**. GC chromatogram using FID detector for the in situ and ex situ catalytic pyrolysis of beech wood using e-FCC at a 5:1 C/B ratio.*

AlSBA15(5)

The gas chromatogram FID trace for the ex situ and in situ catalytic pyrolysis of beech wood using AlSBA15(5) is presented in **Fig. 61** and was much more crowded compared to e-FCC. However, many of the peaks have smaller relative peak heights and areas suggesting that there was a wider range of products formed in lower individual quantities. Similarly to e-FCC, many of the peak areas appear to be greater in the ex situ GC trace compared to the in situ one.

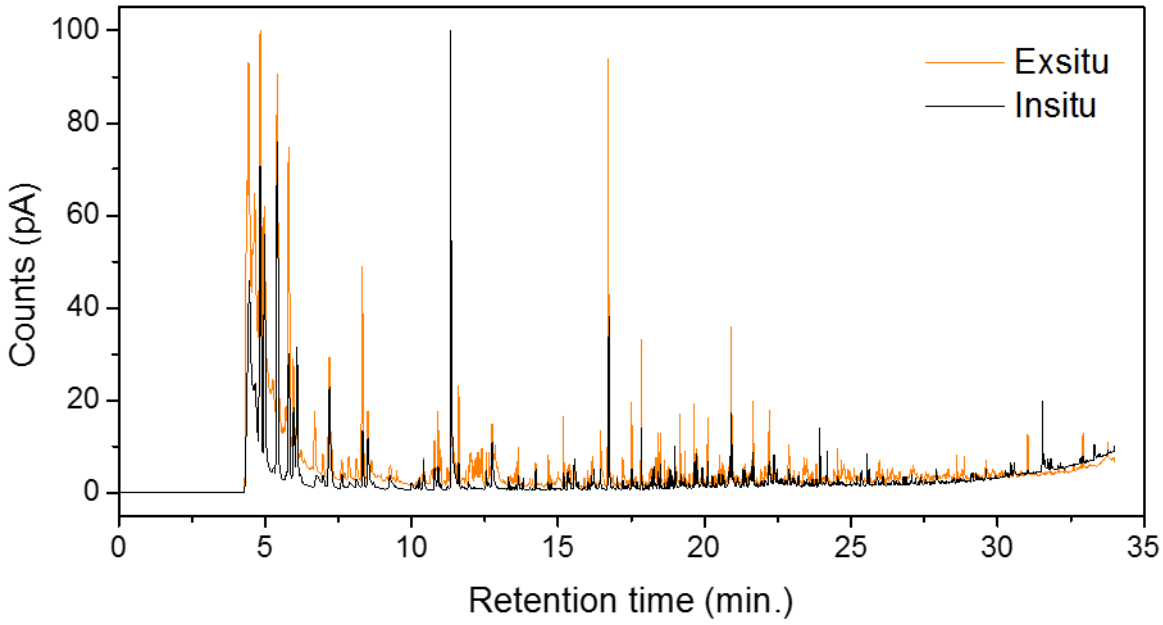

***Fig. 61**. GC chromatogram using FID detector forthe in situ and ex situ catalytic pyrolysis of beech wood using AlSBA15(5) at a 5:1 C/B ratio.*

ZSM-5

A comparison of the FID chromatogram traces for both the ex situ and in situ catalytic pyrolysis of beech wood using ZSM-5 is presented in **Fig. 62**. As with the other catalysts, the GC chromatograms for both in situ and ex situ are very similar. This implies there are only small differences between the two configurations. It is apparent that there are fewer peaks using ZSM-5 than both AlSBA15(5) and e-FCC, suggesting that ZSM-5 is more selective towards certain products. This has been investigated further via peak identification using mass spectrometry and quantification using calibration standards.

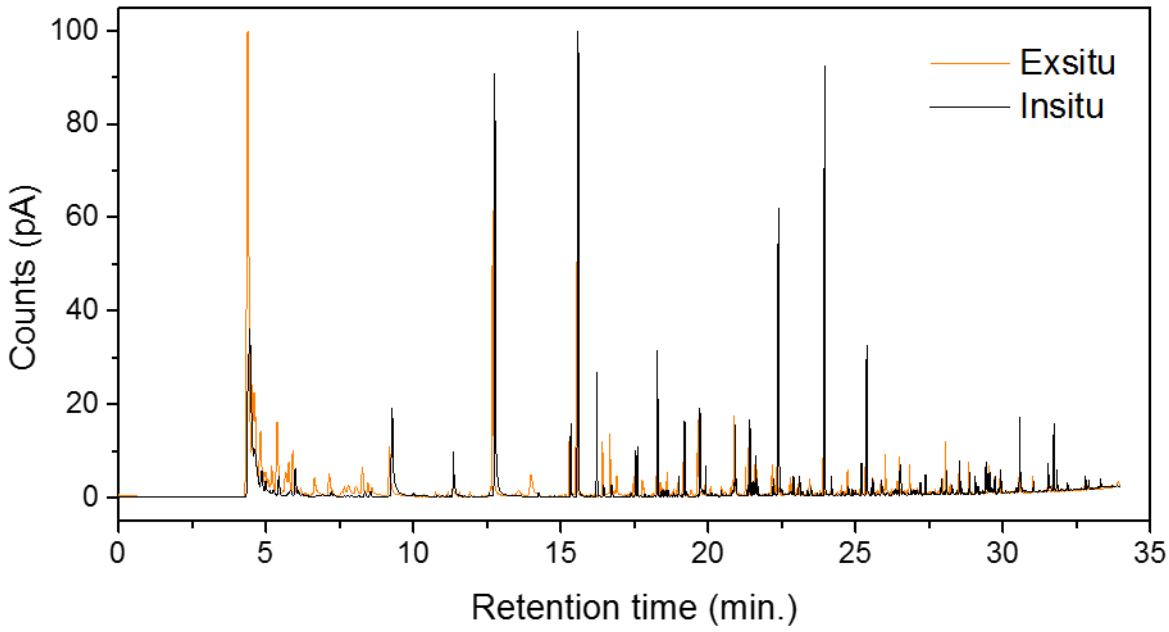

***Fig. 62**. GC chromatogram using FID detector for the in situ and ex situ catalytic pyrolysis of beech wood using ZSM-5 at a 5:1 C/B ratio.*

Product quantification

Quantification of the volatile components revealed subtle differences between the two reactor configurations (in situ/ex situ). With the catalyst employed in the in situ configuration, the catalyst comes into direct contact with the beech wood during pyrolysis. In contrast, for the ex situ configuration, the vapours come into contact with the catalyst after they are transferred to the catalyst bed. A comparison of the main groups of compounds produced for the in situ and ex situ catalytic fast pyrolysis of beech wood at a C/B ratio of 5:1 is presented in **Fig. 63**.

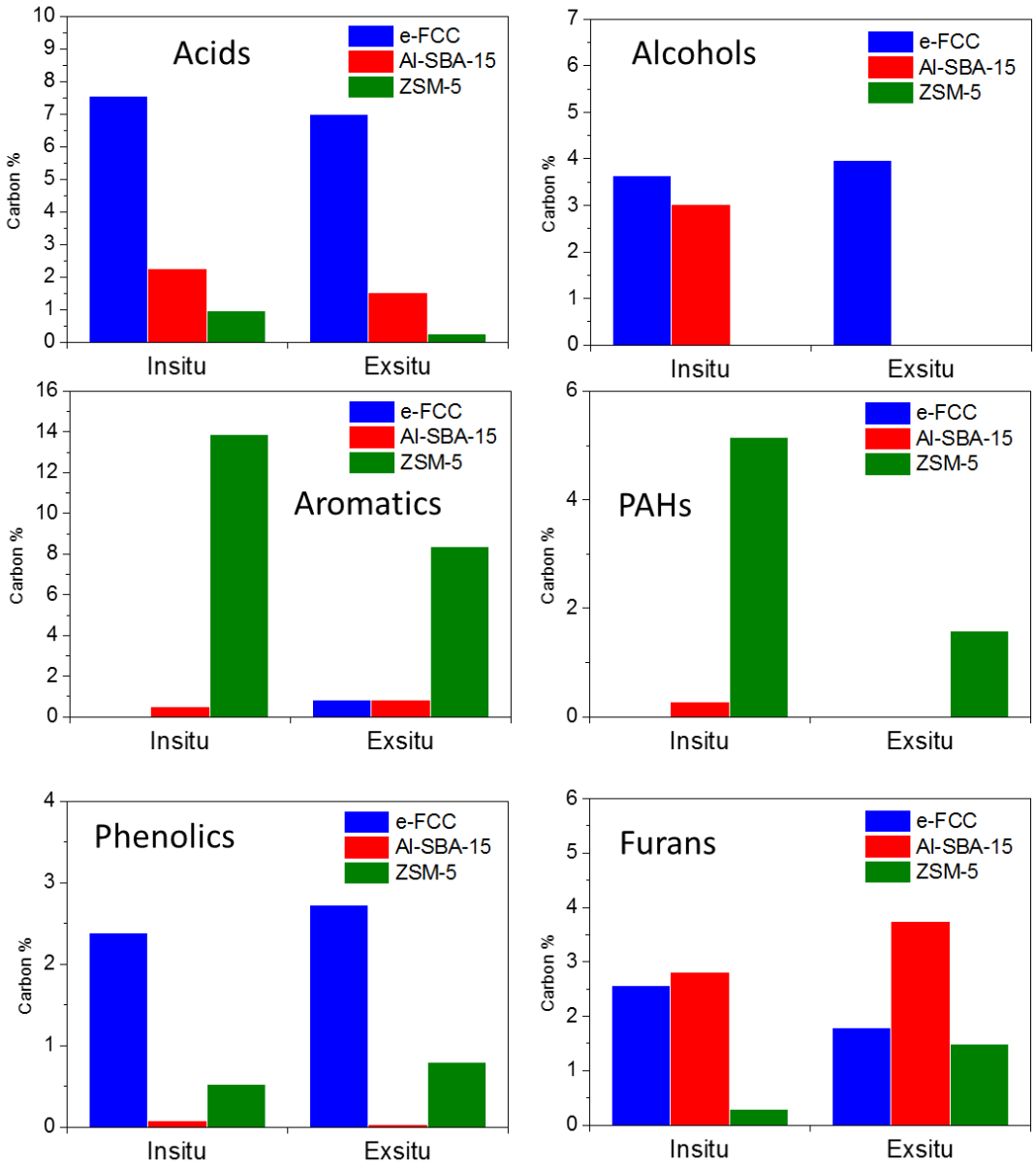

***Fig. 63**. Comparison between in situ and ex situ catalytic pyrolysis of beech wood.*

For all catalysts, acidic compounds were reduced using the ex situ configuration compared to the in situ configuration. There was no significant difference between the in situ and ex situ configurations for the degradation of larger anhydrosugar molecules for all catalysts and as such, they are not presented here. The ex situ catalytic fast pyrolysis using ZSM-5 reduced the yield of monocyclic aromatics products (8.35 C %) produced compared to the in situ configuration (13.89 C %). This reduction was also mirrored for the production of PAHs, 5.16 C % for in situ compared to 1.58 C % for ex situ. These results can be rationalised by attempting to determine the reaction mechanism. Previous studies cited in the literature have investigated the production of aromatics; especially in the methanol to olefin synthesis (MTO) process [379].

Bjorgen et al. [380] proposed a dual catalytic cycle mechanism in their work on the conversion of methanol to hydrocarbons over ZSM-5. In the dual catalytic cycle, methanol is competitively converted to either to aromatics or olefins. According to their results, the two cycles do not operate independently as the olefins produced can be further aromatised to produce aromatic products. Similar observations were made by K. Wang, P. Johnston and R. Brown [381], in a comparison between in situ and ex situ catalytic fast pyrolysis of hybrid poplar over ZSM-5. One hypothesis for this observation is the difference in mass transfer rates. For in situ catalytic fast pyrolysis, the catalyst is in direct contact with the produced vapours, thus the catalyst is exposed to a concentrated stream pyrolysis vapour. In contrast, for the ex situ configuration, the pyrolysis vapours are diluted by the carrier gas during the transfer to the catalyst bed. Therefore, there is a reduction in catalyst contact time between the catalyst and the vapours in the ex situ configuration. The lower catalyst contact time of the vapours may result in less oligomerisation of the olefins to form aromatics and hence they remained as olefins in the gas phase.

For AlSBA15(5) and e-FCC, the ex situ configuration had the opposite effect on aromatic production which increased compared to the in situ catalytic pyrolysis. In this case, a shorter vapour residence time was advantageous. This could be possibly due to the lack of shape selectivity of these catalysts, therefore the aromatics formed may be further cracked with increased catalyst contact time. Phenolics and furans, with the exception of e-FCC, were generally increased in ex situ catalytic fast pyrolysis. This could also be due to the shorter contact time with the catalyst, as the phenolics and furans are not further deoxygenated and cracked.

The difference between in situ and ex situ configurations was also evident in the production of gases. The total gas produced in all ex situ experiments increased by almost a third with all catalysts compared to the in situ experiments as is evident in **Table 17** below. Furthermore, for both the e-FCC catalyst and AlSBA15(5) the quantity of CO and CO_2 were both increased, signifying more decarbonylation and deoxygenation reactions occurred during the catalysis in the ex situ configuration. Interestingly, the yield of alkene gases such as ethene, propene and 1-butene were all increased by all catalysts. The greater yield of alkenes supports the previously discussed dual catalytic mechanism, with the olefin cycle being preferred over the aromatic cycle for ex situ catalytic fast pyrolysis.

***Table 17**. Distribution of non-condensable gaseous products for in situ and ex situ CFP of beech wood at 500 °C using a C/B of 5:1.*

Gases	e-FCC		AlSBA15(5)		ZSM-5	
	In situ 5:1	Ex situ 5:1	In situ 5:1	Ex situ 5:1	In situ 5:1	Ex situ 5:1
Yield (carbon %)						
CO	5.20	6.31	8.95	10.48	14.22	12.44
CO_2	3.83	5.45	4.25	6.01	5.05	6.64
Ethene	0.00	0.26	0.00	0.69	2.34	3.34
Propene	0.00	0.20	0.00	0.72	1.20	4.41
1-Butene	0.00	0.60	0.00	0.20	0.00	0.52
Total Gas	9.03	12.82	13.20	18.10	22.82	27.36

Although carbonaceous deposits and char formation was not measured during these experiments, it can be assumed that for ex situ catalytic fast pyrolysis char has already been successfully separated as a by-product or be burnt to provide heat for the process. In addition, char can also find value as a soil amendment and as a carbon sequestration agent [382]. In summary, differences in catalyst placement evidently had an effect on catalyst selectivity as shown in **Fig. 63** and **Table 17** above. This should be considered in the design of catalytic reactors for the fast pyrolysis of biomass when taking into account the advantages and disadvantages of each reactor configuration.

5.2.6. Deactivation of catalysts in the ex situ catalytic pyrolysis of beech wood

The deactivation of the catalyst and the increased O/C ratio of the liquid product due to carbonaceous deposits (coke) on the catalyst is a major challenge in catalytic fast pyrolysis. All three catalysts (AlSBA15(5), ZSM-5 and e-FCC), positioned in the ex situ catalyst bed, were subjected to sequential intermittent shots of beech wood pyrolysis vapour in order to detect evidence of deactivation. The results from these experiments are presented in **Table 18** below. Unsurprisingly, gradual deactivation was observed by all catalysts after five shots of beech wood pyrolysis vapour. The effect of deactivation was more pronounced in the two more acidic catalysts, AlSBA15(5) and ZSM-5, while the lower acidity e-FCC catalyst was less affected. For e-FCC, the yield of all products, with the exception of larger anhydrosugars, remained fairly constant across the five shots. Anhydrosugars increased with the increasing number of shots of pyrolysis vapour to the catalyst, from 0.71 C % in experiment number 1 to 2.18 C % by experiment number 5. The decreased conversion of larger anhydrosugars to lower molecular weight products indicated the deactivation of the catalytic active acid sites.

***Table 18**. The distribution of products after increasing shots of beech wood fast pyrolysis vapour in the ex situ configuration with a C/B of 5:1.*

	e-FCC					AlSBA15(5)					ZSM-5				
Shot #	1	2	3	4	5	1	2	3	4	5	1	2	3	4	5
Yield (carbon %)															
Acids	6.98	7.86	7.94	8.25	7.88	1.51	2.19	2.47	2.59	2.58	0.27	0.29	0.59	0.74	0.90
Alcohols	3.97	2.54	3.24	3.19	3.58	5.83	0.00	0.00	0.00	0.00	0.00	0.00	0.00	0.00	0.00
Aldehyde	6.40	7.11	3.47	3.70	3.89	0.00	0.00	0.00	0.00	0.00	0.00	0.00	0.00	0.00	0.00
Ester/Ether	6.40	7.11	3.47	3.70	3.89	0.00	0.00	0.00	0.00	0.00	0.00	0.00	0.00	0.00	0.00
Aromatics	0.84	0.73	0.06	0.08	0.09	0.83	0.50	0.38	0.34	0.42	8.35	6.28	7.45	6.77	5.20
PAHs	0.00	0.00	0.00	0.00	0.00	0.00	0.00	0.00	0.00	0.00	1.58	1.18	1.01	0.27	0.20
Furans	1.79	1.46	1.50	1.45	1.21	3.74	3.43	3.42	3.38	2.92	1.48	1.87	2.57	4.49	3.40
Phenolics	2.72	2.99	2.87	3.01	2.90	0.03	0.11	0.21	0.21	0.33	0.79	0.48	1.06	1.79	1.66
Anhydrosugars	0.71	0.73	1.15	1.18	2.18	0.00	0.00	0.00	0.00	0.00	0.00	0.00	0.00	0.00	0.00
Total Gas	12.82	11.81	11.75	11.19	12.14	18.10	16.34	15.19	14.87	14.23	27.36	25.25	25.30	21.34	19.29
CO	6.31	5.51	5.74	5.22	5.33	10.48	9.56	8.54	8.45	7.74	12.44	11.97	12.15	11.26	9.71
CO_2	5.45	5.35	4.70	4.30	5.94	6.01	5.54	5.18	5.05	4.98	6.64	6.36	7.12	5.61	5.79
Ethene	0.26	0.20	0.18	0.17	0.24	0.69	0.51	0.38	0.30	0.30	3.34	3.01	2.43	2.02	1.50
Propene	0.20	0.22	0.15	0.15	0.21	0.72	0.36	0.25	0.24	0.23	4.41	3.70	3.34	2.22	2.12

As discussed above, the deactivation was more pronounced in the higher acidity catalysts AlSBA15(5) and ZSM-5. The number of acid products was increased by both AlSBA15(5) and ZSM-5 as the number of shots progressed. Monocyclic aromatic hydrocarbons, the most abundant products of ZSM-5, gradually decreased from 8.35 C % to 5.20 C % by the fifth experiment (see **Table 18**). A similar decrease was also replicated for the production of PAHs, supporting the link between the formation of monocyclic aromatic hydrocarbons and excessive aromatisation to PAHs. Phenolic products were increased by both AlSBA15(5) and ZSM-5 as the number of experiments was increased. This was due to the occurrence of fewer dealkylation and decarbonylation reactions as an increased number of active acid sites became deactivated.

The yield of furans was generally increased by ZSM-5 after progressive shots, as the catalyst became more deactivated. This suggested that the acid sites are crucial for the conversion of furans into smaller products as shown in the mechanism in **Fig. 58**. This was confirmed by a decrease in furan as the number of shots is increased, the lowest possible MW furan type product. The reverse effect was observed with AlSBA15(5), where the yield of furans decreased as the AlSBA15(5) catalyst became increasingly deactivated. Notwithstanding, the selectivity of the furans changed in favour of the production of larger MW furan products as the acid sites became deactivated. As discussed earlier, the absence of shape selectivity in AlSBA15(5) may result in the favourable production of furans rather than aromatics as in the shape selective catalyst ZSM-5.

The yield of gaseous products provided a good indicator of catalyst resistance to deactivation. ZSM-5 had the greatest production of total gases of the three catalysts with a yield of 27.36 C %. However, this was considerably reduced by the fifth shot of pyrolysis vapour over the catalyst producing 19.26 C % of total gas. Similar results were also observed for AlSBA15(5) but to a lesser degree. Although it was shown in the in situ experiments that the mesopores of AlSBA15(5) may enhance the formation of coke, the larger pore size of AlSBA15(5) may limit the blockage of the pores by carbonaceous deposits compared to the microporous structure of ZSM-5. The lower acidity e-FCC catalyst was less affected by the exposure to an increasing amount of pyrolysis vapour evident by the negligible reduction in the production of gaseous products. Nevertheless, the CO_2:CO selectivity increased with an increasing number of experiments. The selectivity observed was similar to non-catalytic pyrolysis. Without char/coke yields and hence the ability to produce a full mass balance, the complete deactivation of these catalysts cannot be fully determined.

5.3. Conclusions

The major products of the catalytic fast pyrolysis of beech wood were quantified using Py-GC-MS/FID/TCD which was performed using a mesoporous, high acidity Al-SBA-15 catalyst (AlSBA15(5)),

a microporous ZSM-5 catalyst and an industrial equilibrium FCC catalyst (e-FCC). It was shown that the acidity and the structure/textural properties of the catalyst had a substantial effect on the product distribution. However, despite their different structural properties, all three solid acid catalysts displayed similar reaction pathways such as the cracking of larger intermediates (levoglucosan) and the reduction of less desirable acids. As the C/B ratio of ZSM-5 increased, the catalytic shape selectivity became more important and led to the production of aromatics. It was also shown that ZSM-5's shape selectivity suppressed the excessive aromatization of intermediates and allowed for high yields of monocyclic aromatic hydrocarbons. On the other hand, the high acidity and larger pore size of AlSBA15(5) promoted excessive aromatisation of the pyrolysis intermediates, resulting in the formation of less desirable high molecular weight PAHs and significant increases in the yield of coke. In addition, there appeared to be an optimum C/B ratio, as increasing the amount of catalyst did not lead to proportional increases of desired products. The experimental results highlighted the importance of shape-selectivity for the effective catalytic conversion of the reactive biomass pyrolysis intermediates into desirable products.

The effect of catalyst location was also investigated with the catalyst either located in situ or ex situ to the pyrolysis reactor. It was found that catalyst placement, i.e. either in situ or ex situ, had a significant effect on the products obtained with all three solid acid catalysts. For ZSM-5, the yield of aromatic products was increased when located in situ compared to ex situ which was attributed to an increased vapour residence time over the catalyst. Interestingly, the opposite effect was observed for both AlSBA15(5) and e-FFC which increased the yield of aromatic products obtained in the ex situ configuration. It was postulated that the shorter vapour residence time of the ex situ configuration promoted the formation of aromatic products in the larger pore catalysts. These findings may have major implications on the decision of catalyst placement when designing reactor configuration and therefore the overall economics of the process.

Finally, the catalysts' resistance to deactivation by coking (see the Introduction, Section 1.4.5 Challenges of CFP) was investigated by subjecting the catalysts to increasing shots of beech wood pyrolysis vapours in Section 5.2.6. The gradual deactivation of the catalysts was more pronounced in the higher acidity catalysts, ZSM-5 and AlSBA15(5). At increased levels of deactivation, the production of aromatics was reduced by both catalysts. However, AlSBA15(5) seemed to be slightly more resistant to deactivation than ZSM-5 which could be due to the larger pores being less likely to be blocked by coke generation. The lower acidity e-FCC showed the highest resistance to deactivation, although it had the lowest activity of all catalysts. Therefore, deactivation due to coke deposition appears to be correlational to the acidity of the catalyst, with larger quantities of coke being formed by more active catalysts. Hence, for an active catalyst, coke formation seems inevitable and therefore to fully limit

coke production would be impossible. Proper consideration should be given to the trade-off between catalyst activity and coke formation when selecting solid acid catalysts for the catalytic fast pyrolysis of biomass. Furthermore, if fully considered, catalytic coke production may be beneficial to the overall process economics by providing process heat during regeneration cycles.

6. Thesis Conclusions

One of the primary objectives of this PhD research project was to synthesise a mesoporous material with similar acidic properties, in terms of Brønsted acid loading and strength, to microporous zeolites such as ZSM-5. Therefore, a series of mesoporous SBA-15 catalysts were successfully synthesised containing increasing concentrations of aluminium (see Section 3.2.1). The following main objective was to assess the series of mesoporous catalysts (Al-SBA-15) in comparison to the current high-performance catalyst stated in the literature, ZSM-5, for the catalytic pyrolysis of biomass. All measurable objectives were achieved.

The relatively novel synthesis method employed in Section 2.1.2 for the synthesis of the series of Al-SBA-15 catalysts was successful and provided greater control over the incorporation of aluminium into the catalyst's structure. The detailed characterisations of the material's structural properties by XRD confirmed the long-range ordering of the hexagonal porous structure was unaffected. However, the incorporation of aluminium led to a proportional loss of surface area of the material. Acidity measurements demonstrated a correlational increase in Brønsted acidity with increased aluminium loading. The Al-SBA-15 catalyst with the highest aluminium to silicon ratio (AlSBA15(5)) exhibited a total acidity of 564 μmol g^{-1}. This is one of the highest acidities achieved by an Al-SBA-15 catalyst in the literature currently (May 2019).

Subsequent testing of the catalysts for the catalytic pyrolysis of a simple hydrocarbon polymer, Low Density Polyethylene(LDPE) demonstrated the superiority of the mesoporous nature of the Al-SBA-15 in comparison to the micropores of the ZSM-5. Therefore, the increased activity was attributed to the reduced diffusional limitations of the mesopores in Al-SBA-15 compared to the microporous ZSM-5. Identification of the catalytic pyrolysis of LDPE products by Py-GC/MS showed that the product distribution depended strongly on the Al loading of the Al-SBA-15 materials. Consequently, by tuning the Al content of Al-SBA-15 materials, the selectivity of the LPDE catalytic cracking can be altered, directing the reaction towards a different range of products. It was shown there was a positive correlation between aluminium incorporation of the Al-SBA-15 catalysts (increased acidity) and an increase in the cracking of the LDPE polymer, generating low molecular weight hydrocarbon products.

In Section 0, the research progressed from the catalytic pyrolysis of a simple hydrocarbon polymer (LDPE) to the more complex oxygenated components comprising biomass, cellulose, hemicellulose and lignin. Measurements of the thermal decomposition properties of the three components by TGA and DSC evidenced significant differences in thermal degradation behaviour. Of the three main components, hemicellulose was the easiest to degrade, while lignin degraded steadily with increasing

temperature. Both hemicellulose and lignin produced high yields of char. In contrast, cellulose resulted in the highest percentage of volatile components and lowest char yield.

Three industrially employed catalysts (SAPO-34, K10 and Al_2O_3) were selected for the catalytic fast pyrolysis of the three main components using Py-GC/MS, in comparison to ZSM-5 and AlSBA15(5). All the catalysts affected the distribution of products obtained from the catalytic pyrolysis of each component. In general, the products obtained from the catalytic pyrolysis were influenced by the composition of the biomass component e.g. Relative waste percentage of biomass waste. However, lignin being the most challenging to catalytically decompose, produced predominantly phenolics as products. In addition, the low catalyst to biomass ratio (C/B) employed limited the activity of the catalysts due to the complexity of each of the components. Of all the catalysts, ZSM-5 displayed significant selectivity to aromatic hydrocarbons (monocyclic aromatics and PAHs) in the catalytic pyrolysis of all three components. Although AlSBA15(5) possessed larger pore sizes and similar acidity to ZSM-5, the conversion to aromatics was much lower, approximately 2 % of the peak area of ZSM-5. Whereas for the catalytic pyrolysis of lignin and hemicellulose, aromatic production was even suppressed by AlSBA15(5). Furthermore, both lignin and hemicellulose produced a high yield of char compared to cellulose. Therefore, of the three biomass components, cellulose represents the most promising for the catalytic thermochemical conversion to more desirable products (see Recommendations, Section 7).

In Section 5, the products of the catalytic pyrolysis of beech wood using ZSM-5, AlSBA15(5) and e-FCC, an industrially relevant FCC catalyst (e-FCC), were quantified. Both ZSM-5 and AlSBA15(5) displayed superior conversion compared to e-FCC, which only slightly differed to the non-catalytic experiment. All catalysts reduced the large anhydrosugars such as levoglucosan in favour of the lower molecular weight products. AlSBA15(5) was the most successful of the three reducing the percentage yield of the anhydrosugars from 7.6 C % to 1 C % at a catalyst to biomass ratio of 1. This suggests a greater ability to catalyse the breakdown of larger molecular weight pyrolysis intermediates compared to ZSM-5 and e-FCC. Nevertheless, these experiments demonstrated ZSM-5's superior shape selectivity for the formation of aromatics due to its complimentary shaped pore geometries. AlSBA15(5) on the other hand, lacked shape selectivity and increased the yield of coke. While e-FCC had significantly less acidity and therefore was less active than the other two.

The location of the catalyst, whether it was either in situ or ex situ to the pyrolysis reactions, had a noteworthy effect on the products obtained. Aromatic production by ZSM-5 was 13.9 C % in the in situ configuration compared to 8.5 C % for the ex situ configuration. The opposite effect was observed for AlSBA15(5) and e-FCC. The difference in product yields was hypothesised to be due to differences in

vapour residence times of the two catalyst configurations. A longer vapour residence time was beneficial for the conversion to aromatics in ZSM-5, whereas a shorter vapour residence time increased the yield of aromatics in larger pore catalysts such as AlSBA15(5). For AlSBA15(5), with the absence of shape selectivity, the longer vapour residence time resulted in increased cracking of vapours, (see section 5.2.5). For commercial catalytic fast pyrolysis, the ex situ catalytic reactor should be used to overcome the deactivation of the catalyst by AAEMs. Additionally, the temperature of fast pyrolysis and catalysis can be independently controlled to optimise the yields of desirable products. Finally, catalyst deactivation experiments showed that catalyst deactivation due to coking was more pronounced in higher acidity catalysts such as ZSM-5 and AlSBA15(5). The larger pores of AlSBA15(5) may be beneficial in preventing pore blockage due to coke build up and hence may improve resistance to deactivation. However, additional experiments are required to prove this hypothesis.

To summarise the main findings of this thesis:

- The shape selectivity of ZSM-5 is vital for aromatic production in CFP across multiple feedstocks (LDPE, the main lignocellulosic model biopolymers and beech wood).
- Mesoporous catalysts such as Al-SBA-15 with similar acidic properties to zeolites lack shape selectivity to monocyclic aromatic hydrocarbons.
- Mesoporous solid acid catalysts are still effective at cracking large molecular weight molecules to smaller ones.
- Ex situ catalytic fast pyrolysis of biomass waste should be investigated further to optimise fast pyrolysis and catalyst reaction temperatures.

This research will have beneficial impacts to industries working towards valorisation of biomass wastes in several ways:

- Aid in the selection of biomass wastes with high cellulosic contents which are best suitable for catalytic fast pyrolysis for the formation of more desirable compounds such as furans and aromatics.
- Assist the design or selection of appropriate catalysts for the catalytic fast pyrolysis of biomass wastes and how the properties of the catalytic material affect the formation of desirable functional groups.

7. Recommendations

The aim of this chapter is to provide recommendations for future investigations into catalytic fast pyrolysis of biomass, derived from the findings presented in this thesis and the understanding developed during associated research activities.

Although it was found that the mesoporous high acidity Al-SBA-15 catalysts lacked shape selectivity in the catalytic pyrolysis of lignocellulosic biomass, these catalysts were successful at overcoming mass transport limitations for the catalytic cracking of high molecular weight pyrolysis intermediates into lower molecular weight compounds. These compounds could be further upgraded or deoxygenated. Therefore, it is suggested that high acidity Al-SBA-15 catalysts be used as an initial cracking catalyst, while a more shape selective catalyst can subsequently upgrade or deoxygenate the lower MW products, more valuable products. To optimise the use of the catalyst in the catalytic fast pyrolysis process, it may be beneficial in terms of product yields and lower catalyst deactivation to have a two-stage catalytic process. In addition, the use of mesoporous acidic catalysts may be more valuable in the cracking of high molecular weight feedstocks such as plastics.

This thesis evidenced the superior selectivity of ZSM-5 for the production of aromatics, compared to larger pore mesoporous Al-SBA-15 catalysts. One area of investigation could be to determine whether the enlargement of the pore openings and channels in ZSM-5 is advantageous to catalytic fast pyrolysis in terms of activity and selectivity. Strong acid or alkali treatment could be investigated to create larger pore openings in ZSM-5.

Differences in aromatic hydrocarbon yields were evident in the catalytic fast pyrolysis of beech wood using ZSM-5, for both the in situ and ex situ configuration. This was hypothesised to be due to vapour residence time based on previous literature (discussed earlier). Therefore, further research is required to determine whether this is the case. That way, the catalyst placement and vapour residence time can be properly optimised for maximal aromatic yields in CFP. Furthermore, research is needed to further elucidate differences in aromatic formation pathways in microporous zeolites compared to mesoporous and non-porous catalysts.

An important aspect that enabled the proper comparison of catalysts for catalytic fast pyrolysis was the ability to quantify the main products obtained. When considering catalysts, a full breakdown of by-products such as CO, CO_2 and valuable non-condensable gases such as propene should be investigated. This can be achieved using gas chromatography with multiple detectors (MS, FID, TCD). Furthermore, the quantity of coke generated by the catalyst should also be measured which will have implications on the process economics and suitability of the catalyst.

This research project only considered one type of biomass, beech wood, for catalytic fast pyrolysis product comparisons. It was shown in Chapter 3 that lignin produced predominantly phenolic products during catalytic fast pyrolysis. In contrast, cellulose and hemicellulose produced a wide range of products including more valuable monocyclic aromatic hydrocarbons and furan products. Therefore, an alternative feedstock that is high in these two components would be worthy of investigation. For example, delignified wastes from paper manufacturing might be a useful source of valuable chemicals via catalytic fast pyrolysis. Due to the wide variability of biomass, alternative biomass feedstocks with higher proportions of cellulose and hemicellulose compared to lignin should produce high yields of more desirable products. Therefore, more research into alternative low lignin feedstocks in combination with promising catalysts should be conducted.

Much of the current research into catalytic fast pyrolysis of biomass is directed towards the deoxygenation of the pyrolysis vapours to produce a hydrocarbon fuel. However, as vehicle transportation is gradually moving towards electrification, there will be a less immediate need for drop-in fuels for transportation. Furthermore, biomass is inherently composed of approximately 50 wt. % of oxygen, therefore the removal of oxygen decreases yields and efficiencies of the process. In the future, there may be more value in the production of select oxygenates which serve as platform chemicals and intermediates. Catalytic fast pyrolysis may be a superior technique for the production of selected oxygenated molecules from biomass or refined biomass components (cellulose, hemicellulose, lignin). For example, furfural and 5-hydroxymethylfurfural derived from cellulose as well as aromatic hydrocarbons such as benzene, toluene and xylene (BTX) from sustainable biomass sources.

The progressive deactivation of catalysts over multiple regeneration cycles is a major problem affecting the economics of the process. It was shown in this thesis that all solid acid catalysts were deactivated to some extent after sequential shots of fast pyrolysis vapour. Further research should be undertaken to characterise the mechanism of deactivation in order to lessen the degree of, or possibly prevent deactivation. In addition, the parameters of catalyst regeneration, such as the temperature of coke combustion, should be optimised to moderate the progressive long-term deactivation of the material and therefore increase the overall lifetime of the expensive catalyst.

Based on the results of this thesis, it would be possible to conduct a techno-economic feasibility study to establish costs of using combinations of Al-SBA-15 and ZSM-5 or an alternative cheaper but less active catalyst for the CFP of biomass. This would highlight whether the increased costs associated with an active and selective catalyst is economically worthwhile to achieve high yields of desirable products suitable for selected applications.

Once a superior catalyst, both in terms of activity, selectivity and economic feasibility have been established, the fine-tuning of the catalyst properties and reactor/process parameters need to be optimised to produce close to the highest possible theoretical product yields. The outcome of this thesis in combination with the above recommendations should provide a basis for further research to develop catalytic fast pyrolysis as a fully commercial process for the effective transformation of biomass into useful fuels and chemicals.

8. References

[1] A. V. Bridgwater, Biomass and Bioenergy 38 (2012) 68–94.
[2] C.A. Mullen, A.A. Boateng, N.M. Goldberg, I.M. Lima, D.A. Laird, K.B. Hicks, Biomass and Bioenergy 34 (2010) 67–74.
[3] A. Demirbaş, Fuel 76 (1997) 431–434.
[4] J.P. Diebold, C.P. Corporation, (1997).
[5] T. Milne, in:, Biomass Pyrolysis Oil Prop. Combust., 1994, pp. 90–108.
[6] T. Chen, C. Wu, R. Liu, W. Fei, S. Liu, Bioresour. Technol. 102 (2011) 6178–6185.
[7] J.P. Diebold, S. Czernik, Energy and Fuels 11 (1997) 1081–1091.
[8] J.A. Martin, C.A. Mullen, A.A. Boateng, Energy & Fuels 28 (2014) 5918–5929.
[9] A. Corma, G.W. Huber, L. Sauvanaud, P. O'Connor, J. Catal. 247 (2007) 307–327.
[10] M. Bertero, U. Sedran, in:, Recent Adv. Thermochem. Convers. Biomass, 2015, pp. 355–381.
[11] D.C. Elliott, Curr. Opin. Chem. Eng. 9 (2015) 59–65.
[12] A.A. Lappas, S. Bezergianni, I.A. Vasalos, Catal. Today 145 (2009) 55–62.
[13] L. Ciddor, J.A. Bennett, J.A. Hunns, K. Wilson, A.F. Lee, J. Chem. Technol. Biotechnol. 90 (2015) 780–795.
[14] R.N. Hilten, B.P. Bibens, J.R. Kastner, K.C. Das, in:, Energy and Fuels, American Chemical Society, 2010, pp. 673–682.
[15] P.M. Mortensen, J.D. Grunwaldt, P.A. Jensen, K.G. Knudsen, A.D. Jensen, Appl. Catal. A Gen. 407 (2011) 1–19.
[16] F. de Miguel Mercader, M.J.J. Groeneveld, S.R.A.R.A. Kersten, N.W.J.W.J. Way, C.J.J. Schaverien, J.A.A. Hogendoorn, Appl. Catal. B Environ. 96 (2010) 57–66.
[17] D.C. Elliott, T.R. Hart, G.G. Neuenschwander, L.J. Rotness, A.H. Zacher, Environ. Prog. Sustain. Energy 28 (2009) 441–449.
[18] R. Venderbosch, W. Prins, Biofuels, Bioprod. Biorefining 4 (2010) 178–208.
[19] C.-H. Zhou, X. Xia, C.C.-X. Lin, D.-S. Tong, J. Beltramini, Chem. Soc. Rev. 40 (2011) 5588–5617.
[20] T.M. Huynh, U. Armbruster, H. Atia, U. Bentrup, B.M.Q. Phan, R. Eckelt, L.H. Nguyen, D.A. Nguyen, A. Martin, React. Chem. Eng. 1 (2016) 239–251.
[21] S. Czernik, A. V. Bridgwater, Energy and Fuels 18 (2004) 590–598.
[22] F.H. Isikgor, C.R. Becer, Polym. Chem. 6 (2015) 4497–4559.
[23] J.V. Bomtempo, F. Chaves Alves, F. De Almeida Oroski, Faraday Discuss. 202 (2017) 213–225.
[24] M. Kunioka, K. Taguchi, F. Ninomiya, M. Nakajima, A. Saito, S. Araki, M. Kunioka, K. Taguchi, F. Ninomiya, M. Nakajima, A. Saito, S. Araki, Polymers (Basel). 6 (2014) 423–442.
[25] S.H. Lamlom, R.A. Savidge, Biomass and Bioenergy 25 (2003) 381–388.
[26] D. Lithner, Å. Larsson, G. Dave, Sci. Total Environ. 409 (2011) 3309–3324.
[27] M. Sjögren, H. Li, U. Rannug, R. Westerholm, Fuel 74 (1995) 983–989.
[28] D.L. Klass, Biomass for Renewable Energy, Fuels and Chemicals, 1998.
[29] R.A. Sheldon, in:, Catal. Today, Elsevier, 2011, pp. 3–13.
[30] D.J. Tenenbaum, Environ. Health Perspect. 116 (2008) A254.
[31] M.A.C. Xiaodong, D. Govinda, T. The, W. Bank, Second-Generation Biofuels Economics and Policies, 2010.
[32] R.A. Sheldon, Green Chem. 16 (2014) 950–963.
[33] A. Philbrook, A. Alissandratos, C.J. Easton, in:, Environ. Biotechnol. - New Approaches Prospect. Appl., 2013, pp. 39–62.
[34] N.H. Leibbrandt, J.H. Knoetze, J.F. Görgens, Biomass and Bioenergy 35 (2011) 2117–2126.
[35] L. Zhang, Z. Bao, S. Xia, Q. Lu, K. Walters, Catalytic Pyrolysis of Biomass and Polymer Wastes, 2018.
[36] A.V. Bridgwater, Appl. Catal. A Gen. 116 (1994) 5–47.
[37] S.K. Sansaniwal, M.A. Rosen, S.K. Tyagi, Renew. Sustain. Energy Rev. 80 (2017) 23–43.
[38] S. Mahesh Kumar, G.M. Madhu, S. Roy, Sep. Purif. Technol. 57 (2007) 25–36.

[39] A.R.K. Gollakota, N. Kishore, S. Gu, Renew. Sustain. Energy Rev. 81 (2018) 1378–1392.
[40] P. Quaak, H. Knoef, H. Stassen, Energy from Biomass, The World Bank, 1999.
[41] T. Nussbaumer, Energy and Fuels 17 (2003) 1510–1521.
[42] R. Salzmann, T. Nussbaumer, Energy and Fuels 15 (2001) 575–582.
[43] E. Houshfar, Ø. Skreiberg, D. Todorović, A. Skreiberg, T. Løvås, A. Jovović, L. Sørum, Fuel 98 (2012) 29–40.
[44] A.V. Bridgwater, G.V.C. Peacocke, Renew. Sustain. Energy Rev. 4 (2002) 1–73.
[45] G.W. Huber, S. Iborra, A. Corma, Chem. Rev. 106 (2006) 4044–4098.
[46] H. Pourzolfaghar, F. Abnisa, W.M.A. Wan Daud, M.K. Aroua, J. Anal. Appl. Pyrolysis 133 (2018) 117–127.
[47] Y. Elkasabi, C.A. Mullen, A.L.M.T. Pighinelli, A.A. Boateng, Fuel Process. Technol. 123 (2014) 11–18.
[48] Z. Si, X. Zhang, C. Wang, L. Ma, R. Dong, Catalysts 7 (2017) 169.
[49] M.B. Shemfe, S. Gu, P. Ranganathan, Fuel 143 (2015) 361–372.
[50] M. Saidi, F. Samimi, D. Karimipourfard, T. Nimmanwudipong, B.C. Gates, M.R. Rahimpour, Energy Environ. Sci. 7 (2014) 103.
[51] J. Chi, H. Yu, Chinese J. Catal. 39 (2018) 390–394.
[52] K. Treusch, A.M. Mauerhofer, N. Schwaiger, P. Pucher, S. Müller, D. Painer, H. Hofbauer, M. Siebenhofer, React. Chem. Eng. (2019).
[53] J.D. Adjaye, N.N. Bakhshi, Biomass and Bioenergy 8 (1995) 131–149.
[54] S. Vitolo, B. Bresci, M. Seggiani, M.G. Gallo, Fuel 80 (2001) 17–26.
[55] G. Fogassy, N. Thegarid, G. Toussaint, A.C. van Veen, Y. Schuurman, C. Mirodatos, Appl. Catal. B Environ. 96 (2010) 476–485.
[56] F. Gong, Z. Yang, C. Hong, W. Huang, S. Ning, Z. Zhang, Y. Xu, Q. Li, Bioresour. Technol. 102 (2011) 9247–9254.
[57] D.A. Bulushev, J.R.H. Ross, Catal. Today 171 (2011) 1–13.
[58] S. Vitolo, M. Seggiani, P. Frediani, G. Ambrosini, L. Politi, Fuel 78 (1999) 1147–1159.
[59] S.D. Stefanidis, K.G. Kalogiannis, E.F. Iliopoulou, A.A. Lappas, P.A. Pilavachi, Bioresour. Technol. 102 (2011) 8261–7.
[60] S.D. Stefanidis, K.G. Kalogiannis, A.A. Lappas, Wiley Interdiscip. Rev. Energy Environ. 7 (2018) e281.
[61] R.H. Venderbosch, ChemSusChem 8 (2015) 1306–1316.
[62] S. V. Vassilev, D. Baxter, L.K. Andersen, C.G. Vassileva, Fuel 89 (2010) 913–933.
[63] N. Sorek, T.H. Yeats, H. Szemenyei, H. Youngs, C.R. Somerville, Bioscience 64 (2014) 192–201.
[64] D.M. Alonso, S.G. Wettstein, J.A. Dumesic, Chem. Soc. Rev. 41 (2012) 8075–8098.
[65] D. Mohan, C.U. Pittman, P.H. Steele, Energy and Fuels 20 (2006) 848–889.
[66] L.K. Tolonen, M. Bergenstråhle-Wohlert, H. Sixta, J. Wohlert, J. Phys. Chem. B 119 (2015) 4739–4748.
[67] M. Möller, U. Schröder, RSC Adv. 3 (2013) 22253.
[68] D.J. Nowakowski, J.M. Jones, J. Anal. Appl. Pyrolysis 83 (2008) 12–25.
[69] F. Delbecq, Y. Wang, A. Muralidhara, K. El Ouardi, G. Marlair, C. Len, Front. Chem. 6 (2018) 146.
[70] R. Santiago, J. Barros-Rios, R.A. Malvar, Int. J. Mol. Sci. 14 (2013) 6960–6980.
[71] R. Rinaldi, R. Jastrzebski, M.T. Clough, J. Ralph, M. Kennema, P.C.A. Bruijnincx, B.M. Weckhuysen, Angew. Chemie - Int. Ed. 55 (2016) 8164–8215.
[72] D.J. Nowakowski, A. V. Bridgwater, D.C. Elliott, D. Meier, P. de Wild, J. Anal. Appl. Pyrolysis 88 (2010) 53–72.
[73] G. Yang, P. Jaakkola, Wood Chemistry and Isolation of Extractives from Wood Literature Study for BIOTULI Project, 2011.
[74] X. Guo, S. Wang, K. Wang, Q. Liu, Z. Luo, J. Fuel Chem. Technol. 38 (2010) 42–46.
[75] E. Ranzi, A. Cuoci, T. Faravelli, A. Frassoldati, G. Migliavacca, S. Pierucci, S. Sommariva, Energy and Fuels 22 (2008) 4292–4300.

[76] T.T. Tiemann, L.H. Franco, M. Peters, E. Frossard, M. Kreuzer, C.E. Lascano, H.D. Hess, Grass Forage Sci. 64 (2009) 255–265.
[77] B.M. Jenkins, L.L. Baxter, T.R. Miles, T.R. Miles, Fuel Process. Technol. 54 (1998) 17–46.
[78] G. Zając, J. Szyszlak-Bargłowicz, W. Gołębiowski, M. Szczepanik, Energies 11 (2018) 1–15.
[79] S. Banks, Ash Control Methods to Limit Biomass Inorganic Content and Its Effect on Fast Pyrolysis Bio-Oil Stability, Aston University, 2014.
[80] T. Dahou, F. Defoort, S. Thiéry, M. Grateau, M. Campargue, S. Bennici, M. Jeguirim, C. Dupont, Energies 11 (2018) 1–15.
[81] S.W. Banks, D.J. Nowakowski, A. V Bridgwater, Energy & Fuels (2016) 8009–8018.
[82] S. Julien, E. Chornet, P.K. Tiwari, R.P. Overend, J. Anal. Appl. Pyrolysis 19 (1991) 81–104.
[83] A. Pappa, K. Mikedi, N. Tzamtzis, M. Statheropoulos, J. Anal. Appl. Pyrolysis 67 (2003) 221–235.
[84] M.J. Antal, W.S.L. Mok, J.C. Roy, A.T. -Raissi, D.G.M. Anderson, J. Anal. Appl. Pyrolysis 8 (1985) 291–303.
[85] F.A. Agblevor, S. Besler, Energy & Fuels 10 (1996) 293–298.
[86] J. Wise, D. Vietor, T. Provin, S. Capareda, C. Munster, A. Boateng, Environ. Prog. Sustain. Energy 31 (2012) 251–255.
[87] B.M. Jenkins, R.R. Bakker, J.B. Wei, Biomass and Bioenergy 10 (1996) 177–200.
[88] H. Tan, S. Wang, J. Fuel Chem. Technol. 37 (2009) 668–672.
[89] S.W. Banks, D.J. Nowakowski, A. V. Bridgwater, Fuel Process. Technol. 128 (2014) 94–103.
[90] P. Harmsen, W. Huijgen, L. Bermudez, R. Bakker, Literature Review of Physical and Chemical Pretreatment Processes for Lignocellulosic Biomass, Wageningen UR Food & Biobased Research, 2010.
[91] P. Gupta, S. Paul, Catal. Today 236 (2014) 153–170.
[92] P.T. Anastas, M.M. Kirchhoff, T.C. Williamson, Appl. Catal. A Gen. 221 (2001) 3–13.
[93] K. Caspary, H. Gehrke, M. Heinritz-Adrian, M. Schwefer, Handbook of Heterogeneous Catalysis, Wiley-VCH Verlag GmbH & Co. KGaA, Weinheim, Germany, 2008.
[94] C.H. Bartholomew, R.J. Farrauto, Fundamentals of Industrial Catalytic Processes: Second Edition, John Wiley & Sons, Inc., Hoboken, NJ, USA, 2010.
[95] K. Kakaei, M.D. Esrafili, A. Ehsani, in:, Interface Sci. Technol., Elsevier B.V., 2019, pp. 1–21.
[96] K. Wilson, A.F. Lee, Heterogeneous Catalysts for Clean Technology: Spectroscopy, Design, and Monitoring, Wiley-VCH Verlag GmbH & Co. KGaA, Weinheim, Germany, 2013.
[97] J.R.H. Ross, Heterogeneous Catalysis: Fundamentals and Applications, Elsevier, 2011.
[98] G.J. Leigh, in:, Catal. Nitrogen Fixat., Springer Netherlands, Dordrecht, 2004, pp. 33–54.
[99] E.T.C. Vogt, B.M. Weckhuysen, Chem. Soc. Rev 7342 (2015) 7342–7370.
[100] J. Li, A. Corma, J. Yu, Chem. Soc. Rev. 44 (2015) 7112–7127.
[101] J. Čejka, A. Corma, S. Zones, Zeolites and Catalysis, 2010.
[102] A. Marcilla, A. Gómez, S. Menargues, J. García-Martínez, D. Cazorla-Amorós, A. Gó Mez, S. Menargues, J. García-Martínez, D. Cazorla-Amorós, J. Anal. Appl. Pyrolysis 68–69 (2003) 495–506.
[103] O. Korkuna, R. Leboda, J. Skubiszewska-Zie¸ba, T. Vrublevs'ka, V.M. Gun'ko, J. Ryczkowski, Microporous Mesoporous Mater. 87 (2006) 243–254.
[104] R. Davis, J. Catal. 216 (2003) 396–405.
[105] J. Čejka, H. van Bekkum, A. Corma, F. Schüth, Introduction to Zeolite Science and Practice, Volume 168 (3rd Edition), Elsevier, 2007.
[106] A. Corma, Curr. Opin. Solid State Mater. Sci. 2 (1997) 63–75.
[107] N. Rahimi, R. Karimzadeh, Appl. Catal. A Gen. 398 (2011) 1–17.
[108] N.A. Kalinin, S. V., Spaldin, Science 341 (2013) 858–859.
[109] J.C. Védrine, C. V. Jacques, Heterogeneous Catalysis on Metal Oxides, Multidisciplinary Digital Publishing Institute, 2017.
[110] Y. Zhu, X. Liu, S. Jin, H. Chen, W. Lee, M. Liu, Y. Chen, J. Mater. Chem. A 7 (2019) 5875–5897.
[111] D.W. Lee, B.R. Yoo, J. Ind. Eng. Chem. 20 (2014) 3947–3959.

[112] M. Li, X. Pan, J. Li, H. Ma, F. Qi, Y. Zhu, J. Yang, X. Bao, F. Jiao, M. Wei, Q. Fu, T. He, Y. Pan, H. Li, J. Xiao, S. Miao, Z. Zhou, D. Xiao, Science (80-.). 351 (2016) 1065–1068.
[113] T. Blasco, J.M.L. Nieto, Appl. Catal. A Gen. 157 (1997) 117–142.
[114] C.-H. Zhang, Y. Yang, B.-T. Teng, T.-Z. Li, H.-Y. Zheng, H.-W. Xiang, Y.-W. Li, J. Catal. 237 (2006) 405–415.
[115] G. Jacobs, T.K. Das, Y. Zhang, J. Li, G. Racoillet, B.H. Davis, Appl. Catal. A Gen. 233 (2002) 263–281.
[116] J. Kijeński, P. Radomski, E. Fedoryńska, J. Catal. 203 (2001) 407–425.
[117] S. Benjapornkulaphong, C. Ngamcharussrivichai, K. Bunyakiat, Chem. Eng. J. 145 (2009) 468–474.
[118] P.M. Shah, A.N. Day, T.E. Davies, D.J. Morgan, S.H. Taylor, Appl. Catal. B Environ. 253 (2019) 331–340.
[119] S.A.C. Carabineiro, X. Chen, O. Martynyuk, N. Bogdanchikova, M. Avalos-Borja, A. Pestryakov, P.B. Tavares, J.J.M. Órfão, M.F.R. Pereira, J.L. Figueiredo, Catal. Today 244 (2015) 103–114.
[120] H. Huang, Y. Xu, Q. Feng, D.Y.C. Leung, Catal. Sci. Technol. 5 (2015) 2649–2669.
[121] M. Kang, E.D. Park, J.M. Kim, J.E. Yie, Appl. Catal. A Gen. 327 (2007) 261–269.
[122] J.M. Andersson, Controlling the Formation and Stability of Alumina Phases, 2005.
[123] J. Zhou, Z. Hua, Z. Liu, W. Wu, Y. Zhu, J. Shi, ACS Catal. 1 (2011) 287–291.
[124] J. Ding, J. Hu, T. Xue, Y. Wang, H. Wu, P. Wu, M. He, RSC Adv. 6 (2016) 38671–38679.
[125] M. Zhou, A. a. Rownaghi, J. Hedlund, RSC Adv. 3 (2013) 15596.
[126] L. Wang, Z. Zhang, C. Yin, Z. Shan, F.S. Xiao, Microporous Mesoporous Mater. 131 (2010) 58–67.
[127] J. Zhu, X. Meng, F. Xiao, Front. Chem. Sci. Eng. 7 (2013) 233–248.
[128] W. Li, D. Zhao, Chem. Commun. 49 (2013) 943–946.
[129] A. Taguchi, F. Schu, F. Schüth, Microporous Mesoporous Mater. 77 (2005) 1–45.
[130] W. Wang, R. Qi, W. Shan, X. Wang, Q. Jia, J. Zhao, C. Zhang, H. Ru, Microporous Mesoporous Mater. 194 (2014) 167–173.
[131] J.C. Manayil, A. Osatiashtiani, A. Mendoza, C.M.A. Parlett, M.A. Isaacs, L.J. Durndell, C. Michailof, E. Heracleous, A. Lappas, A.F. Lee, K. Wilson, ChemSusChem 10 (2017) 3506–3511.
[132] J.C. Manayil, C.V.M. Inocencio, A.F. Lee, K. Wilson, Green Chem. (2015) 1–6.
[133] K. Wilson, A.F. Lee, K. Wilson, (2016).
[134] C.M. a Parlett, K. Wilson, A.F. Lee, Chem. Soc. Rev. 42 (2013) 3876–93.
[135] C.M.A. Parlett, L.J. Durndell, A. Machado, G. Cibin, D.W. Bruce, N.S. Hondow, K. Wilson, A.F. Lee, Catal. Today 229 (2014) 46–55.
[136] C. Liu, H. Wang, A.M. Karim, J. Sun, Y. Wang, Chem. Soc. Rev. 43 (2014) 7594–7623.
[137] G. Lyu, S. Wu, H. Zhang, Front. Energy Res. 3 (2015) 28.
[138] R. Amirante, E. Distaso, M. Napolitano, P. Tamburrano, S. Di Iorio, P. Sementa, B.M. Vaglieco, R.D. Reitz, Int. J. Engine Res. 18 (2017) 606–620.
[139] Focus Economics, Gasoil Price Outlook (2018).
[140] Platts, Glob. Aromat. Pricing Anal. (2018).
[141] J. van Haveren, E.L. Scott, J. Sanders, Biofuels, Bioprod. Biorefining 2 (2008) 41–57.
[142] B. Girisuta, H.J. Heeres, in:, 2017, pp. 143–169.
[143] J. Li, L. Lin, T. Sun, J. Xu, J. Ji, Q. Liu, C. Tian, Metab. Eng. (2019).
[144] B.H. Shanks, P.L. Keeling, Green Chem. 19 (2017) 3177–3185.
[145] E. Hu, X. Hu, X. Wang, Y. Xu, K.D. Dearn, H. Xu, Tribol. Int. 55 (2012) 119–125.
[146] M. Sasaki, K. Goto, K. Tajima, T. Adschiri, K. Arai, Green Chem. 4 (2002) 285–287.
[147] M. Al-Sabawi, J. Chen, S. Ng, Energy and Fuels 26 (2012) 5355–5372.
[148] N.Y. Chen, J.T.F. Degnan, L.R. Koenig, Chemtech 16 (1986) 506–511.
[149] A. Schriesheim, in:, Energy Chem. Sci., Pergamon, 1978, pp. 103–122.
[150] H. Zhang, Y.-T. Cheng, T.P. Vispute, R. Xiao, G.W. Huber, Energy Environ. Sci. 4 (2011) 2297.
[151] T.R. Carlson, Y.T. Cheng, J. Jae, G.W. Huber, Energy Environ. Sci. 4 (2011) 145–161.

[152] S. Wang, E. Iglesia, J. Catal. 345 (2017) 183–206.
[153] J.R. Howard, Fluidized Bed Technology : Principles and Applications, A. Hilger, 1989.
[154] A.N. Hayhurst, Combust. Flame 160 (2013) 138–144.
[155] P.E. Mason, L.I. Darvell, J.M. Jones, A. Williams, Energy & Fuels 30 (2016) 2158–2163.
[156] J. Shen, X.S. Wang, M. Garcia-Perez, D. Mourant, M.J. Rhodes, C.Z. Li, Fuel 88 (2009) 1810–1817.
[157] D. V. Suriapparao, R. Vinu, Waste and Biomass Valorization 9 (2018) 465–477.
[158] M.B. Pecha, M. Garcia-Perez, T.D. Foust, P.N. Ciesielski, ACS Sustain. Chem. Eng. 5 (2017) 1046–1053.
[159] K.M. Jiang, C.G. Cheng, M. Ran, Y.G. Lu, Q.L. Wu, Xinxing Tan Cailiao/New Carbon Mater. 33 (2018) 183–187.
[160] Q. Wang, K. Han, J. Gao, H. Li, C. Lu, Fuel 199 (2017) 488–496.
[161] C.J. Atkinson, J.D. Fitzgerald, N.A. Hipps, C.J. Atkinson, J.D. Fitzgerald, N.A. Hipps, Plant Soil 337 (2010) 1–18.
[162] E.F. Iliopoulou, E. V. Antonakou, S.A. Karakoulia, I.A. Vasalos, A.A. Lappas, K.S. Triantafyllidis, Chem. Eng. J. 134 (2007) 51–57.
[163] Y. Cheng, Y. Jin, Multiphase Reactor Engineering for Clean and Low-Carbon Energy Applications, 2017.
[164] Güray Yildiz, Catalytic Fast Pyrolysis of Biomass, Ghent, 2015.
[165] V. Paasikallio, K. Kalogiannis, A. Lappas, J. Lehto, J. Lehtonen, Energy Technol. 5 (2017) 94–103.
[166] S.D. Stefanidis, K.G. Kalogiannis, P.A. Pilavachi, C.M. Fougret, A.A. Lappas, E. Jordan, A.A. Lappas, Catal. Sci. Technol. 6 (2016) 2807–2819.
[167] Y.-T. Cheng, J. Jae, J. Shi, W. Fan, G.W. Huber, Angew. Chemie (2012).
[168] C.A. Mullen, A.A. Boateng, Ind. Eng. Chem. Res. 52 (2013) 17156–17161.
[169] V. Paasikallio, C. Lindfors, E. Kuoppala, Y. Solantausta, A. Oasmaa, J. Lehto, J. Lehtonen, Green Chem. 16 (2014) 3549–3559.
[170] G. Yildiz, F. Ronsse, R. van Duren, W. Prins, Renew. Sustain. Energy Rev. 57 (2016) 1596–1610.
[171] R. French, S. Czernik, Fuel Process. Technol. 91 (2010) 25–32.
[172] P. Sannigrahi, A.J. Ragauskas, G.A. Tuskan, Biofuels, Bioprod. Biorefining 4 (2010) 209–226.
[173] J. Hytönen, J. Nurmi, Wood Res. 60 (2015) 71–82.
[174] K. Iisa, D.J. Robichaud, M.J. Watson, J. Ten Dam, A. Dutta, C. Mukarakate, S. Kim, M.R. Nimlos, R.M. Baldwin, Green Chem. 20 (2018) 567–582.
[175] M.W. Nolte, M.W. Liberatore, Energy and Fuels 24 (2010) 6601–6608.
[176] Y. Sekiguchi, F. Shafizadeh, J. Appl. Polym. Sci. 29 (1984) 1267–1286.
[177] J.E. Prenosil, D. Vlach, Conserv. Recycl. 8 (1985) 173–179.
[178] W.G. Appleby, J.W. Gibson, G. Good, Ind. Eng. Chem. Process Des. Dev. 1 (1962) 102–110.
[179] S. Shao, H. Zhang, Y. Wang, R. Xiao, L. Heng, D. Shen, Energy and Fuels 29 (2015) 1751–1757.
[180] P.T. Williams, P.A. Horne, Fuel 74 (1995) 1839–1851.
[181] V. Fouche, P. Magnoux, M. Guisnet, Appl. Catal. 58 (1990) 189–198.
[182] J. Zhang, H. Zhang, X. Yang, Z. Huang, W. Cao, J. Nat. Gas Chem. 20 (2011) 266–270.
[183] S.-J. Jong, A.R. Pradhan, J.-F. Wu, T.-C. Tsai, S.-B. Liu, J. Catal. 174 (1998) 210–218.
[184] E.F. Iliopoulou, P.A. Lazaridis, K.S. Triantafyllidis, in:, Nanotechnol. Catal., Wiley-Blackwell, Weinheim, Germany, 2017, pp. 655–714.
[185] A. Sharma, V. Pareek, D. Zhang, Renew. Sustain. Energy Rev. 50 (2015) 1081–1096.
[186] J. Čejka, G. Centi, J. Perez-Pariente, W.J. Roth, Catal. Today 179 (2012) 2–15.
[187] M.M. Yung, A.R. Stanton, K. Iisa, R.J. French, K.A. Orton, K.A. Magrini, Energy and Fuels 30 (2016) 9471–9479.
[188] E.F. Iliopoulou, S. Stefanidis, K. Kalogiannis, a. C. Psarras, A. Delimitis, K.S. Triantafyllidis, a. a. Lappas, Green Chem. 16 (2014) 662–674.
[189] A. De Angeli, F. Wolff, L. Romary, W. Gerbino, in:, Lect. Notes Comput. Sci. (Including Subser. Lect. Notes Artif. Intell. Lect. Notes Bioinformatics), 1999, pp. 49–52.
[190] P.A. Horne, P.T. Williams, Renew. Energy 7 (1996) 131–144.

[191] H. Zhang, R. Xiao, H. Huang, G. Xiao, Bioresour. Technol. 100 (2009) 1428–1434.
[192] P.T. Williams, N. Nugranad, Energy 25 (2000) 493–513.
[193] T.R. Carlson, G.A. Tompsett, W.C. Conner, G.W. Huber, Top. Catal. 52 (2009) 241–252.
[194] M. Cook, W.C. Conner, in:, How Big Are Pores Zeolites?, Materials Research Society, Warrendale, USA, 1999, p. 3029.
[195] J. Jae, G.A. Tompsett, A.J. Foster, K.D. Hammond, S.M. Auerbach, R.F. Lobo, G.W. Huber, J. Catal. 279 (2011) 257–268.
[196] C.D. Baertsch, H.H. Funke, J.L. Falconer, R.D. Noble, J. Phys. Chem. 100 (1996) 7676–7679.
[197] D.J. Mihalcik, C.A. Mullen, A.A. Boateng, J. Anal. Appl. Pyrolysis 92 (2011) 224–232.
[198] J.W. Kim, S.H. Park, J. Jung, J.K. Jeon, C.H. Ko, K.E. Jeong, Y.K. Park, Bioresour. Technol. 136 (2013) 431–436.
[199] E.L. Schultz, C.A. Mullen, A.A. Boateng, Energy Technol. 5 (2017) 196–204.
[200] E.F. Iliopoulou, S.D. Stefanidis, K.G. Kalogiannis, A. Delimitis, A.A. Lappas, K.S. Triantafyllidis, Appl. Catal. B Environ. 127 (2012) 281–290.
[201] Y. Wan, Y. Liu, Y. Wang, G. Luo, Ind. Eng. Chem. Res. 56 (2017) 8888–8894.
[202] O.I. Platonov, Coke Chem. 55 (2012) 242–246.
[203] H. Knözinger, Angew. Chemie Int. Ed. English 7 (1968) 791–805.
[204] Q. Lu, Z.-F.F. Zhang, C.-Q.Q. Dong, X.-F.F. Zhu, Q. Lu, Z.-F.F. Zhang, C.-Q.Q. Dong, X.-F.F. Zhu, Energies 3 (2010) 1805–1820.
[205] Q. Lu, Y. Zhang, Z. Tang, W.Z. Li, X.F. Zhu, Fuel 89 (2010) 2096–2103.
[206] K.G. Kalogiannis, S.D. Stefanidis, S.A. Karakoulia, K.S. Triantafyllidis, H. Yiannoulakis, C. Michailof, A.A. Lappas, Appl. Catal. B Environ. 238 (2018) 346–357.
[207] S.D. Stefanidis, S.A. Karakoulia, K.G. Kalogiannis, E.F. Iliopoulou, A. Delimitis, H. Yiannoulakis, T. Zampetakis, A.A. Lappas, K.S. Triantafyllidis, Appl. Catal. B Environ. 196 (2016) 155–173.
[208] Y. Deng, T. Yu, Y. Wan, Y. Shi, Y. Meng, D. Gu, L. Zhang, Y. Huang, C. Liu, X. Wu, D. Zhao, J. Am. Chem. Soc. 129 (2007) 1690–1697.
[209] M.C. Samolada, A. Papafotica, I.A. Vasalos, Energy and Fuels 14 (2000) 1161–1167.
[210] J. Aadam, M. Blazso, E. Meszaros, M. Stocker, M. Nilsen, A. Bouzga, J. HUSTAD, M. GRONLI, G. OYE, Fuel 84 (2005) 1494–1502.
[211] E. Antonakou, A. Lappas, M.H. Nilsen, A. Bouzga, M. Stöcker, Fuel 85 (2006) 2202–2212.
[212] K.S. Triantafyllidis, E.F. Iliopoulou, E. V. Antonakou, A.A. Lappas, H. Wang, T.J. Pinnavaia, Microporous Mesoporous Mater. 99 (2007) 132–139.
[213] M.-J.J. Jeon, J.-K.K. Jeon, D.J. Suh, S.H. Park, Y.J. Sa, S.H. Joo, Y.-K.K. Park, Catal. Today 204 (2013) 170–178.
[214] P.F. Fulvio, S. Pikus, M. Jaroniec, J. Mater. Chem. 15 (2005) 5049–5053.
[215] H. Xiong, H.N. Pham, A.K. Datye, Green Chem. 16 (2014) 4627–4643.
[216] E. Yaman, A.S. Yargic, N. Ozbay, B.B. Uzun, K.G. Kalogiannis, S.D. Stefanidis, E.P. Pachatouridou, E.F. Iliopoulou, A.A. Lappas, J. Clean. Prod. 185 (2018) 52–61.
[217] D. Zhao, J. Feng, Q. Huo, N. Melosh, G. Fredrickson, B. Chmelka, G. Stucky, Science (80-.). 279 (1998) 548–52.
[218] S. Wu, Y. Han, Y.C. Zou, J.W. Song, L. Zhao, Y. Di, S.Z. Liu, F.S. Xiao, Chem. Mater. 16 (2004) 486–492.
[219] A. Ungureanu, B. Dragoi, V. Hulea, T. Cacciaguerra, D. Meloni, V. Solinas, E. Dumitriu, Microporous Mesoporous Mater. 163 (2012) 51–64.
[220] R. Jenkins, R.L. Snyder, Introduction to X-Ray Powder Diffractometry, John Wiley & Sons, Inc., Hoboken, NJ, USA, 1996.
[221] W.H. Bragg, W.L. Bragg, R. Soc. 88 (1913) 428–438.
[222] J.M. Cowley, Diffraction Physics, 1995.
[223] C.-Y. Chen, H.-X. Li, M.E. Davis, Microporous Mater. 2 (1992) 17–26.
[224] M. Kruk, M. Jaroniec, J.M. Kim, R. Ryoo, Langmuir 15 (1999) 5279–5284.
[225] N. Muroyama, T. Ohsuna, R. Ryoo, Y. Kubota, O. Terasaki, J. Phys. Chem. B 110 (2006) 10630–

10635.
[226] P.I. Ravikovitch, D. Wei, W.T. Chueh, G.L. Haller, A.V. Neimark, J. Phys. Chem. B 101 (1997) 3671–3679.
[227] A. Lopez Molinero, L. Martinez, A. Villareal, J.R. Castillo, Talanta 45 (1998) 1211–1217.
[228] G.A. Meyer, Anal. Chem. 59 (1987) 1345A-1354A.
[229] J.W. Olesik, Anal. Chem. 63 (1991) 12–21.
[230] E. Korin, N. Froumin, S. Cohen, ACS Biomater. Sci. Eng. 3 (2017) 882–889.
[231] K. F. Moulder, J, F. Stickle, W, E. Sobol, P, and D. Bomben, (1991).
[232] L.D. Gelb, K.E. Gubbins, Langmuir 14 (1998) 2097–2111.
[233] P. Voogd, J.J.F. Scholten, H. van Bekkum, Colloids and Surfaces 55 (1991) 163–171.
[234] J. Villarroel-Rocha, D. Barrera, K. Sapag, Microporous Mesoporous Mater. 200 (2014) 68–78.
[235] F. Rouquerol, J. Rouquerol, K. Sing, Adsorption by Powders & Porous Solids - Principles, Methodology and Applications, 1999.
[236] E. Brunauer, L. Deming, W.E. Deming, E. Teller, Theory of the Van Der Waals Adsorption of the Gases, 1940.
[237] K.S.W. Sing, Pure Appl. Chem. 54 (1982) 22–22.
[238] A.K. Ladavos, A.P. Katsoulidis, A. Iosifidis, K.S. Triantafyllidis, T.J. Pinnavaia, P.J. Pomonis, Microporous Mesoporous Mater. 151 (2012) 126–133.
[239] A.I. Biaglow, D.J. Parrillo, R.J. Gorte, J. Catal. 144 (1993) 193–201.
[240] B. R. G. Leliveld, J. W. Geus, M. J. H. V. Kerkhoffs, D. C. Koningsberger, F. A. Broersma, J. A. J. van Dillen, J. Chem. Soc. Faraday Trans. 94 (2005) 315.
[241] A. Platon, W.J. Thomson, Quantitative Lewis/Brönsted Ratios Using DRIFTS, American Chemical Society, 2003.
[242] S.J. Pennycook, A.R. Lupini, M. Varela, A.Y. Borisevich, Y. Peng, M.P. Oxley, K. Van Benthem, M.F. Chisholm, (n.d.).
[243] T.G. Rochow, P.A. Tucker, Introduction to Microscopy by Means of Light, Electrons, X Rays, or Acoustics. Second Edition, 1994.
[244] ASTM, Standard Test Method for Ash in Biomass E1755 - 01, 2015.
[245] J. Aguado, D.P. Serrano, G.S. Miguel, J.M. Escola, J.M. Rodríguez, J. Anal. Appl. Pyrolysis 78 (2007) 153–161.
[246] R.L. Blaine, J.E. Rose, TA Instruments (2004) 1–10.
[247] K. Wang, J. Zhang, B.H. Shanks, R.C. Brown, Green Chem. 17 (2015) 557–564.
[248] A. Saraeian, M.W. Nolte, B.H. Shanks, Renew. Sustain. Energy Rev. 104 (2019) 262–280.
[249] J. Rouquerolt, D. Avnir, C.W. Fairbridge, D.H. Everett, J.H. Haynes, N. Pernicone, J.D.F. Ramsay, K.S.W. Sing, K.K. Unger, Pure Appl. Chem. 66 (1994) 1739–1758.
[250] S. Storck, H. Bretinger, W.F. Maier, Appl. Catal. A Gen. 174 (1998) 137–146.
[251] J. Zhu, Y. Zhu, L. Zhu, M. Rigutto, A. Van Der Made, C. Yang, S. Pan, L. Wang, L. Zhu, Y. Jin, Q. Sun, Q. Wu, X. Meng, D. Zhang, Y. Han, J. Li, Y. Chu, A. Zheng, S. Qiu, X. Zheng, F.S. Xiao, J. Am. Chem. Soc. 136 (2014) 2503–2510.
[252] H. Zhang, Y. Ma, K. Song, Y. Zhang, Y. Tang, J. Catal. 302 (2013) 115–125.
[253] S. BECK, Jeffrey, T.-W. CHU, Cynthia, D. JOHNSON, Ivy, T. KRESGE, Charles, E. LEONOWICZ, Michael, J. ROTH, Wieslaw, C. VARTULI, James, SYNTHETIC POROUS CRYSTALLINE MATERIAL ITS SYNTHESIS AND USE, WO/1991/011390, 1991.
[254] V. Chiola, J.E. Ritsko, C.D. Vanderpool, United States Pat. Off. (1971) 1–3.
[255] A. Corma, Q. Kan, M.T. Navarro, J. Pérez-Pariente, F. Rey, Synthesis of MCM-41 with Different Pore Diameters without Addition of Auxiliary Organics, 1997.
[256] Y. Deng, J. Wei, Z. Sun, D. Zhao, Chem. Soc. Rev. 42 (2013) 4054–4070.
[257] A. Galarneau, D. Desplantier-Giscard, F. Di Renzo, F. Fajula, Thermal and Mechanical Stability of Micelle-Templated Silica Supports for Catalysis, 2001.
[258] S. El Mourabit, M. Guillot, G. Toquer, J. Cambedouzou, F. Goettmann, A. Grandjean, RSC Adv. 2 (2012) 10916–10924.

[259] Y. Li, W. Zhang, L. Zhang, Q. Yang, Z. Wei, Z. Feng, C. Li, J. Phys. Chem. B 108 (2004) 9739–9744.
[260] J.M.R. Gallo, C. Bisio, G. Gatti, L. Marchese, H.O. Pastore, Langmuir 26 (2010) 5791–5800.
[261] Y. Yue, A. Gédéon, J.-L. Bonardet, J.-B. D'Espinose, J. Fraissard, N. Melosh, Chem. Commun. (1999) 1967–1968.
[262] Z. Luan, M. Hartmann, D. Zhao, W. Zhou, L. Kevan, Chem. Mater. 11 (1999) 1621–1627.
[263] S. Sumiya, Y. Oumi, T. Uozumi, T. Sano, J. Mater. Chem. 11 (2001) 1111–1115.
[264] Y.S. Ooi, R. Zakaria, A.R. Mohamed, S. Bhatia, Catal. Commun. 5 (2004) 441–445.
[265] W. Li, S.J. Huang, S. Bin Liu, M.O. Coppens, Langmuir 21 (2005) 2078–2085.
[266] S. Zeng, J. Blanchard, M. Breysse, Y. Shi, X. Shu, H. Nie, D. Li, Microporous Mesoporous Mater. 85 (2005) 297–304.
[267] W. Hu, Q. Luo, Y. Su, L. Chen, Y. Yue, C. Ye, F. Deng, Microporous Mesoporous Mater. 92 (2006) 22–30.
[268] G. Muthu Kumaran, S. Garg, K. Soni, M. Kumar, L.D. Sharma, G. Murali Dhar, K.S. Rama Rao, Appl. Catal. A Gen. 305 (2006) 123–129.
[269] R. Van Grieken, J.M. Escola, J. Moreno, R. Rodríguez, Appl. Catal. A Gen. 305 (2006) 176–188.
[270] M. Gómez-Cazalilla, J.M. Mérida-Robles, A. Gurbani, E. Rodríguez-Castellón, A. Jiménez-López, J.M. Me, J. Solid State Chem. 180 (2007) 1130–1140.
[271] C. Li, Y.Y. Wang, Y.Y. Guo, X. Liu, Y.Y. Guo, Z. Zhang, Y.Y. Wang, G. Lu, Chem. Mater. 19 (2007) 173–178.
[272] G. Muthu Kumaran, S. Garg, K. Soni, M. Kumar, J.K. Gupta, L.D. Sharma, K.S. Rama Rao, G. Murali Dhar, Microporous Mesoporous Mater. 114 (2008) 103–109.
[273] J. Wang, Q. Liu, Solid State Commun. 148 (2008) 529–533.
[274] A. Zukal, H. Siklová, J. Cejka, Langmuir 24 (2008) 9837–9842.
[275] B. Dragoi, E. Dumitriu, C. Guimon, A. Auroux, Microporous Mesoporous Mater. 121 (2009) 7–17.
[276] L. Qiang, L. Wen-zhi, Z. Dong, Z. Xi-feng, J. Anal. Appl. Pyrolysis 84 (2009) 131–138.
[277] Q. Li, Z. Wu, B. Tu, S.S. Park, C.-S.S. Ha, D. Zhao, Microporous Mesoporous Mater. 135 (2010) 95–104.
[278] P. Bhange, D.S. Bhange, S. Pradhan, V. Ramaswamy, Appl. Catal. A Gen. 400 (2011) 176–184.
[279] T. Jiang, H. Tao, J. Ren, X. Liu, Y. Wang, G. Lu, Microporous Mesoporous Mater. 142 (2011) 341–346.
[280] A.L. de Lima, A. Mbengue, R. a. S. San Gil, C.M. Ronconi, C.J. a. Mota, Catal. Today 226 (2014) 210–216.
[281] A.J.J. Koekkoek, J.A. Rob van Veen, P.B. Gerrtisen, P. Giltay, P.C.M.M. Magusin, E.J.M. Hensen, Microporous Mesoporous Mater. 151 (2012) 34–43.
[282] C. Liang, M.C. Wei, H.H. Tseng, E.C. Shu, Chem. Eng. J. 223 (2013) 785–794.
[283] S. Lin, L. Shi, T. Yu, X. Li, X. Yi, A. Zheng, Microporous Mesoporous Mater. 207 (2015) 111–119.
[284] D. Meloni, D. Perra, R. Monaci, M.G. Cutrufello, E. Rombi, I. Ferino, Appl. Catal. B Environ. 184 (2016) 163–173.
[285] S. Xing, P. Lv, J. Fu, J. Wang, P. Fan, L. Yang, Z. Yuan, Microporous Mesoporous Mater. 239 (2017) 316–327.
[286] D.P. Serrano, J. Aguado, J.M. Escola, ACS Catal. 2 (2012) 1924–1941.
[287] A. Corma, Chem. Rev. 95 (1995) 559–614.
[288] I.C. Neves, G. Botelho, A. V. Machado, P. Rebelo, Eur. Polym. J. 42 (2006) 1541–1547.
[289] K. Li, S.W. Lee, G. Yuan, J. Lei, S. Lin, P. Weerachanchai, Y. Yang, J.-Y. Wang, K. Li, S.W. Lee, G. Yuan, J. Lei, S. Lin, P. Weerachanchai, Y. Yang, J.-Y. Wang, Energies 9 (2016) 431.
[290] J.M. Escola, D.P. Serrano, M. Arroyo, A. Alba, J. Mater. Cycles Waste Manag. 16 (2014) 435–441.
[291] B. Onida, B. Bonelli, L. Borello, S. Fiorilli, F. Geobaldo, E. Garrone, Stud. Surf. Sci. Catal. 142 (2002) 143–150.
[292] R. Borade, A. Sayari, A. Adnot, S. Kaliaguine, J. Phys. Chem. 94 (1990) 5989–5994.

[293] A. Osatiashtiani, B. Puértolas, C.C.S. Oliveira, J.C. Manayil, B. Barbero, M. Isaacs, C. Michailof, E. Heracleous, J. Pérez-Ramírez, A.F. Lee, K. Wilson, Biomass Convers. Biorefinery 7 (2017) 331–342.
[294] M. Kruk, M. Jaroniec, Chem. Mater. 13 (2001) 3169–3183.
[295] J. Fan, C. Yu, L. Wang, B. Tu, D. Zhao, Y. Sakamoto, O. Terasaki, J. Am. Chem. Soc. 123 (2001) 12113–12114.
[296] M. Hartmann, A. Vinu, Langmuir 18 (2002) 8010–8016.
[297] S.S. Kim, A. Karkamkar, T.J. Pinnavaia, M. Kruk, M. Jaroniec, J. Phys. Chem. B 105 (2001) 7663–7670.
[298] R. Carvajal, P.-J. Chu, J.H. Lunsford, J. Catal. 125 (1990) 123–131.
[299] D. Coster, A.L. Blumenfeld, J.J. Fripiat, J. Phys. Chem. 98 (1994) 6201–6211.
[300] D.P. Serrano, R.A. García, G. Vicente, M. Linares, D. Procházková, J. Čejka, J. Catal. 279 (2011) 366–380.
[301] S. Wu, Y. Han, Y. Zou, J. Song, L. Zhao, Y. Di, (2004) 486–492.
[302] Q. Li, K.C. Hunter, A.L.L. East, J. Phys. Chem. A 109 (2005) 6223–6231.
[303] B. Nagel, H. Dellweg, L.M. Gierasch, H. Dellweg, J.W. Engels, J.L. Fox, L.M. Gierasch, R.P. Gregson, B. Heinritz, H.G.W. Leuenberger, M. Moo-Young, A. Moser, B. Nagel, L. Nyeste, L. Pcnasse, G.B. Petersen, M. Van Montagu, Y. Yamada, Int. Union Pure Appl. Chem. 64 (1992) 143–168.
[304] THE EUROPEAN PARLIAMENT AND THE COUNCIL OF THE EUROPEAN UNION, Onn the Promotion of the Use of Energy from Renewable Sources and Amending and Subsequently Repealing Directives 2001/77/EC and 2003/30/EC, 2009.
[305] J.J.M. Orfão, F.J.A. Antunes, J.L. Figueiredo, Fuel 78 (1999) 349–358.
[306] S.D. Stefanidis, K.G. Kalogiannis, E.F. Iliopoulou, C.M. Michailof, P.A. Pilavachi, A.A. Lappas, J. Anal. Appl. Pyrolysis 105 (2014) 143–150.
[307] K. Raveendran, A. Ganesh, K.C. Khilar, Fuel 75 (1996) 987–998.
[308] H. Yang, R. Yan, H. Chen, C. Zheng, D.H. Lee, D.T. Liang, Energy and Fuels 20 (2006) 388–393.
[309] S. Wang, X. Guo, K. Wang, Z. Luo, J. Anal. Appl. Pyrolysis 91 (2011) 183–189.
[310] Q. Lu, X. Yang, C. Dong, Z. Zhang, X. Zhang, X. Zhu, J. Anal. Appl. Pyrolysis 92 (2011) 430–438.
[311] Y.C. Lin, J. Cho, G.A. Tompsett, P.R. Westmoreland, G.W. Huber, J. Phys. Chem. C 113 (2009) 20097–20107.
[312] S. Matsuoka, H. Kawamoto, S. Saka, J. Anal. Appl. Pyrolysis 106 (2014) 138–146.
[313] S. Maduskar, V. Maliekkal, M. Neurock, P.J. Dauenhauer, ACS Sustain. Chem. Eng. 6 (2018) acssuschemeng.8b00853.
[314] G. Dobele, G. Rossinskaja, G. Telysheva, D. Meier, S. Radtke, O. Faix, in:, Prog. Thermochem. Biomass Convers., Blackwell Science Ltd, Oxford, UK, n.d., pp. 1500–1508.
[315] J.B. Paine, Y.B. Pithawalla, J.D. Naworal, J. Anal. Appl. Pyrolysis 83 (2008) 37–63.
[316] S. Yaman, Energy Convers. Manag. 45 (2004) 651–671.
[317] P.R. Patwardhan, R.C. Brown, B.H. Shanks, ChemSusChem 4 (2011) 636–643.
[318] H. Yang, R. Yan, H. Chen, D.H. Lee, C. Zheng, Fuel 86 (2007) 1781–1788.
[319] F. Shafizadeh, G.D. McGinnis, R.A. Susott, H.W. Tatton, J. Org. Chem. 36 (1971) 2813–2818.
[320] E. Adler, Wood Sci. Technol. 11 (1977) 169–218.
[321] F.H.M. Graichen, W.J. Grigsby, S.J. Hill, L.G. Raymond, M. Sanglard, D.A. Smith, G.J. Thorlby, K.M. Torr, J.M. Warnes, Ind. Crops Prod. 106 (2017) 74–85.
[322] H. Kawamoto, J. Wood Sci. 63 (2017) 117–132.
[323] A.N. Glazer, H. Nikaido, Microbial Biotechnology : Fundamentals of Applied Microbiology, W.H. Freeman, 1995.
[324] U. Flessner, D.J. Jones, J. Roziere, J. Zajac, L. Storaro, M. Lenarda, M. Pavan, A. Jimenez-Lopez, E. Rodriguez-Castellon, M. Trombetta, G. Busca, J. Rozière, J. Zajac, L. Storaro, M. Lenarda, M. Pavan, A. Jiménez-lópez, M. Trombetta, G. Busca, J. Mol. Catal. A Chem. 168 (2001) 247–256.
[325] N. Kaur, D. Kishore, J. Chem. Pharm. Res. 4 (2012) 991–1015.

[326] Q. Sun, Z. Xie, J. Yu, Natl. Sci. Rev. 5 (2018) 542–558.
[327] S. Wilson, P. Barger, Microporous Mesoporous Mater. 29 (1999) 117–126.
[328] S. Iranica, M. Salmasi, S. Fatemi, S.J. Hashemi, Sci. Iran. C 19 (2012) 1632–1637.
[329] S.W. Kaiser, Production of Hydrocarbons with Aluminophosphate Molecular Sieves, 1984.
[330] A.S. Ivanova, Kinet. Catal. 53 (2012) 425–439.
[331] J. Gangwar, B.K. Gupta, S.K. Tripathi, A.K. Srivastava, Nanoscale 7 (2015) 13313–13344.
[332] C.A. Koufopanosi, ; G Maschio, A. Lucchesit, Can. J. Chem. Eng. 67 (1989) 75–84.
[333] T.R. Rao, A. Sharma, Energy 23 (1998) 973–978.
[334] R.J. Evans, T.A. Milne, Energy and Fuels 1 (1987) 311–319.
[335] R. Ball, A.C. McIntosh, J. Brindley, Combust. Theory Model. 8 (2004) 281–291.
[336] K.S.W. Sing, R.T. Williams, Adsorpt. Sci. Technol. 22 (2004) 773–782.
[337] J. Liang, H. Li, S. Zhao, W. Guo, R. Wang, M. Ying, Appl. Catal. 64 (1990) 31–40.
[338] A. Pattiya, J.O. Titiloye, A.V. Bridgwater, J. Anal. Appl. Pyrolysis 81 (2008) 72–79.
[339] F. Ates, N. Erginel, Fuel Process. Technol. 142 (2016) 279–286.
[340] D. Fabbri, C. Torri, V. Baravelli, J. Anal. Appl. Pyrolysis 80 (2007) 24–29.
[341] P.R. Patwardhan, J.A. Satrio, R.C. Brown, B.H. Shanks, J. Anal. Appl. Pyrolysis 86 (2009) 323–330.
[342] Q. Lu, W.-M. Xiong, W.-Z. Li, Q.-X. Guo, X.-F. Zhu, Bioresour. Technol. 100 (2009) 4871–6.
[343] T. Shoji, H. Kawamoto, S. Saka, J. Anal. Appl. Pyrolysis 109 (2014) 185–195.
[344] H. Kawamoto, M. Murayama, S. Saka, J. Wood Sci. 49 (2003) 469–473.
[345] X. Chen, Y. Chen, Z. Chen, D. Zhu, H. Yang, P. Liu, T. Li, H. Chen, J. Anal. Appl. Pyrolysis 129 (2018) 53–60.
[346] D.K. Shen, S. Gu, Bioresour. Technol. 100 (2009) 6496–6504.
[347] S. Wang, X. Guo, T. Liang, Y. Zhou, Z. Luo, Bioresour. Technol. 104 (2012) 722–728.
[348] R. Alén, E. Kuoppala, P. Oesch, J. Anal. Appl. Pyrolysis 36 (1996) 137–148.
[349] S. rong Wang, T. Liang, B. Ru, X. juan Guo, Chem. Res. Chinese Univ. 29 (2013) 782–787.
[350] Z. Ma, E. Troussard, J.A. van Bokhoven, Appl. Catal. A Gen. 423–424 (2012) 130–136.
[351] C.A. Mullen, A.A. Boateng, Fuel Process. Technol. 91 (2010) 1446–1458.
[352] K.G. Kalogiannis, S. Stefanidis, A. Marianou, C. Michailof, A. Kalogianni, A. Lappas, Waste and Biomass Valorization 6 (2015) 781–790.
[353] R.J.M. Westerhof, H.S. Nygård, W.P.M. Van Swaaij, S.R.A. Kersten, D.W.F. Brilman, Energy and Fuels 26 (2012) 2274–2280.
[354] R. Bodirlau, C.A. Teaca, L. Spiridon, BioResources 3 (2008) 789–800.
[355] D. Carpenter, T.L. Westover, S. Czernik, W. Jablonski, Green Chem. 16 (2014) 384–406.
[356] D.J.D.J. Nowakowski, T. Bridgwater, C.E.E. Greenhalf, D.J.D.J. Nowakowski, A.B.B. Harms, J.O.O. Titiloye, A.V. V. Bridgwater, Fuel 108 (2013) 216–230.
[357] G. Yildiz, K.M. van Geem, M. Djokic, R. Van Duren, M. Pronk, F. Ronsse, W. Prins, M. Djokic, K.M. van Geem, F. Ronsse, R. Van Duren, W. Prins, Validation of a New Set-up for Continuous Catalytic Fast Pyrolysis of Biomass Coupled with Vapour Phase Upgrading, Elsevier, 2013.
[358] A. Güngör, S. Önenç, S. Uçar, J. Yanik, J. Anal. Appl. Pyrolysis 97 (2012) 39–48.
[359] R. Mahadevan, S. Adhikari, R. Shakya, K. Wang, D. Dayton, M. Lehrich, S.E. Taylor, Energy and Fuels 30 (2016) 3045–3056.
[360] K. Murakami, S. Fujioka, K. Mitani, M. Yamashita, M. Taguchi, Kurinikaru Sutadi 4 (1983) 1063–1069.
[361] L. Ye, Y. Xiping, Z. Yuxia, Y. Aidi, ACTA Pet. Sin. 33 (2017) 1053–1060.
[362] M. Zhang, F.L.P. Resende, A. Moutsoglou, Fuel 116 (2014) 358–369.
[363] Y. Wan, D. Zhao, Chem. Rev. 107 (2007) 2821–2860.
[364] J. Socci, A. Osatiashtiani, G. Kyriakou, T. Bridgwater, Appl. Catal. A Gen. 570 (2019) 218–227.
[365] J.C. Groen, L.A. Peffer, J. Pérez-Ramírez, Microporous Mesoporous Mater. 60 (2003) 1–17.
[366] V.B.F. Custodis, S.A. Karakoulia, K.S. Triantafyllidis, J.A. Van Bokhoven, ChemSusChem 9 (2016) 1134–1145.

[367] S. Al-Khattaf, Energy and Fuels 17 (2003) 62–68.
[368] A.M. Azeez, D. Meier, urgen Odermatt, T. Willner, J. Odermatt, T. Willner, J. Anal. Appl. Pyrolysis 24 (2010) 2078–2085.
[369] L.B. McCusker, D.H. Olson, C. Baerlocher, Atlas of Zeolite Framework Types, 2007.
[370] D.H. Olson, G.T. Kokotallo, S.L. Lawton, Meler, J. Phys. Chem. 85 (1981) 2238–2243.
[371] P. Charoenwiangnuea, T. Maihom, P. Kongpracha, J. Sirijaraensre, J. Limtrakul, RSC Adv. 6 (2016) 105888–105894.
[372] W.L. Fanchiang, Y.C. Lin, Appl. Catal. A Gen. 419–420 (2012) 102–110.
[373] A.T. To, D.E. Resasco, Appl. Catal. A Gen. 487 (2014) 62–71.
[374] J. Adam, E. Antonakou, A. Lappas, M. Stöcker, M.H. Nilsen, A. Bouzga, J.E. Hustad, G. Øye, Microporous Mesoporous Mater. 96 (2006) 93–101.
[375] a. G. Gayubo, B. Valle, a. T. Aguayo, M. Olazar, J. Bilbao, J. Chem. Technol. Biotechnol. 85 (2010) 132–144.
[376] S. Müller, Y. Liu, M. Vishnuvarthan, X. Sun, A.C. van Veen, G.L. Haller, M. Sanchez-Sanchez, J. a. Lercher, J. Catal. 325 (2015) 48–59.
[377] A.J. Foster, J. Jae, Y.-T. Cheng, G.W. Huber, R.F. Lobo, Appl. Catal. A Gen. 423–424 (2012) 154–161.
[378] H.J. Park, H.S. Heo, J.-K. Jeon, J. Kim, R. Ryoo, K.-E. Jeong, Y.-K. Park, Appl. Catal. B Environ. 95 (2010) 365–373.
[379] T.R. Carlson, J. Jae, G.W. Huber, ChemCatChem 1 (2009) 107–110.
[380] M. Bjørgen, S. Svelle, F. Joensen, J. Nerlov, S. Kolboe, F. Bonino, L. Palumbo, S. Bordiga, U. Olsbye, J. Catal. 249 (2007) 195–207.
[381] K. Wang, P.A. Johnston, R.C. Brown, Bioresour. Technol. 173 (2015) 124–131.
[382] K. Jindo, H. Mizumoto, Y. Sawada, M.A. Sanchez-Monedero, T. Sonoki, Biogeosciences 11 (2014) 6613–6621.

9. Appendix A – Py-GC/MS chromatograms for the catalytic fast pyrolysis of LDPE

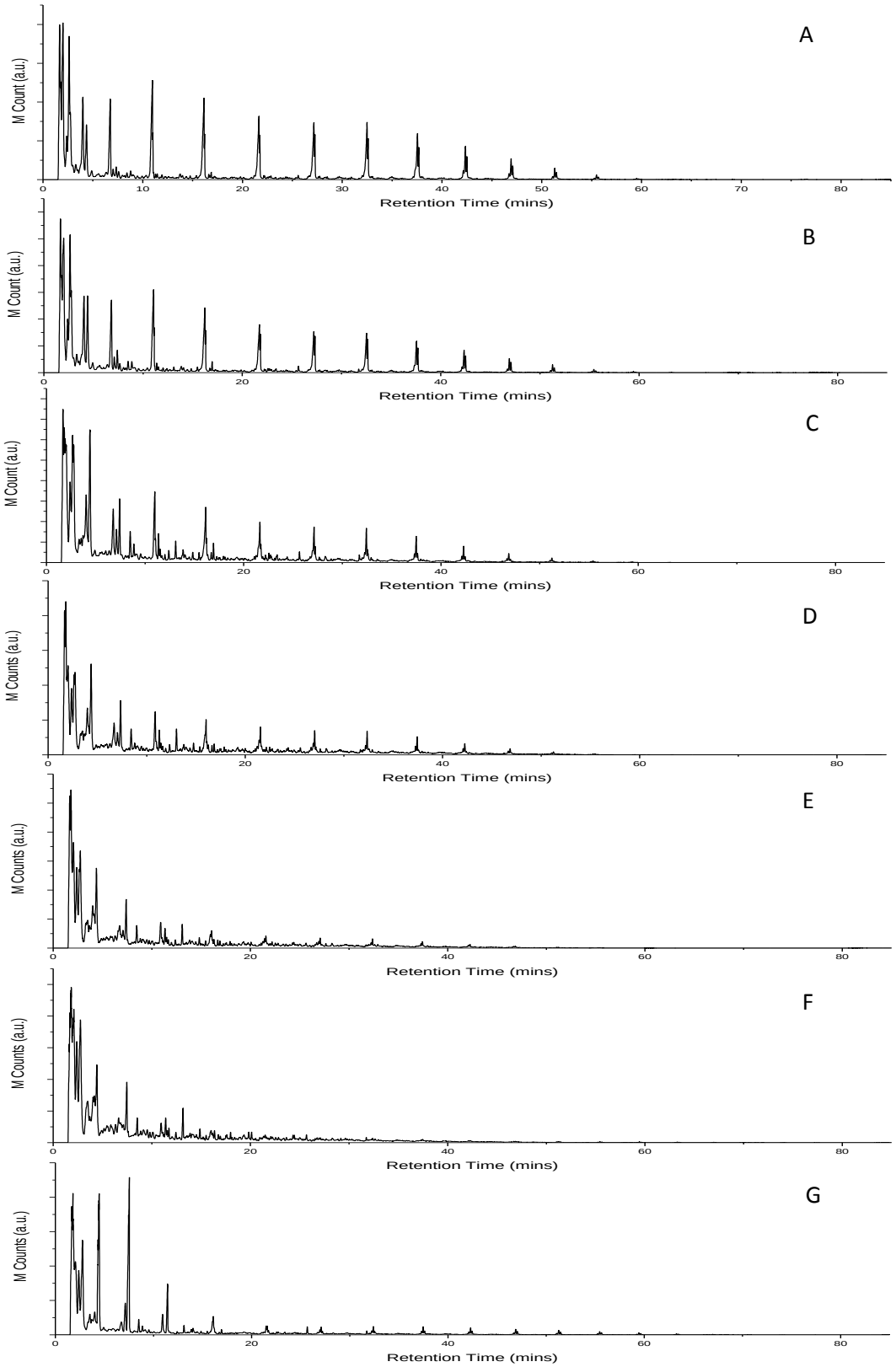

Fig. A 1. Py-GC/MS chromatograms for LDPE catalyst mixtures at 700 °C for 10 s. A) Thermal, B) SBA-15, C) AlSBA15(100), D) AlSBA15(35), E) AlSBA15(15), F) AlSBA15(15), and G) AlSBA15(5)

10. Appendix B – Pyroprobe identified products by mass spectrometry using NIST database

***Table A 1**. Identified products by mass spectrometry using NIST database for the non-catalytic and catalytic pyrolysis of biomass components (cellulose, hemicellulose and lignin)*

Compound	Formula	MW (g mol $^{-1}$)	Group
2-Butene	C4H8	56.11	Hydrocarbons
Butene	C4H8	56.11	Hydrocarbons
Acetic acid	C2H4O2	60.05	Acids
Methyl formate	C2H4O2	60.05	Ester/Ether
Cyclopentadiene	C5H6	66.10	Hydrocarbons
Cyclopentatriol	C5H6	66.10	Alcohols
Furan	C4H4O	68.08	Furans
1,3 Butadien-1-ol	C4H6O	70.09	Alcohols
2-Butanal	C4H6O	70.09	Aldehydes
2-propen-1-ol 2-methyl	C4H8O	72.11	Alcohols
Propanoic acid	C3H6O2	74.08	Acids
Benzene	C6H6	78.11	Aromatics
Furan 2-methyl	C5H6O	82.10	Furans
Furan 3-methyl	C5H6O	82.10	Furans
2-cyclopentan-1-one	C5H6O	82.10	Ketones
Furanone	C4H4O2	84.07	Furans
2(5H) Furanone	C4H4O2	84.07	Furans
Cyclopentanone	C5H8O	84.12	Ketones
Furan 2,3-dihydro 3-methyl	C5H8O	84.12	Furans
2-Butene 2,3-dimethyl	C6H12	84.16	Hydrocarbons
1,3-dioxol 2-one	C3H2O3	86.05	Ketones
3-penten-1-ol	C5H10O	86.13	Alcohols
1-methyl cyclopropanemethanol	C5H10O	86.13	Alcohols
3-Pentanone	C5H10O	86.13	Ketones
1-Hydroxy-2-butanone	C4H8O2	88.11	Ketones
Toluene	C7H8	92.14	Aromatics
Phenol	C6H6O	94.11	Phenolics
Furfural	C5H4O2	96.09	Furans
3-Furaldehyde	C5H4O2	96.09	Furans
2-cyclopenten-1-one 2-methyl	C6H8O	96.13	Ketones
Furan 2,5-dimethyl	C6H8O	96.13	Furans
2-cyclopeten-1-one 3-methyl	C6H8O	96.13	Ketones
2,4-dimethyl Furan	C6H8O	96.13	Furans
Maleic anhydride	C4H2O3	98.06	Ketones
2-cyclopenten-1-one 2-hydroxy	C5H6O2	98.10	Ketones
Furanone 5-methyl	C5H6O2	98.10	Furans
2(5H) Furanone 5-methyl	C5H6O2	98.10	Furans
2(3H) Furanone 5-methyl	C5H6O2	98.10	Furans
1,2-cyclopentadione	C5H6O2	98.10	Ketones
1,5-hexadien-3-ol	C6H10O	98.15	Alcohols
2-pentenal 2-methyl	C6H10O	98.15	Aldehydes
Butenoic acid 2-methyl	C5H8O2	100.12	Acids
3-cyclopentene-1,2-diol	C5H8O2	100.12	Alcohols

Pentadione	C5H8O2	100.12	Ketones
3-cyclopentene 1,2-diol cis	C5H8O2	100.12	Ketones
Hexanal	C6H12O	100.16	Aldehydes
Styrene	C8H8	104.15	Aromatics
p-Xylene	C8H10	106.17	Aromatics
Ethyl benzene	C8H10	106.17	Aromatics
o-Xylene	C8H10	106.17	Aromatics
Phenol 3-methyl	C7H8O	108.14	Phenolics
Phenol 2-methyl	C7H8O	108.14	Phenolics
p-Cresol	C7H8O	108.14	Phenolics
2-Furancarboxaldehyde 5-methyl	C6H6O2	110.11	Furans
Ethanone 1,2-Furanyl	C6H6O2	110.11	Furans
Reorcinol	C6H6O2	110.11	Phenolics
Furan 2-ethyl 5-methyl	C7H10O	110.15	Furans
3,5-Heptadien-2-one	C7H10O	110.16	Ketones
3,4-dimethyl-2-cyclopenten-1-one	C7H10O	110.16	Ketones
2,3-dimethyl 2-cyclopenten-1-one	C7H10O	110.16	Ketones
Furan 2-propyl	C7H10O	110.16	Furans
1,4-Hexadiene 2,3-dimethyl	C8H14	110.20	Hydrocarbons
Cyclopenten-1-one 2-hydroxy 3-methyl	C6H8O2	112.13	Ketones
Furan 2-methoxy methyl	C6H8O2	112.13	Furans
3-methyl 1,2-cyclopentadione	C6H8O2	112.13	Ketones
Cyclohexene-1,2-diol	C6H10O2	114.14	Alcohols
2,4-hexanedione	C6H10O2	114.14	Ketones
2H-Pyran-3(4H)-one, dihydro-6-methyl	C6H10O2	114.14	Ketones
Heptanal	C7H14O	114.19	Aldehydes
Oxetane 2-methyl 4-propyl	C7H14O	114.19	Ester/Ether
Butanoic acid 4-hydroxy methylene	C5H8O3	116.12	Acids
Hexanoic acid	C6H12O2	116.16	Acids
1,2-cyclohexanediol	C6H12O2	116.16	Alcohols
Indene	C9H8	116.16	Aromatics
Heptan-1-ol	C7H16O	116.88	Alcohols
Succinic acid	C4H6O4	118.09	Acids
Benzofuran	C8H6O	118.14	Aromatics
2,4,3,5-dimethylene-1-diol	C6H14O2	118.18	Alcohols
Benzene 1-ethyl 2-methyl	C9H12	120.19	Aromatics
Benzene 1-ethyl 3-methyl	C9H12	120.19	Aromatics
Benzene 1,2,4-trimethyl	C9H12	120.20	Aromatics
Mesitylene	C9H12	120.20	Aromatics
Phenol 3,5-dimethyl	C8H10O	122.16	Phenolics
Phenol 2,4-dimethyl	C8H10O	122.16	Phenolics
Phenol 2,5-dimethyl	C8H10O	122.17	Phenolics
Phenol 3,4-dimethyl	C8H10O	122.17	Phenolics
2,5-Furandicarboxaldehyde	C6H4O3	124.10	Furans
Phenol 2-methoxy	C7H8O2	124.14	Phenolics
5-Hydroxy methyl furfural	C6H6O3	126.11	Furans
Furfural hydroxy methyl ketone	C6H6O3	126.11	Furans
Levoglucosenone	C6H6O3	126.11	Anhydrosugars
3-ethyl-2-hydroxy-2-cyclopenten-1-one	C7H10O2	126.16	Ketones

2,5-dimethyl-4-hydroxy 3(2H) furanone	C6H8O3	128.13	Furans
1(H) Indene 1-methylene	C10H8	128.17	Aromatics
Naphthalene	C10H8	128.17	Polycyclic Aromatics
3-octen-1-ol	C8H16O	128.21	Alcohols
2-butanone (1-acetloxy)	C6H10O3	130.14	Ketones
1(H) Indene 3-methyl	C10H10	130.19	Aromatics
Cinnamaldehyde	C9H8O	132.16	Aldehydes
Benzofuran 2-methyl	C9H8O	132.16	Aromatics
Benzene 1-methyl-2-propyl-	C10H14	134.22	Aromatics
Benzene butyl	C10H14	134.22	Aromatics
Benzene-4-ethenyl 1,2-dimethyl	C10H14	134.22	Aromatics
Creosol	C8H10O2	138.16	Phenolics
Cyclohexene 3-methyl 6-(1-methylethyl) trans	C10H18	138.25	Hydrocarbons
1,2-benzenediol 3-methoxy	C7H8O3	140.14	Phenolics
4-pyran-4-one 3,5-dihydroxy methyl	C6H6O4	142.11	Anhydrosugars
1H-Indene 1-ethlidiene	C11H10	142.20	Aromatics
Naphthalene 2-methyl	C11H10	142.20	Polycyclic Aromatics
1,4:3,6-dianhydro-a-d-glucopyranose	C6H8O4	144.13	Anhydrosugars
Cinnamaldehyde b-methyl	C10H10O	146.19	Aldehydes
Benzofuran 4,7-dimethyl	C10H10O	146.19	Aromatics
Benzene [(1-methyl 2-propenyl)oxy]	C10H12O	148.20	Phenolics
Benzene pentyl	C11H16	148.25	Aromatics
2-methoxy 4-vinyl phenol	C9H10O2	150.18	Phenolics
R-Vanillin	C8H8O3	152.15	Phenolics
Phenol 4-ethyl 2-methoxy	C9H12O2	152.19	Phenolics
1,4-benzenediol 2,3,5-trimethyl	C9H12O2	152.19	Phenolics
3,5-dimethoxy toluene	C9H12O2	152.19	Phenolics
1,1-bicyclopentyl 2-one	C10H16O	152.23	Ketones
Phenol 2,6-dimethoxy	C8H10O3	154.17	Phenolics
2,6-dimethylocta 2,6-dien-1-ol	C10H18O	154.25	Ketones
(3E)-3,5,7-trimethyl-3-octene	C11H22	154.29	Hydrocarbons
3-octene 2,5-diene-6,6,7-trimethyl	C11H22	154.29	Hydrocarbons
Naphthalene 1,7-dimethyl	C12H12	156.22	Polycyclic Aromatics
Naphthalene 1,3-dimethyl	C12H12	156.22	Polycyclic Aromatics
Levoglucosan	C6H10O5	162.14	Anhydrosugars
Furan 2-(2-furan,1-methyl) 5-methyl	C10H10O2	162.19	Furans
2H-1-Benzopyran-2-one 3,4-dihydro-6-hydroxy	C9H8O3	164.16	Ketones
Eugenol	C10H12O2	164.20	Phenolics
Trans-isoeugenol	C10H12O2	164.20	Phenolics
Cyclopentyl proponoic acid benzyl ester	C10H12O2	164.20	Ester/Ether
Phenol 3-methoxy 2,4,5-trimethyl	C10H14O2	166.22	Phenolics
2,5-dimethoxy benzyl alcohol	C9H12O3	168.19	Phenolics
1,2,4-trimethyloxy benzene	C9H12O3	168.19	Phenolics
2-cyclohexen-1-one 2-hydroxy 6-methyl-3	C10H16O2	168.23	Alcohols
Heptane (1,2-butenyloxy)	C11H22O	170.30	Ester/Ether
Furan 2,2-methylene bis 5-methyl	C11H12O2	176.21	Furans
3-tertbutyl 4-hydroxy anisole	C11H16O2	180.25	Phenolics
Benzaldehyde 4-hydroxy 3,5-dimethoxy	C9H10O4	182.17	Phenolics
5-tert butylpyrogallol	C10H14O3	182.22	Phenolics

5,7-octadiene-3-ol 2,4,4,7-tetramethyl	C12H22O	182.30	Alcohols
2-cyclopenten-1-one 2-hydroxy 4-methyl	C8H12O5	188.18	Alcohols
Glucopyranoside	C7H14O6	194.18	Anhydrosugars
Phenol 2,6 dimethoxy 4,2-propenyl	C11H14O3	194.23	Phenolics
2-allyl 1,4-dimethoxy 3-methyl benzene	C11H14O3	194.23	Phenolics
Ethanone 1,4-hydroxy 3,5-dimethoxy phenyl	C10H12O4	196.20	Phenolics
Cantharidin	C10H12O4	196.20	Misc
4-acetoxy 3-methoxyacetephenone	C11H12O4	208.21	Phenolics
Desapidinol	C11H14O4	210.23	Phenolics
Hexadecanoic acid ethyl ester	C18H36O2	284.48	Ester/Ether
Glucopyranosole	C18H32O16	504.44	Anhydrosugars

11. Appendix C – Quantification of the catalytic fast pyrolysis of beech wood products

***Table A 2**. Table of standards used for calibration of GC-FID for quantification of pyrolysis products.*

Compound	RT (FID)	Formula	MW (g mol $^{-1}$)	Group	R^2
Methanol	4.971	CH3OH	32.04	Alcohol	0.9998
Furan	5.343	C4H4O	68.07	Furan	1.0000
2-methylfuran	5.343	C5H6O	82.10	Furan	1.0000
Methyl acetate	6.085	C3H6O2	74.08	Ester/Ether	0.9997
Pyruvic acid	6.212	C3H4O3	88.06	Acid	0.9998
Cyclohexane	7.88	C6H12	84.16	Hydrocarbon	0.9990
Cyclohexene	8.739	C6H10	82.14	Hydrocarbon	0.9992
Benzene	9.141	C6H6	78.11	Aromatic	0.9999
Glycolaldehyde	10.052	C2H4O2	60.05	Aldehyde	0.9998
2,5-dimethylfuran	10.391	C6H8O	96.13	Furan	1.0000
Acetic acid	11.347	CH3COOH	60.05	Acid	0.9955
Toluene	12.668	C7H8	92.14	Aromatic	0.9998
Ethyl benzene	15.336	C8H10	106.17	Aromatic	0.9996
m-Xylene	15.502	C8H10	106.17	Aromatic	0.9997
o-Xylene	16.165	C8H10	106.17	Aromatic	0.9996
Methyl pyruvate	16.391	C4H6O3	102.09	Ester/Ether	0.9994
Succindialdehyde	16.455	C4H6O2	86.09	Aldehyde	0.9997
Furfural	16.792	C5H4O2	96.08	Furan	0.9997
Anisole	17.262	C7H8O	108.14	Aromatic	0.9984
Benzene 1-ethyl-2-methyl	17.532	C9H12	120.20	Aromatic	0.9986
Benzene 1-ethyl-4-methyl	17.594	C9H12	120.19	Aromatic	0.9999
Mesitylene	17.705	C9H12	120.19	Aromatic	0.9999
1,2,4-trimethylbenzene	18.274	C9H12	120.19	Aromatic	0.9999
Benzaldehyde	19.04	C7H6O	106.12	Aromatic	0.9999
Indane	19.198	C9H10	118.18	Aromatic	0.9997
Diethyl benzene	19.234	C10H14	134.22	Aromatic	0.9994
2-furanmethanol	19.253	C5H6O2	98.10	Furan	0.9994
2-furaldehyde	19.359	C6H6O2	110.1106	Furan	0.9984
Indene	19.713	C9H8	116.16	Aromatic	0.9984
Benzene 4-ethenyl-1,2-dimethyl	19.913	C10H14	134.22	Aromatic	0.9994
Phenol	20.878	C6H5OH	94.11	Phenolic	0.9994
Benzyl alcohol	20.894	C7H8O	108.14	Phenolic	0.9987
1H-Indene 3-methyl	20.917	C10H10	130.19	Aromatic	0.9981
Acetophenone	20.944	C8H8O	120.15	Phenolic	0.9994
o-Cresol	21.213	C7H8O	108.14	Phenolic	0.9984
Guaiacol	21.311	C7H8O2	124.14	Phenolic	0.9998
m-Cresol	22.218	C7H8O	108.14	Phenolic	0.9998
p-Cresol	22.225	C7H8O	108.14	Phenolic	0.9998
Acetovanillone	22.229	C9H10O3	166.17	Phenolic	0.9998

Naphthalene	22.406	C10H8	128.17	PAHs	0.9513
Naphthalene 1,2-dihydro-4-methyl	22.406	C11H12	144.21	PAHs	0.9997
Naphthalene 2-methyl	22.406	C11H10	142.20	PAHs	0.9997
Naphthalene 1,7-dimethyl	22.406	C12H12	156.22	PAHs	0.9997
Creosol	22.822	C8H10O2	138.16	Phenolic	0.9997
3-Ethylphenol	23.457	C8H10O	122.17	Phenolic	1.0000
5-Hydroxymethylfuran	25.22	C6H8O3	128.126	Furan	1.0000
Syringol	25.4	C8H10O3	154.16	Phenolic	0.9832
Isoeugenol	25.739	C10H12O2	164.20	Phenolic	0.9708
Catechol	26.416	C6H6O2	110.11	Phenolic	0.9996
1,2,4-Trimethoxybenzene	26.515	C9H12O3	168.19	Phenolic	0.9708
Vanillin	26.797	C8H8O3	152.15	Phenolic	0.9708
3-Hydroxybenzyl alcohol	27.205	C7H8O2	124.14	Phenolic	0.9985
Vanillyl alcohol	27.498	C8H10O3	154.17	Phenolic	0.9944
3',5'-dimethoxyacetophenone	27.757	C10H12O3	180.20	Phenolic	0.9967
Phenol 2,6-dimethoxy-4-(2-propenyl)	28.269	C11H14O3	194.23	Phenolic	0.9987
Levoglucosan	29.505	C6H10O5	162.14	Anhydrosugar	0.9996
Syringaldehyde	30.627	C9H10O4	182.17	Phenolic	0.9770
3-(4-methoxyphenoxy)benzaldehyde	30.632	C14H12O3	228.25	Phenolic	0.9985
3-Phenoxybenzyl alcohol	30.807	C13H12O2	200.24	Phenolic	0.9984
Anthracene	31.049	C14H10	178.23	PAHs	0.9982
Anthracene 2-methyl	31.724	C15H12	192.26	PAHs	0.9997

Table A 3*. Table of standards used for calibration of GC-TCD for quantification of pyrolysis products.*

Compound	RT (TCD)	Formula	MW (g mol $^{-1}$)	Group	R^2
CO	2.613	CO	28.01	Gas	0.9745
CO_2	3.423	CO2	44.01	Gas	0.9806
Ethene	3.793	C2H4	28.05	Gas	0.9651
Propene	10.558	C3H6	42.08	Gas	0.9804
1-Butene	15.309	C4H8	56.11	Gas	0.9825

Table A 4*. Product distribution of quantified products for the non-catalytic and catalytic in-situ pyrolysis of beech wood at 500 °C. All values are reported in C. % of total carbon in feed. Greyed cells are noteworthy outcomes. Results are an average of 2 experiments.*

	Beech Wood	e-FCC			AlSBA15(5)			ZSM-5		
		1:1	5:1	10:1	1:1	5:1	10:1	1:1	5:1	10:1
Non-aromatic hydrocarbons	**0.00**	**0.00**	**0.00**	**0.00**	**0.00**	**0.00**	**0.00**	**0.00**	**0.00**	**0.00**
Cyclohexane	0.00	0.00	0.00	0.00	0.00	0.00	0.00	0.00	0.00	0.00

Cyclohexene	0.00	0.00	0.00	0.00	0.00	0.00	0.00	0.00	0.00	0.00
Acids	**7.01**	**7.59**	**7.56**	**7.13**	**6.26**	**2.25**	**0.72**	**5.74**	**0.95**	**0.41**
Acetic acid	3.78	4.14	4.25	4.40	3.95	2.25	0.72	3.63	0.95	0.41
Pyruvic acid	3.23	3.45	3.32	2.73	2.31	0.00	0.00	2.11	0.00	0.00
Alcohols	**2.35**	**2.73**	**3.64**	**3.45**	**4.15**	**3.02**	**4.14**	**0.00**	**0.00**	**0.00**
Methanol	2.35	2.73	3.64	3.45	4.15	3.02	4.14	0.00	0.00	0.00
Aldehydes	**7.27**	**6.91**	**3.49**	**1.65**	**1.52**	**0.00**	**0.00**	**1.21**	**0.00**	**0.00**
Succindialdehyde	3.17	3.22	1.89	0.00	0.00	0.00	0.00	0.00	0.00	0.00
Glycolaldehyde	4.11	3.69	1.60	1.65	1.52	0.00	0.00	1.21	0.00	0.00
Ester/Ethers	**4.18**	**2.25**	**2.07**	**1.69**	**2.27**	**2.22**	**1.95**	**1.39**	**0.00**	**0.00**
Methyl acetate	2.35	0.44	0.73	1.69	2.27	2.22	1.95	1.39	0.00	0.00
Methyl pyruvate	1.82	1.80	1.34	0.00	0.00	0.00	0.00	0.00	0.00	0.00
Acetic acid (acetolxy)	0.00	2.05	0.00	0.00	1.16	0.00	0.00	0.69	0.00	0.00
Monocyclic Aromatics	**0.00**	**0.00**	**0.04**	**0.05**	**0.00**	**0.52**	**0.67**	**1.99**	**13.89**	**15.66**
Benzene	0.00	0.00	0.00	0.00	0.00	0.00	0.00	0.12	1.55	1.98
Toluene	0.00	0.00	0.04	0.05	0.00	0.19	0.36	0.97	4.01	5.01
m-xylene	0.00	0.00	0.00	0.00	0.00	0.10	0.10	0.82	4.91	5.75
o-xylene	0.00	0.00	0.00	0.00	0.00	0.00	0.00	0.00	0.00	0.00
Mesitylene	0.00	0.00	0.00	0.00	0.00	0.00	0.00	0.09	0.00	0.00
diethyl benzene	0.00	0.00	0.00	0.00	0.00	0.00	0.00	0.00	0.00	0.00
Ethyl benzene	0.00	0.00	0.00	0.00	0.00	0.00	0.00	0.00	0.42	0.33
Benzene 1-ethyl-2-methyl	0.00	0.00	0.00	0.00	0.00	0.00	0.00	0.00	0.21	0.16
Benzene 1-ethyl-4-methyl	0.00	0.00	0.00	0.00	0.00	0.00	0.00	0.00	0.23	0.14
Benzene 1,2,4-trimethyl	0.00	0.00	0.00	0.00	0.00	0.04	0.08	0.00	0.66	0.79
Indane	0.00	0.00	0.00	0.00	0.00	0.00	0.00	0.00	0.37	0.31
Indene	0.00	0.00	0.00	0.00	0.00	0.06	0.08	0.00	0.57	0.52
Benzene 4-ethenyl-1,2-dimethyl	0.00	0.00	0.00	0.00	0.00	0.00	0.00	0.00	0.15	0.10
1H-Indene 3-methyl	0.00	0.00	0.00	0.00	0.00	0.12	0.05	0.00	0.83	0.57
Polycyclic Aromatic Hydrocarbons (PAHs)	**0.00**	**0.00**	**0.00**	**0.00**	**0.00**	**0.28**	**0.43**	**1.46**	**5.16**	**5.77**
Naphthalene	0.00	0.00	0.00	0.00	0.00	0.05	0.05	0.53	1.58	2.10
Naphthalene 1,2-dihydro-4-methyl	0.00	0.00	0.00	0.00	0.00	0.00	0.00	0.06	0.00	0.00
Naphthalene 2-methyl	0.00	0.00	0.00	0.00	0.00	0.15	0.16	0.69	1.95	2.14

Naphthalene 1,7-dimethyl	0.00	0.00	0.00	0.00	0.00	0.06	0.00	0.08	0.96	0.77
Anthracene	0.00	0.00	0.00	0.00	0.00	0.02	0.22	0.10	0.36	0.44
Anthracene 2-methyl	0.00	0.00	0.00	0.00	0.00	0.00	0.00	0.00	0.30	0.33
Furans	**0.76**	**1.75**	**2.57**	**3.17**	**2.60**	**2.81**	**1.88**	**2.71**	**0.29**	**0.00**
Furan	0.05	0.25	0.84	1.35	1.32	1.64	1.34	1.65	0.29	0.00
2,5-dimethylfuran	0.00	0.00	0.00	0.00	0.00	0.08	0.00	0.00	0.00	0.00
Furfural	0.46	0.88	1.27	1.19	0.60	0.49	0.16	0.51	0.00	0.00
2-methylfuran	0.00	0.21	0.46	0.62	0.60	0.60	0.38	0.55	0.00	0.00
2-Furanmethanol	0.00	0.25	0.00	0.00	0.08	0.00	0.00	0.00	0.00	0.00
2-Furancarboxaldehyde 5-methyl	0.00	0.00	0.00	0.00	0.00	0.00	0.00	0.00	0.00	0.00
5-hydroxymethylfuran	0.25	0.17	0.00	0.00	0.00	0.00	0.00	0.00	0.00	0.00
Phenolics	**2.38**	**2.63**	**2.39**	**1.80**	**1.37**	**0.08**	**0.00**	**2.92**	**0.53**	**0.14**
Anisole	0.00	0.00	0.00	0.00	0.00	0.00	0.00	0.00	0.00	0.00
Benzaldehyde	0.00	0.00	0.00	0.00	0.00	0.00	0.00	0.00	0.00	0.00
phenol	0.00	0.09	0.15	0.24	0.18	0.04	0.00	0.40	0.07	0.00
Benzyl alcohol	0.00	0.00	0.00	0.00	0.00	0.00	0.00	0.00	0.00	0.00
Acetophenone	0.00	0.00	0.00	0.00	0.00	0.00	0.00	0.00	0.00	0.00
Guaiacol	0.18	0.25	0.32	0.34	0.20	0.00	0.00	0.19	0.00	0.00
p-cresol	0.00	0.00	0.08	0.00	0.00	0.00	0.00	0.10	0.00	0.00
Acetovanillone	0.00	0.00	0.00	0.00	0.00	0.00	0.00	0.00	0.00	0.00
Creosol	0.12	0.13	0.17	0.14	0.07	0.00	0.00	0.11	0.00	0.00
3-ethylphenol	0.00	0.00	0.00	0.00	0.00	0.00	0.00	0.00	0.00	0.00
Isoeugenol	0.21	0.22	0.15	0.14	0.11	0.00	0.00	0.15	0.00	0.00
Catechol	0.00	0.00	0.00	0.00	0.00	0.00	0.00	0.00	0.00	0.00
Vanillin	0.00	0.00	0.00	0.00	0.00	0.00	0.00	0.00	0.00	0.00
3-hydroxybenzyl alcohol	0.00	0.00	0.00	0.00	0.00	0.00	0.00	0.00	0.00	0.00
Vanillyl alcohol	0.00	0.00	0.00	0.00	0.00	0.00	0.00	0.00	0.00	0.00
3',5'-dimethoxy-acetophenone	0.15	0.13	0.06	0.02	0.04	0.00	0.00	0.13	0.00	0.00
3-(4-methoxyphen-oxy)benzaldehyde	0.00	0.00	0.00	0.00	0.00	0.00	0.00	0.00	0.00	0.00
3-Phenoxybenzyl alcohol	0.00	0.00	0.00	0.00	0.00	0.00	0.00	0.00	0.00	0.00
Phenol 2-methyl	0.00	0.00	0.00	0.04	0.00	0.04	0.00	0.00	0.00	0.00
m-Cresol	0.00	0.00	0.00	0.00	0.00	0.00	0.00	0.00	0.12	0.00
Syringol	0.49	0.60	0.70	0.55	0.34	0.00	0.00	0.47	0.00	0.00
1,2,4-trimethoxybenzene	0.36	0.38	0.35	0.15	0.16	0.00	0.00	0.41	0.22	0.14
Phenol 2,6-dimeth-oxy-4-(2-propenyl)	0.65	0.66	0.30	0.13	0.20	0.00	0.00	0.81	0.06	0.00
Syringaldehyde	0.22	0.17	0.11	0.06	0.06	0.00	0.00	0.16	0.06	0.00

Anhydrosugars	**7.61**	**3.96**	**0.78**	**0.00**	**0.97**	**0.00**	**0.00**	**2.50**	**0.00**	**0.00**
Levoglucosan	7.61	3.96	0.78	0.00	0.97	0.00	0.00	2.50	0.00	0.00